

**CENTER OF EXCELLENCE
FOR
MATERIALS RESEARCH**

Final Progress Report

DISTRIBUTION STATEMENT A
Approved for Public Release
Distribution Unlimited



UMBC

MECHANICAL ENGINEERING
University of Maryland, Baltimore County
1000 Hilltop Circle
Baltimore, Maryland 21250

20010116 121

**CENTER OF EXCELLENCE
FOR
MATERIALS RESEARCH**

Final Progress Report

**By
Dr. Akhtar S. Khan**

**U.S. Army Research Office
Contract/Grant No: DAAH04-95-2-0004**

**The University of Maryland Baltimore County
1000 Hilltop Circle
Baltimore, MD 21250**

APPROVED FOR PUBLIC RELEASE; DISTRIBUTION UNLIMITED

**THE VIEWS, OPINIONS, AND /OR FINDINGS CONTAINED IN THIS REPORT ARE
THOSE OF THE AUTHOR(S) AND SHOULD NOT BE CONSTRUED AS AN OFFICIAL
DEPARTMENT OF THE ARMY POSITION, POLICY, OR DECISION, UNLESS SO
DESIGNATED BY OTHER DOCUMENTATION**

REPORT DOCUMENTATION PAGE

Form Approved
OMB NO. 0704-0188

Public reporting burden for this collection of information is estimated to average 1 hour per response, including the time for reviewing instructions, searching existing data sources, gathering and maintaining the data needed, and completing and reviewing the collection of information. Send comment regarding this burden estimate or any other aspect of this collection of information, including suggestions for reducing this burden, to Washington Headquarters Services, Directorate for Information Operations and Reports, 1215 Jefferson Davis Highway, Suite 1204, Arlington, VA 22202-4302, and to the Office of Management and Budget, Paperwork Reduction Project (0704-0188), Washington, DC 20503.

1. AGENCY USE ONLY (Leave blank)		2. REPORT DATE 10/28/98 <i>12/11/98 Revised</i>	3. REPORT TYPE AND DATES COVERED Final (15 June 95 - 31 July 98)
4. TITLE AND SUBTITLE Center of Excellence for Materials Research			5. FUNDING NUMBERS DAAH04 - 95-2-0004
6. AUTHOR(S) Dr. Akhtar S. Khan			
7. PERFORMING ORGANIZATION NAMES(S) AND ADDRESS(ES) University of Maryland Baltimore County Dept. of Mechanical Engineering ECS Building, Baltimore, MD 21250			8. PERFORMING ORGANIZATION REPORT NUMBER ENME - 98-6
9. SPONSORING / MONITORING AGENCY NAME(S) AND ADDRESS(ES) U.S. Army Research Office P.O. Box 12211 Research Triangle Park, NC 27709-2211			10. SPONSORING / MONITORING AGENCY REPORT NUMBER ARO 34819.2-MS
11. SUPPLEMENTARY NOTES The views, opinions and/or findings contained in this report are those of the author(s) and should not be construed as an official Department of the Army position, policy or decision, unless so designated by other documentation.			
12a. DISTRIBUTION / AVAILABILITY STATEMENT Approved for public release; distribution unlimited.			12 b. DISTRIBUTION CODE Unlimited
13. ABSTRACT (Maximum 200 words) This report contains final results of four distinct tasks that were funded under this grant. Each task starts on a different page, starting with an overview, followed by results. At the end of each task report, the name of the doctoral student who recieved Ph.D degree with funding of the task, and a publication list are given. The four tasks are, "Thermomechanics of Fiber - Reinforced Elastomeric Composites," Evaluations and Modification of Constitutive Models for Finite Viscoplastic Deformation Related to Armor Design," "Nanocrystalline Material by Mechanical Alloying and Investigation of Suitability for Armor Applications," and "High Strain Rate Behavior and Damage Measurements in Glass Reinforced Plastics." It should be pointed out here that the final reports of the subcontracts to the University of Maryland College Park (Drs. W. Chappas & J. Silverman, and Drs. K. W. Armstrong & X. Zhang) were submitted seperately.			
14. SUBJECT TERMS Nanocrystalline Materials, Viscoplasticity, Thermomechanics of Elastomers, High Strain Rate Behavior, Glass Reinforced Plastic			15. NUMBER IF PAGES 164
			16. PRICE CODE
17. SECURITY CLASSIFICATION OR REPORT UNCLASSIFIED	18. SECURITY CLASSIFICATION OF THIS PAGE UNCLASSIFIED	19. SECURITY CLASSIFICATION OF ABSTRACT UNCLASSIFIED	20. LIMITATION OF ABSTRACT UL

Table of Contents

Task I.	Device of Evaluating Multiaxial Finite Strain Thermomechanical Behavior of Elastomers	1
Task II.	Evaluating and Modification of Constitutive Models for Finite Viscoplastic Deformation Related to Armor Design	45
Task III.	Nanocrystalline Material by Mechanical Alloying and Investigation of Suitability for Armor Design	113
Task IV.	High Strain Rate Behavior and Damage Measurements in Glass Reinforced Plastics	148
	Report of Inventions and Subcontracts	164

Device for Evaluating Multiaxial Finite Strain Thermomechanical Behavior of Elastomers

Jay D. Humphrey, Neil T. Wright, David J. Doss, Earl M. Ortt, and Edwin LeGall

Department of Mechanical Engineering
University of Maryland, Baltimore County
and

Feng-Jon Chang, Joseph Silverman, Walter J. Chappas
Materials and Nuclear Engineering Department
University of Maryland, College Park

PREFACE

Our long term goal remains the identification of multiaxial phenomenological constitutive relations for the finite strain, thermomechanical behavior of unswollen and swollen fiber-reinforced elastomers. The efforts supported by this year of Army Research Office funding have lead to a Ph.D. dissertation [17], two M.S. theses [10, 31], and, thus far, three archival publications [11, 18, 32]. The archival publications contain the distilled achievements discussed in the dissertation and theses, and are attached as appendices C, D, and E, respectively. This work has also provided the foundation for continuing studies in the multiaxial thermomechanical behavior of elastomeric composite materials and biological tissues.

A detailed description is given of the design and development of a unique computer-controlled device capable of measuring the finite strain thermomechanical behavior of a general class of materials such as neoprene rubber, polyurethane, and biological soft tissue. The utility of the device for thermoelastic and thermophysical investigations is demonstrated by the direct measurement of the in-plane stress-stretch response of neoprene rubber and native and irradiated polyurethane and the in-plane and out-of-plane components of thermal diffusivity of stiff polyvinyl chloride sheet and of neoprene rubber undergoing finite deformations. In addition, the abrasion resistance of polyurethane is contrasted with the improved performance of polyurethane grafted with polyacrylonitrile.

INTRODUCTION

The thermomechanical behavior of elastomeric, and specifically rubber-like, materials has generated considerable interest in the mechanics community for close to two centuries. Polymers, composites materials and biological tissues may exhibit thermally and mechanically anisotropic response, their properties changing with temperature level, processing, composition, or deformation. Because of the variety of possible processes and compositions, handbooks can only list values for a limited number of circumstances. Models are increasingly used for design of products made with new materials that may not be fully characterized. The uncertainty of the material property values limits the accuracy of these sophisticated analytical and numerical models. Moreover, in the neighborhood of phase transitions, polymers may experience severely altered mechanical performance for temperature changes of just a few degrees, making accurate thermal analysis essential. And while several methods might be employed to estimate the effective thermal properties of a composite material based

on its constituents, there are no generally applicable methods for homogeneous polymers and how their properties change with processing.

Others have made measurements of the directional thermal properties of materials. Choy et al. [12] measured the orthotropic components of thermal diffusivity of highly drawn polyethylene using the 1-D flash method (Parker et al., [33]). This required cutting of the polyethylene sheet into strips and then using epoxy to hold the strips together for measurement of the three directions. Nevertheless, while the undeformed material had isotropic thermal diffusivity, after being pulled to a draw ratio of 25, the thermal conductivity increased by 25 times in the direction of the deformation, and decreased by 2.2 times the undeformed value in the direction perpendicular to the deformation.

Donaldson and Taylor [16] and Chu et al. [13] extended the 1-D flash method to measure the radial and axial components of thermal diffusivity in thin graphite disc. Their method required separate tests for each component of the diffusivity tensor. This could add uncertainty due to specimen variability, especially in the testing of biological materials. Taylor and Kelsic [39] measured the normal and in-plane components of thermal diffusivity of unidirectional, fiber-reinforced, polymer composites also using the 1-D flash method by varying the angle of orientation of the fiber to the direction of heat flow. These measurements required a sample of unique fiber orientation for each direction measured, and due to the nature of the flash method, required variations in the geometry of the manufactured specimens.

In soft biological tissues, Valvano et al. [44] measured the axial component of the thermal conductivity of bovine aorta to be about 25% greater than the radial component, measured from the intima to the adventitia, at both 25 and 50 °C. They used the guarded hot-plate method, which requires careful attention to peripheral heat losses when measuring materials of moderate to low thermal conductivity. As with the other directional measurements, simultaneous measurements of the axial and radial components are not possible, instead, they require two specimens for a single axial/radial data pair, raising the possibility of systemic difference in the treatment of the axial and radial specimens and a potential source of variability in the data.

Sawaf and Özişik [36] suggested using the Marquardt parameter estimation algorithm, coupled with a finite difference solution of the heat diffusion equation, to determine the three components of thermal diffusivity in an orthotropic material. Their illustrative analysis consisted of a cube with constant temperature boundary conditions. Maillet et al. [27] and Lachi and Degiovanni [26] employed a more practical boundary value problem to measure the out-of-plane and radial in-plane components of thermal diffusivity. Only a portion of the specimen is illuminated and the temperature on the rear-face is measured at two points: the center of the projection of the flash area and a point outside this projection. The out-of-plane and radial in-plane components of thermal diffusivities can then be determined using the method of moments. They examined isotropic specimens of stainless steel and PVC to calibrate their 2-D flash device over a wide range of thermal diffusivities and reported accuracy of better than 2%. In addition, they measured two components of the thermal diffusivity tensor of anisotropic Kevlar composite specimens of varying thickness.

Wright et al. [46] proposed extending the 2-D measurements to measure three orthotropic components of thermal diffusivity of elastomers subject to finite strain. As with the 2-D method, a portion of the front face would be illuminated, but now temperatures at three points on the rear surface would be measured. Then, the Marquardt algorithm and heat

diffusion equation would be used to determine the three components of thermal diffusivity in an orthotropic material. Wright et al. [46] illustrated how such a device might be coupled with a biaxial load frame and an environmental chamber for measuring the parameters for general thermo-mechanical constitutive relations.

Of course, a general thermomechanical analysis of elastomers requires both thermoelastic and thermophysical data. Likewise, appropriate theoretical frameworks are needed to effectively design and interpret experiments that are used to formulate nonlinear constitutive relations [43]. For example, theory reveals that a complete description of the reversible finite strain thermomechanical behavior of elastomers requires identification of two independent constitutive functions [6], the Helmholtz potential

$$\psi = \hat{\psi}(\mathbf{C}, T) \quad (1)$$

and the referential heat flux vector

$$\mathbf{q}_0 = \hat{\mathbf{q}}_0(\mathbf{C}, T, \nabla_0 T) \quad (2)$$

where $\mathbf{C} (= \mathbf{F}^T \cdot \mathbf{F})$ is the right Cauchy-Green deformation tensor, $\mathbf{F} (= \partial \mathbf{x} / \partial \mathbf{X})$ the deformation gradient tensor, T the temperature, $\nabla_0 T (= \partial T / \partial \mathbf{X})$ the referential temperature gradient, and \mathbf{x} and \mathbf{X} the position of a material particle in the current and reference configurations, respectively. Stress-strain-temperature relations result from derivatives of ψ with respect to \mathbf{C} . Although a number of functional forms for ψ have been suggested [9, 21, 28, 30], a widely accepted form remains elusive due, in large part, to the continuing lack of multiaxial thermoelastic data. That is, most investigators have focused on describing the available uniaxial data [2, 3, 4, 37] and hence the peculiar 1-D Gough-Joule and thermoelastic inversion effects. Recently, however, Ogden [30] proposed a method for finding ψ as a function of biaxial stretches and temperature. Humphrey and Rajagopal [23] showed that in-plane biaxial tests allow measurement of thermoelastic response functions (e.g., $\partial \psi / \partial \mathbf{I}_C$ where $\mathbf{I}_C = \text{tr} \mathbf{C}$) similar to the isothermal results of Rivlin and Saunders [35]. Both cases require measuring the biaxial stress and stretch at multiple temperatures.

Alternatively, there has been little attention to the possible finite strain dependence of the heat flux. Rather, most reports assume Fourier conduction $\mathbf{q}(\mathbf{x}, T) = -k(T) \nabla T$ where $\mathbf{q}(\mathbf{x}, T)$ is the spatial heat flux, $\nabla T (= \partial T / \partial \mathbf{x})$ the spatial gradient of temperature, and $k(T)$ the scalar (i.e., isotropic) spatial thermal conductivity [14]. For finite strains, referring the conductivity tensor to the reference configuration simplifies material symmetry considerations, and thus facilitates the formulation of general constitutive relations. Thus, note that $\mathbf{q} = (1/J) \mathbf{F} \cdot \mathbf{q}_0$, where $J = \det \mathbf{F}$. Moreover, a generalized Fourier conduction may be employed, where

$$\mathbf{q}(\mathbf{x}, T) = \frac{1}{J} \mathbf{F} \cdot (-\mathbf{K}(\mathbf{C}, T) \cdot \nabla_0 T(\mathbf{X}, T)) \quad (3)$$

and $\mathbf{K}(\mathbf{C}, T)$ is the referential thermal conductivity tensor. Of the tractable finite strain tests (e.g., combined extension and torsion of a cylinder, membrane inflation, etc.), the in-plane biaxial extension of a thin rectangular sheet [35, 42] is also convenient for thermophysical testing. Not only is the resulting strain field homogeneous in the central region and the state of stress planar, the thin specimens facilitate isothermal testing and measurement

of thermal diffusivity. For example, Doss and Wright [17] recently demonstrated that the transient flash diffusivity method may be extended in the biaxial test setting to measure the diagonal components of the spatial thermal diffusivity tensor α of stiff polyvinyl chloride (PVC). Specifically, the flash diffusivity method yields α via the spatial energy equation which, in the absence of stress power and volumetric heat addition, is

$$\frac{\partial T(\mathbf{x}, T)}{\partial t} = \alpha(\mathbf{C}, T) : \nabla(\nabla T(\mathbf{x}, t)) \quad (4)$$

where t is time. Appendix A contains an outline of the 1-D solution of Eq. 4 that Parker et al. [33] employed in the initial description of the flash method. Here, Eq. 4 is solved using a finite difference formulation as part of a Marquardt parameter estimation algorithm for both the traditional (1-D) flash method (measuring the out-of-plane component α_3 only) and the extended flash method (measuring the three diagonal components of α). This allows for more accurate representation of the boundary conditions. Also, note that finite strain constitutive relations are more easily formulated in terms of the referential thermal diffusivity α_0 . Fortunately, one can infer α_0 from the measurable α via $\alpha = (1/J)\mathbf{F} \cdot \alpha_0 \cdot \mathbf{F}^T$ and $\alpha_0(\mathbf{C}, T) = \mathbf{K}(\mathbf{C}, T)/(\rho_0 c_F(\mathbf{C}, T))$; here ρ_0 is the referential mass density and c_F the specific heat at constant deformation.

There is, therefore, a clear need for a multiaxial thermomechanical test system that can exploit the available theoretical results. This report describes the design and construction of a new device capable of both in-plane biaxial thermoelastic testing and measurement of orthogonal components of α . Biaxial mechanical testing is demonstrated by measurements of finite strain in neoprene and irradiated and native polyurethane. Illustrative thermal property measurements are presented for the simultaneous measurement of three orthogonal components of thermal diffusivity in PVC sheet and in neoprene rubber, the latter subjected to equibiaxial stretch ratios $\lambda_1 = \lambda_2$ ($\lambda_i = l_i/L_i$ with l and L being the current and reference lengths, respectively) with $\lambda \in [1, 1.5]$, at temperature levels between 21 and 41 °C. The measured anisotropy in the PVC sheet, as contrasted to the homogeneous diffusivity measured in PVC rod, illustrates that manufacturing processes may introduce directional dependence in the thermal properties of polymers, and hence the need for measurements beyond those that presume material isotropy. Another key result is quantification of the role of coupled heat conduction in the air adjacent to the bottom of the specimen, significant in materials of low or moderate thermal diffusivity. This technique of measuring simultaneously the directional components of the thermal diffusivity in planar specimens could be employed such that samples of specific materials being considered for a design may be examined and the results used in the thermal modeling of the component and system.

METHODS AND MATERIALS

Figure 1 is a schema of the overall optical-thermomechanical system. Briefly, the system consists of five subsystems, one each for (a) biaxial loading, (b) in-plane strain measurement, (c) environmental control, (d) flash illumination, and (e) point-wise temperature measurement.

Biaxial Loading System

The load frame is machined from one piece of mild steel to outer dimensions of 45.7×45.7 cm with a 2.54 cm square cross-section. The outer and inner surfaces are ground to ensure that opposing sides are flat and parallel. The frame is mounted on an optical table using standard 2.54 cm diameter, 15.2 cm long optical rods at each corner. A pair of horizontal through-holes (1.27 cm diameter and 4.45 cm apart) are centered on each side of the frame (Fig. 2a) such that the axes of any pair of holes are collinear with those of the opposing pair and perpendicular to the other two pairs. Each of the eight holes is fitted with a 1.91 cm long linear recirculating ball bearing specifically designed for linear travel of shafts with minimal transverse play.

Nearly uniformly distributed in-plane biaxial forces are applied to the square specimen through four load carriages (Fig. 2b). Each edge of the specimen is attached to a single carriage using Kevlar thread, or 3-0 silk suture for biological tissues. The load carriages consist of two parallel 0.635 cm diameter solid, hardened stainless steel rods. Each rod is supported in one of the aforementioned through-holes by one of the ball bearings in the load frame and a neoprene O-ring sandwiched between two Rulon bearings, which form a watertight seal for the environmental chamber. Proper alignment of this chamber within the load frame ensures free and smooth translation of the load carriages. The outside end of each pair of rods is attached to a cross bar that separates the shafts and facilitates application of the axial force. The inside end of the load carriage consists of four separate pieces made of aluminum. First, a cross bar connects the two rods, similar to the outside end. Second, two load cells, which are watertight and temperature compensated over the range $-29 < T < 93$ °C, are attached on two of the cross bars on perpendicular axes. Third, is a coupling bar. Fourth, attached to the coupling bar is a T-bar that has a series of equally spaced holes (0.75 cm apart) which serve as rigging points for the specimen loading threads.

The last component of the loading subsystem is the mechanism for inducing axial load. Each of the four carriage assemblies is independently loaded via a 1 mm lead ball-screw driven by a stepper motor. Ball-nuts attached to the outer cross bar of the load carriages convert the rotation of the motor into linear displacement of the carriage assemblies, thus this is a hard-loading device. The stepper motors are individually controlled by a four-axis indexer card in the Pentium personal computer (PC). Such a drive system allows implementation of fully automated stretching protocols.

Strain Measurement

In-plane finite strains are measured optically by tracking the position histories of four small, contrasting markers that are affixed to the bottom surface of the specimen (Fig. 2b). This approach has been described previously (Humphrey et al. [22]), and is sufficient because of the homogeneity of the strain field in the central region, as confirmed experimentally and by finite element analysis. For example, finite element analysis (ABAQUS), assuming a Mooney-Rivlin material response, revealed that the strain field is essentially homogeneous and extensional ($< 5\%$ shear) in the central sixteenth of the square specimen. A CCD video camera and custom software record the position of each of the $200\text{ }\mu\text{m}$ tracking markers at a 30 Hz frame rate. These marker positions, extracted from the video image by a frame-grabber board in the PC, serve as input to a bilinear interpolation algorithm that provides the components of \mathbf{F} in the central region at each configuration (see Appendix B). The components of \mathbf{F} provide information for feedback control of the thermoelastic tests at thermal

equilibrium. In thermophysical tests, the components of \mathbf{F} are registered prior to the flash illumination (i.e., at mechanical equilibrium), which only slightly perturbs the strain field.

Environmental Chamber

The environmental chamber allows testing of the sample in air or liquid at constant temperatures. The chamber is made of 1.27 cm thick polycarbonate sheet, sealed with silicone adhesive to prevent leakage of the fluid. With outside dimensions $40.0 \times 40.0 \times 7.62$ cm, the polycarbonate shell fits inside of the load frame (Fig. 2a). Though not shown for clarity, top and bottom face plates are screwed onto the polycarbonate shell. The face plates are separated from the shell by 1.6 mm thick silicone rubber gaskets to reduce heat loss and leakage from the chamber.

The top face of the chamber has a central port that allows the flash lamp (described below) to be placed in close proximity to the specimen, thereby ensuring that enough energy is absorbed by the sample to obtain a desirable temperature rise on its bottom surface. The separation between the lamp and an approximately 2 mm thick specimen may be adjusted between 1.0 and 3.0 cm. In addition, the top allows access by the thermocouple probe for measurement of the temperature on the bottom face of the sample. The bottom face of the chamber has a central $96 \times 96 \times 1.5$ mm plate glass window to allow the camera view of the aforementioned markers for strain measurement. Additionally, the bottom plate has drains to remove liquid from the chamber.

The chamber can be maintained between room temperature and 100°C by a 750 W, 1.27 cm diameter, 30.5 cm long submersible heater that is mounted to the chamber (Fig. 2a) and is modulated by a thermostatic controller.

Temperature Measurement and Flash System

The 1-D flash method [33] has evolved to become a standard (ASTM E-1461-92) for determining the thermal diffusivity of solids: Briefly, the front surface of a thin opaque planar specimen absorbs a burst of intense radiant energy and the temperature history of the rear surface is recorded. The out-of-plane thermal diffusivity α_3 can then be determined simply as

$$\alpha_3 = \frac{c_x d^2}{\pi^2 t_x} \quad (5)$$

where d is the thickness of the specimen, t_x is the time required for the rear surface to reach the fraction x of its maximum temperature excess T_{max} , and c_x is a constant based on the value of t_x being used. Appendix A contains an outline of the development of Eq. 5 from Eq. 4. The principles of the flash technique and the many of the improvements in data reduction are described elsewhere [1, 7, 26, 27, 33, 38]. The extension of the flash device to measure the diagonal components of α is described in Doss and Wright [17].

Here, a linear xenon flashtube, mounted in an aluminum reflector, illuminates the top face of the specimen (Fig. 3a). When the components of α are to be measured, a 50×50 mm aperture plate with a 20×20 mm opening is mounted between the flash and the specimen; the aperture is removed for measurement of α_3 alone. Three 0.25 mm diameter E-type thermocouple probes are mounted in an aluminum bar and form the apexes of a right isosceles

triangle which has two 15 mm sides and, when aligned with the aperture, measure the temperature at the center of the projection of the lighted area and at two points outside this projection along the two in-plane axes. The aperture plate is mounted on a linear translation stage that allows adjustment of the spacing between the aperture and the thermocouples while maintaining accurate alignment of the aperture and the thermocouples. An error of 100 μm in the thermocouple positions or aperture dimensions will cause an error of as much as 10% in the measured in-plane thermal diffusivities, thus requiring great care in alignment. For measurements of α_3 alone, only the central thermocouple output is used. A small amount of high thermal conductivity silicon paste is used to insure good contact between the thermocouple probe and the specimen surface. This paste is applied under magnification to maintain a consistent and small application because it increases the effective mass of the temperature sensor, and may result in a slowed sensor response. The thermocouple fixture is attached, through the port in the top plate of the environmental chamber, to a micrometer head that may raise or lower the thermocouples as required. A second CCD camera is used to monitor initial contact between the specimen and the thermocouples. Consistent contact force between the thermocouple probe and the specimen is indicated by monitoring the output of the in-plane load cells.

Measurements with a broad band (320-1100 nm) photodetector (Thorlabs) indicated that the energy from the flash reaches its peak at 400 μs with over 94% of the flash energy being released within 1 ms. The flash output is consistent with a standard deviation of only 0.37% and uniform over the specimen. The ASTM standard stipulates that the flash must last less than 6.0 ms for the most restrictive specimens used here (stainless steel) for Eq. (5) to be valid in the 1-D tests.

Data Acquisition and Control

Eight independent channels of information are recorded simultaneously using an analog-to-digital (A/D) conversion board located in the PC and equipped with a cold junction compensation circuit, recorded on one of the channels, and high gain amplifier specifically designed for acquisition of thermocouple data. The E-type thermocouples occupy three channels, whereas two T-type thermocouples, one at the quartz window to signal the flash and another above the specimen to record the ambient temperature, occupy two channels. The two load cells are connected to a signal conditioner, the output of which occupies the last two channels (Fig. 1).

The control strategy employed in the biaxial finite deformation involves rotating the two motors in one stretching direction at a constant velocity and varying the velocity of the two motors in the orthogonal direction so that the measured stretch in that direction is within a small error ϵ of the desired stretch. Let λ_d be the desired value of the stretch ratio (either λ_1 or λ_2) and let λ_a be the measured stretch ratio. Furthermore, calculate the difference δ between λ_a and λ_d . If $|\delta| \leq \epsilon$, then the velocities of the motors on that axis are set to zero. However, if $|\delta| > \epsilon$, then the motor velocities must be adjusted to bring λ_a back to within ϵ of λ_d . The velocities ω of the controlled motors are adjusted proportionally to δ using $\omega = K_1 \cdot \delta$, where K_1 is a suitably valued parameter determined by trial-and-error during preliminary tests until the control of the specimen is acceptable. If K_1 is too small, the stepper motors continuously move in the same direction, indicating that ω is too slow

and not keeping the stretches within ϵ . Conversely, if K_1 is too large, the motors oscillate, indicating that the motors cause an overshoot of λ_d , thus requiring the motors to reverse. A suitable value of K_1 between these two extremes should thus be selected. Note that if $\delta > 0$, then $\lambda_a > \lambda_d$ and the direction of rotation of the motors must be such that λ_a is decreased; if $\delta < 0$ then the specimen must be stretched more. Once the controlling velocity is determined, its value is sent to the motor controller card and takes effect immediately (i.e., O(nanoseconds)). The control cycle is repeated throughout the experiment by calculating the new stretch ratios, determining the controlling velocity, and sending the new velocity to the motor controller card.

The amplified thermocouple signal is sent to a temperature-compensated terminal strip, which is connected to an eight-channel A/D board mounted in a 90 MHz Pentium PC. The overall response time of the temperature measurement system for the 1-D flash system must be less than 10% of $t_{1/2}$ to avoid significant error (ASTM E-1461-92). The response time of the temperature measurement system can be evaluated indirectly by evaluating the measured thermal diffusivity of a reference material which has a higher diffusivity than the polymers for which this system is intended. Stainless steel (AISI 304), which has a thermal diffusivity about 40 times larger than that of PVC, has a $t_{1/2}$ of 0.18 s for a 2.25 mm thick plate, as compared with 12.8 s for a 3 mm thick PVC specimen. The average measured out-of-plane thermal diffusivity $\bar{\alpha}_3$ was $3.91 \times 10^{-6} \text{ m}^2/\text{s}$ for AISI 304 sample, within 1.0% of the reference value (Incropera and DeWitt [24]). By extension, if the temperature measurement system accurately captures the temperature response of AISI 304, then it is sufficient for measurements made with PVC specimens of similar thickness.

Flash Data Reduction

A Marquardt algorithm (Press et al. [34]) estimates the components of α from the rear-face temperature histories and the calculations of a finite-difference model. Some 1-D measurements are also made by illuminating the entire front face and measuring only the temperature at the center of the specimen. Data reduction for these is performed using both Eq. (5) and the Marquardt algorithm with a 1-D finite difference model.

The governing equation used with the Marquardt algorithm is the diffusion equation, assuming no thermal property variation with temperature or internal heat generation, and written as

$$\frac{\partial T}{\partial t} = \alpha \nabla^2 T \quad (6)$$

For the 1-D measurements, the boundary conditions are

$$\begin{aligned} z = 0 \text{ and } t < t_f &\rightarrow q'' = f(t) \\ z = 0 \text{ and } t > t_f &\rightarrow k_3 dT/dz = h(T - T_\infty) \\ z = d &\rightarrow dT/dz = 0 \end{aligned}$$

where q'' is the top surface heat flux, t_f the flash duration, $f(t)$ the time varying energy function measured by the photodetector, T_∞ the ambient temperature, k_3 the thermal conductivity of the test specimen and h the convective heat transfer coefficient. Note, k_3 is

estimated as part of these measurements using the estimated value of α_3 and reference values of the specific heat and mass density. A variety of boundary conditions were examined, but the 1-D tests presented used insulated top and bottom face boundaries with a time dependent flash energy distribution on the top face, and the results were found to match closely the measured temperature history. The results of the model were checked to insure that they were independent of the coarseness of the grid used and that an overall energy balance was maintained to four decimal places.

For the orthogonal measurements, symmetry is used to reduce the computational domain. Adiabatic boundaries were specified on the sample centerline edges and convective heat loss boundaries on the specimen edges (Fig. 4). On the top-face, in the illuminated region under the aperture opening, there is a spatially-uniform, time-varying heat flux for times less than the flash duration and a convective boundary condition following the flash. The non-illuminated area on the top face has a convective boundary specified for all times. At the bottom surface, conduction into the air underneath is modeled.

$$\begin{aligned}
 z = 0, t < t_f, \text{ and } x, y < x_f, y_f &\rightarrow q'' = f(t) \\
 z = 0, t > t_f, \text{ and } x, y < x_f, y_f &\rightarrow k_3 dT/dz = h(T - T_\infty) \\
 z = 0 \text{ and } x, y > x_f, y_f &\rightarrow k_3 dT/dz = h(T - T_\infty) \\
 z = d &\rightarrow k_3 dT/dz = k_a dT_a/dz \\
 x, y = l &\rightarrow dT/dn = 0
 \end{aligned}$$

where x_f and y_f are the dimensions of half of the illuminated region, k_a the thermal conductivity of the air, l the dimensions of half of the specimen, and n the normal to a boundary surface. Calculations and pilot measurements indicated that for the materials tested (other than the AISI 304), conduction in the air underneath the specimen is an important path of energy transport. The thickness of the specimen is ≈ 3 mm while the distance between the central thermocouple and the two offset ones is 15 mm. Once the air has been heated by the central region of the rear-face of the specimen, it provides an alternative path for energy transport. Since the total temperature rise of the transverse thermocouples in the 3-D tests run here is on the order of 0.3°C , even a small addition of energy from the air can cause significant error in the determination of transverse thermal diffusivity. Figure 5a shows *calculated* temperature histories, varying the thickness of the modeled air layer, for an orthogonal test with isotropic thermal diffusivity on the order of that of PVC. The response of central thermocouple is similar to that expected of a 1-D test except that by illuminating only the central region of the specimen, there is a more noticeable decline after the illumination. The transverse thermocouples respond identically for this calculation with isotropic thermal diffusivity. As the air layer is increased from 3.25 to 13.0 mm, these calculated temperature histories tend to a common line, indicating that the response reaches an asymptote with respect to the air layer thickness (Fig. 5b). (Note that the abscissa in Fig. 5b is time, not air layer thickness, and that the asymptotic behavior is not with respect to time, that is the trend lines become closer together with increase air layer thickness.) Also, while the absolute error for the central thermocouple is greatest when neglecting conduction in the air, the in-plane values of thermal diffusivity are more sensitive to inaccurate modeling of the conduction in the air layer. This is the result of the out-of-plane thermal diffusivity being largely determined during the initial rise in temperature and the signal being higher for

the central thermocouple. For expediency, the air is neglected for higher thermal diffusivity materials, as is borne out by modeling and the measured results. The Rayleigh number is small enough to indicate that conduction governed heat transfer in the air underneath the specimen [20], and this has been confirmed by computational fluid mechanics modeling of the coupled problem. As with the 1-D model, the orthogonal model was evaluated rigorously to insure that the results were independent of the grid coarseness.

For the 1-D tests only two parameters, α_3 and $q''/\rho C$, where ρ is the mass density and C the specific heat, are estimated. The orthotropic program estimates five parameters: the three components of thermal diffusivity (α_1 , α_2 and α_3), heat flux term defined $q''/\rho C$; and heat loss term defined $2hdt/\rho Cdx$, where dx the node spacing and dt the timestep.

Flash Measurement Protocol

The PVC specimens were first coated with flat black paint, about 0.02 mm thick, to enhance absorption of the flash energy on the top surface and then placed into the specimen holder. Next, the thermocouples were positioned on the rear face and the aperture plate was adjusted to within 0.5 mm of the top surface. Data acquisition was started, the bulb flashed, and the temperature history recorded for the three thermocouples. Following data acquisition, the specimen was allowed to cool to the ambient temperature. After testing, the geometry of the illuminated area and thermocouple locations were checked and recorded for data reduction. The thermal diffusivities were then calculated using the Marquardt algorithm. The neoprene specimens were opaque to the flash at low stretches and required no coating there. At higher stretches, some light appeared to be transmitted into the specimens, requiring additional steps in the data reduction, as is described below.

RESULTS

Finite Deformation of Neoprene

Tests were performed on specimens measuring 50 mm square, cut from 1.59 mm thick precast sheets of high-grade neoprene rubber with a Shore A hardness value of 35-45 (McMaster Carr). Outside of the biaxial device, each edge of specimen was sewn to a T-bar using a 0.254 mm diameter sewing needle and 0.2 mm diameter Kevlar thread. Seven holes spaced about 3.75 mm apart and 10 mm from the edge of the specimen were used on each edge. Four white 200 μ m spots of titanium white acrylic paint were placed in the central 5 \times 5 mm square of the specimen on the bottom face of the black specimen. The T-bars were then screwed to the load carriages. Prior to testing, each specimen was systematically preconditioned, thermally and mechanically; each neoprene sample was held at an in-plane equibiaxial stretch ratio of $\lambda = 1.45$ at 41 $^{\circ}$ C for 24 hours. Figure 6 shows the stress relaxation response of a typical specimen. The relaxation response was 86% complete after two hours and more than 95% complete after twelve hours. After 24 hours of preconditioning, the sample was then unloaded and ready for testing.

Figure 7 illustrates the advantage of the feedback control in a) constant λ_1 tests, with $\lambda_1 \in [1, 1.2, 1.4]$, and b) proportional stretch tests where $(\lambda_2 - 1)/(\lambda_1 - 1) = m$, with $m \in [2, 1, 0.5]$; equibiaxial stretch is a special case with $m = 1$. Each of the tests consisted of three cycles at a frequency of about 0.017 Hz. The robust control is illustrated by the

repeatability of the three cycles used for each type of test. With the automated control of the motors using the video strain measurement as feedback, the in-plane stretches are corrected at 30 Hz and maintained as desired throughout their range. Constant λ_1 tests prior to the implementation of feedback control, during which the stretches were induced by turning four lead-screws by hand, had λ_1 vary by as much as 20%, as opposed to the $< 0.6\%$ with the automated control. As expected, the loading and unloading response is independent of the cycle, after preconditioning.

For homogeneous principal extensions $\mathbf{F} = \text{diag}[\lambda_1, \lambda_2, \lambda_3]$, $J = \det \mathbf{F} = \lambda_1 \lambda_2 \lambda_3 = \rho_0 / \rho$ (where ρ_0 and ρ are the reference and current mass densities, respectively), hence λ_3 can be determined at each temperature, given $\rho = \rho(T)$. Data obtained from Anter Laboratories (Pittsburgh, PA) on neoprene samples tested at $T \in [20, 30, \dots, 60^\circ\text{C}]$ suggest that, to first order,

$$\rho(T) = \rho_0 [1 + \beta(T - T_0)]^{-1} \quad (7)$$

where $\rho_0 = 1.317 \text{ g/cm}^3$, $\beta = 3.915 \times 10^{-4} (^\circ\text{C})^{-1}$, and $T_0 = 20^\circ\text{C}$ is the reference temperature at which ρ_0 is measured.

Figure 8 shows illustrative in-plane Cauchy stress as a function of modified stretch ratio $\lambda_1^* (= J^{-1/3} \cdot \lambda_1)$ for one sample at three temperature levels ($T \in [25, 33.2, 41.2^\circ\text{C}]$). The stretches are calculated with respect to the individual stress-free reference configuration at the reference temperature. The characteristic nonlinear behavior is well known and has been well documented in the past [2, 25, 29, 37]. Similar measurements will greatly add to the existing thermoelastic database that is needed to evaluate current constitutive thermoelastic models [21, 23, 30] as well as to develop new constitutive descriptors of other such materials.

Thermal Diffusivity of PVC and Neoprene

Before applying the method outlined above to PVC and neoprene sheets, measurements of α were made in materials with isotropic thermal properties, AISI 304, plate glass, and PVC rod. These represent a range of α with a ratio of approximately 40 at room temperature. Most metals exhibit thermal isotropy due to their well-ordered microstructure and this result was also demonstrated by Lachi and Degiovanni [26].

Stainless Steel Of metals, stainless steels have comparatively low values of α ($3.95 \times 10^{-6} \text{ m}^2/\text{s}$ for AISI 304 at 300 K [24, 41]), but since this device is designed to measure thermal diffusivity of polymers, such as rubber and biological tissues, which have α on the order of $1 \times 10^{-8} \text{ m}^2/\text{s}$, AISI 304 provides a convenient upper bound. Specimens were cut to $50 \times 70 \text{ mm}$ from a 2.25 mm thick sheet (McMaster Carr). Each specimen was in turn mounted and the aforementioned alignment and measurement protocol was used for all tests.

As discussed above, α of AISI 304 is large enough that the coupled air conduction produces negligible changes in the reported values, as was indicated by the results of data analyzed with and without the coupled air conduction agreeing to within 1%. Typical temperature histories for the central and one of the transverse thermocouples, along with the Marquardt fits, are shown in Fig. 9, illustrating the close agreement between the measured and calculated responses. The average of 10 tests are $\alpha_1 = 3.86 \times 10^{-6}$, $\alpha_2 = 3.98 \times 10^{-6}$, $\alpha_3 = 3.88 \times 10^{-6} \text{ m}^2/\text{s}$. The components are in good agreement with each other and deviate from a reference value of $3.95 \times 10^{-6} \text{ m}^2/\text{s}$ [24] by less than 2.3%. The repeatability is

demonstrated by the low data scatter (ratio of standard deviation to average value) of less than 3.4% for each of the components.

Plate Glass Next, the thermal diffusivity of plate glass, about four times greater than that of PVC and one tenth that of AISI 304, was measured using the orthotropic system. A $2.28 \times 50 \times 70$ mm specimen was cut from a $2.28 \times 305 \times 305$ mm sheet purchased locally. Again, the front face of the glass was coated with about 0.02 mm of flat black paint to prevent transmission of the flash energy directly to the central thermocouple. The reference thermal diffusivity of the glass was first measured in a series of 15 1-D flash tests because its composition was unknown. The effectiveness of the coating was assured by evaluating α_3 using different fractions of the rear surface temperature rise, as suggested by Taylor [38]. If excessive heat loss, energy addition via conduction or convection, or energy transmission through the material was present, α_3 would have varied by more than 5% as a function of τ , where $\tau = t/t_{1/2}$ [38]. The variation in α_3 was less than 2% for $1.0 < \tau < 4.5$, demonstrating the effectiveness of the coating and that the 1-D tests were accurate. The average α_3 of all 15 tests is 4.30×10^{-7} m²/s with a standard deviation of 0.12×10^{-7} m²/s.

Ten 3-D tests were run on the coated plate glass specimen. Here, inclusion of the conjugate heat conduction was required to evaluate the data for plate glass. The data reduction was performed using the two-layer air conduction model since conjugate conduction effects in the air reduce the in-plane value of diffusivity by about 5% for glass if not included in the modeling. The measured components of diffusivity, $\alpha_1 = 4.36 \times 10^{-7}$, $\alpha_2 = 4.33 \times 10^{-7}$, $\alpha_3 = 4.28 \times 10^{-7}$ m²/s, varied from the 1-D value by less than 1.5%, and the scatter exhibited in the nine tests was less than 2.1% in each direction. The out-of-plane thermal diffusivity does not vary substantially with the total time of the temperature history used. Using temperature histories of less than 30 s caused the in-plane diffusivities to vary substantially. For temperature histories greater than 30 seconds, the measured in-plane diffusivities were bounded by less than 5%, demonstrating the accurate and repeatable measurement of in-plane thermal diffusivities intermediate to that of steel and PVC.

PVC Rod Initial measurements with PVC sheet produced seemingly anomalous results. Lachi and Degiovanni [26] measured the radial in-plane and out-of-plane components of α of PVC and found agreement to within 3% in the two directions. This suggests that PVC should have isotropic thermal diffusivity. Measurements in highly drawn polyethylene have demonstrated potential anisotropic thermal diffusivity in semi-crystalline polymers subject to plastic deformation [12]. In order to determine if the initial measurements of PVC sheet were an experimental artifact, other PVC specimens of the same composition were sought that had not undergone the same deformation during manufacturing. A thick PVC rod was chosen because specimens may be cut along orthogonal axes of the rod and 1-D tests performed to confirm its isotropy.

Three $3.2 \times 50 \times 70$ mm specimens were cut from a 102 mm diameter \times 305 mm long PVC extruded rod (Fig. 10). The round rod was first cut into a rectangle using a band saw. The six rectangular specimens were then cut so that the normal of each specimen was oriented along an axis of the rectangular coordinate system. The specimens were first rough cut using a band saw and then milled to the final dimensions. The specimens tested had thicknesses of 3.32, 3.28 and 3.26 mm and were flat to within 0.02 mm.

Fifteen 1-D diffusivity tests were run on each of three specimens. The average 1-D thermal diffusivity for all three specimens was 1.08×10^{-7} m²/s with a standard deviation

of $0.04 \times 10^{-7} \text{ m}^2/\text{s}$. This value of α_3 is 7.7% lower than that reported by Lachi and Degiovanni [26]; the precise formulation of the PVC used in each study is not known. As with most polymers, however, properties of PVC may vary substantially with composition and processing. Reported values for the thermal diffusivity of rigid PVC vary from 1.07 to $2.69 \times 10^{-7} \text{ m}^2/\text{s}$ [40]. As with plate glass, the variation of α_3 over a range of τ from 1 to 4.5 is less than 2%, indicating an experiment essentially free of the corrupting heat gains or losses.

Next, five orthogonal tests were performed on each of the three specimens for a total of 15 tests. A sample temperature history plot for thermocouples 1 and 2 is shown in Figure 11 along with the Marquardt model results. Only half of the measured points are shown so that the Marquardt reduction line is clearly visible. Comparing Figs. 9 and 11, each in terms of dimensional time, shows the much longer time required for the PVC to reach its maximum temperature, as compared with the AISI 304. Calculations based on the measurements indicate that transverse conduction in the air, on the bottom face of the specimen, may cause errors on the order of 20% in the in-plane thermal diffusivity values. Thus, it is essential that the two-layer conduction model be used to reduce the PVC data. The effect of coupled heat conduction in the air was confirmed for the PVC by measuring the temperature history of the transverse thermocouples at the surface and 0.5 mm below the surface following the flash. The shape of the temperature history curves for both tests are similar, demonstrating that conduction governs the heat transfer in the air below the specimen. In addition, the temperature level of the air at the transverse thermocouple locations is higher than the temperature measured at the surface. The same tests were repeated for stainless steel, for which the transverse conduction effects were found to be insignificant. In addition, similar tests run on the top face of the specimen confirmed that convection effects dominate there and that the convective loss boundary condition in the model was appropriate.

The results of these 15 tests on three specimens were $\alpha_1 = 1.09 \times 10^{-7}$, $\alpha_2 = 1.10 \times 10^{-7}$, and $\alpha_3 = 1.07 \times 10^{-7} \text{ m}^2/\text{s}$, all within 2% of the 1-D value, with scatter of less than 4%, demonstrating the ability of the orthogonal tests to accurately determine the three components of the thermal diffusivity of PVC.

PVC Sheet A total of nine $3.2 \times 50 \times 70 \text{ mm}$ specimens were cut from three separate $3.2 \times 305 \times 305 \text{ mm}$ PVC sheets. These sheets were obtained from the supplier at different times, but came from the same manufacturer as the PVC rod (Vycom Inc., Moosic, PA). Five 3-D tests were performed on each specimen for a total of 45 tests. All specimens were coated as before and oriented in the same direction relative to the rolling during manufacturing. Heat conduction in the air layer underneath the specimen was modeled for all data reduction. Figure 12 summarizes the means and standard deviations of the measurements of α for the PVC sheet and compares it with those measured in the PVC rod. The out-of-plane (labeled 3) diffusivity for the three sheets are not significantly different from the isotropic value measured in the rod. Striking is the difference in the values of the thermal diffusivities in in-plane directions: an average of 21.8% higher in the 1 direction and 19% higher in the 2-direction. Both the rod and sheet specimens were tested using the same test protocols, experimental apparatus, and data reduction, suggesting that the difference is due to the PVC material processing for the sheet.

The manufacturer of both the PVC sheet and rod was contacted for details concerning the differences in the processing. The sheet undergoes significantly more deformation during

the manufacturing processes. After manufacturing, only small changes in dimension occur when a rod is heated above the glass transition temperature T_g , whereas the processed sheets heated above T_g may shrink by 7 to 15% [45]. In addition, the mechanical deformation the top and bottom surfaces of the sheet imposed at the first roller may induce orientation in the in-plane directions. In this case, since the overall thickness of the specimen is only about 3 mm, this surface effect may play a role throughout the thickness of the specimen. The rod specimens were cut well below the surface and the specimen thickness is small, about 3% of the total diameter of the rod. Thus, an extrusion reduction of up to 15% appears to cause a 20% change in the in-plane components of thermal diffusivity.

Neoprene Rubber Sheets The neoprene has a magnitude of α of the same order of magnitude as the PVC and the neoprene sheets are manufactured in a similar fashion. The neoprene, however, may also undergo significant reversible deformation. Two types of tests illustrate the ability of the device to measure thermal diffusivity of specimens subjected to finite in-plane deformation: measurements of a) α_3 for three specimen thicknesses and multiple equibiaxial stretches and b) the diagonal components of α as a function of finite equibiaxial deformation at room temperature.

First, α_3 was measured for three neoprene specimens of different thicknesses ($l = [1.59, 2.38, 3.18 \text{ mm}]$). Following registration of the unloaded reference configuration (i.e. recording of the marker positions) at $T_0 \approx 21^\circ\text{C}$, the top surface of each specimen was subjected to a series of five pulses from the flash lamp, each separated by 10 minutes to allow the specimen to regain thermal equilibrium. After the five pulses, the specimen was pulled equibiaxially to the next desired stretch, its marker positions recorded in this equilibrium configuration, and the flash procedure repeated. Once all data were collected at room temperature, another series of stretch and flash data were collected at 40°C . After increasing the temperature level, the sample was allowed to reach thermal equilibrium prior to inducing mechanical stretch.

Since the transient temperature rise on the bottom surface due to each flash was about 3.0°C and of similar magnitude on the top face, after a brief initial transient, data were collected at nearly mechanical and thermal equilibrium. Here, the bottom surface temperature history was measured directly and α_3 was calculated using a Marquardt nonlinear estimation algorithm coupled with a finite difference solution of Eq. 4. Figure 13 shows close agreement between the measurements, the temperature histories calculated as part of the data reduction, and those calculated assuming the boundary conditions originally used by Parker et al. [33] and the value of α_3 determined by the Marquardt data reduction. This result is typical of the device for all the materials so far tested.

Figure 14 shows measured α_3 for equibiaxial stretches of $\lambda_{1,2} \in [1.0, 1.4]$ (corresponding to $0.51 \leq \lambda_3 \leq 1.0$) for the three specimens. Each point is the mean of the five flashes at each stretch state. Similar to observations by Wright et al. [46] for uniaxial deformations of natural gum rubber, α_3 appears to be insensitive to the in-plane stretch, for the range of stretch considered here. The average value of α_3 for all room temperature tests was $1.19 \times 10^{-7} \text{ m}^2/\text{s}$ and for 40°C , $1.17 \times 10^{-7} \text{ m}^2/\text{s}$. These values are within 5% of the values measured by a commercial flash system at Anter Labs, and the decrease in α_3 with increased temperature matches closely the trend measured at Anter Labs.

A second set of tests measured the diagonal components of α for three specimens with a nominal thickness of 2.2 mm. Following preconditioning, the three specimens were tested

at two equibiaxial stretch states of approximately $\lambda_{1,2} = 1.03$ and 1.52 . The preconditioning protocol for these tests consisted of an equibiaxial stretch of $\lambda_{1,2} = 1.52$ at 25°C for 16 hours. A minimum of five tests were performed at each of the two deformation states. As with the AISI 304 and the PVC, there is close agreement between the data and the response calculated by the model.

At the smaller deformation, α_3 is measured as $1.16 \times 10^{-7} \text{ m}^2/\text{s}$, within 2.4% of the value measured with the 1-D test and within the standard deviation of both tests. The in-plane values are measured as 1.51×10^{-7} and $1.53 \times 10^{-7} \text{ m}^2/\text{s}$, about 31% higher than α_3 . As was suggested by the results of Doss and Wright [17] for PVC, this is likely the result of extrusion processes during the manufacturing of the neoprene sheets. Likewise, Choy et al. [12] measured increased diffusivity in the draw direction and decreased diffusivity in the direction normal to the draw of highly drawn polyethylene using a 1-D flash method. At $\lambda_{1,2} = 1.52$, the average value of α_3 is measured as $1.12 \times 10^{-7} \text{ m}^2/\text{s}$, about 5.9% lower than the undeformed value. Note that $\lambda_{1,2} = 1.52$ used in these 3-D measurements corresponds to a 25% greater in-plane stretch than was considered in the 1-D measurements. The in-plane values increase to 1.65×10^{-7} and $1.59 \times 10^{-7} \text{ m}^2/\text{s}$. It should be noted that at the stretched state, there appeared to be reduced absorption of the energy at the front face of the specimen. This resulted in the measured value of α_3 changing as larger fractions of the temperature history were used in the data reduction and, thus, required using the correction method suggested by Taylor [38]. The values of α_1 and α_2 remained independent of the fraction of the temperature history used in data reduction.

Abrasion Resistance of Irradiated Polyurethane

Polyurethane (PU) samples supplied by the U.S. Army Belvoir Research, Development, and Engineering Center were irradiated with a low energy electron treatment. This treatment was intended to enhance the abrasion resistance of the PU by increasing the crosslink density at the surface. The energy of the electrons controls their penetration depth into a polymer. Here, the PU was irradiated by electrons with 175 keV energy with a dose rate of 50 kGy/pass at the EPS, Inc. (Massachusetts) accelerator, making the useful penetration a few microns [10]. Figure 15 compares the abrasion resistance of the native PU with material that has undergone increased dosages of irradiation. As may be seen in the figure, there is only marginal increase in the abrasion resistance due to the electron irradiation.

Abrasion loss was better reduced by the grafting polyacrylonitrile (PAN) to PU (PAN-g-PU). ("Graft polymerization" is loosely defined as a reaction whereby a polymer undergoes a weight gain consisting of (1) a true chemically bonded fraction of pendant chains and (2) occluded homopolymer which is alloyed with or heterogeneously dispersed in the matrix.) Figure 16 shows the weight loss per cycle due to abrasion in an oscillatory cylinder abrasion test machine (conforming to ASTM D 4157). As may be seen in Fig. 16, increased graft yield (shown as a percentage of specimen weight) produced increased abrasion resistance. Interestingly, for graft yields of 5.9% and greater, the greatest loss rate occurs between 60 and 100 cycles, as opposed to the ungrafted PU, for which the greatest loss rate occurs during the initial 60 cycles.

Finite Deformation of Irradiated Polyurethane

Potential changes in the mechanical response of PU after irradiation, nominally a surface treatment, were also investigated. Native and irradiated PU samples were subjected to finite deformation tests similar to those conducted with the biaxial deformation of the neoprene described above, though the PU was significantly stiffer than the neoprene. The strains were calculated using the unloaded configuration as the reference configuration; the specimens were relatively flat in the central region. The nominal geometry of the specimens and the location of the Kevlar threads are shown in Fig. 17.

Rather than static preconditioning, each specimen was tested for 10 cycles at equibiaxial stretch levels of 1.25, 1.3, and 1.35. The native material specimen withstood an additional 9 cycles at a stretch of 1.4, while the irradiated sample withstood 3 cycles at 1.4. This test protocol amounted to dynamic preconditioning and the data were repeatable after the seventh loading cycle (Fig. 18). The data shown below were measured during the tenth cycle of $\lambda = 1.35$.

The native sample showed no residual stresses, whereas the radiated sample had residual stresses in the unloaded configuration, as demonstrated by its curling in one direction (Fig. 17). This is likely due to the irradiation as the material was irradiated at 50 kGy/pass, suggesting a directional bias [10]. Mechanically, the native material appeared to be isotropic without question (Fig. 19a). Conversely, for the irradiated specimen, the Cauchy stress in the 1-direction was less than that in the 2-direction (Fig. 19b). This could have been due to anisotropy, caused by preferential crosslinking of the polymer chains during irradiation, or possibly to nonideal loading. The anisotropy becomes less apparent when multiple cycles are plotted together. (Calibration of the load cells after testing showed agreement within 0.5 N). Figure 20 suggests that the native material was stiffer than the irradiated material below stretches of 1.2. However, above stretches of 1.2, the data from the two materials are very similar.

Conclusions

The ability to measure the biaxial mechanical response of elastomers presents the opportunity to collect more complete data for the formulation of constitutive models for finite strain. The active control of the finite deformation, via the real-time video feedback to the motor controllers, allows measurement of the material response to equibiaxial, proportional, and constant stretch tests. Data from tests of this kind are not readily available in the literature. Adding the temperature controlled environmental chamber allows multiaxial thermoelastic behavior of elastomers to be examined.

Formulating models of the general thermoelastic response requires that the temperature field within the material also be modeled. To this end, a new method for measuring the orthogonal components of α , essential for modeling of transient temperature fields, using a single specimen has been developed. Careful measurements in AISI 304, plate glass, and PVC rod indicated that the system measures the in-plane and out-of-plane components of thermal diffusivity accurately, over a wide range of thermal diffusivities. The necessity of including the parallel heat conduction in the air has been demonstrated in materials of moderate α . This is especially important for the many materials, such as the tissues and elastomers, that cannot be tested in a vacuum. Data presented illustrate that neoprene rubber at low stretches may have anisotropic thermal diffusivity and that these values may

change with stretch, even over the range of equibiaxial stretches examined. This may be even more apparent for other materials, specifically, elastomeric composites.

Comparing the measurements on PVC sheet and rod illustrates the affect material processing can have on α and demonstrates the importance of measuring the components of thermal diffusivity, rather than relying on a single bulk value. Compared with the large diameter PVC rod, the PVC sheet used in this study has undergone considerably more deformation during its manufacture. This appears to have resulted in material anisotropy, not generally considered in PVC. Compared with the out-of-plane diffusivities the average in-plane values from nine specimens were 19% higher in one in-plane direction and 22% higher in the other. These results are in qualitative agreement with Choy et al. [12], who measured the thermal conductivity of extruded polyethylene, a semi-crystalline polymer. The methods developed here improve substantially on previous measurements which required that the specimen be cut and glued to measure both directions.

The existence of anisotropy in the thermal properties of common polymers, such as PVC and neoprene rubber, and in the biaxial mechanical response of PU further demonstrates the need for such multi-axial thermo-mechanical testing. As materials with complex microstructures are increasingly used in engineering applications, and as sophisticated models are ever more used to optimize such designs, reliable multi-axial material properties are critical. These measurements may now be made for specimens undergoing well-defined biaxial deformation using a single specimen.

Nomenclature

- C - constant volume specific heat (J/kg K)
- c_x - parameter in 1-D data reduction
- d - specimen thickness (m)
- h - convective heat transfer coefficient (W/m² K)
- k - isotropic thermal conductivity (W/m K)
- k_a - thermal conductivity of air (W/m K)
- k_i - through the specimen component of thermal conductivity tensor in the i -th direction (W/m K)
- $\mathbf{k}(T)$ - thermal conductivity tensor (W/m K)
- l - in-plane half-span of the specimen (m)
- n - normal to a boundary surface (m)
- q'' - heat flux vector (W/m²)
- t - time (s)
- t_f - flash duration (s)
- t_x - time after flash at which rear surface reaches fraction x of T_{max}
- T - temperature (K)
- T_∞ - ambient temperature surrounding specimen (K)
- T_{max} - maximum rear face temperature of the specimen (K)
- x - an in-plane component (m)
- x_f - half-span of the illuminated region in x -direction (m)
- y - an in-plane component (m)
- y_f - half-span of the illuminated region in y -direction (m)
- z - the out-of-plane component (m)

Greek letters

α - isotropic thermal diffusivity (m^2/s)

$\boldsymbol{\alpha}$ - thermal diffusivity tensor (m^2/s)

α_i - Component of thermal diffusivity tensor in i th direction (m^2/s)

ρ - mass density (kg/m^3)

τ - scaled time defined as $t/t_{1/2}$

Bibliography

- [1] Agari, Y., Ueda, A. and Nagai, S., "Measurement of Thermal Diffusivity and Specific Heat Capacity of Polymers by Laser Flash Method", *J. Poly. Sci.: Part B: Polymer Physics*, vol. 33, pp. 33-42 (1994)
- [2] Allen, G., Bianchi, U. and Price, C., "Thermodynamics of Elasticity of Natural Rubber", *Trans. Faraday Soc.*, vol. 59, pp. 2493-2502 (1963)
- [3] Allen, G., Kirkham, M.J., Padget, J. and Price, C., "Thermodynamics of Rubber Elasticity at Constant Volume", *Trans. Faraday Soc.*, vol. 67, pp. 1278-1292 (1971)
- [4] Anthony, R.L., Caston, R.H. and Guth, E., "Equations of State for Natural and Synthetic Rubber-like Materials I. Unaccelerated Natural Rubber", *J. Phys. Chem.*, vol. 46, pp. 826-840 (1942)
- [5] ASTM, "Standard Test Method for Thermal Diffusivity of Solids by the Flash Method", E 1461-92, Philadelphia (1992)
- [6] Bowen, R. M., *Introduction to Continuum Mechanics for Engineers*, Plenum Press, New York, (1989)
- [7] Balageas, D. L., "Thermal diffusivity measurement by pulsed methods", *High Temp.-High Pres.*, v. 21, pp. 85-96 (1989)
- [8] Carslaw, H.S. and Jaeger, J.C., *Conduction of Heat in Solids*, 2nd Ed., Clarendon Press, Oxford Scientific Publications (1959)
- [9] Chadwick, P. and Creasy, C.F.M., "Modified Entropic Elasticity of Rubber-like Materials", *J. Mech. Phys. Solids*, vol. 32, no. 5, pp. 337-357 (1984)
- [10] Chang, F.J., "Abrasion Resistance of Elastomers Cured by Ionizing Radiation", M.S. Thesis, University of Maryland, College Park, Maryland (1996)
- [11] Chang, F.J., Silverman, J., Chappas, W.J., "Abrasion Resistance of Polyurethane Modified by Ionizing Radiation", *Trans. Am. Nuc. Soc.* Vol. 76, p. 152 (1997)
- [12] Choy, C.L., Luk, W.H., and Chen, F.C., *Polymer*, vol. 19, pp. 155-62, (1978)
- [13] Chu, F.I, Taylor, R.E. and Donaldson, A.B., "Thermal Diffusivity Measurements at High Temperatures by the Radial Flash Method", *J. Applied Physics*, vol. 51, pp. 336-341 (1980)

- [14] Dashora, P., "A Study of Variation of Thermal Conductivity of Elastomers with Temperature", *Physica Scripta*, vol. 49, pp. 611-614 (1994)
- [15] Degiovanni, A., "Diffusivité et méthode Flash", *Rev. Gén. Therm. Fr.*, n. 185, (1977)
- [16] Donaldson, A.B. and Taylor, R.E., 1975, "Thermal diffusivity measurement by a radial heat flow method", *J. Applied Physics*, v. 46, pp.4585 (1975)
- [17] Doss, D.J., "Thermal Diffusivity of Vascular Tissue and Polymers: Effects of Deformation and Direction", Ph.D. Dissertation, University of Maryland, Baltimore, Maryland (1999)
- [18] Doss, D.J. and Wright, N.T., "Simultaneous Measurement of the Orthogonal Components of Thermal Diffusivity in PVC Sheet", accepted by ASME *J. Heat Transfer* (1999)
- [19] Downs, J., Halperin, H.R., Humphrey, J.D. and Yin, F.C.P, "An Improved Video-based Computer Tracking System for Soft-Biomaterials Testing", *IEEE Transactions BME*, vol. 37, pp. 903-907 (1990)
- [20] Gebhart, B., Jaluria, Y., Mahajan, R., Samakia, B., *Buoyancy Induced Flows and Transport*, Hemisphere, New York (1988)
- [21] Zheng, N. and Haslach, H.W. Jr., "Thermoelastic Generalization of Isothermal Elastic Constitutive Models for Rubber-like Materials", *Rubber Chemistry and Technology*, vol. 69, pp. 313-324 (1995)
- [22] Humphrey, J.D., Vawter, D.L. and Vito, R.P., "Quantification of Strains in Biaxially Tested Soft-Tissues", *J. Biomechanics*, vol. 20, no. 1, pp. 59-65 (1987)
- [23] Humphrey, J. and Rajagopal, K. R., "Finite Thermoelasticity of Constrained Elastomers Subject to Biaxial loading", *J. Elasticity*, vol. 49, pp. 189-200 (1998)
- [24] Incropera, F. P. and DeWitt, D. P., *Fundamentals of Heat and Mass Transfer*, 4th ed., J. Wiley & Sons, New York. (1996)
- [25] Kawabata, S. and Kawai, H., "Strain Energy Function of Rubber Vulcanizates from Biaxial Extension", *Adv. Poly. Sc.*, Cantow, H.J. et al., eds., Springer Verlag, vol. 24, pp. 89-124 (1977)
- [26] Lachi, M. and Degiovanni, A., "Determination des Diffusivites Thermiques des Matériaux Anisotropes par Methode Flash Bidirectionelle", *Journal de Physique III*, n. 12, pp. 2027-2046 (1991)
- [27] Maillet, D., Lachi, M. and Degiovanni, A., "Simultaneous Measurements of Axial and Radial Thermal Diffusivities of an Anisotropic Solid in Thin Plate: Application to Multi-Layered Materials", *Thermal Conductivity 21*, Cremers, C.J. and Fine, H.A., eds., Plenum Press, New York, pp. 91-107 (1990)

- [28] Mormon, K.N. Jr., "A Thermomechanical Model for Amorphous Polymers in the Glassy, Transition and Rubbery Regions", *Recent Research in Thermo-mechanics of Polymers in the Rubbery-Glassy Range*, (M. Negahban, Ed.) AMD vol. 203, pp. 89-114, ASME, NY (1995)
- [29] Obata, Y., Kawabata, S. and Kawai, H., "Mechanical Properties of Natural Rubber Vulcanizates in Finite Deformation", *J. Poly. Sc.*, A-2 8, pp. 903-919 (1970)
- [30] Ogden, R.W., "On the Thermoelastic Modeling of Rubber-like Solids", *J. Thermal Stress*, vol. 15, pp. 533-557 (1992)
- [31] Ortt, E.M., Computer-Aided Testing of Rubberlike Materials: Constitutive Behavior of Neoprene, M.S. Thesis, University of Maryland, Baltimore, Maryland (1998)
- [32] Ortt, E.M., Doss, D.J., Legall, E., Wright, N.T., and Humphrey, J.D., "Device for Evaluating Multiaxial Finite Strain Thermomechanical Behavior of Elastomers", submitted to ASME *J. Applied Mechanics* (1999)
- [33] Parker, W.J., Jenkins, R.J., Butler, C.P. and Abbott, G.L., "Flash Method of Determining Thermal Diffusivity, Heat Capacity and Thermal Conductivity", *J. Appl. Phys.*, vol. 32, no. 9, pp. 1679-1684 (1961)
- [34] Press, Flanery, Teukolsky and Vetterling, *Numerical Recipes*, Cambridge University Press, (1986)
- [35] Rivlin, R.S. and Saunders, D.W. "Large Elastic Deformations of Isotropic Materials VII. Experiments on the Deformation of Rubber" *Phil. Trans. Roy. Soc. London*, Ser. A, vol. 243, A. 865, pp. 252-288 (1951)
- [36] Sawaf, B. and Özişik, N, "Determination of the constant thermal conductivity of orthotropic materials by inverse analysis", *Int. Comm Heat Mass Trans* (1995)
- [37] Shen, M.C., McQuarrie, D.A. and Jackson, J.L., "Thermoelastic Behavior of Natural Rubber", *J. App. Physics*, vol. 38, no. 2, pp. 791-797 (1967)
- [38] Taylor, R.E., "Critical Evaluation of Flash Method for Measuring Thermal Diffusivity", *Rev. Int. Htes. Temp. et Refract.*, vol. 12, pp. 141-145 (1975)
- [39] Taylor R.E. and Kelsic B.H., "Parameters Governing Thermal Diffusivity Measurements of Unidirectional Fiber-Reinforced Composites", *J. Heat Trans.*, v. 108, p.161. (1986)
- [40] Titow, W.V., *PVC Plastics - Properties, Processing and Applications*, Elsevier Science Publishing Co., New York (1990)
- [41] Touloukian, Y.S., Powell, R.W., Ho, C.Y., and Klemens, P.G., 1970, *Thermophysical Properties of Matter*, IFI Plenum Press, New York.
- [42] Treloar, L.R.G., *The Physics of Rubber Elasticity*, 3rd Ed., Clarendon, Oxford (1975)

- [43] Truesdell, C. and Noll, W., "The Nonlinear Field Theories of Mechanics", *Arch. Rat. Mech. Anal.*, vol. 51, pp. 192-208 (1965)
- [44] Valvano, J.W., Dalvi, V.P. and Pearce, J.A., "Directional Thermal Conductivity Measured in Bovine Aorta", *ASME-HTD Advances in Bioheat and Mass Transfer*, v. 268, pp. 37-40 (1993)
- [45] Wagner, J., personal communication, (1998)
- [46] Wright, N. T., da Silva, M. G., Doss, D. J. and Humphrey, J., "Measuring Thermal Properties of Elastomers Subject to Finite Strain", *Thermal Conductivity 23*, Wilkes, K.E. et al., eds., Technomic Publishing Co., pp. 639-646 (1995)

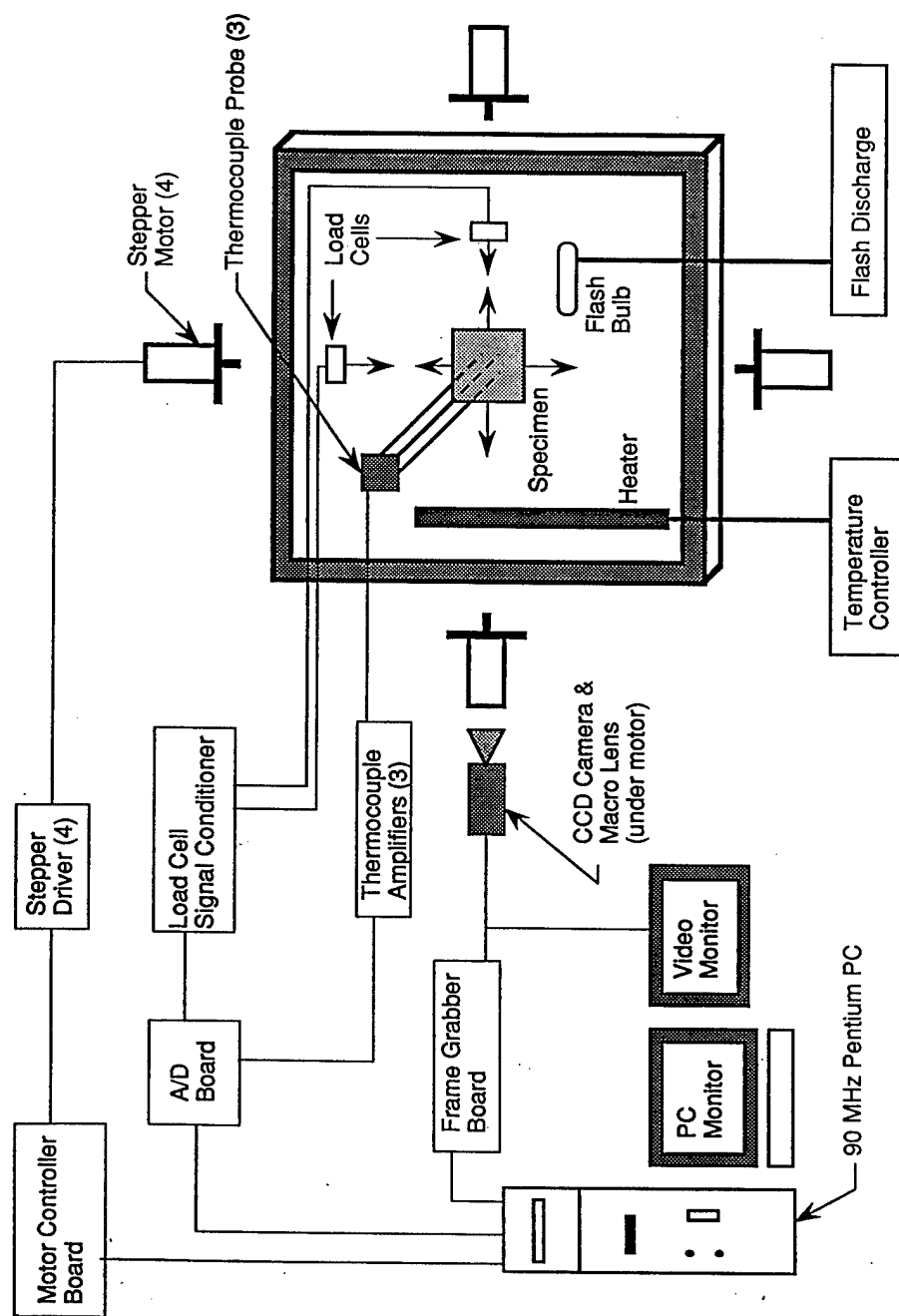


Figure 1 A schematic drawing of the overall experimental system.

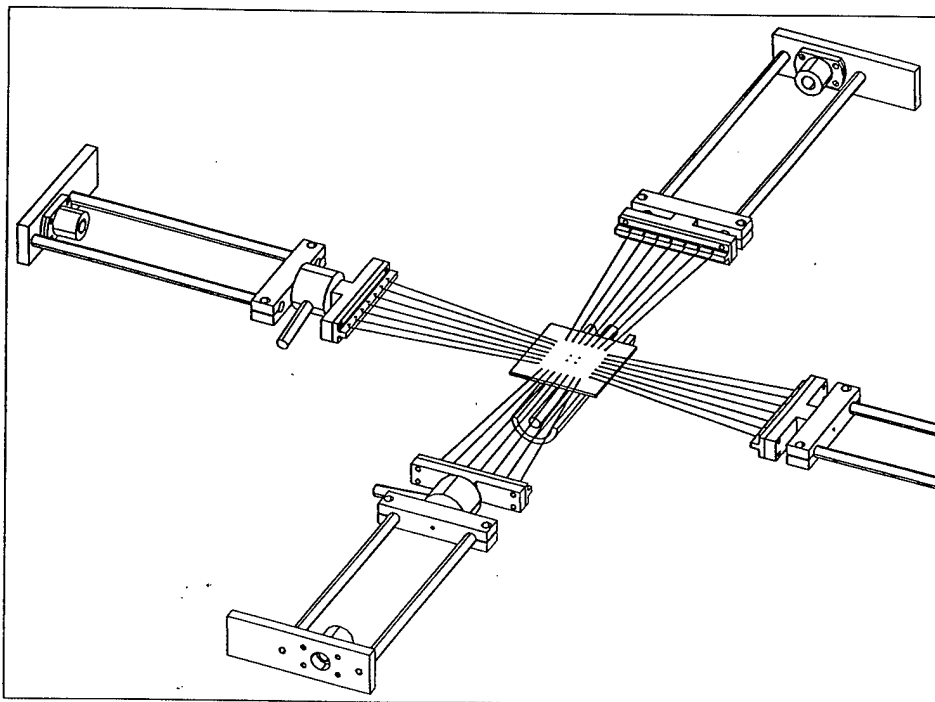
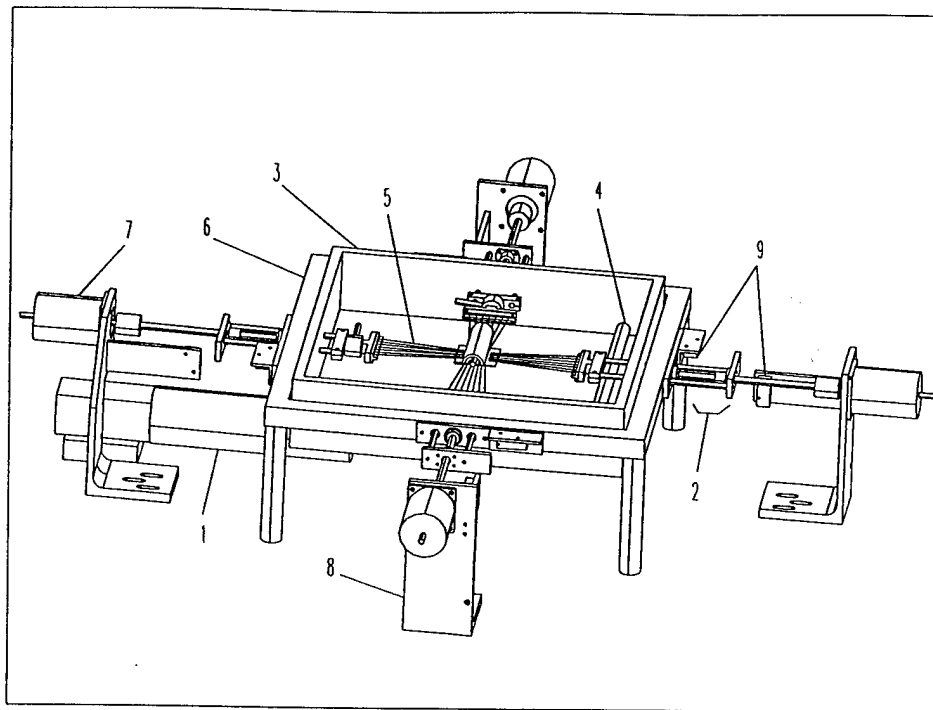
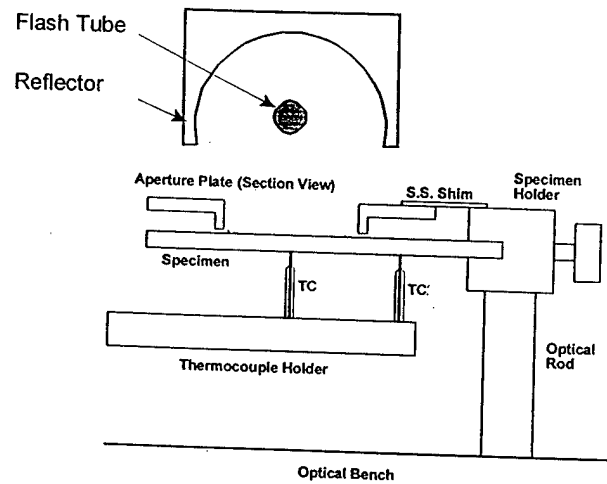
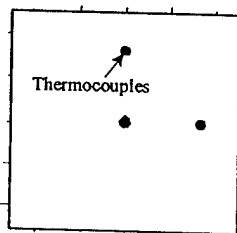


Figure 2 Biaxial Extension Device. Panel (a) is an oblique view of the device where 1) camera, 2) load carriage, 3) environmental chamber, 4) heater, 5) Kevlar threads, 6) load frame, 7) motors, 8) motor supports, and 9) limit switches; in-plane directions defined as 1 and 2. Panel (b) is a schema of the specimen with centrally placed tracking markers, loading carriages, and flashbulb and reflector, as seen from below.



Rear Face (Bottom)



Front Face (Top)

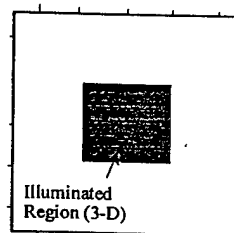


Figure 3 a) Schematic diagram of the orthogonal thermal diffusivity test device and b) illustration of the illuminated central region and the thermocouple locations.

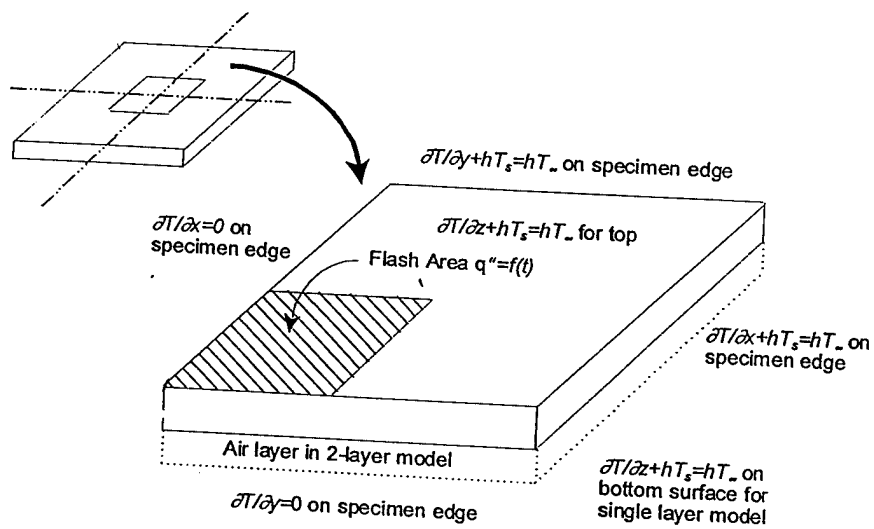


Figure 4 Schematic diagram of the geometry for the 3-D model.

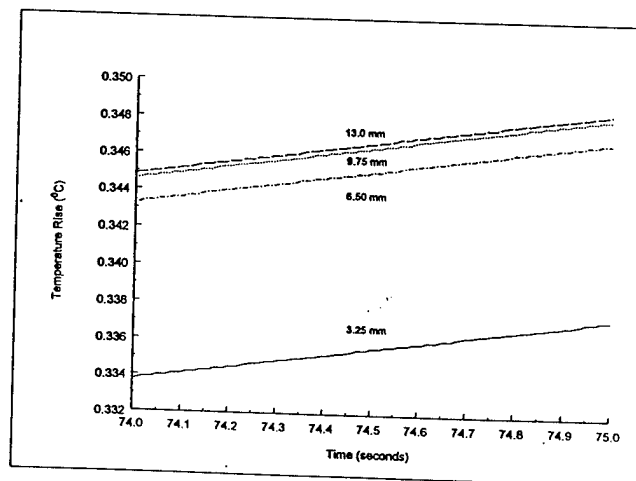
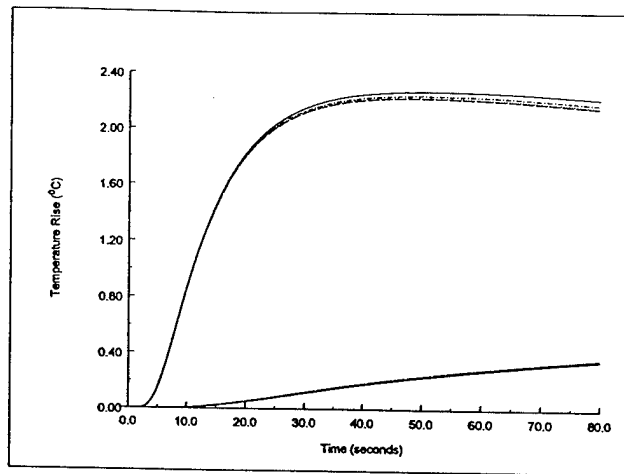


Figure 5 a) Calculated temperature histories for varying air layer thicknesses, b) expansion of the transverse thermocouple calculated response.

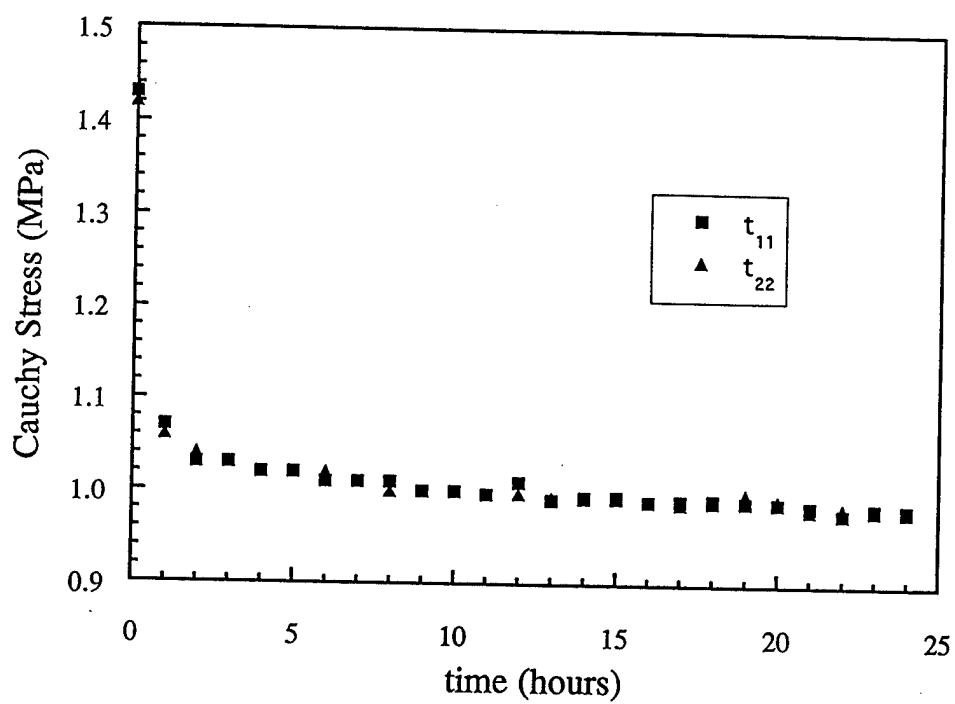


Figure 6 Stress relaxation curve of a neoprene rubber specimen during preconditioning.

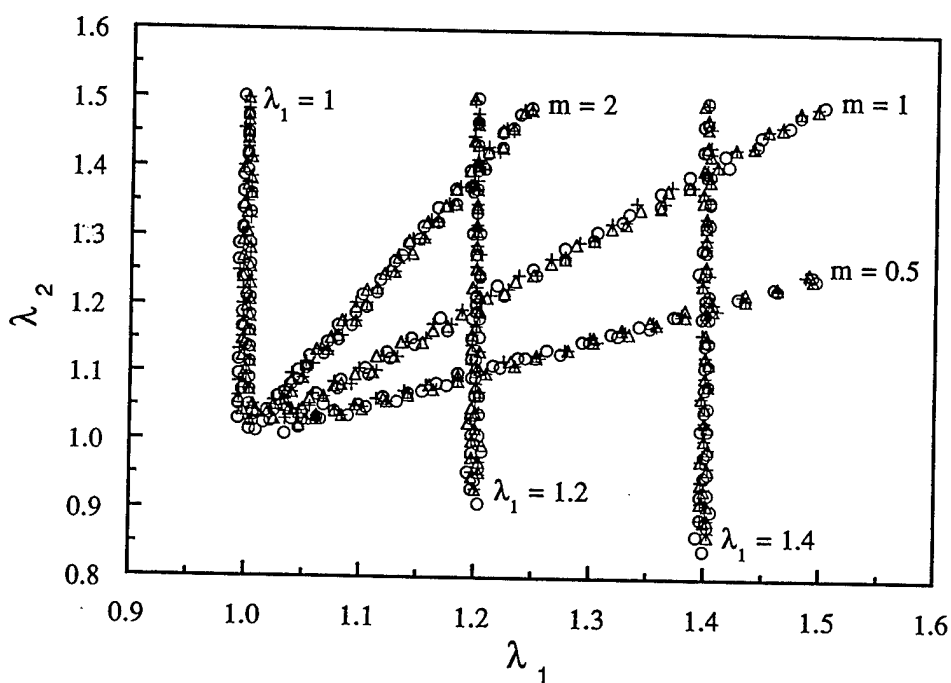


Figure 7 Illustrative in-plane stretches λ_1 and λ_2 for computer controlled equibiaxial, proportional, and constant λ_1 stretching protocols. Data are for three cycles each (cycle 1: +, 2: Δ , 3: \circ), thus showing reproducibility and robust control.

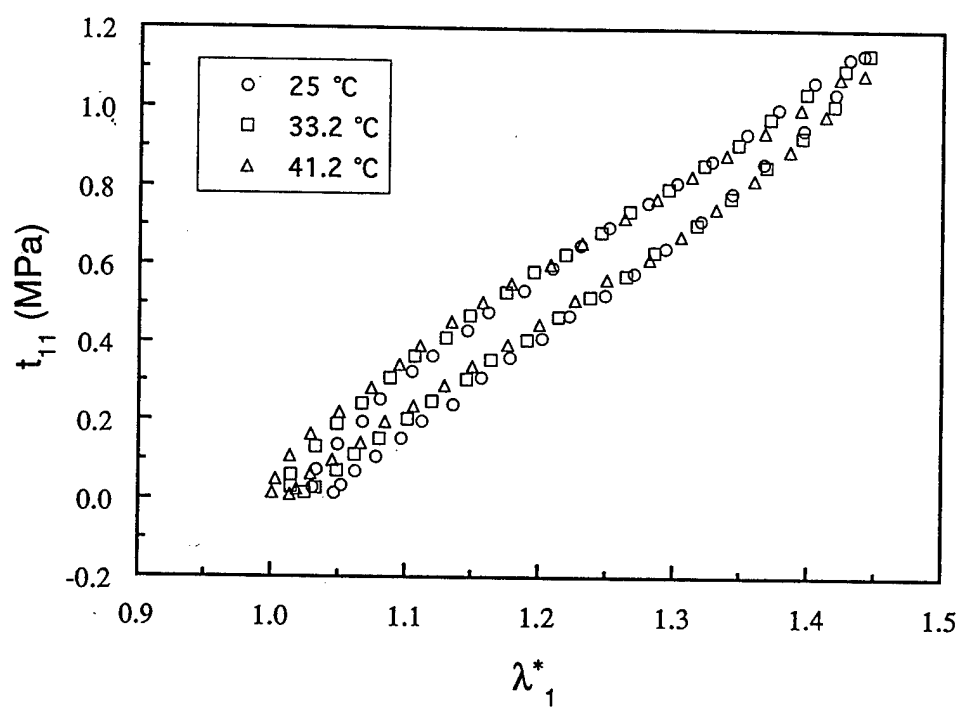


Figure 8 Typical Cauchy stress-stretch curves for neoprene at three temperatures for equibiaxial stretch tests.

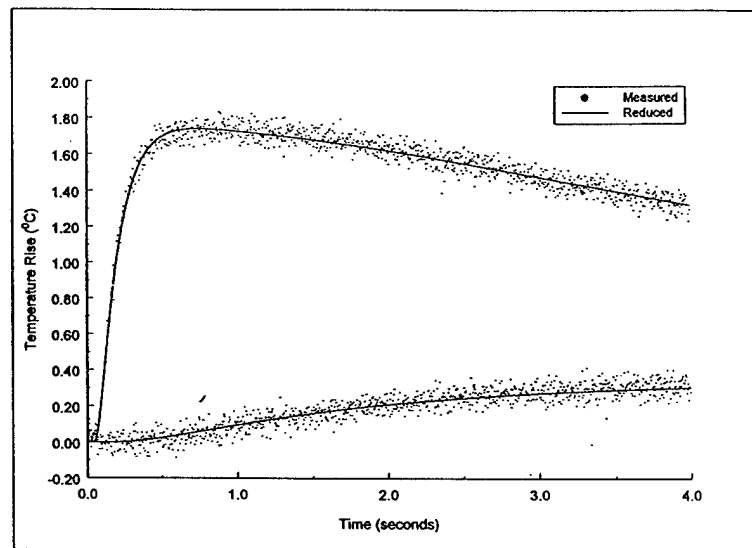


Figure 9 Measured temperature history for an AISI 304 specimen with the calculated response from the Marquardt algorithm.

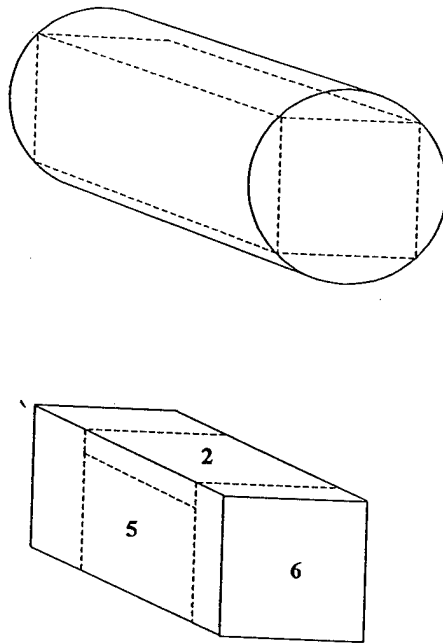


Figure 10 Specimen orientation with respect to the PVC rod.

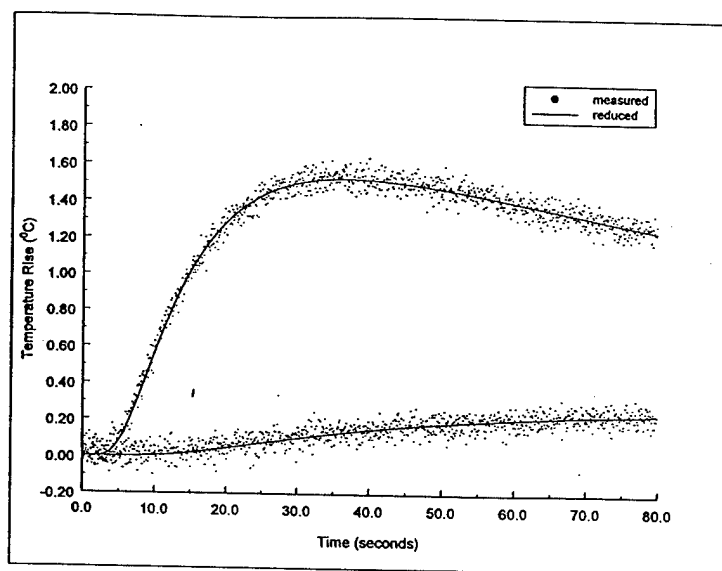


Figure 11 Measured temperature history for a PVC rod specimen compared with the calculated response from the Marquardt algorithm.

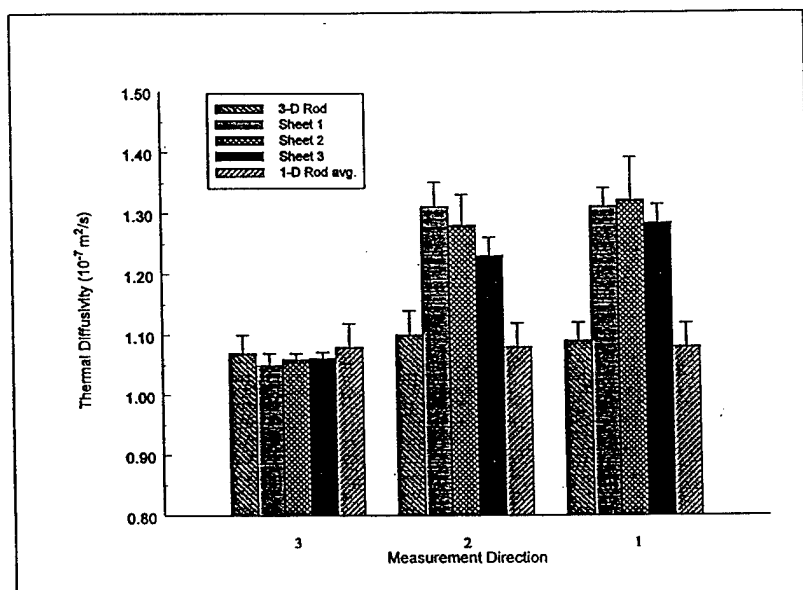


Figure 12 Comparison of the measured thermal diffusivities for PVC rod (1-D and 3-D tests) and sheet (3-D).

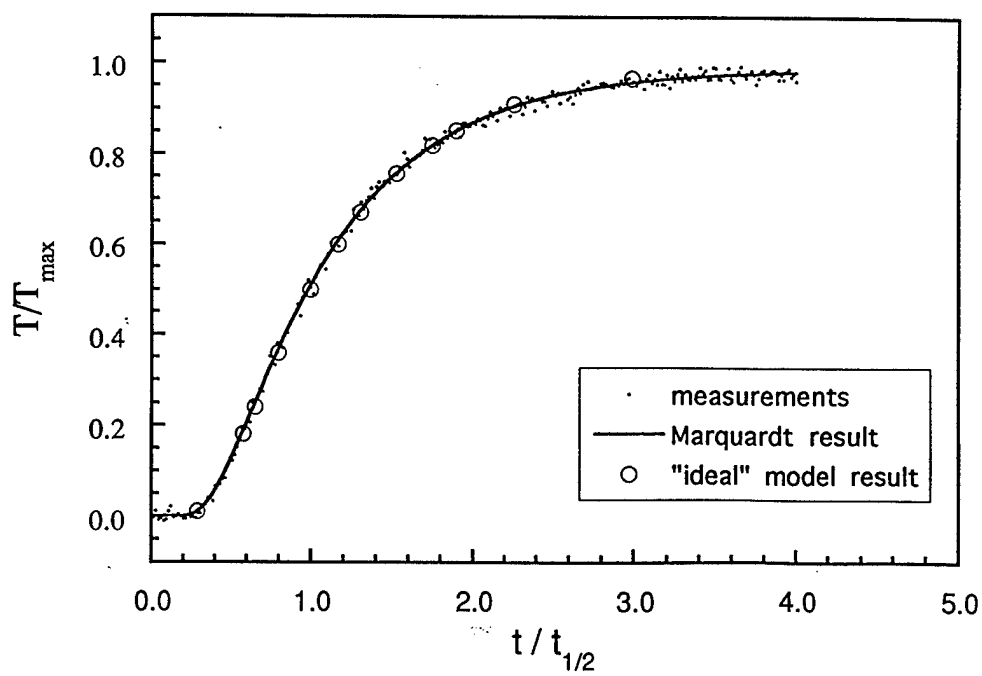


Figure 13 Typical temperature history of for neoprene in the 1-D flash test. Solid line is model result and the open circles are from Eq. 5.

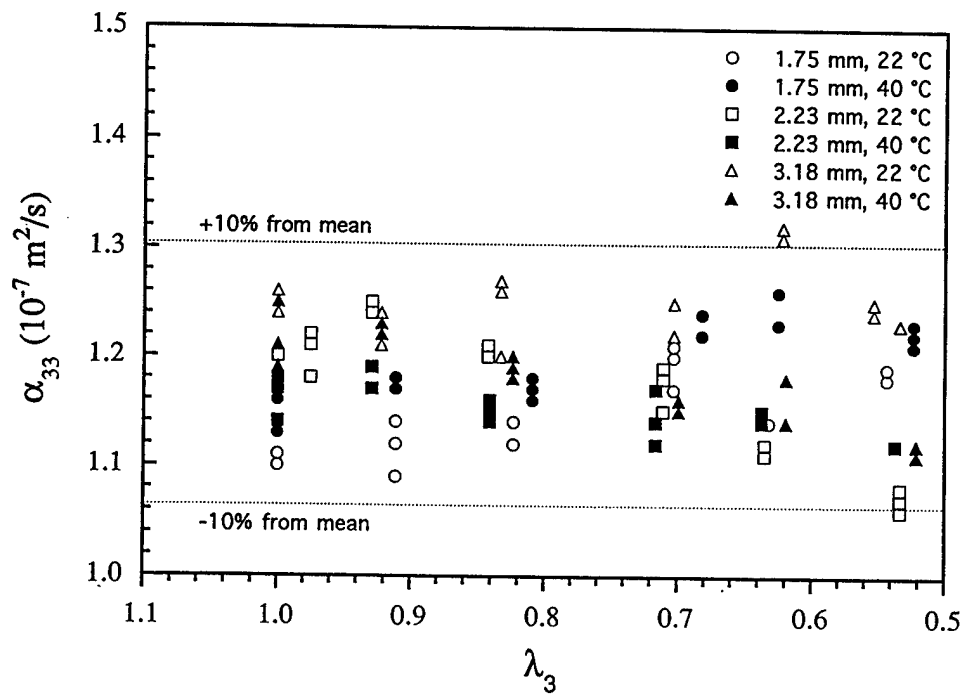


Figure 14 Variation of α_{33} of neoprene with deformation λ_3 for three thicknesses.

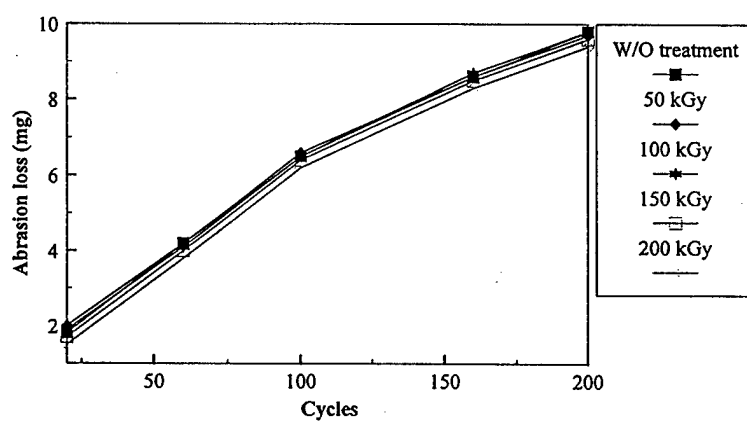


Figure 15 Abrasion loss of PU with low energy EB treatment.

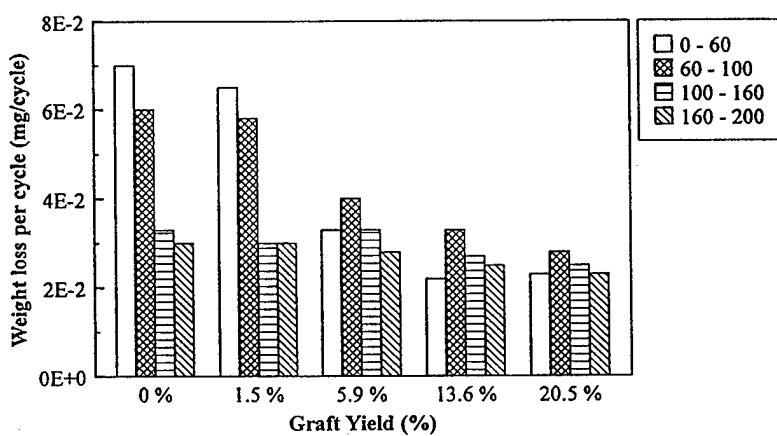


Figure 16 Abrasion loss rate of PAN-g-PU.

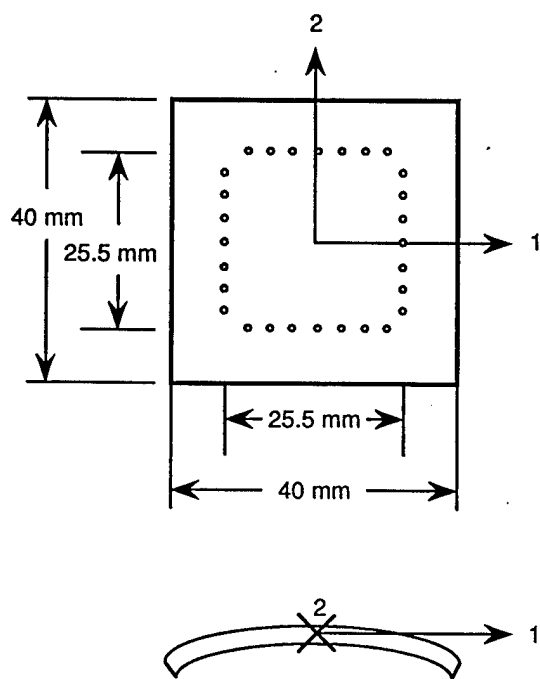


Figure 17 Orientation of irradiated specimens for biaxial testing.

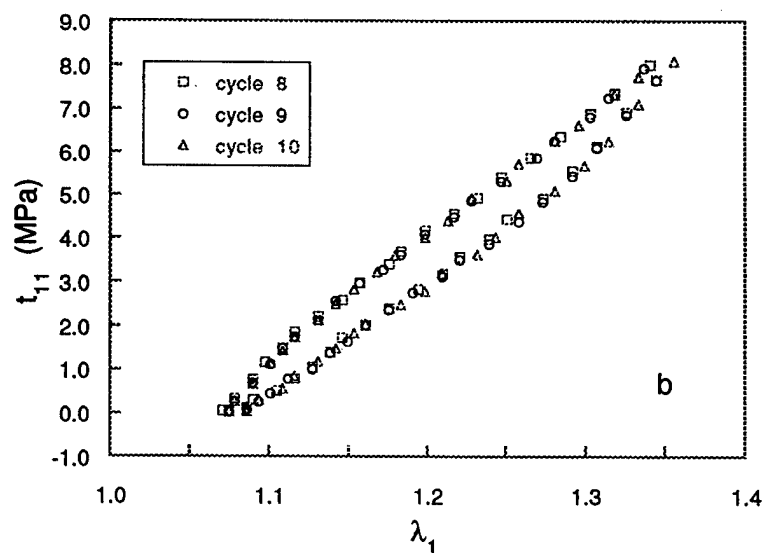
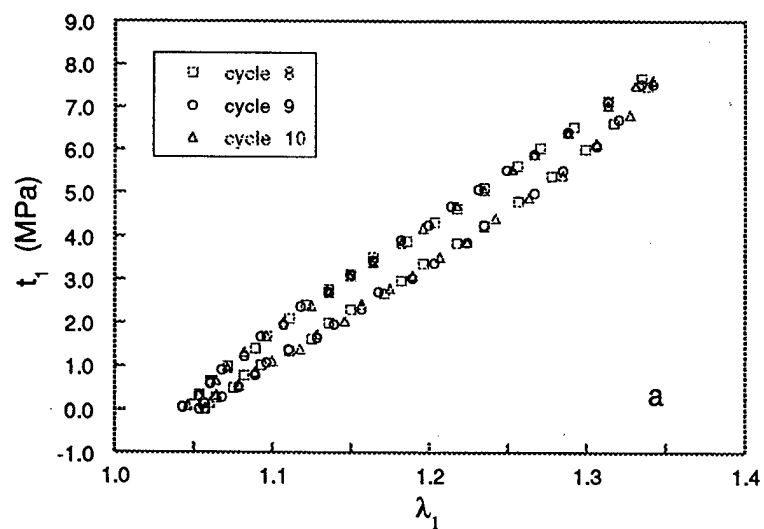


Figure 18 Comparison of the Cauchy stress-stretch curves for the last three cycles tested at $\lambda_1=1.35$ for the a) native (non-irradiated) and b) irradiated specimens.

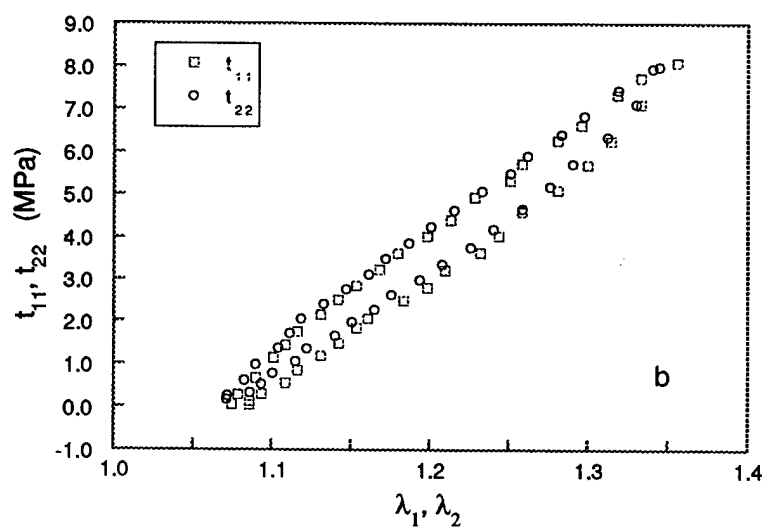
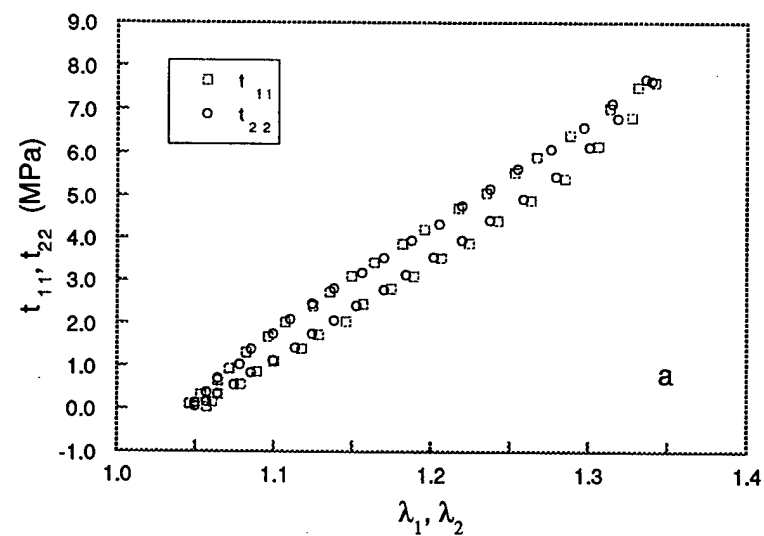


Figure 19 Comparison of the directional Cauchy stress-stretch curves for a) native (non-irradiated) and b) irradiated specimens. Note the comparatively anisotropic response of the irradiated specimen.

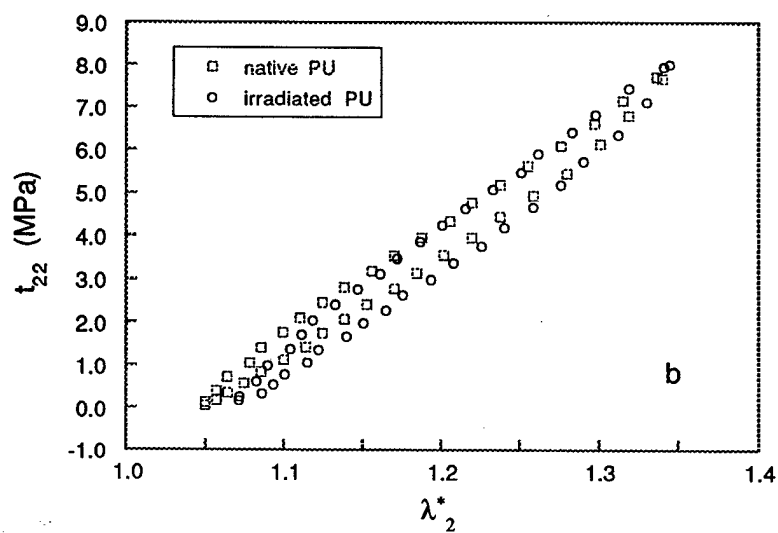
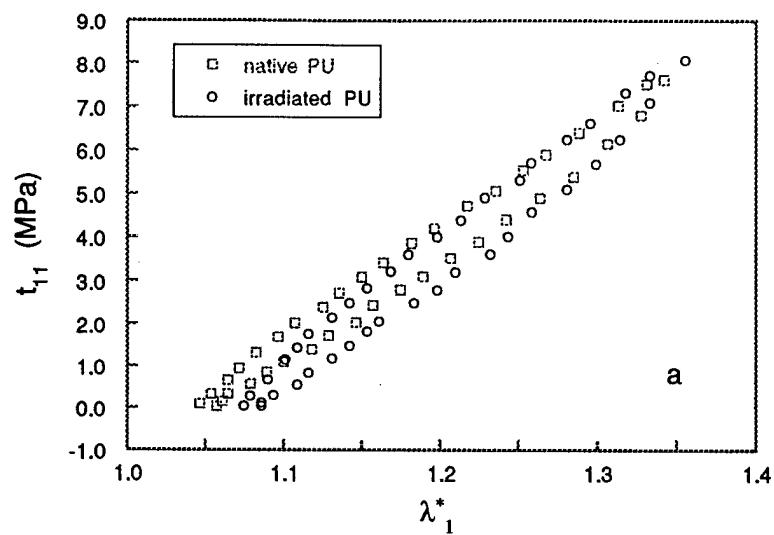


Figure 20 Comparison of the directional Cauchy stress-stretch curves for a) native (non-irradiated) and b) irradiated specimens. Note the comparatively anisotropic response of the irradiated specimen.

A One-Dimensional Heat Analysis

If the front face of a biaxially loaded specimen is uniformly illuminated, Eq. 4 simplifies to a 1-D heat transfer problem through the thickness. That is,

$$\frac{\partial T}{\partial t} = \alpha_3 \frac{\partial^2 T}{\partial x_3^2} \quad (\text{A.1})$$

where $x_3 \in [0, l]$, l being the current thickness, and the subscript 3 indicates the out-of-plane direction. Parker *et al.* [33] proposed an approximate method to calculate the α_3 based on an analytical solution to Eq. A.1 obtained by Carslaw and Jaeger [8] for insulated boundaries. The temperature rise at the rear surface of the specimen is

$$T(l, t) = \frac{Q}{\rho c_F l} \left[1 + \sum_{n=1}^{\infty} (-1)^n \exp \left(-\frac{n^2 \pi^2}{l^2} \alpha_3 t \right) \right] \quad (\text{A.2})$$

where Q is the flux associated with a pulse of radiant energy that is assumed to be instantaneously and uniformly absorbed in a thin layer at the front face of the specimen. Noticing that the rear face temperature history contains the parameter $\gamma = (-\pi^2 \alpha_3 t / l^2)$, this solution provides a simple expression for measuring α_3 from a single point on the temperature history curve defined by Eq. A.2. Choosing $t_{1/2}$ as the time at which the temperature reaches one-half its maximum value $T_{max} = Q / \rho c_F l$ yields $\gamma = 1.38$. The result is

$$\alpha_3 = \frac{1.38 l^2}{\pi^2 t_{1/2}} \quad (\text{A.3})$$

B Strain Measurement

Assuming a homogeneous deformation in the central region, the in-plane components of \mathbf{F} can be found via (Humphrey et al. [22])

$$F_{11} = 1 + \frac{\partial u_1}{\partial X_1} \quad F_{12} = \frac{\partial u_1}{\partial X_2} \quad (\text{B.1})$$

$$F_{21} = \frac{\partial u_2}{\partial X_1} \quad F_{22} = 1 + \frac{\partial u_2}{\partial X_2} \quad (\text{B.2})$$

where u_i and X_i are the components of the displacement ($= x_i - X_i$) and original position vectors, respectively. The displacement gradients $\partial u_i / \partial X_i$ can be found via a bilinear isoparametric interpolation of any four markers that define a quadrilateral. For example, let

$$X_i = \sum_{j=1}^n f^j(\zeta, \eta) X_i^j \quad (\text{B.3})$$

$$u_i = \sum_{j=1}^n f^j(\zeta, \eta) u_i^j \quad (\text{B.4})$$

where n ($= 4$) denotes the number of markers and

$$f^j(\zeta, \eta) = \frac{1}{4} (1 + \zeta \zeta^j) (1 + \eta \eta^j) \quad (\text{B.5})$$

is a standard bilinear interpolation. In the case of equibiaxial extension (with no rotations), $F_{11} = \lambda$, $F_{22} = \lambda$ and $F_{12} = F_{21} = 0$.

Evaluations and Modification of Constitutive Models for Finite Viscoplastic Deformation Related to Armor Design

Four currently utilized constitutive models for metals (i.e. Johnson – Cook, Zerilli – Armstrong, Bodner-Partom and Khan-Huang) were investigated and used to predict the mechanical behaviors of the materials and compared with experimental results. Limitations for each model in describing work-hardening behavior of metals were discussed. It was shown that the Johnson-Cook model was unable to predict the decrease in work hardening in tantalum with the increase in strain rate. Further it was demonstrated that Zerilli-Armstrong model was unable to model the response of tantalum at increasing finite strains and at different strain rates. Lastly it was found that the Bodner-Partom model gave almost perfectly plastic behavior for deformation in excess of 5 percent of strain. The details of these results are given in the enclosed copy of the paper, entitled “ A critical review of experimental results and constitutive models for BCC and FCC metals over a wide range of strain rates and temperatures”.

The elastic-plastic behaviors of three body-centered cubic metals, tantalum, tantalum alloy with 2.5% tungsten and AerMet 100 steel, were determined over a wide range of strains (15%), strain rates ($10^{-6} - 10^4 \text{ s}^{-1}$) and temperatures (77 – 600°F). Johnson-Cook and Zerilli-Armstrong models were found inadequate to describe the observations. A new viscoplastic model is proposed based on these experimental results. The proposed constitutive model gives good correlations with these experimental results. The proposed constitutive model gives good correlations with these experimental result and strain-rate jump. The details of this investigation is given in the enclosed copy of a paper entitled “ Behaviors of three BCC metals over a wide range of strain rates and temperatures: experiments and modeling”.

Further, non – proportional torsion-tension and biaxial-compressive experimental results were obtained on tantalum, tantalum alloy with 2.5% tungsten, and AerMet 100 steel. These tests results form a comprehensive set of data to show the material behaviors at finite strain and wide strain-rate range. Using the parameter set determined from uniaxial constant strain-rate compressive and tensile tests, the capability of a new constitutive model is shown to accurately predict complex loading paths of current experimental results. Using von Mises equivalent strain, stress, and strain rate, the constitutive model gives excellent predictions of these non-proportional experimental results. An enclosed copy of a paper entitled “ Behaviors of three BCC metals during non-proportional multi-axial loadings: experiment and modeling”, contains the results of this phase of the investigation.

Lastly, compression tests followed by tension tests after re-machining were performed on annealed oxygen-free-high-conductivity copper cylinders. These tests were conducted at nine levels of maximum strain ranging from 5 to 50%. From this data, isotropic and kinematic hardening were calculated using 50, 1000, and 2000 microstrain offset definitions. Both isotropic and kinematic hardening were found to depend on the yield definition. Isotropic

hardening which increased with plastic strain with no signs of saturation, also increases with larger offset definition of yield. Kinematic hardening, which increases to 40% strain and appeared to saturate thereafter, decreases with higher offset definitions of yield. The enclosed copy of a paper "On the evolution of isotropic and kinematic hardening with finite plastic deformation, Part I: compression/tension loading of OFHC copper cylinders" contain the results of this study.

Scientific Personnel:

In addition to the P.I., Dr. A.S. Khan, a doctoral student, Mr. Riqiang Liang, and two M.S. students, Ms. Kamili Jackson and Mr. Mike Watts, were supported on the project. Mr. Riqiang Liang received a Ph.D. degree and Ms. Kamili Jackson received a M.S. degree under the support of this project.

List of Manuscripts Published :

- (i) Riqiang Liang & Akhtar S. Khan, "A critical review of experimental results and constitutive models for BCC and FCC metals over a wide range of strain rates and temperatures" The International Journal of Plasticity, vol. 15, pp. 963-980, 1999.
- (ii) Akhtar S. Khan & Riqiang Liang, "Behavior of three BCC metals over a wide range of strain rates and temperatures: experiments and modeling," The International Journal of Plasticity, vol 15, pp. 1089-1109, 1999.
- (iii) Akhtar S. Khan & Riqiang Liang, "Behaviors of three BCC metals during non-proportional multi-axial loadings; experiments and modeling," The International Journal of Plasticity, vol.16, pp. 1443-1458, 2000.
- (iv) Akhtar S. Khan & Kamili M. Jackson, "On the evolution of isotropic and kinematic hardening with finite plastic deformation, Part I: compression/tension loading of OFHC copper cylinders," The International Journal of Plasticity, vol. 15, pp. 1265-1275, 1999 .

Inventions:

None.



PERGAMON

International Journal of Plasticity 15 (1999) 963–980

INTERNATIONAL JOURNAL OF
Plasticity

A critical review of experimental results and constitutive models for BCC and FCC metals over a wide range of strain rates and temperatures

Riqiang Liang, Akhtar S. Khan*

Department of Mechanical Engineering, University of Maryland, Baltimore County, MD 21250, USA

Received in final revised form 26 February 1999

Abstract

Four currently utilized constitutive models for metals (i.e. Johnson–Cook, Zerilli–Armstrong, Bodner–Partom and Khan–Huang) are investigated and used to predict the mechanical behaviors of the materials and compared with experimental results. Limitations for each model in describing work-hardening behavior of metals are discussed. © 1999 Elsevier Science Ltd. All rights reserved.

Keywords: Constitutive models; High strain rate; Impact loading; C. Kolsky bar

1. Introduction

It is now well known that the mechanical behaviors, such as yield stress, ductility, and strength, etc., of materials will change under different strain-rate loadings and temperatures. The consideration of rate and temperature dependence of material behavior is very important in the design of structures. An understanding of deformation behavior of metals over a wide range of temperatures and strain rates is of importance in metal forming, high-speed machining, high-velocity impact, penetration mechanics, explosive-metal interaction, and other similar dynamic conditions.

Flow stress measures the strength and is the resistance to plastic flow of the material at any instant under any strain rate. The rate sensitivity, defined as the amount of change of flow stress because of a change of strain rate, is the major resistance to instability. Therefore, the accurate determination and description of the

* Corresponding author.

rate dependence of mechanical behavior of materials, along with the temperature dependence and work hardening of those materials have attracted considerable attention from material and mechanics scientists for more than five decades. Since the pioneering works of von Karman (1950) and Taylor (1942), great progress has been made both experimentally and analytically and several constitutive models have been proposed based on experimental observations.

For ductile metals, large plastic deformation often leads to failure by localized deformation and shear band. This process is strain, strain rate, and temperature dependent. Realistic constitutive modeling of materials at large strains and high strain rates, including temperature effects, is a complex task. Body-centered cubic (BCC) metals, such as tantalum, exhibit a high-temperature and strain-rate sensitivity, and their mechanical properties are strongly affected by impurities. Armstrong et al. (1988) had attributed this behavior to the rate-controlling mechanism of the thermal component of the flow stress, whereas in face-centered cubic (FCC) metals the rate-controlling mechanism is the overcoming of dislocation forests by individual dislocations. It has been shown that the activation volume (or area) decreases with plastic strain for FCC metals and is constant for BCC metals. Therefore an increase in strain rate should only produce a translation, (upward or downward) of the stress–strain curve for BCC metals, whereas the work-hardening curves should “fan out” in FCC metals. The activation volume for BCC metals is much smaller than for FCC metals, yielding a much higher temperature and strain-rate sensitivity. While a large number of studies have probed the mechanical behaviors of a broad spectrum of metals, the details of the underlying deformation mechanisms remain poorly understood and in some cases controversial, (Hoge and Mukherjee, 1977; Christian, 1983; Gray and Rollett, 1992; and Gourdin and Lassila, 1995).

Heat is generated by the plastic deformation in high strain-rate flows, resulting in thermal softening. If the deformation occurs slowly, such as in quasi-static loading conditions, most of the generated heat is conducted and/or convected away from the slowly deforming regions and the body remains in an isothermal condition. At the other extreme, when deformations occur rapidly, for example in high velocity impact or explosive loading, the process is essentially adiabatic, as there is not sufficient time for redistribution of the generated heat. For the intermediate rates of deformation, both the heat generation and heat conduction need to be considered.

The main objective of the present investigation is to get an understanding of several currently utilized constitutive models and to see the applicability to correlate with the measured finite plastic deformation for BCC materials.

In the development of material constitutive models, the main interest is on the description of work-hardening behavior of materials at different strains, strain rates, and temperatures. An accurate description of a material response over a wide range of loading environments, as well as having predictive capabilities outside the measured range, is in great demand. In most published studies the experiments and constitutive modeling were based on the uniaxial deformation. The same uniaxial experimental results that were used to determine material constants were used again to show “good agreement” with the same constitutive model. This approach is

wrong, as this process only demonstrates that the values of material constants in the constitutive model are chosen properly. The correct approach is to perform non-proportional multi-axial experiments and to use these experiments to check the applicability of a particular constitutive model. Only models with comparable number of material constants are included in this review. Thus, for example models of Krempl and associates (Yao and Krempl, 1985; Krempl et al., 1996), Kothari and Anand (1998), and MTS (Follansbee and Kocks 1988) model are not included as these models have many more material constants than Bodner and Partom (1975), Johnson and Cook (1983) or Zerilli and Armstrong (1987, 1990) models.

2. Constitutive models

An ideal plasticity model in general for metals should be able to describe the materials' properties such as strain-rate dependence, temperature dependence, strain and strain-rate history dependence, work-hardening or strain-hardening behavior (both isotropic and anisotropic hardening); however, a complete description of all of these phenomena is an extremely difficult, if not impossible, task. Assumptions have to be introduced according to the need of the application to simplify the modeling. In this study, attention is focused on the modeling of strain-rate and temperature dependence of large plastic deformation.

Accurate modeling of deformation processes of materials over a wide range of strain rates and temperatures requires a reliable constitutive description of the stress-strain behavior. Several physically and phenomenologically based models have been developed for use in computational mechanics. Four constitutive models with approximately the same number of material constants, Johnson–Cook model, Zerilli–Armstrong model, Bodner–Partom model, and Khan–Huang model, will be discussed. In selecting constitutive models, it is focused on the constitutive models that are widely utilized, have relatively the same number of material constants, and are easy for using in computational procedures. Constitutive models, such as mechanical threshold stress (MTS) model (Follansbee and Kocks, 1988), that have many more material constants or have difficulties for computation are not included in the investigation. The applicability of these constitutive models to the measured finite plastic deformations will be investigated.

2.1. Johnson–Cook (JC) model

Johnson and Cook (1983) proposed a constitutive model for metals subjected to large strains, high strain rates and high temperatures. The JC constitutive model has enjoyed much success because of its simplicity and the availability of parameters for various materials of interest. It is a constitutive model that is primarily intended for computations and the basic form of the model is well suited for computations because it uses variables that are readily available in most of the applicable computer codes. It is recognized that more complicated models may indeed give more accurate descriptions of material behavior. Similarly, various models may give better

descriptions for various materials. However, in many instances, the computational codes cannot readily incorporate complicated and diverse models.

In the JC model, the von Mises flow stress, σ is expressed as

$$\sigma = (A + B\epsilon^n)(1 + C\ln\dot{\epsilon}^*)(1 - T^{*m}) \quad (1)$$

where ϵ is the equivalent plastic strain, $\dot{\epsilon}^* = \dot{\epsilon}/\dot{\epsilon}_0$ is the dimensionless strain rate, ($\dot{\epsilon}_0$ is normally taken to be 1.0 s^{-1}), and

$$T^* = \frac{T - T_r}{T_m - T_r} \quad (2)$$

where T_r is a reference temperature and T_m is the melting temperature of the material. T_r must be chosen as the lowest temperature of interest or of the lowest temperature of experiments because parameter m is normally a decimal number; T should be larger or equal to T_r to make Eq. (1) valid. The five material constants are A , B , n , C , and m .

In Eq. (1), the expression in the first set of brackets gives the dependence on strain, the second represents instantaneous strain-rate sensitivity, and the third term represents the temperature dependence of stress. This approach does not represent any thermal or strain-rate history effects, but is simple to implement and the parameters are readily obtained from a limited number of experiments. While this model is purely empirically designed for ease of computational implementation, it is a widely used and successful constitutive model.

In general, the JC model represents a set of models that consider that the mechanical behaviors of material are the multiplication effects of strain, strain rate, and temperature. This form is simple and has a clear physical interpretation; but the main problem for this form is the characteristic behavior of work hardening it represents.

From Eq. (1), if the temperature is constant, the stress increment due to the strain rate increase is

$$\Delta\sigma = (A + B\epsilon^n) \left(C \ln \frac{\dot{\epsilon}_{II}}{\dot{\epsilon}_I} \right) (1 - T^{*m}) \quad (3)$$

where $\dot{\epsilon}_I$ and $\dot{\epsilon}_{II}$ are simply two different strain rates.

From Eq. (3), the stress increment at strain ϵ_1 and ϵ_2 can be written as:

$$\Delta\sigma_1 = \Delta\sigma|_{\epsilon=\epsilon_1} = (A + B\epsilon_1^n) \left(C \ln \frac{\dot{\epsilon}_{II}}{\dot{\epsilon}_I} \right) (1 - T^{*m}) \quad (4)$$

$$\Delta\sigma_2 = \Delta\sigma|_{\epsilon=\epsilon_2} = (A + B\epsilon_2^n) \left(C \ln \frac{\dot{\epsilon}_{II}}{\dot{\epsilon}_I} \right) (1 - T^{*m}) \quad (5)$$

and it is obvious that

$$\Delta\sigma_1 < \Delta\sigma_2 \text{ when } \epsilon_1 < \epsilon_2, \dot{\epsilon}_I < \dot{\epsilon}_{II} \quad (6)$$

This can also be seen from Fig. 1(a). This means that in the JC model, the work-hardening rate, $d\sigma/d\epsilon$, at certain strain will increase when strain rate increases; the stress-strain curve is upward when strain rate increases. This characteristic implies that the JC model or Eq. (1) is appropriate to model the work-hardening behavior of metals such as OFHC copper and nickel, (Follansbee, 1986; Follansbee et al., 1990) (Fig. 2). But it still fails to predict sequential loading experimental data (Fig. 3). It is certainly not appropriate for modeling any metals where the work-hardening rate decreases when strain rate increases, such as tantalum (see Fig. 4). It is also not appropriate for materials where the work hardening remains constant with increasing strain rate.

Since the parameters can be selected to make the increasing behavior of work hardening in the JC model insignificant, Eq. (1) can still give a good fitting to the materials when the hardening behaviors have not changed too much at different strain rates such as aluminum and steel, but the inherent feature is still upward stress-strain curves when strain rate increases.

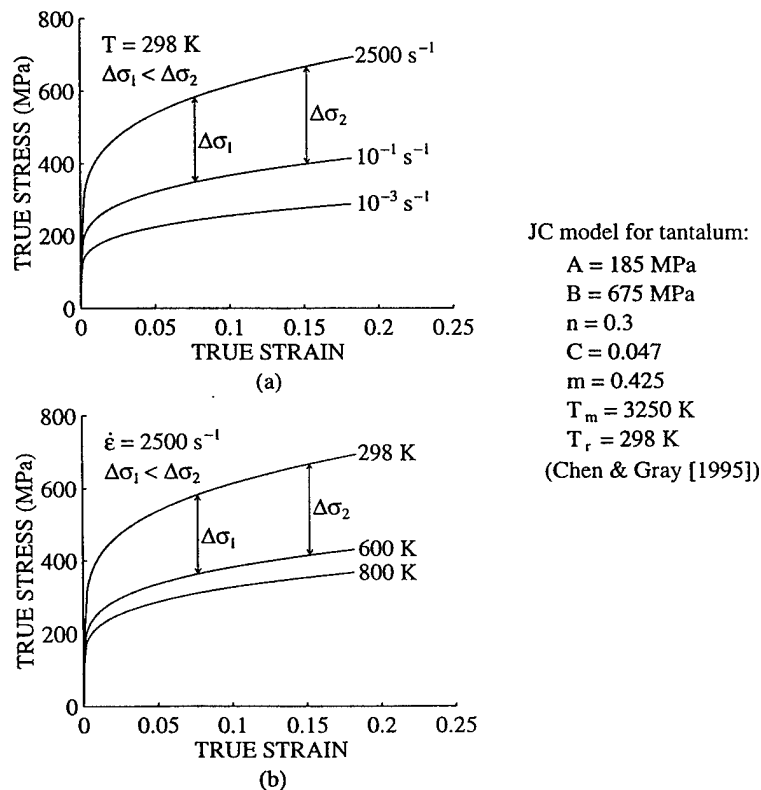


Fig. 1. Stress-strain relations of tantalum predicted by the Johnson-Cook model using the material parameters given by Chen and Gray (1995) (a) different strain rates 10^{-3} , 10^{-1} , and 2500 s^{-1} , same temperature (298 K); (b) different temperatures (298, 600, and 800 K), same strain rate (2500 s^{-1}).

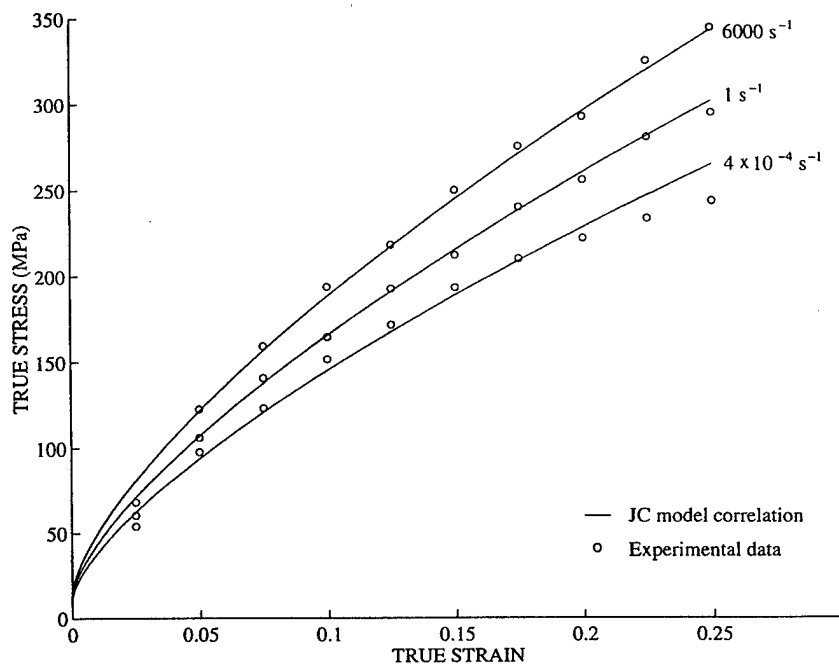


Fig. 2. Comparison of experimental data and the Johnson–Cook model correlations (Follansbee, 1986; Tanner et al., 1998) for OFHC copper.

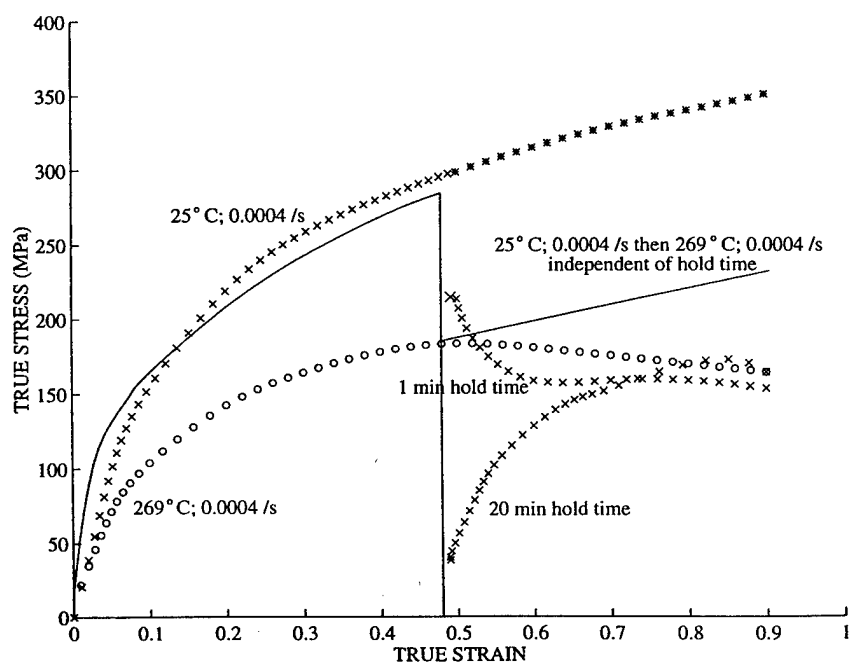


Fig. 3. Temperature sequence prediction for OFHC Cu using the JC model. Solid lines represent the model prediction, while symbols represent data (Tanner et al., 1998).

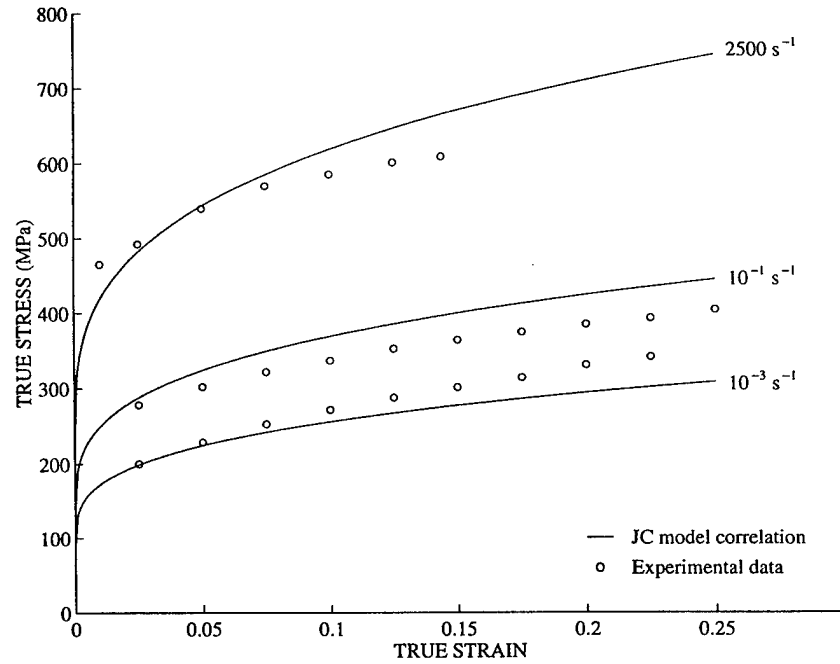


Fig. 4. Comparison of experimental data (Chen and Gray, 1995) and the Johnson–Cook model correlations (Chen and Gray, 1995) for tantalum.

On the other hand, If the strain rate keeps constant, and the temperature changes, then from Eq. (1), the stress decrement due to temperature increment will be

$$\Delta\sigma = (A + B\epsilon^n)(1 + C\ln\dot{\epsilon}^*)(T_{II}^{*m} - T_I^{*m}) \quad (7)$$

where T_I^* and T_{II}^* are two different temperatures and $T_I^* < T_{II}^*$.

From Eq. (7), the stress decrement at strain ϵ_1 and ϵ_2 can be written as:

$$\Delta\sigma_1 = \Delta\sigma|_{\epsilon=\epsilon_1} = (A + B\epsilon_1^n)(1 + C\ln\dot{\epsilon}^*)(T_{II}^{*m} - T_I^{*m}) \quad (8)$$

$$\Delta\sigma^2 = \Delta\sigma|_{\epsilon=\epsilon_2} = (A + B\epsilon_2^n)(1 + C\ln\dot{\epsilon}^*)(T_{II}^{*m} - T_I^{*m}) \quad (9)$$

and it is obvious that

$$\Delta\sigma_1 < \Delta\sigma_2 \text{ when } \epsilon_1 < \epsilon_2, T_I^* < T_{II}^* \quad (10)$$

which can also be seen in Fig. 1(b). This characteristic is consistent with most of the experimental results for most of the metals, which suggests that work-hardening rate, $d\sigma/d\epsilon$, is a decreasing function of temperature. Therefore, the JC model in its multiplication form is appropriate for describing the temperature dependence of metals, even though it has a simple temperature-dependent term. Many other researchers tried to change the temperature dependent term to get a more satisfactory fitting results, but all of these modifications lead to introduction of additional material constants.

2.2. Zerilli–Armstrong (ZA) Model

Zerilli and Armstrong, (1987) proposed dislocation-mechanics-based constitutive relations for material dynamic calculations. The effects of strain hardening, strain-rate hardening, and thermal softening based on the thermal activation analysis have been incorporated into a constitutive relation. The relation has a relatively simple expression compared to other dislocation based constitutive models. One of the main points they proposed is that each material structure type (FCC, BCC, HCP) will have a different constitutive behavior based on the different rate-controlling mechanism for that particular structure. Therefore, they gave two different constitutive relations for FCC and BCC materials.

For BCC material, the ZA model has the following relation:

$$\sigma = c_0 + B_0 e^{-(\beta_0 - \beta_1 \ln \dot{\epsilon})T} + K \epsilon^n \quad (11)$$

where σ is the von Mises equivalent stress, ϵ is the equivalent strain, $\dot{\epsilon}$ is the strain rate, and T is the absolute temperature. Six material constants, c_0 , B_0 , β_0 , β_1 , K , and n , are used for a given material, although several of the parameters have a relatively weak temperature and strain-rate dependence. The upper and lower yield point phenomena typical of BCC metals are not described by Eq. (11) hence, at small strains, the equation applies only in an average sense.

From Eq. (11), it can be easily seen that the work-hardening rate, $d\sigma/d\epsilon$, is independent of temperature and strain rate:

$$\frac{d\sigma}{d\epsilon} = Kn\epsilon^{n-1} \quad (12)$$

The ZA model for BCC metals in its addition form is actually a constant work-hardening behavior model (Fig. 5). This is the major problem for this model since the work-hardening behaviors for most BCC metals are, to some degree, dependent on strain rate and temperature.

Although the ZA model gives a fairly good correlation of the yield stress for tantalum for many experimental results as shown in Fig. 6, obviously because material constants were determined from the same data, it does not predict the work-hardening behavior of tantalum very well. Some of the experimental results of Hoge and Mukherjee (1977) for tantalum and the ZA model correlations are shown in Figs. 7 and 8. The data were digitized from plots in Hoge and Mukherjee's paper. Fig. 7 is the correlation using material constants from Zerilli and Armstrong (1987), while Fig. 8 is the correlation using material constants from Chen and Gray (1995). Zerilli and Armstrong used a systematic method to determine the material constants. Their data set representing Hoge and Mukherjee's data, derived from plots in Hoge and Mukherjee's (1977) paper, are very different from the original data; the reason is not clear. Therefore, the correlations shown here are poor and not as good as those given by Zerilli and Armstrong (1987). Chen and Gray (1995) used an optimized procedure to best fit the entire range of data. In Fig. 8, predictions are given using

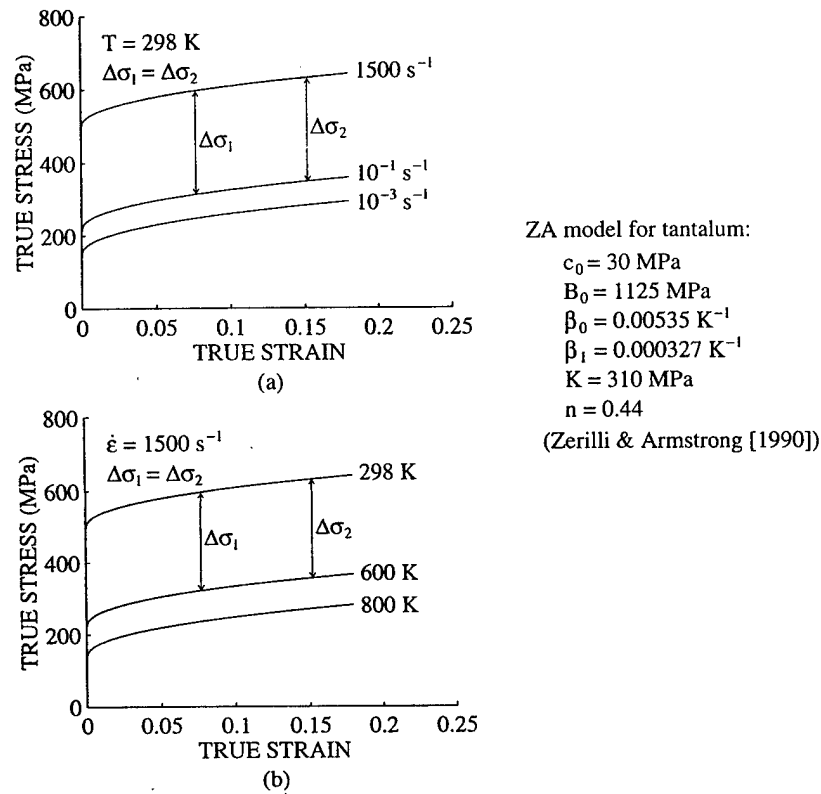


Fig. 5. Stress-strain relations of tantalum predicted by the Zerilli-Armstrong model using the material parameters given by Zerilli and Armstrong (1990): (a) different strain rates 10^{-3} , 10^{-1} , and 1500 s^{-1} , same temperature (298 K); (b) different temperatures (298, 600, and 800 K), same strain rate (1500 s^{-1}).

their material constants; correlation with the experimental data is somewhat better but still poor. It is clear that because of the inherent problem of the ZA model, the work-hardening behavior can not be predicted very well for tantalum over a wide range of strain. In both Figs. 7 and 8, the difference between predictions and data is quite large after about 8% strain. The temperature dependence is shown in Fig. 9, again the correlations with the experimental data of Hoge and Mukherjee (1977) and Nemat-Nasser and Isaacs (1996) with ZA and JC models are poor except the room temperature data points that were used to determine material constants by Zerilli and Armstrong (1990) and Chen and Gray (1995).

2.3. Bodner-Partom (BP) model

Bodner and Partom, (1975) formulated a set of constitutive equations to represent elastic-viscoplastic strain-hardening material behavior for large deformations and arbitrary loading histories. An essential feature of the formulation is that the total deformation rate is considered to be separable into elastic and inelastic components, which are functions of state variables at all stages of loading and unloading. The formulation is independent of any yield criteria or loading and unloading conditions.

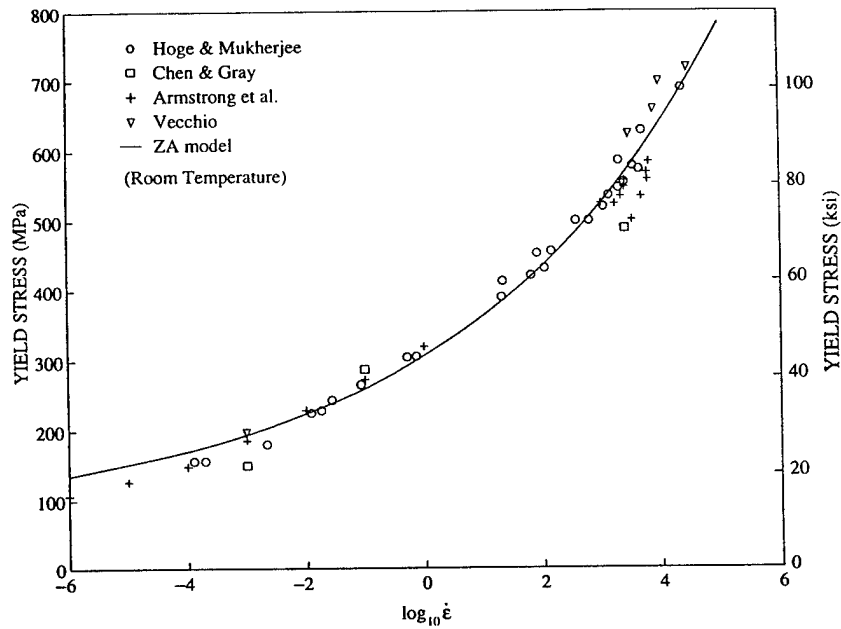


Fig. 6. Lower yield stress versus strain rate for Zerilli–Armstrong equation fitted to Hoge and Mukherjee (1977) and other results (Zerilli and Armstrong, 1990; Armstrong et al., 1997).

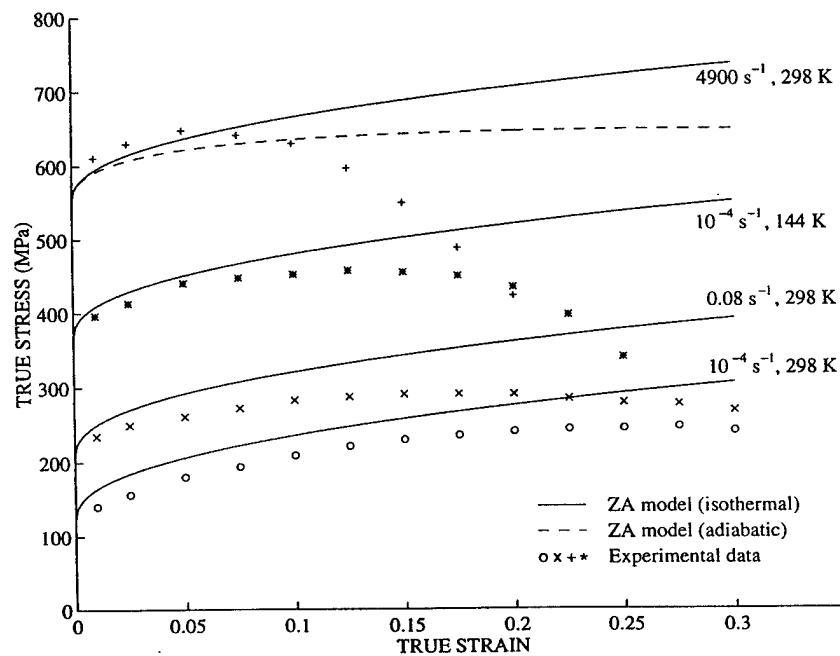


Fig. 7. Comparison of experimental data (Hoge and Mukherjee, 1977) and the Zerilli–Armstrong model correlations (Zerilli and Armstrong, 1990) for tantalum.

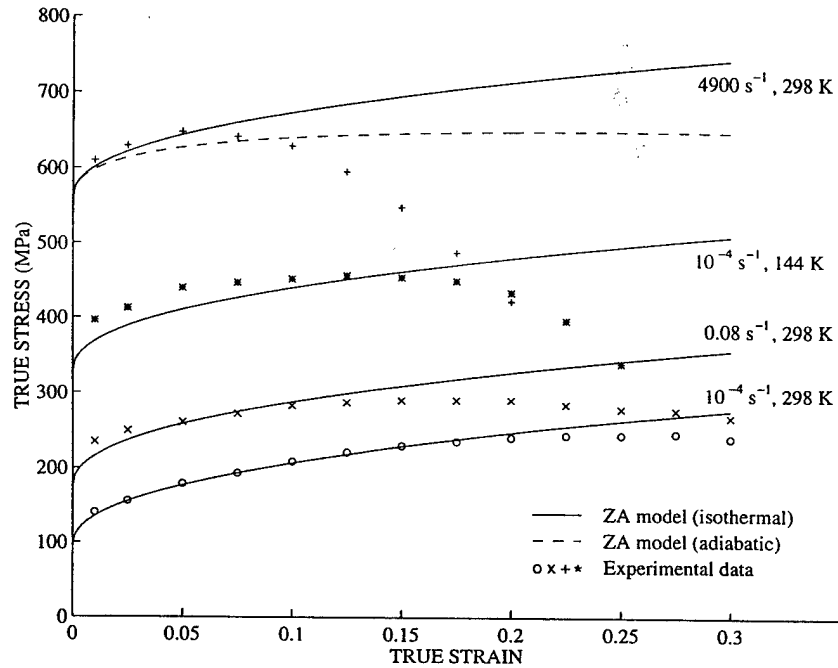


Fig. 8. Comparison of experimental data (Hoge and Mukherjee, 1977) and the Zerilli–Armstrong model correlations (Chen and Gray, 1995) for tantalum.

The deformation rate components are determinable from the current state, which permits an incremental formulation of problems. Strain hardening is considered in the equations by introducing plastic work as the representative state variable. The assumptions of isotropy and isothermal conditions are maintained in this formulation, although strain hardening is known to induce anisotropy.

The general formula of the BP model is based on separation of the total deformation rate $\mathbf{d} = \{d_{ij}\}$ into elastic (reversible) and plastic (irreversible) components at all stages of deformation

$$\mathbf{d} = \mathbf{d}^e + \mathbf{d}^p \text{ or } d_{ij} = d_{ij}^e + d_{ij}^p \quad (13)$$

where $\mathbf{d} = \{d_{ij}\}$ is the symmetric part of the velocity gradient

$$\mathbf{d} = \frac{1}{2}(\mathbf{L} + \mathbf{L}^T) = \frac{1}{2}(\mathbf{v}\nabla + \nabla\mathbf{v}) \text{ or } d_{ij} = \frac{1}{2}(v_{ij} + v_{j,i}) \quad (14)$$

The elastic deformation rate $\mathbf{d}^e = \{d_{ij}^e\}$ can be related to the Cauchy stress rate by the generalized Hooke's law

$$d_{ij}^e = \frac{\dot{\epsilon}_{ij}}{G} - \frac{\lambda \dot{\epsilon}_{kk} \delta_{ij}}{2G(3\lambda + 2G)} \quad (15)$$

where G is the elastic shear modulus and λ is an elastic Lamé constant.

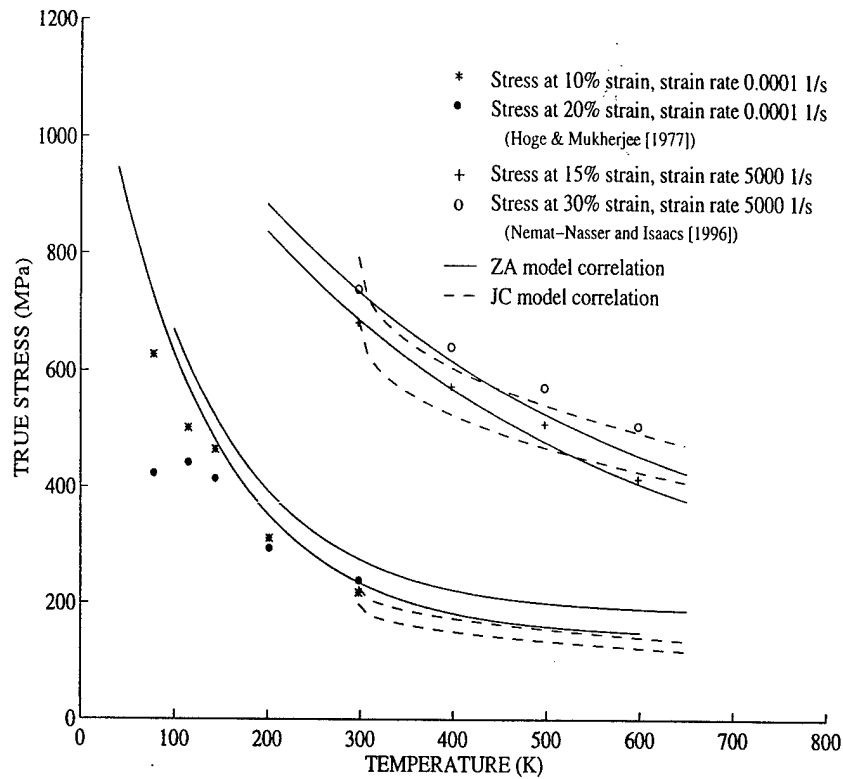


Fig. 9. Experimental stress data at different temperatures (Hoge and Mukherjee, 1977; Nemat-Nasser and Isaacs, 1996) and ZA and JC model correlations for Ta using material constants based on Hoge and Mukherjee's data from Zerilli and Armstrong (1990) and Chen and Gray (1995).

When finite deformation and finite rotation are involved, the objective *Jaumann* rate of the Cauchy stress must be used here,

$$\dot{\mathbf{t}} = \mathbf{t} - (\mathbf{w} \cdot \mathbf{t} - \mathbf{t} \cdot \mathbf{w}) \quad \text{or} \quad \dot{t}_{ij} = t_{ij} - (w_{ik}t_{kj} - t_{ik}w_{kj}) \quad (16)$$

$\mathbf{w} = \{w_{ij}\}$ is the antisymmetric part of the velocity gradient

$$\mathbf{w} = \frac{1}{2}(\mathbf{L} - \mathbf{L}^T) = \frac{1}{2}(\mathbf{v}\nabla - \nabla\mathbf{v}) \quad \text{or} \quad w_{ij} = \frac{1}{2}(v_{ij} - v_{j,i}) \quad (17)$$

The plastic deformation rate $\mathbf{d}^p = \{d_{ij}^p\}$ is related to the deviator of Cauchy stress, as in the classical Prantl–Ruess equation

$$\mathbf{d}^p = \gamma \mathbf{s} \quad \text{or} \quad d_{ij}^p = \gamma s_{ij} \quad (18)$$

$\mathbf{s} = \{s_{ij} = t_{ij} - \frac{1}{3}t_{kk}\delta_{ij}\}$ is the deviator of the Cauchy stress and γ is a proportional factor. Squaring Eq. (18) gives

$$\gamma^2 = \frac{D_2^p}{J_2} \quad (19)$$

D_2^p is the second invariant of the plastic deformation rate. J_2 is the second invariant of \mathbf{s} .

$$D_2^p = \frac{1}{2} d_{ij}^p d_{ij}^p \quad (20)$$

$$J_2 = \frac{1}{2} s_{ij} s_{ij} \quad (21)$$

γ will be determined by specifying D_2^p as a function of J_2

$$D_2^p = f(J_2) \quad (22)$$

This formula can be considered to be a multi-dimensional generalization of the uniaxial result. The particular forms of Eq. (22) that seem applicable are those used to relate dislocation velocity with stress. In those equations, the dislocation velocity is represented as a power function or as an exponential function of the stress.

The particular function used in the BP model is

$$D_2^p = D_0^2 \exp\left(-\left(\frac{n+1}{n}\right)\left(\frac{Z^2}{3J_2}\right)^n\right) \quad (23)$$

where D_0 is the limiting or maximum strain rate; Z is a loading history dependent internal variable; n is a material parameter governing the strain-rate sensitivity. The preferred functional form of Eq. (22) for a particular material would be essentially empirically based and any monotonically increasing function of D_2^p with J_2 is admissible.

For the constitutive equation of the internal variable, it is assumed that Z is a function of the plastic work

$$\dot{Z} = \frac{m(Z_1 - Z)\dot{W}^p}{Z_0} \quad (24)$$

where m is a material parameter, Z_0 is the initial value of Z , Z_1 is the saturation value of Z , and \dot{W}^p the plastic work:

$$\dot{W}^p = \mathbf{t} : \mathbf{d}^p = t_{ij} d_{ij}^p \quad (25)$$

From Eq. (24), Z can be integrated as

$$Z = Z_1 + (Z_0 - Z_1) \exp\left(-\frac{mW^p}{Z_0}\right) \quad (26)$$

For one dimensional case, the BP model reduces to the following equations

$$\dot{\epsilon}^e = \frac{\dot{\sigma}}{E}$$

$$\dot{\epsilon}^p = \frac{2}{\sqrt{3}} \left(\frac{\sigma}{|\sigma|} \right) D_0 \exp \left(-\frac{n+1}{2n} \left(\frac{Z}{\sigma} \right)^{2n} \right) \quad (27)$$

$$Z = Z_1 + (Z_0 - Z_1) \exp \left(-\frac{m \int \sigma d\epsilon^p}{Z_0} \right)$$

where the quantity $\sigma/|\sigma|$ imposes the condition that the plastic strain rate has the same sign as that of the applied stress.

There are five material parameters in the BP model. In most of the cases, the experimental data for characterizing the material parameters are in the form of stress–strain curves at constant strain rates. For the BP model, two stress–strain curves at different strain rates are sufficient to calculate the material parameters. D_0 is the maximum strain rate that the material can experience. It was recommended by Bodner and Partom that $D_0 = 10^4 \text{s}^{-1}$ for quasi-static modeling and $D_0 = 10^6 \text{s}^{-1}$ for dynamic modeling.

The predictions of the BP model for commercially pure titanium under uniaxial deformation are shown in Fig. 10(a) and (b) using the material parameters determined by Bodner and Partom (1975). The material constants were determined by fitting computed stress–strain curves to the experimental ones at the slowest and fastest rates. The correlations between the experimental data for titanium and the model are very good (see Bodner and Partom, 1975). Huang and Khan (1992) has proposed a systematic method to determine the material constants for the BP model when modeling the 1100 aluminum.

For the BP model, the work-hardening behavior is not easy to see from Eq. (27) directly. When calculating the stress increment due to strain-rate change, it can be seen from Fig. 10(c) that $\Delta\sigma$ first increases and then decreases beyond certain strain level; but in general, for large deformation, the strain-hardening behavior does not change much at different strain rates.

From Fig. 10(b), the BP model shows an elastic and almost perfectly plastic behavior at very high strain rate. At very low strain rate, the BP model also reduces to perfectly plastic behavior model after 5% strain. The BP model, using the published constants, does not show a very strong strain-hardening behavior. It is not very sensitive to the parameter m . Therefore, for materials that exhibit strong work-hardening behavior like OFHC copper, m was made a function of W_p by Bodner and Merzer (1978). The expression for m was

$$m = m_0 + m_1 e^{-\alpha W_p} \quad (28)$$

which adds two more constants. When m is defined by Eq. (28), the relationship given by Eq. (26) is not valid. The expression for Z when integrated after replacing m by the Eq. (28), yields the following relationship between Z and W_p :

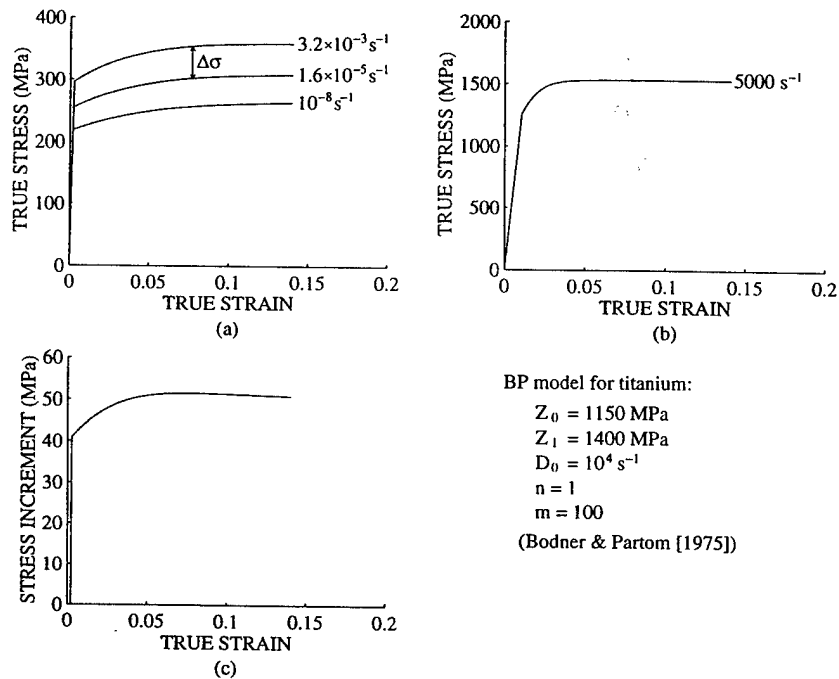


Fig. 10. Predictions of the Bodner–Partom model for titanium under uniaxial deformation (Bodner and Partom, 1975). (a) Stress–strain relations at different strain rates: 10^{-8} , 1.6×10^{-5} , and $3.2 \times 10^{-3} \text{ s}^{-1}$; (b) stress–strain relation at strain rate 5000 s^{-1} ; (c) stress increment ($\Delta\sigma$) between strain rate 3.2×10^{-3} and $1.6 \times 10^{-5} \text{ s}^{-1}$.

$$Z = Z_1 + (Z_0 - Z_1) \exp(-m_0 W_p) \exp\left(-\frac{m_0 + m_1 - m}{\alpha}\right) \quad (29)$$

Bonder and Rubin (1994) also presented a modification to the BP model to include a strong strain-rate dependence of strain hardening. The original form of the BP model did not take the temperature effect into consideration. Bodner and Rajendran (1995) presented a modification to the BP model on temperature effect for copper. All of these modifications introduced more material constants to the model.

2.4. Khan–Huang (KH) model

In the study of mechanical behavior of 1100 aluminum in the strain rate range 10^{-5} – 10^4 s^{-1} Khan and Huang (1992) proposed a new constitutive model that can predict the experimental results in a very large strain-rate range including the high work-hardening region.

The assumption of the KH model is similar to that of the BP model. The only difference is to determine the proportionality parameter γ in Eq. (19)

$$\gamma^2 = \frac{D_2^p}{J_2} \quad (30)$$

A constitutive equation is proposed for J_2 as

$$J_2 = f_1(\epsilon_2^p) f_2(D_2^p) \quad (31)$$

where ϵ_2^p is the equivalent plastic strain defined by

$$\epsilon_2^p = \frac{1}{2} \epsilon_{ij}^p \epsilon_{ij}^p \quad (32)$$

For one dimensional case, Eq. (31) can be written as

$$\sigma = g_1(\epsilon^p) g_2(\dot{\epsilon}^p) \quad (33)$$

where

$$g_1(\epsilon^p) = \left[3 f_1 \left(\frac{3}{4} (\epsilon^p)^2 \right) \right]^{1/2} \quad (34)$$

$$g_2(\dot{\epsilon}^p) = \left[f_2 \left(\frac{3}{4} (\dot{\epsilon}^p)^2 \right) \right]^{1/2} \quad (35)$$

The particular form of $g_1(\epsilon^p)$ and $g_2(\dot{\epsilon}^p)$ were proposed to be

$$g_1(\epsilon^p) = \sigma_0 + E_\infty \epsilon^p - a e^{-\alpha \epsilon^p} \quad (36)$$

$$g_2(\dot{\epsilon}^p) = \frac{1}{\left[1 - \frac{\ln(\dot{\epsilon}^p)}{\ln(D_0^p)} \right]^n} \quad (37)$$

Five material constants are n , E_∞ , σ_0 , a , and α . D_0^p is arbitrarily chosen to be 10^6 s^{-1} in Khan and Huang's work.

The particular form of the KH model describing 1100 aluminum has the same features of work-hardening behavior as that of the JC model when strain rate changes. The KH model is more capable of predicting the strong work-hardening behavior in a large strain-rate range than that of the BP model. Since the KH model does not consider the temperature effect in the original equations, some modifications will be needed in order to incorporate the temperature effect into the model.

3. Conclusions

Four constitutive models have been examined for describing the strain, strain-rate, and temperature relations for metals in the large strain, high strain-rate regime. It should be mentioned here that other models, e.g. Mechanical Threshold Stress model, were not included in this comparison as they use many more material constants than the four models selected here. Also the material constant determinations are quite complicated and require a large array of experiments.

The Johnson–Cook model is a work-hardening rate increasing model, with increasing strain rate, in its original form. It has the inherent problem of describing the work-hardening behavior of metals, such as tantalum, where the work-hardening rate decreases when strain rate increases.

The Zerilli–Armstrong model presumes that the work-hardening rate is independent of the temperature and strain rate. For most metals, work-hardening behaviors are actually dependent on the temperature and strain rate. Therefore, the Zerilli–Armstrong model is not a good candidate for modeling the work-hardening behaviors of materials with strong temperature and strain-rate dependences.

The Bodner–Partom model, in its original form, is not very sensitive to the strain rate. It can be seen as a constant work-hardening model when the strain rate change is not too much. The BP model also does not take the temperature effect into consideration. Many modification have been made to the model; all lead to adding more material constants.

Based on similar assumption as that of the BP model, the KH model proposed a new relation to describe the dependence of work-hardening behavior on strain and strain rate. The KH model is more capable of predicting the strong work-hardening behavior in a large strain-rate range than that of the BP model.

From these analyses, the simple multiplication form, such as the JC model, or addition form, such as the ZA model, has inherent problems of modeling the dependence of work-hardening behavior of materials on strain-rate and temperature. It is clear that to better predict the work-hardening behavior, strain and strain rate must have some coupled effects on the description of work-hardening relation of the materials.

Acknowledgement

The authors are grateful for the funding of this project by the Army Research Office under the cooperative agreement DAAH04-95-2-0004.

References

- Armstrong, R.W., Ramachandran, V., Zerilli, F.J., 1988. In: Rama Rao, P. (Ed.), *Advances in Materials and Their Applications*. Wiley Eastern Ltd., New Delhip. 201.
- Armstrong, R.W., Chen, C.C., Dick, R.D., Zhang, X.J., 1997. Evaluation and improvement in constitutive equations for finite viscoplastic deformation and fracturing behavior relating to armor design. Internal Report, The University of Maryland.
- Bodner, S.R., Merzer, A., 1978. Viscoplastic constitutive equations for copper with strain rate history and temperature effects. *Journal of Engineering Materials and Technology* 100, 388–394.
- Bodner, S.R., Partom Y., 1975. Constitutive equations for elastic–viscoplastic strain-hardening materials. *Journal of Applied Mechanics*, June, pp. 385–389.
- Bodner, S.R., Rajendran, A.M., 1995. On the strain rate and temperature dependence of hardening of copper. In: Schmidt, S.C., Tao, W.C. (Eds.), *Proceedings of the Conference on Shock Compression of Condensed Material*, 1995. American Institute of Physics Press, pp. 499–502.
- Bodner, S.R., Rubin, M.B., 1994. Modeling of hardening at very high strain rate. *Journal of Applied Physics* 76 (5), 2742–2747.

- Chen, S.R., Gray III, G.T., 1995. Constitutive behavior of tungsten and tantalum experiments and modeling. In: Bose, A., Dowding, R.J. (Eds.), 2nd International Conference on Tungsten and Refractory Metals. McLean, VA, 17–19 October. Metal Powder Industries Federation, Princeton, NJ, 1995, pp. 489–498.
- Christian, J.W., 1983. Some surprising features of the plastic deformation of body-centered cubic metals and alloys. *Metall. Trans.* 14A, 1237–1256.
- Follansbee, P.S., 1986. High-strain-rate deformation of FCC metals and alloys. In: Murr, L.E., Staudhammer, K.P., Meyers, M.A. (Eds.), *Metallurgical Applications of Shock-Wave and High-Strain-Rate Phenomena*. New York, 1986, pp. 451–478.
- Follansbee, P.S., Kocks, U.F., 1988. A constitutive description of the deformation of copper based on the use of the mechanical threshold stress as an internal state variable. *Acta Metall.* 36 (1), 81–93.
- Follansbee, P.S., Huang, J.C., Gray, G.T., 1990. Low-temperature and high-strain-rate deformation of nickel and nickel-carbon alloys and analysis of the constitutive behavior according to an internal state variable model. *Acta Metallurgical and Materials* 38 (7), 1241–1254.
- Gourdin, W.H. Lassial, D.H., 1995. Multiple mechanisms in the thermally activated plastic flow of tantalum. 1995 APS Topical Conference, Seattle, WA, 1995.
- Gray III, G.T., Rollett, A.D., 1992. The high-strain-rate and spallation response of tantalum, Ta-10W, and T-111. In: Asfhani, R., Chen, E., Crowson, A. (Eds.), *High Strain Rate Behavior of Refractory Metals and Alloys*. TMS, Warrendale, PA, pp. 303–315.
- Hoge, K.G., Mukherjee, A.K., 1977. The temperature and strain rate dependence of the flow stress of tantalum. *Journal of Materials Science* 12, 1666–1672.
- Huang, S., Khan, A.S., 1992. Modeling the mechanical behavior of 1100-0 aluminum at different strain rates by the Bodner–Partom model. *International Journal of Plasticity* 8, 501–517.
- Johnson, G.R., Cook, W.H., 1983. A constitutive model and data for metals subjected to large strains, high strain rates and high temperatures. *Proceedings of the Seventh International Symposium on Ballistic*, The Hague, The Netherlands, 1983, pp. 541–547.
- Khan, A.S., Huang, S., 1992. Experimental and theoretical study of mechanical behavior of 1100 aluminum in the strain rate range 10^{-5} – 10^4 s $^{-1}$. *International Journal of Plasticity* 8, 397–424.
- Kothari, M., Anand, L., 1998. Elasto-visoplastic constitutive equations for polycrystalline metals: application to tantalum. *Journal of the Mechanical and Physics of Solids* 46 (1), 51–83.
- Krempf, E., Gleason, J.M., 1996. Isotropic viscoplasticity theory based on overstress (VBO). The influence of the direction of the dynamic recovery term in the growth law of the equilibrium stress. *International Journal of Plasticity* 12 (6), 719–735.
- Nemat-Nasser, S., Isaacs, J.B., 1996. Direct measurement of isothermal flow stress of metals at elevated temperatures and high strain rates with application to Ta and Ta–W alloys, Internal report, Center of Excellence for Advanced Materials, UCSD, San Diego, CA.
- Tanner, A.B., McGinty, R.D., McDowell, D.L., 1998. Modeling temperature and strain rate history effects of OFHC Cu. *International Journal of Plasticity* (preprint).
- Taylor, G.I., 1942. The Plastic Wave in a Wire Extended by an Impact Load. British Ministry of Home Security, Civil Defense Research Committee Report RC 323.
- von Karman, Th., Duwez, P., 1950. The propagation of plastic deformation in solids. *Journal of Applied Physics* 21, 987.
- Yao, D., Krempf, E., 1985. Viscoplasticity theory based on overstress. The prediction of monotonic and cyclic proportional and nonproportional loading paths of an aluminum alloy. *International Journal of Plasticity* 1 (3), 259–274.
- Zerilli, F.J., Armstrong, R.W., 1987. Dislocation-mechanics-based constitutive relations for material dynamics calculations. *Journal of Applied Physics* 61 (5), 1816–1825.
- Zerilli, F.J., Armstrong, R.W., 1990. Description of tantalum deformation behavior by dislocation mechanics based constitutive relations. *Journal of Applied Physics* 68 (4), 1580–1591.



PERGAMON

International Journal of Plasticity 15 (1999) 1089–1109

INTERNATIONAL JOURNAL OF
Plasticity

Behaviors of three BCC metal over a wide range of strain rates and temperatures: experiments and modeling

Akhtar S. Khan*, Riqiang Liang

*Department of Mechanical Engineering, University of Maryland, Baltimore County,
Maryland 21250, USA*

Received in final revised form 6 June 1999

Abstract

The elastic–plastic behaviors of three body-centered cubic metals, tantalum, tantalum alloy with 2.5% tungsten, and AerMet 100 steel, are presented over a wide range of strains (15%), strain rates (10^{-6} – 10^4 s $^{-1}$) and temperatures (77–600°F). Johnson-Cook and Zerilli-Armstrong models were found inadequate to describe the observations. A new viscoplastic model is proposed based on these experimental results. The proposed constitutive model gives good correlations with these experimental results and strain-rate jump experiments. In the next paper (Liang, R., Khan A.S., 2000. Behaviors of three BCC metals during non-proportional multi-axial loadings and predictions using a recently proposed model. *International Journal of Plasticity*, in press), multi-axial loading results on these materials and comparison with the proposed model will be presented. © 1999 Published by Elsevier Science Ltd. All rights reserved.

Keywords: Constitutive models; High strain rate; Impact loading; C. Kolsky bar

1. Introduction

In the previous paper (Liang and Khan, 1999), several constitutive models were reviewed and found inadequate to describe the behavior of tantalum where the work-hardening rate decreased with increasing strain rate.

A series of experiments under uniaxial loading conditions were conducted to obtain the stress–strain relations of three body-centered cubic metals: tantalum, tantalum alloy with 2.5% tungsten, and AerMet 100 steel, at large strain (15%),

* Corresponding author. Tel.: +1-410-455-3300; fax: +1-410-455-1052.

E-mail address: khan@engr.umbc.edu

different strain rates (10^{-6} – 10^4 s $^{-1}$), and temperatures (77–600°F). Experiments were conducted to obtain comprehensive data sets for the understanding of the measurement behaviors of three materials and for the development and evaluation of constitutive models.

The experiments at high strain rates were performed using the split Hopkinson pressure bar and the direct disc impact (Huang, 1990; Huang and Khan, 1991, 1992) techniques, while quasi-static constant strain rate and strain-rate jump tests were conducted using an MTS loading frame system. Strain gages were used for the measurement of large plastic deformation with the corrections of nonlinearity of the Wheatstone bridge and gage factor.

Hoge and Mukherjee (1977) published relatively complete experimental data for tantalum on the temperature and strain-rate dependence of the flow stress. In their studies, the yield strength of tantalum increased by more than 400% when tested at temperatures from 298 to 77 K at a strain rate of order of 10^{-4} s $^{-1}$. Their data were often used by other researchers for constitutive modeling, although no one had discussed the early softening phenomena (around 10% deformation) in their test results.

Zerilli and Armstrong (1990) conducted constitutive modeling using Hoge and Mukherjee's data and many other researchers' data, such as Regazzoni and Montheillet (1984). Their model presented a satisfactory description of the relation between yield stress and strain rate, but the work-hardening behavior was not well described.

Nemat-Nasser et al. (1994), Nemat-Nasser and Isaacs (1996) performed a high strain-rate recovery test, which they used to address the thermal softening behavior of tantalum at high strain-rate deformation. From their test results, the effect of thermal softening at high strain deformation for tantalum dominated the work-hardening behavior due to the combined effects of strain and strain-rate hardening.

Chen and Gray (1996) performed a series of tests on the strain-rate and temperature dependence of the yield stress and the strain-hardening behavior of tantalum. They examined several existing constitutive models, namely the Mechanical Threshold Stress model, the Johnson-Cook model (Johnson and Cook, 1983), and the Zerilli-Armstrong model (Zerilli and Armstrong, 1987, 1990), using the same data set to derive the parameters for each model. All of their data were under uniaxial compression with different strain rates and temperatures. Their results show no thermal softening phenomena in their high strain-rate tests up to 20–25% deformation, which are in direct contradiction to other results mentioned above. Although they discussed the thermal softening problem, they concluded that there was no such temperature change at strain less than 20%. Perhaps, the discrepancy is either due to a variation in the material, or due to the dimensions of specimens used in their tests. For split Hopkinson pressure bar test, it is required that length to diameter ratio of the specimen is around 0.3–0.5 (Davies and Hunter, 1963; Bertholf and Karnes, 1975). But in Chen and Gray's tests, their length/diameter ratio of the specimen is 1.0 (Chen and Gray, 1995, 1996). Several tests were performed with different length/diameter ratios for tantalum on our split Hopkinson pressure bar test setup. These results suggest that larger length/diameter ratio may give artificially higher work hardening behavior in the test for the material (see Fig. 1).

Lee et al. (1997) tried to model the mechanical behavior of tantalum at high strain rate using a crystal plasticity model to describe the thermal softening behavior shown in the tests of Nemat-Nasser et al. and Meyers and Vecchio. Recently, Kothari and Anand (1998) also provided predictions using their crystal plasticity model and compared these to the experimental results.

In all of these studies, the main interest was on the description of work-hardening behavior of tantalum at different strains, strain rates, and temperatures. Differences in test results at high strain rates among different researchers are quite diverse. Most of the experiments and constitutive modeling were based on the uniaxial loading deformation. The same uniaxial loading experimental results that were used to determine material constants were used again to show agreement with a particular constitutive model. This approach only demonstrates that the material constants were chosen properly. The correct approach is to perform non-proportional multi-axial experiments and use these experiments to check the applicability of a particular constitutive model. In the next paper (Liang and Khan, to be submitted), the multi-axial loading experiments will be presented and compared to the predictions from constitutive models with material constants determined from uniaxial loading tests to evaluate the applicability of constitutive models.

2. Materials

Three body-centered cubic metals, tantalum, tantalum-tungsten alloy (2.5%W), and AerMet 100 steel, were used in this investigation.

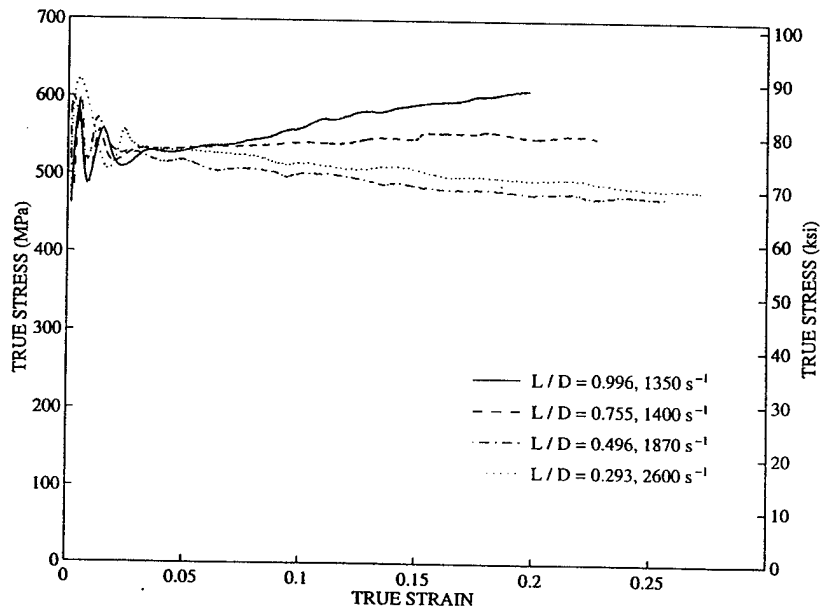


Fig. 1. Stress-strain response for Ta at high strain rate for the specimens with different length/diameter ratios (L/D).

2.1. Tantalum and tantalum-tungsten alloy (2.5%W)

Tantalum and tantalum-tungsten alloy (2.5%W) specimens used in this investigation are machined from commercially pure tantalum (Ta) and tantalum alloy with 2.5% tungsten (Ta-2.5W). These two materials were supplied by Cabot Corporation (Boyetown, PA). The materials are initially (triple-electron-beam) annealed in the form of round bars with two different diameters, 12.7 mm (0.5 in) and 25.4 mm (1 in), respectively. The as-tested micro-structures of Ta and Ta-2.5W exhibit equiaxed grains with average grain sizes of 42 and 45 μm , respectively. The chemical compositions, as given by the supplier, are listed in Tables 1 and 2. Some of the physical properties are also given in Table 3.

The properties of tantalum and tantalum-based alloys continue to attract scientific and engineering interest because of their high density, melting point, excellent formability, good heat conductivity, good fracture toughness, corrosion resistance, and weldability. Tantalum and its alloys have received increased interest as a model BCC metal and for defense-related applications. They are suited for a number of engineering and structural applications, such as armor penetrators and explosively forged projectiles.

2.2. AerMet 100 Steel

AerMet 100 steel material was purchased from Carpenter Technology Corporation (Reading, PA); they also developed this material. The material was shipped in

Table 1
Chemical compositions of Ta (in parts per million unless noted)

Element	Ta	W	O	N	Nb	B	C H Ti Fe Mn Si Sn Ni Cr Ca Al Mo Cu Zr Co Mg
Result	Bal.	<25	<10	20	100	<1	<5

Table 2
Chemical compositions of Ta-2.5W (in parts per million unless noted)

Element	Ta	W	C	O	N	Nb	Cu	B	H Ti Fe Mn Si Sn Ni Cr Ca Al Mo Zr Co Mg
Result	Bal.	2.4%	15	55	20	330	5	1	<5

Table 3
Physical properties of Ta and Ta-2.5W

Property	Ta	Ta-2.5W
Yield strength (MPa/ksi)	117.9/17.1	178.6/25.9
Young's modulus (GPa/ksi)	185.5/26.9 $\times 10^3$	187/27 $\times 10^3$
Density (kg-m ⁻³ /lb-in ⁻³)	16608/0.600	16677/0.603

the form of round bars with two different diameters, 12.7 mm (0.5 in) and 25.4 mm (1 in), respectively. They were all in fully annealed status. The chemical compositions of the material given by the manufacturer are listed in Table 4 and some of its physical properties are given in Table 5.

The need for high strength, high toughness, and weldable structural steels was the driving force behind the development of ultra high-strength steels, such as AerMet 100. AerMet 100 steel is an alloy possessing high hardness and strength combined with exceptional ductility and toughness. It can attain 280 ksi ultimate tensile strength combined with 100 ksi $\sqrt{\text{in}}$ fracture toughness. The alloy is designed for components requiring high strength, high fracture toughness, and exceptional resistance to stress corrosion cracking and fatigue. AerMet 100 alloy is considered a candidate for use in applications involving high rate of loading (armor, landing gear).

3. Uniaxial loading experiments

Uniaxial compressive and tensile loading experiments were performed over a wide range of strains, strain rates, and temperatures.

3.1. Quasi-static loading

The quasi-static (low to medium strain-rate) tensile and compressive experiments were carried out on an MTS axial/torsional material test system. The load capacity of the machine was 250 kN/55 kip in axial and 2200 N-m/20,000 in-lb in torsional, respectively. The machine was well calibrated. Configuration files and test programs were fine tuned for different materials at different tests. Several experiments were conducted at the same conditions to verify repeatability and the results were very repeatable and indicate that the machine response, testing procedure, and material response were consistent.

Table 4
Chemical compositions of AerMet 100 steel (wt%)

Element	C	Cr	Ni	Mo	Co	Iron
Result	0.23	3.10	11.10	1.20	13.40	Bal.

Table 5
Physical properties of AerMet 100 steel

Property	AerMet 100
Yield strength (MPa/ksi)	965/140
Young's modulus (GPa/ksi)	194.4/28.2 $\times 10^3$
Density ($\text{kg}\cdot\text{m}^{-3}/\text{lb}\cdot\text{in}^{-3}$)	7892/0.285

The quasi-static experiments at room temperature were compressive tests. The advantages and difficulties of the compressive test are well established (ASTM Standard E209-65, 1983). As compared to the tensile test, larger strains can be achieved because of the absence of necking. Another advantage is the simplicity of fixtures and specimens for compressive tests. Uniform deformation was achieved by reducing the effects of friction between the specimen and the compression platens. VascoMax C350 steel was used as compression platen material and heat treated to its maximum strength. The surfaces of the platens were polished to maintain a smooth contact with the specimen.

The specimens used in compressive test for Ta and Ta-2.5W were solid cylindrical samples 12.7 mm (0.5 in) in diameter and 25.4 mm (1 inch) in length. For AerMet 100, the cylindrical specimens were 10.16 mm (0.4 in) in diameter and 20.32 mm (0.8 in) in length. The diameter and length ratio was 0.5 for all the quasi-static compressive specimens.

In order to reduce the friction between both ends of the specimen and the compressive platens of the machine and to avoid barrelling, one or two layers of thin Teflon sheets (0.003 in) were used as lubrication material. For AerMet 100 steel, concentric grooves were machined into the ends of some specimens that underwent very large deformation to hold special powdered graphite lubricant to further reduce the friction and achieve homogeneous compression because of its high strength.

The stroke data given by the MTS machine included the deformation of the machine itself, the compressive platens, and the lubrication materials. They were found to be much greater than the actual deformation of the specimen, especially at small strain. The differences were affected by the material, loading rate, and machine condition, which were not easy to compensate. Therefore, strain gages (KFE-2-120-C1, KYOWA, Inc., Japan) were used for measuring the deformation of specimens. All gages were bonded with M-Bond AE-15 adhesive (Measurements Group, Inc.) in the middle of the cylindrical specimen. To eliminate the possible bending effect, two gages were mounted on diametrically opposite sides of the specimen along the axial direction. In addition to these axial gages, two gages were sometimes mounted on diametrically opposite positions along the circumferential direction to measure the change of the circumference of the cylindrical specimen.

The outputs of the strain gages were connected to a Model P-3500 strain indicator (Measurements Group, Inc.) using a Wheatstone bridge circuit. All of the strain gages were measured separately in order to carry out the data corrections.

Load data were directly obtained from the MTS machine's load output. All of the information (time, load, and strain gages) were recorded using a digital acquisition system to capture the data set at different sampling rates for different strain-rate tests.

3.2. *Dynamic loading*

The high strain-rate experiments were performed using the split Hopkinson pressure bar (SHPB) and the direct disc impact (DDI) techniques.

The SHPB test is a well-developed technique for dynamic experiments (Fig. 2). A disc specimen is sandwiched between two bars known as the incident bar and the

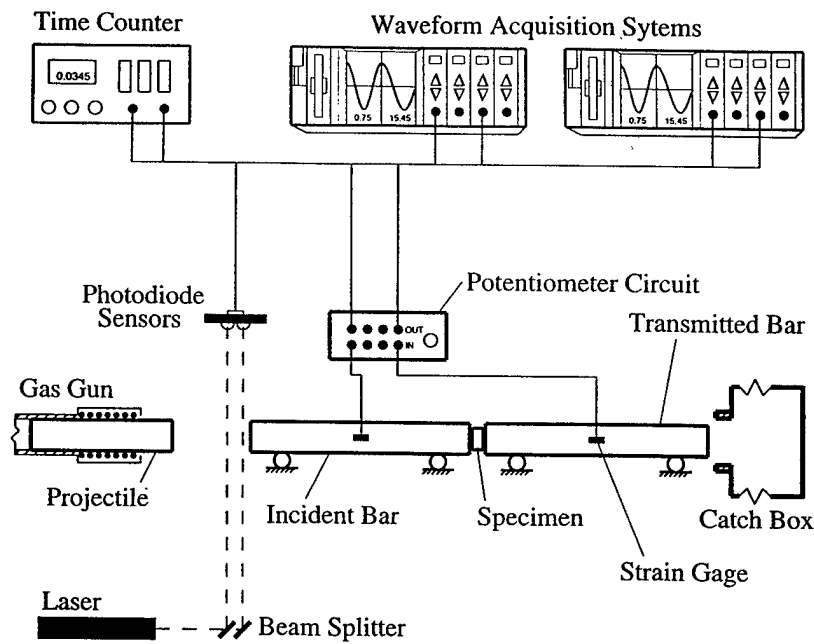


Fig. 2. Schematic diagram of the split Hopkinson pressure bar experiment.

transmitted bar. The projectile is propelled from a uniform bore compressed-nitrogen gas gun. The elastic deformation signals in the incident and the transmitted bars are captured using strain gages mounted on the two bars. The strain-time histories of the three pulses, incident, reflected, and transmitted waves, are recorded on oscilloscopes (Nicolet SYSTEM 440) through a potentiometer circuit. The nominal stress and strain in the specimen up to any time duration can be calculated using the three waves under the assumption that the specimen undergoes uniform stress deformation.

$$\varepsilon(t) = \frac{c_0}{L} \int_0^t (\varepsilon_I - \varepsilon_R - \varepsilon_T) dt, \quad \sigma(t) = \frac{EA_0}{2A} (\varepsilon_T + \varepsilon_I + \varepsilon_R) \quad (1)$$

where c_0 is the longitudinal wave velocity of the pressure bar, E and A_0 are the Young's modulus and the cross-sectional area of the bar. A and L are the cross-sectional area and length of the specimen, ε_R and ε_T are reflected and transmitted waves, respectively.

The SHPB technique is widely used in the high strain-rate experiments (Follansbee, 1979). It has been used successfully to perform dynamic compression tests at strain rates from 200 s^{-1} to 10^5 s^{-1} and strains up to 30%.

The equations relating strain-gage measurements on the incident and the transmitted bars to stress-strain behavior in the specimen require that the specimen must deform uniformly during the test. The equilibration of stress throughout the test sample requires a few reverberations of the stress wave. Davies and Hunter (1963) estimated that at least three reverberations are required for stress equilibration. Therefore, the data at the very beginning of impact deformation may not be valid

because it cannot be assumed that the specimen is deforming uniformly. That means that the strain-gage measurements obtained from the very beginning to some critical time may be invalid to calculate stress-strain relation since uniform deformation is not achieved. According to an approximate analysis for aluminum, for example, the critical strain at which uniform stress within the specimen is achieved is equal to 0.5–0.6% at a strain rate of 10^3 s^{-1} . This value is far beyond the elastic deformation for aluminum.

There are two sets of SHPB experimental setups used in the current research. One of them is made of AerMet 100 steel. The diameter of bars is 25.4 mm (1 in). This setup is used for relatively soft material such as aluminum, copper, tantalum. The other setup is made of VascoMax C350 steel with 21.34 mm (0.84 in) bar diameter. All the bars are heat treated to attain maximum strength. This setup is used for testing hard material such as AerMet 100 steel.

There are restrictions on the dimensions of test specimen for the SHPB test. One of them is for reducing the longitudinal and radial inertia effects on the deformation behavior. According to Davies and Hunter's (1963) analysis:

$$\sigma(t) = \sigma_m(t) \rho \left[\frac{L^2}{6} - \nu^2 \frac{D^2}{8} \right] \frac{d^2 \varepsilon(t)}{dt^2} \quad (2)$$

where σ_m is the measured stress, ρ is the density of the material, ν is the Poisson's ratio, L is the specimen length, and D is the specimen diameter. It is implied that if the specimen dimensions are chosen to be such that

$$\frac{L}{D} = \frac{\sqrt{3}}{2} \nu \quad (3)$$

then the inertia effects will be minimized even the strain rate is not held constant. For most of the metals, Poisson's ratio is around 0.3, which suggests that the optimum L/D ratio to minimize errors due to inertia is about 0.3.

In current experiments, the diameters of specimens were 19.05 mm (0.75 in) and 12.7 mm (0.5 in) depending on the diameter of the bars. The L/D ratios of the SHPB test specimens were from 0.2 to 0.5. As it is shown previously that large L/D ratio will lead to more work-hardening behavior in tests. But in the range of 0.2–0.5, no significant differences were observed in the tests.

The DDI technique is another effective method to measure the dynamic response of material (Fig. 3). Unlike SHPB tests, the disc specimen, which is backed up by a long bar called the transmitted bar, is directly impacted by the projectile. Strain gages are mounted on the specimen to obtain the axial and transverse strain-time histories of the deformation. The strain gages mounted on the transmitted bar provide the strain-time history of the bar, which is used to compute the stress-time profile. In this setup, higher impacting velocities result in higher strain rates; thus it is not necessary to change the thickness of the disc specimen to achieve different strain rates. Another advantage of this technique is that the strain-time profiles are directly measured without numerical integration of signals and are valid for small

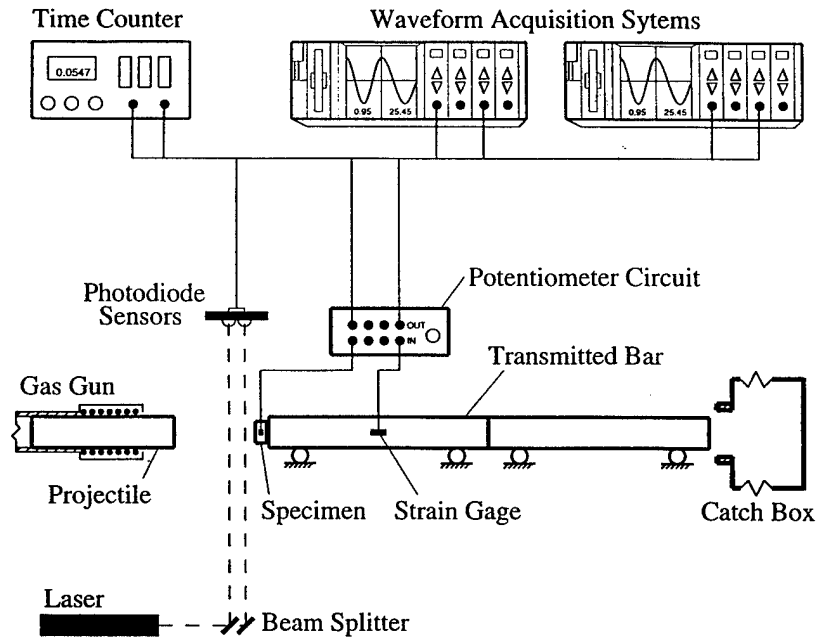


Fig. 3. Schematic diagram of the direct disc impact experiment.

strains. Huang and Khan (1991, 1992) gave a detailed description of this experimental technique. On the use of strain gages for plastic wave measurement, Khan and Hsiao (1988, 1991) had a detailed study.

In general, at high strain rates, some of the heat generated by the plastic work is lost by heat conduction and radiation. However, depending on the level of strain rate, a portion of this heat remains within the specimen, causing thermal softening.

Plastic deformation at low strain rate can often be treated as an isothermal process. A tensile specimen pulled in tension at a strain rate of 10^{-4} – 10^{-3} s^{-1} does not undergo a significant temperature rise. The distance that heat can transit during a certain time is often referred to as the thermal diffusion distance and is given by $2\sqrt{\alpha t}$, where α is the thermal diffusivity. In the case of the tantalum specimen ($\alpha = 0.29 \text{ cm}^2 \text{ s}^{-1}$) being pulled at 10^{-4} s^{-1} , the diffusion distance is 76 cm assuming that the duration of the test is $t = 0.5/10^{-4} = 5 \times 10^3 \text{ s}$. However, if the test was conducted at 10^3 s^{-1} , the same strain would be attained in $t = 5 \times 10^{-4} \text{ s}$, and the corresponding thermal diffusion distance would be 0.45 mm.

Thus, high strain-rate deformation is often adiabatic and part of the deformation work is transformed into heat with the attendant temperature increase of the specimen. This temperature rise has a profound effect on the constitutive behavior of the material at high strain-rate loading because of the thermal softening. The temperature rise associated with plastic deformation can be directly obtained from the constitutive equation by considering that a fraction of plastic work is converted into heat. For most metals, the conversion factor is usually taken as 0.9, which implies that 90% of the work of deformation is changed to heat. Thus, the temperature rise can be expressed as

$$\Delta T = \frac{0.9}{\rho C_p} \int_0^\epsilon \sigma(\epsilon) d\epsilon \quad (4)$$

where ρ is the density and C_p is the heat capacity of the material.

Therefore, once a description between temperature, stress, strain, and strain rate is obtained, this relation can be used to convert the original experimental response at high strain rates under adiabatic heating to isothermal behavior, then re-fit the temperature corrected curves together with quasi-static stress-strain relations to the model to derive the final fitting constants. This may lead to a better set of material constants for the model. In the quasi-static and the DDI experiments, strain gages are used to measure the large plastic deformation using some form of Wheatstone bridge circuit or potentiometer circuit. The nonlinearity of the Wheatstone bridge, as well as the strain gage factor for large deformation, must be corrected. Huang and Khan (1991) performed a series of tests and established a linear gage factor correction formula with respect to nominal strain for a special kind of strain gage, KFE-2-120-C1, made by KYOWA Electronics Instruments, Ltd., Japan.

Most of the analyses of the SHPB results have been based on the assumption that one dimensional wave theory is adequate in the interpretation of pulses travelling along the bars. In order to be more accurate in the analysis of test results, it is desirable to use a more general theory to take into consideration the dispersion of the waves due to the finite size of the bars. The procedure for correcting the recorded waveforms is discussed in details by Follansbee and Frantz (1983).

4. Uniaxial loading experimental results and correlations with constitutive models

Experimental results for Ta, Ta-2.5W, and AerMet 100 under uniaxial quasi-static and dynamic loadings are shown in Figs. 4–7. These results were corrected for Wheatstone bridge nonlinearity (Measurements Group Inc., 1982), gage factor (Huang and Khan, 1991) and dispersion (Follansbee and Frantz, 1983).

For the commercially pure tantalum, the material response at different strain rates changes significantly, as shown in Fig. 4. The yield stress increases significantly and the work-hardening rate decreases as the strain rate increases. At high strain-rate tests, thermal softening behavior can be seen in the experimental results.

Fig. 5 shows the stress-strain relations for tantalum at different strain rates and temperatures (Armstrong et al., 1997). When temperature increases, the yield stress decreases and the work-hardening rate also decreases, which are consistent with most of the metals.

For Ta-2.5W, there is a positive strain-rate sensitivity with respect to yield stress, but the work-hardening behavior does not change significantly with the change of strain rates (see Fig. 6).

AerMet 100 steel is a high strength material. It has a moderate strain-rate sensitivity for the yield stress and work-hardening behavior (Fig. 7). In this case, the strain hardening also decreases slightly when the strain rate increases.

Using the quasi-static test results, material constants of the JC and the ZA constitutive models for tantalum are determined using a least square fitting procedure.

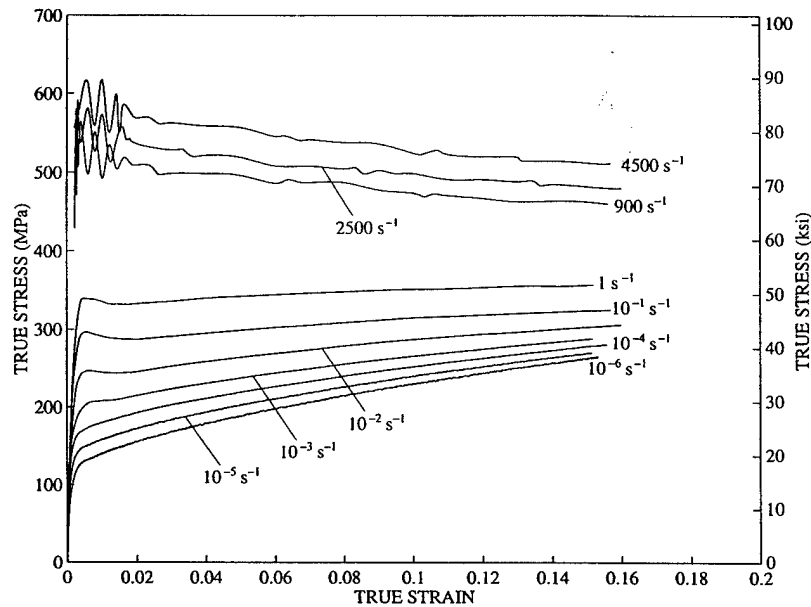


Fig. 4. Stress-strain response for Ta at different strain rates (room temperature).

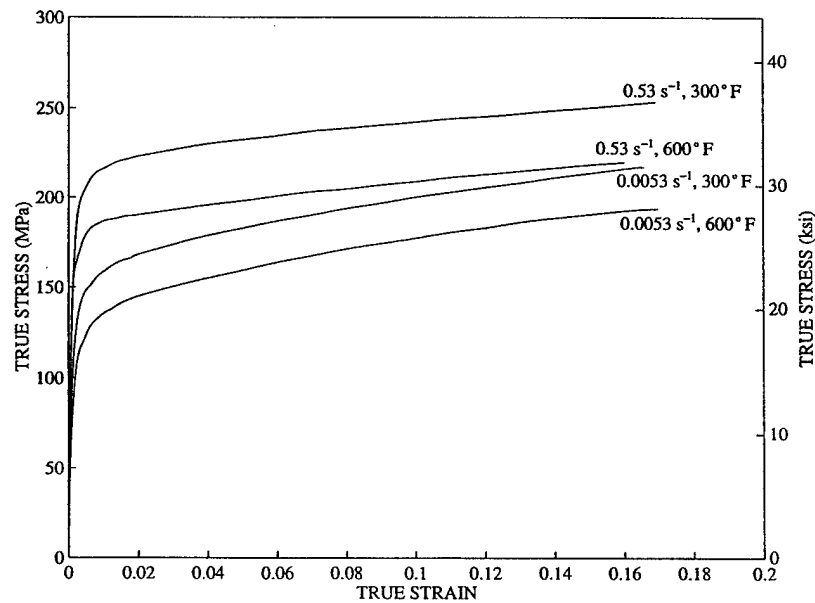


Fig. 5. Stress-strain response for Ta at different strain rates and temperatures (Armstrong et al., 1997).

As it was pointed out in the previous paper (Liang and Khan, 1999), the JC and the ZA constitutive models were unable to accurately describe the decrease of work hardening with the increasing strain rate. For example, even if only parts of the

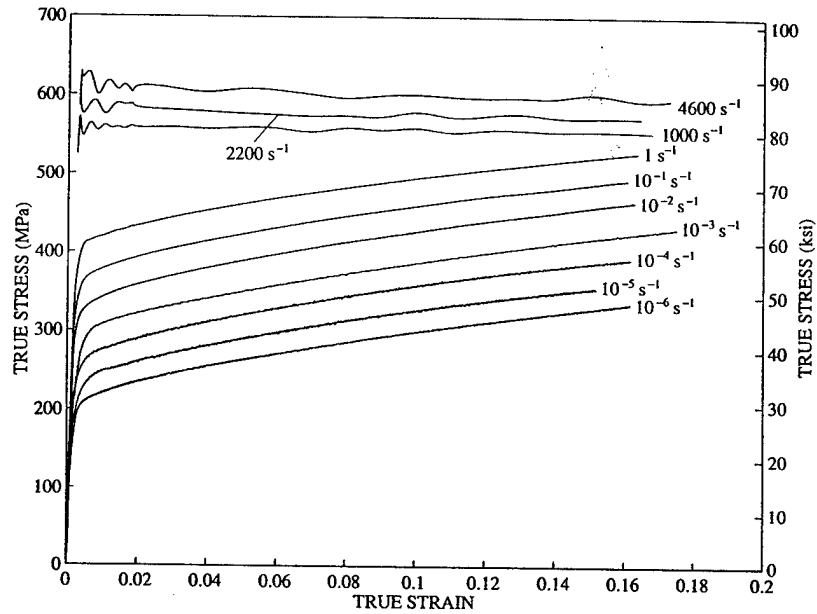


Fig. 6. Stress-strain response for Ta-2.5W at different strain rates (room temperature).

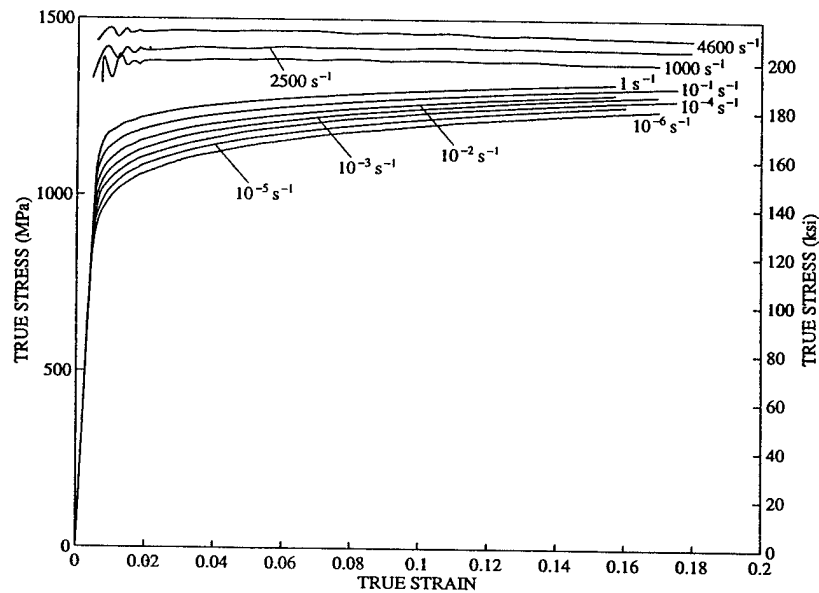


Fig. 7. Stress-strain response for AerMet 100 steel at different strain rates (room temperature).

experimental data (e.g. at strain rate 10^{-5} s^{-1} , 10^{-3} s^{-1} , and 10^{-1} s^{-1}) are used to correlate with the JC model and the ZA model, they cannot give satisfactory correlations for the work-hardening behaviors of tantalum at different strain rates, as shown in Figs. 8 and 9.

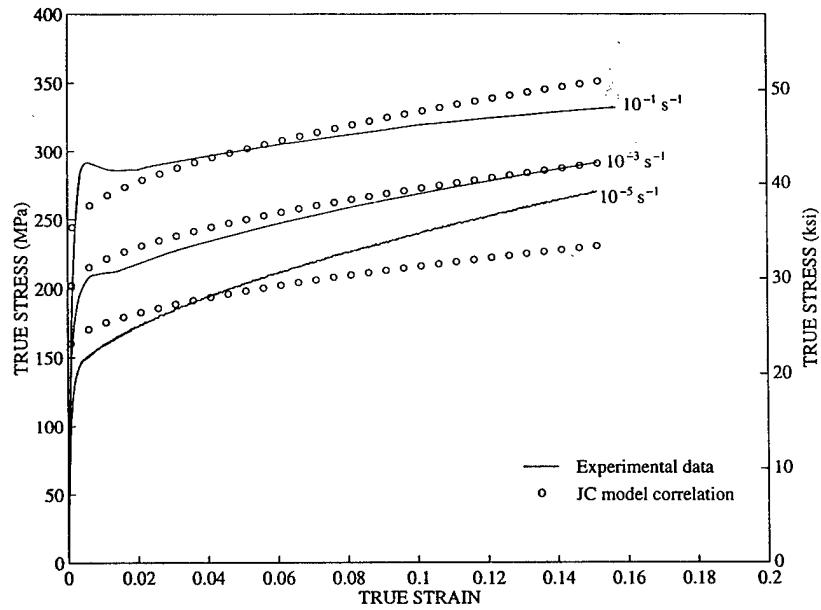


Fig. 8. Experimental data and the JC model correlations for Ta at strain rate 10^{-5} s^{-1} , 10^{-3} s^{-1} , and 10^{-1} s^{-1} .

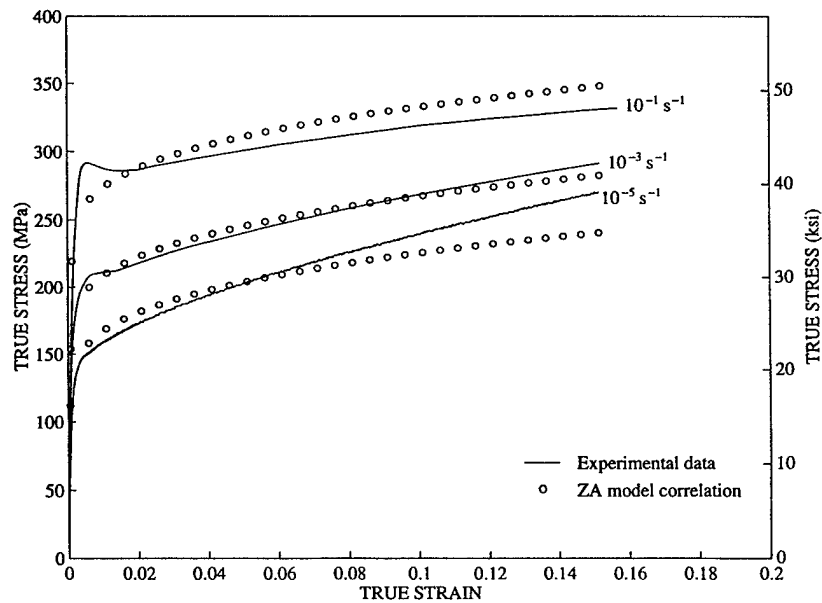


Fig. 9. Experimental data and the ZA model correlations for Ta at strain rate 10^{-5} s^{-1} , 10^{-3} s^{-1} , and 10^{-1} s^{-1} .

5. A viscoplastic model for isotropic hardening materials

From the previous analysis (Liang and Khan, 1999) and model correlations, the simple multiplication form, such as the JC model, or addition form, such as the

ZA model, has inherent problems of modeling the dependence of work-hardening behavior of materials on strain-rate and temperature dependence. It is clear that to better predict the work-hardening behavior, strain and strain rate must have some coupled effects on the description of workhardening relation of the materials. Therefore, a new relation between J_2 and D_2^p in the KH model (Khan and Huang, 1992) is proposed in order to obtain a better correlation with the experimental data

$$J_2 = f_1(\varepsilon_2, D_2^p) f_2(T) \quad (5)$$

where ε_2 is the equivalent strain. $f_1(\varepsilon_2, D_2^p)$ is a function describing the coupled strain and strain-rate effects on the work-hardening behavior.

In the current research, the specific form is chosen to be

$$\sigma = \left[A + B \left(1 - \frac{\ln \dot{\varepsilon}}{\ln D_0^p} \right)^{n_1} \varepsilon^{n_0} \right] e^{C \ln \dot{\varepsilon} (1 - T^{*m})} \quad (6)$$

$$T^* = (T - T_r) / (T_m - T_r)$$

where σ , ε , and $\dot{\varepsilon}$ are von Mises equivalent stress, strain, and strain rate, respectively; T is the absolute temperature; T_m is the melting temperature of the material; and, T_r is a reference temperature. Six materials constants are A , B , n_0 , n_1 , C , and m as compared to five, six, and four material constants in JC, ZA, and BP (without temperature dependence) models, respectively. D_0^p is chosen to be 10^6 s^{-1} in the study.

To determine the material constants for the model, uniaxial loading test results at different strain rates and temperatures were first used to obtain an initial set of values for the material constants with the following steps:

- At room temperature, when strain rate $\dot{\varepsilon} = 1 \text{ s}^{-1}$, Eqn. (6) will reduce to

$$\sigma = A + B \varepsilon^{n_0} \quad (7)$$

$$\ln(\sigma - A) = n_0 \ln \varepsilon + \ln B \quad (8)$$

Using the stress-strain curve at strain rate $\dot{\varepsilon} = 1 \text{ s}^{-1}$, A was determined from the yield stress; then using the plot of $\ln(\sigma - A)$ vs $\ln \varepsilon$, B was found from the interception with the vertical axis and n_0 from the slope. Therefore, A , B , and n_0 were determined.

- The strain at yield point is relatively small, so Eqn. (6), at room temperature, can be approximated as

$$\sigma_Y \approx A e^{C \ln \dot{\varepsilon}} \quad (9)$$

$$\ln(\sigma_Y / A) \approx C \ln \dot{\varepsilon} \quad (10)$$

where σ_Y is the yield stress. So using the plot of $\ln(\sigma_Y / A)$ vs $\ln \dot{\varepsilon}$, C was determined from the slope of the line.

- At room temperature, material constant n_1 in Eqn. (6) can be expressed as

$$n_1 = \frac{\ln\left(\frac{\sigma/e^{C\ln\dot{\epsilon}} - A}{B\dot{\epsilon}^{n_0}}\right)}{\ln(1 - \ln\dot{\epsilon}/\ln D_0^p)} \quad (11)$$

With A , B , n_0 , C determined from previous steps, using stress–strain relations at strain rates other than 1 s^{-1} , n_1 was calculated from the above equation for different strain-rate experiments and an average value of n_1 was obtained.

- The final step was to determine the material constant m . From Eq. (6),

$$m = \frac{\ln(1 - \sigma/K)}{\ln T^*} \quad (12)$$

where

$$K = \left[A + B \left(1 - \frac{\ln \dot{\epsilon}}{\ln D_0^p} \right)^{n_1} \dot{\epsilon}^{n_0} \right] e^{C \ln \dot{\epsilon}}$$

$$T^* = (T - T_r)/(T_m - T_r)$$

Using the quasi-static high temperature test results, m was obtained from the above equation.

In order to get a better set of values, material constants for the proposed constitutive model were determined using a combination of the least square method and a constrained optimization procedure to minimize the error between predicted and actual data. The values obtained from the above steps were used as a set of initial data for the iteration. The experimental data at low strain rates were first used to get a more accurate set of material constants using the least square method. Then, high strain-rate test results under adiabatic condition were correlated to model prediction, with the assumption that 90% plastic work was converted to heat, to get a better set of material constants for both low and high strain-rate material response using a constrained optimization procedure. This was an iterative process that was continued until the constants converged. The core procedures were commercial programs in the MATLAB software. The material constants for the constitutive model for the three materials are listed in Table 6. D_0^p is chosen to be 10^6 s^{-1} .

The proposed constitutive model gives an excellent correlation with the experimental response, see Figs. 10–13. In the following section, strain-rate jump experimental results were used to compare with the model predictions without changing

Table 6
Material constants for the constitutive model

	A MPa	B MPa	n_0	n_1	C	m
Ta	318.47	153.20	0.6088	3.1547	0.0759	0.400
Ta-2.5W	400.76	410.37	0.5989	1.0589	0.0522	0.415
AerMet 100	872.57	536.86	0.1036	1.9284	0.0524	1.150

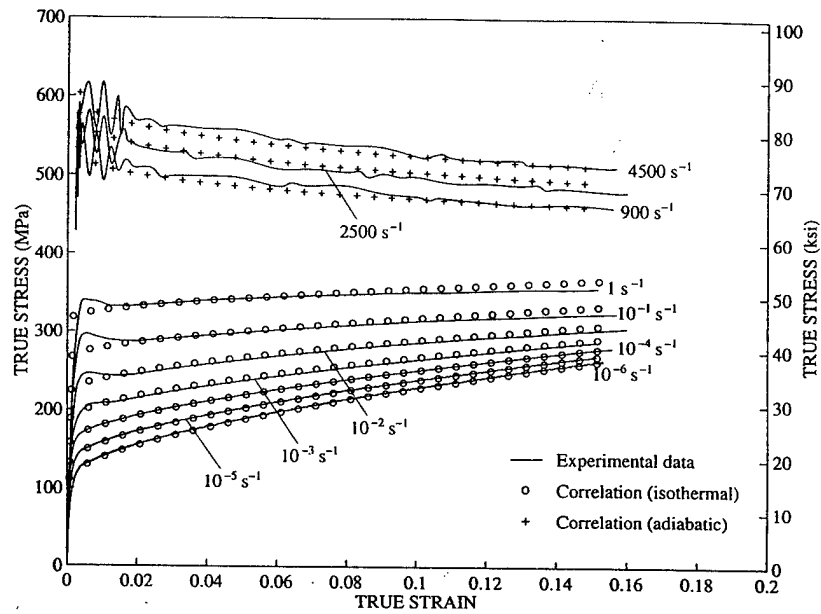


Fig. 10. Stress-strain response for Ta at different strain rates and correlations of the constitutive model (room temperature).

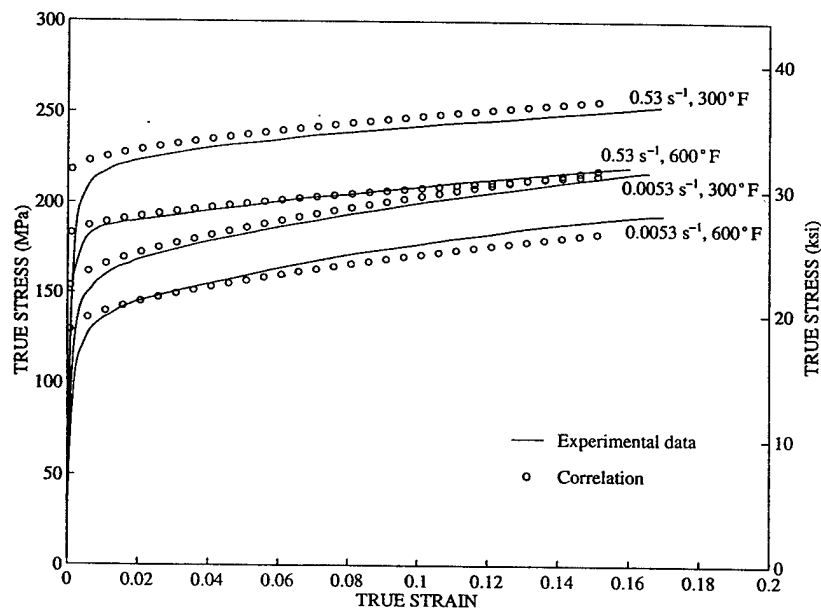


Fig. 11. Stress-strain response for Ta at different strain rates and temperatures and correlations of the constitutive model.

the material constants. In the next paper (Liang and Khan, 2000), the non-proportional experimental results will be used to check the applicability of the model in complex deformation behaviors and loading paths.

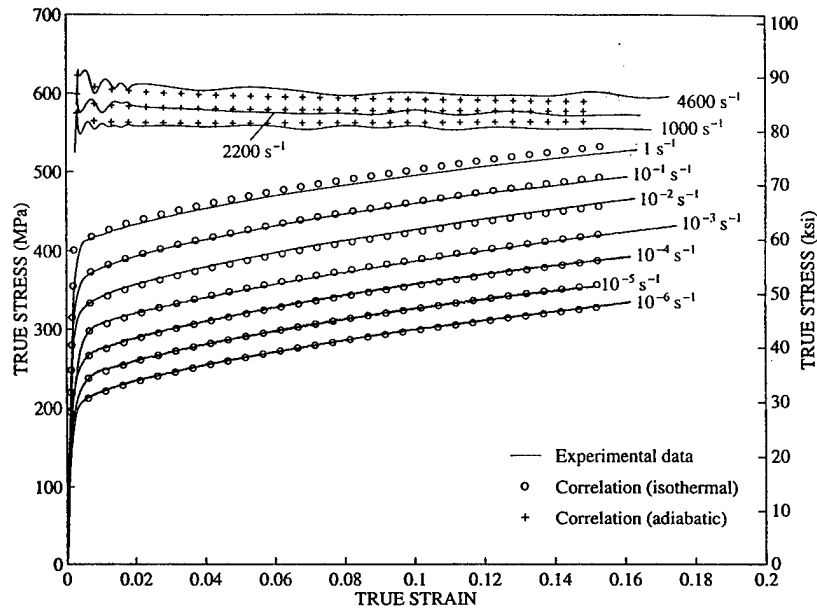


Fig. 12. Stress-strain response for Ta-2.5W at different strain rates and correlations of the constitutive model (room temperature).

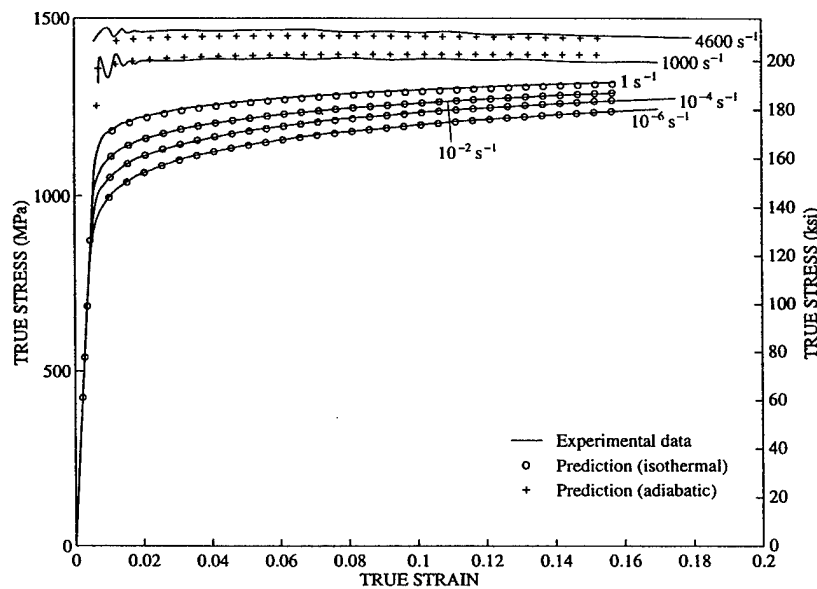


Fig. 13. Stress-strain response for AerMet 100 steel at different strain rates and correlations of the constitutive model (room temperature).

6. Strain-rate jump experiments and the constitutive model predictions

Several strain-rate jump tests were conducted for Ta and Ta-2.5W in uniaxial compressive experiments. There were two steps in these tests. First, the specimen

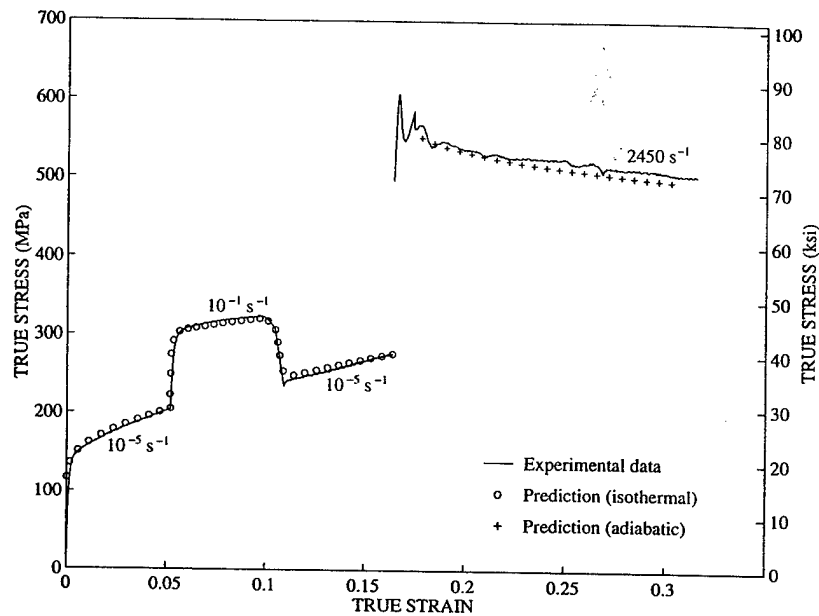


Fig. 14. Comparison of experimental data and predicted stress-strain relation for Ta in strain-rate jump test (strain rate: $10^{-5} \rightarrow 10^{-1} \rightarrow 10^{-5} \rightarrow 2450 \text{ s}^{-1}$). True strain-rate data used in the model prediction for quasi-static test are directly calculated from the experimental strain-time data.

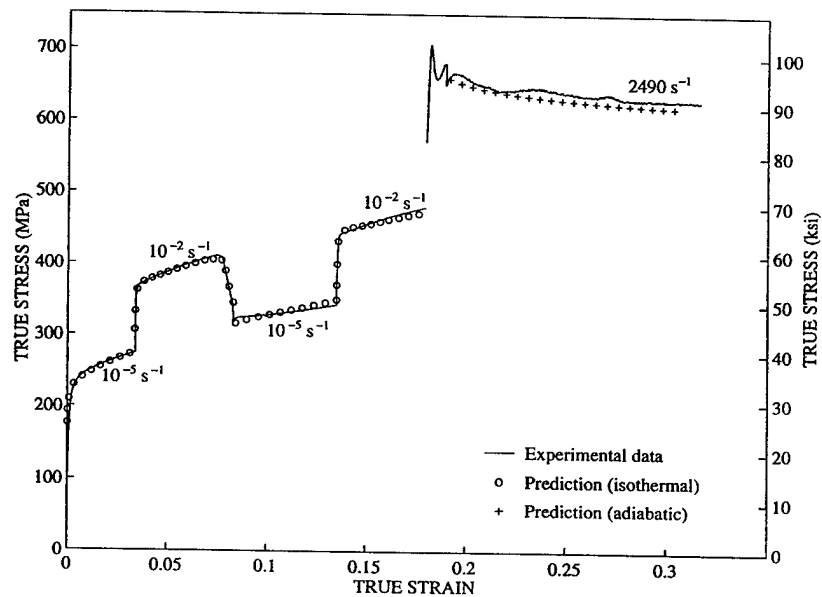


Fig. 15. Comparison of experimental data and predicted stress-strain relation for Ta-2.5W in strain-rate jump test (strain rate: $10^{-5} \rightarrow 10^{-2} \rightarrow 10^{-5} \rightarrow 10^{-2} \rightarrow 2490 \text{ s}^{-1}$). True strain-rate data used in the model prediction for quasi-static test are directly calculated from the experimental strain-time data.

underwent a relatively low strain-rate deformation and then jumped to a higher strain-rate deformation after certain strain in quasi-static test. After that, the specimen was machined for dynamic test from the deformed specimen and the SHPB test was

used for the dynamic experiment. These test results were used for the first evaluation to see the capability of the constitutive model. The experimental results and predictions from constitutive model are shown in Figs. 14 and 15. The strain data used in the constitutive model were the experimental data. In quasi-static test, the strain-rate data needed in the constitutive model to calculate corresponding stress were directly calculated from the actual strain-time history data.

Fig. 14 shows the strain-rate jump test for tantalum. The specimen underwent a deformation at strain rate of 10^{-5} s^{-1} first, then jumped to strain rate of 10^{-1} s^{-1} and then jumped back to strain rate 10^{-5} s^{-1} . After that, a specimen was machined from the deformed specimen and the dynamic test was done using SHPB technique, resulting in a strain-rate of 2450 s^{-1} . The predictions of the model, using material constants based on the previous set of experimental data, are in excellent agreement with the measured data. In Fig. 15, the tantalum alloy specimen was deformed at a strain-rate change sequence of 10^{-5} s^{-1} to 10^{-2} s^{-1} to 10^{-5} s^{-1} and then to 10^{-2} s^{-1} . A dynamic test for the deformed specimen was also carried out using SHPB technique after the quasi-static test to a strain rate 2490 s^{-1} . In this case also, the constitutive model gave an excellent prediction for the material response under strain-rate jump tests.

7. Conclusions

Uniaxial loading tests were conducted using the MTS machine, the split Hopkinson pressure bar, and the direct disc impact techniques for commercially pure tantalum, tantalum-tungsten alloy with 2.5% tungsten, and AerMet 100 steel over a wide range of strain rates and temperatures.

The deformation behaviors of the materials were measured using strain gages. The Wheatstone bridge circuit nonlinearity, gage factor and dispersion corrections were applied to the gage measurements and strain gages were used successfully in measuring finite plastic deformation.

Tantalum was found to be extremely rate sensitive. The yield stress and work-hardening behavior of tantalum exhibited a high sensitivity to strain rate. The yield stress increased significantly and the work-hardening rate decreased as the strain rate increased. When temperature increased, the yield stress decreased and the work hardening also decreased.

Tungsten addition significantly increased the yield stress level of tantalum alloy and increased the work hardening compared to unalloyed tantalum. The work-hardening rate did not change as significantly with the change of strain rate as that of unalloyed tantalum.

AerMet 100 steel is a high strength material. Its yield stress and work-hardening behavior were only moderately sensitive to strain rate.

The Johnson-Cook and the Zerilli-Armstrong constitutive models were demonstrated again to fail in describing experimental results for tantalum. Due to the inherent problems of the two models, they were not able to give a satisfactory correlation with the experimental response.

A new constitutive model was proposed based on the previous work of Khan and Huang (1992). In the new model, strain and strain rate have some coupled effects on the description of work-hardening relation of the materials. The material constants of the proposed constitutive model were determined using the uniaxial loading experimental data. The proposed constitutive model gave an excellent correlation with this experimental data over a wide strain-rate and temperature range for finite deformation. Then using material constants from the previous set of experiments, predictions were made for the strain-rate jump tests for Ta and Ta-2.5W; the agreement between predictions and measured responses was almost perfect.

Acknowledgements

The authors are grateful for the funding of this project by the Army Research Office under cooperative agreement DAAH04-95-2-0004.

References

- Armstrong, R.W., Chen, C.C., Dick, R.D., Zhang, X.J., 1997. Evaluation and improvement in constitutive equations for finite viscoplastic deformation and fracturing behavior relating to armor design. Internal report, The University of Maryland, January, 1997.
- ASTM Standard E209-65, 1993. Standard Practice for compression tests of metallic materials at elevated temperatures with conventional or rapid heating rates and strain rates. ASTM, Philadelphia, PA., p. 383.
- Bertholf, L.D., Karnes, C.H., 1975. Two-dimensional analysis of the split Hopkinson pressure bar system. *Journal of the Mechanics and Physics of Solids* 23, 1–19.
- Chen, S.R., Gray III, G.T., 1995. Constitutive behavior of tungsten, tantalum: experiments, modeling. In: Bose, A., Dowding, R.J. (Eds.), 2nd International Conference on Tungsten and Refractory Metals. McLean, VA, Metal Powder Industries Federation, Princeton, NJ, pp. 489–498 October 17–19.
- Chen, S.R., Gray III, G.T., 1996. Constitutive Behavior of tantalum and tantalum-tungsten alloys. *Metallurgical and Materials Transactions A* 27A, 2994–3006.
- Davies, E.D.H., Hunter, S.C., 1963. The dynamic compression testing of solids by the method of the split Hopkinson pressure bar. *Journal of the Mechanics and Physics of Solids* 11, 155–179.
- Follansbee, P.S., 1979. High strain rate compression testing, American Society for Metals, Mechanical Testing, Metal Handbook, 9th Edition, Volume 8, pp. 190–297.
- Follansbee, P.S., Frantz, C., 1983. Wave propagation in the split Hopkinson pressure bar. *Journal of Engineering Materials and Technology* 105 (39), 61–66.
- Hoge, K.G., Mukherjee, A.K., 1977. The temperature and strain rate dependence of the flow stress of tantalum. *Journal of Materials Science* 12, 1666–1672.
- Huang, S. 1990. Direct disc impact investigation of dynamic large finite plastic behavior of 1100 aluminum. Ph.D. dissertation, The University of Oklahoma.
- Huang, S., Khan, A.S., 1991. On the use of electrical-resistance metallic foil strain gages for measuring large dynamic plastic deformation. *Experimental Mechanics*, June, pp. 122–125.
- Huang, S., Khan, A.S., 1992. Modeling the mechanical behavior of 1100–0 aluminum at different strain rates by the Bodner-Partom model. *International Journal of Plasticity* 8, 501–517.
- Johnson, G.R., Cook, W.H., 1983. A constitutive model and data for metals subjected to large strains, high strain rates and high temperatures. In: *Proceedings of the Seventh International Symposium on Ballistic*, The Hague, The Netherlands, pp. 541–547.
- Khan, A.S. and Hsiao, C., 1988. In the use of electrical-resistance foil strain gages for plastic-wave studies in solids. *Experimental Mechanics*, September, p. 254.

- Khan, A.S., Hsiao, C., 1991. Behavior of fully annealed and as-received polycrystalline 1100 aluminum during propagation of small and large amplitude plastic waves. *International Journal of Plasticity* 7, 733–748.
- Khan, A.S., Huang, S., 1992. Experimental and theoretical study of mechanical behavior of 1100 aluminum in the strain rate range 10^{-1} – 10^4 s $^{-1}$. *International Journal of Plasticity* 8, 397–424.
- Kothari, M., Anand, L., 1998. Elasto-viscoplastic constitutive equations for polycrystalline metals: application to tantalum. *Journal of the Mechanics and Physics of Solids* 46 (1), 51–83.
- Lee, B.-J., Vecchio, K.S., Ahzi, S., Schoenfeld, S., 1997. Modeling the mechanical behavior of tantalum. *Metallurgical and Materials Transactions A* 28A, 113–122.
- Liang, R., Khan, A.S., 1999. A critical review of experimental results and constitutive models of BCC and FCC metals over a wide range of strain rates and temperatures. *International Journal of Plasticity* 15, 963–980.
- Liang, R., Khan, A.S., 2000. Behaviors of three BCC metals during nonproportional multi-axial loadings and predictions using a recently proposed model. *International Journal of Plasticity*, in press.
- Measurements Group Inc., 1982. Errors due to Wheatstone bridge nonlinearity. Tech. Note, TN-507.
- Nemat-Nasser, S., Isaacs, J.B., 1996. Direct measurement of isothermal flow stress of metals at elevated temperatures and high strain rates with application to Ta and Ta-W Alloys. Internal report, Center of Excellence for Advanced Materials, UCSD, San Diego, CA.
- Nemat-Nasser, S., Li, Y.-F., Isaacs, B., 1994. Experimental/computational evaluation of flow stress at high strain rates with application to adiabatic shear banding. *Mechanics of Materials* 17, 111–134.
- Regazzoni, G., Montheillet, F., 1984. Influence of strain rate on the flow stress and ductility of copper and tantalum at room temperature. *Institute of Physics Conference Series Mechanical Properties at High Rates of Strain, Proceedings of the Third Conference*, No.70, pp. 63–70.
- Zerilli, F.J., Armstrong, R.W., 1987. Dislocation-mechanics-based constitutive relations for material dynamics calculations. *Journal of Applied Physics* 61 (5), 1816–1825.
- Zerilli, F.J., Armstrong, R.W., 1990. Description of tantalum deformation behavior by dislocation mechanics based constitutive relations. *Journal of Applied Physics* 68 (4), 1580–1591.



PERGAMON

International Journal of Plasticity 16 (2000) 1443–1458

INTERNATIONAL JOURNAL OF
Plasticity

www.elsevier.com/locate/ijplas

Behaviors of three BCC metals during non-proportional multi-axial loadings: experiments and modeling

Akhtar S. Khan *, Riqiang Liang

*Department of Mechanical Engineering, University of Maryland, Baltimore County,
MD 21250, USA*

Received in final revised form 4 January 2000

Abstract

Non-proportional torsion–tension and biaxial-compressive experimental results are presented on tantalum, tantalum alloy with 2.5% tungsten, and AerMet 100 steel. These test results form a comprehensive set of data to show the material behaviors at finite strain and wide strain-rate range. Using the parameter set determined from uniaxial constant strain-rate compressive and tensile tests, the capability of a new constitutive model (Khan, A.S., Liang, R., 1999. Behaviors of three BCC metal over a wide range of strain rates and temperatures: experiments and modeling. *International Journal of Plasticity* 15, 1089–1109) is shown to accurately predict complex loading paths of current experimental results. Using von Mises equivalent strain, stress, and strain rate, the constitutive model gives excellent predictions of these non-proportional experimental results. © 2000 Elsevier Science Ltd. All rights reserved.

Keywords: Dynamic response; Multi-axial loading; BCC metal behavior; Finite deformation; Tension–torsion

1. Introduction

A critical investigation of constitutive models for plastic deformation requires experiments under complex paths of deformation, temperature, and strain rate. In general, complex loading path experiments reveal more critical material response than do constant strain-rate, isothermal, monotonic deformation experiments such

* Corresponding author. Tel.: +1-410-455-3301; fax: +1-410-455-1052.

E-mail address: khan@engr.umbc.edu (A.S. Khan).

as compression tests. In the current study, experiments under non-proportional multi-axial loadings were conducted for different deformation paths.

Tension–torsion tests using thin-walled cylindrical specimen were performed. Experiments using thin-walled cylindrical specimens under combined axial and torsional loadings have been extensively used for the experimental study of constitutive models in multi-dimensional configuration (e.g. Swift, 1947; Lindholm et al., 1980; Shirivisatava et al., 1982). Non-proportional loading path experiments are obtained when tension is applied first, followed by torsion, or vice versa. In the current study, torsional test was performed first with free-end condition (i.e. the axial load is maintained at zero); after certain deformation, torque was kept constant and axial tension was applied; then axial load was kept constant and torsional deformation was continued.

Biaxial compressive tests were conducted using a special designed die (Wang, 1989; Khan and Wang, 1990) to produce an approximate plane strain deformation for a rectangular block specimen. Non-proportional loading occurs if the specimen is loaded in uniaxial compression followed by biaxial compression.

The materials used in these tests were commercially pure tantalum, tantalum alloy with 2.5% tungsten, and AerMet 100 steel [see Khan and Liang (1999) for details].

These test results will be used to compare with predictions using a constitutive model with the material constants determined from the uniaxial sets of experiments to evaluate the applicability of the constitutive model. The constitutive model details and parameters are given in Khan and Liang (1999), while unsuitability of other constitutive models for these materials are discussed in Liang and Khan (1999).

2. Non-proportional multi-axial experiments

2.1. Torsion–tension loading

The torsion–tension tests were performed using an MTS axial/torsional servo-hydraulic test machine with simultaneous axial and torsional controls. Specimens were gripped with a hydraulic grip system using 25.40 mm (1.00 inch) collet.

The design of the thin-walled cylindrical specimen is shown in Fig. 1. The gage length is 12.70 mm (0.50 inch). The gage section wall thickness is 1.27 mm (0.05 inch)

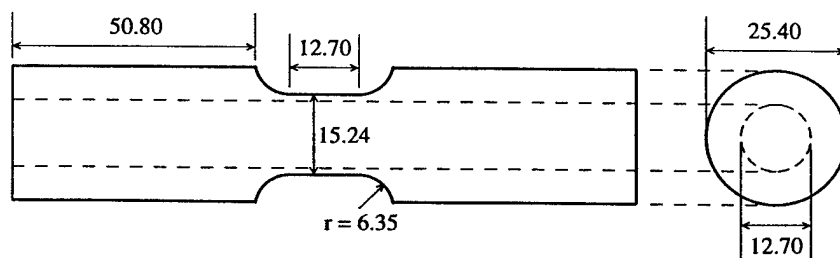


Fig. 1. Details of thin-walled torsion-tension specimen. All dimensions are in mm.

which encompasses an average of 30 grains. This specimen limits the deformation to the gage section even at large strain. A high degree of uniformity of shear strain is maintained within the gage section.

The ends of the specimen were plugged with 12.70 mm (0.50 inch) diameter aluminum inserts to resist significant inelastic deformation during gripping. The inserts extended from the specimen ends, but ended before the beginning of the beveled region so as not to affect the stress or strain distributions in the gage section. The ends of the specimen were also pre-strained before the actual test to have them hardened so as to minimize the gripping effort on the deformation of gage section during the actual test.

The axial loading force and torsional moment were recorded directly from the MTS machine outputs in the experiment. In order to accurately measure the deformation of the gage section, a three-element rosette strain gage (KFE-2-120-D33, Kyowa, Inc., Japan) was used. The strain gage was mounted on the surface of the gage section using M-Bond AE-15 adhesive (Measurements Group, Inc.) Model P-3500 Strain Gage Indicators (Measurements Group, Inc.) and the Wheatstone quarter bridge circuit were used for making accurate and reliable measurements. The outputs from three elements of the gage were captured separately in order to perform data correction due to the configuration change of the specimen.

2.2. *Biaxial compressive loading*

Experiments using rectangular block specimens under plane strain condition played an important role in the studies of plasticity theory at finite deformation. More than 50 years ago, Bridgman (1946) performed a series of two-dimensional compressive tests on steel in an effort to investigate whether the classical theory, which was initially restricted to infinitesimal plastic strain, could be applied to high strength steels at large finite strain. In his version of the tests, two independent hydraulic pressures were used to apply the loads to two pairs of the mutually perpendicular faces of the rectangular block specimen while the third pair of the faces was left free; stresses in the loading and constrained directions, and the strain in the loading direction were measured. This version of tests was modified later by Florenz (1969). In order to confine the block specimen in plane strain condition, the corresponding pair of faces was supported against tool steel walls. The compressive load in another direction was automatically applied due to the constraint in that direction instead of the hydraulic pressures while the third pair of the faces were still left free to deform. In the Florenz version, only stress and strain in the loading direction were measured. This version of tests is often called channel die tests, which has been used for the study of large finite plastic deformation.

Khan and Wang (1990) developed a modified version of this non-proportional and proportional loading channel die experiment. They built a new apparatus and modifications were made on the original Bridgman's test to permit accurate measurements of both stresses and strains simultaneously in all directions. The schematic drawing of the apparatus is shown in Fig. 2. Following the same method, and using apparatus designed by Khan and Wang, non-proportional biaxial compressive

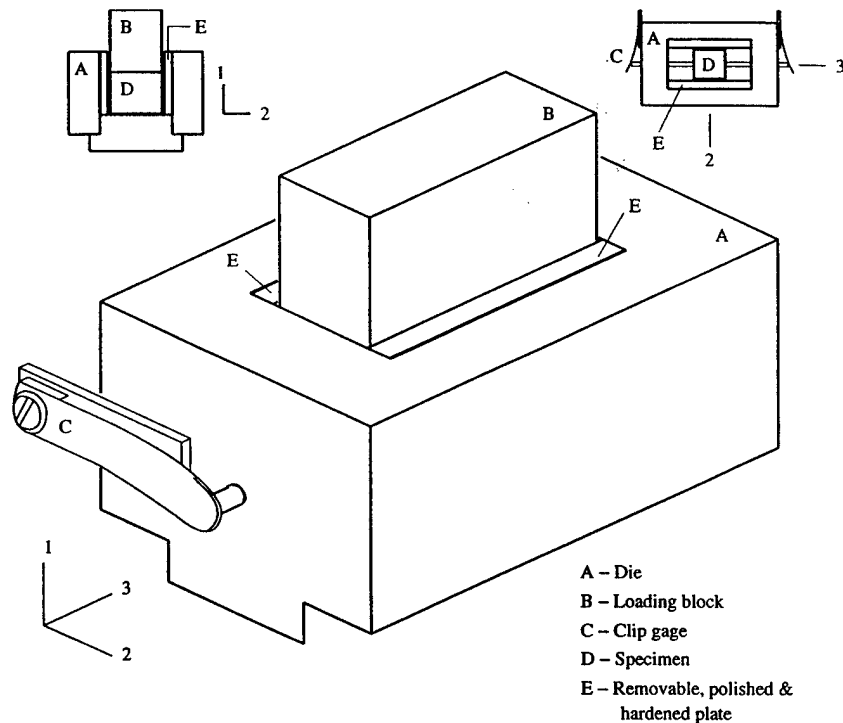


Fig. 2. Schematic diagram of the channel die experiment.

experiments were conducted on the two BCC metals, Ta and Ta–2.5W, where a rectangular block of material first underwent uniaxial compression. Then, after finite deformation, the block was subjected to large deformations under biaxial compression as it was constrained to deform in one of the horizontal direction.

In the biaxial experiments, a rectangular specimen was loaded in direction 1, while it was free to deform in the third direction; in direction 2, it was constrained by channel rigid die walls after undergoing a pre-designed amount of deformation in that direction.

An MTS material test system was used to apply the load in direction 1 to the specimen through a hardened AISI 4340 steel block, called the loading block (B in Fig. 2). The dimension of the loading block in direction 2 was selected so that there was neither pinching nor appreciable plastic flow into the crevasse between the loading block and the side walls during the entire course of experiment.

The pair of faces of the specimen in direction 2 was supported against a pair of tool steel plates (E in Fig. 2), located in a frame made of AISI 4340 steel, to introduce load resulting in almost zero strain in that direction. The frame was so designed that there were no appreciable strains in direction 2 when the load was gradually applied to the specimen in direction 1 and reached its maximum value. The pair of tool steel plates is removable so that the surfaces contacting with the specimen could be easily polished for the best finish. The tool steel is selected merely for its

high hardness. The bottom of the apparatus is also made separable in order to be polished and to facilitate the removal of the deformed specimen after the test is finished.

Holes were drilled in a subsequently hardened 4340 steel frame in direction 3 to allow steel pin probes to activate the clip gage (C in Fig. 2) to measure directly the tensile strain ϵ_3 in that direction. The clip gage is made of two relatively long, thin (0.356 mm in thickness) cantilever strips of high-strength steel, fixed at one end to accommodate the measurement. When the free end of the strip undergoes significant displacement and rotation, the recorded strains, measured by electric resistance gages mounted on both surfaces of the strip at the position near the fixed end, remain infinitesimal. A Wheatstone full bridge circuit was used to increase the sensitivity of the measurement. When the specimen deforms, its faces in direction 3 push the probes to activate the clip gage. Calibrations were conducted for the specific gage length to meet the dimensions of the specimens.

In order to measure the stress σ_2 in direction 2 directly, strain gages were mounted on the side walls of the apparatus along direction 2 and were calibrated for the applied load in the same direction.

The whole frame and the removable side wall plates were hardened. All the surfaces of the apparatus which were in contact with the specimen faces during the experiment were polished before every test using a Buehler's Metaserv Grinder-Polisher in order to further reduce the friction in addition to the lubricant.

The most difficult problem, as pointed out by Bridgman (1946), Bell (1988), and Khan and Wang (1990) was to find a suitable lubricant for a two-dimensional compressive test rather than for an ordinary simple compressive test to eliminate barreling. If the lubrication for face 1 was not good enough, the specimen would be bulged in the middle due to high friction. On the other hand, the specimen would be barreled in at the middle after deformation if the lubrication was excessive. Since there was a high level stress in direction 2, the lubrication in face 2 was also very important for a uniform deformation. As pointed out by Bridgman and Bell, only patience and time were needed to solve this problem. In the experiments for Ta and Ta-2.5W, a layer of thin Teflon sheet (0.003 inch) was finally used as the suitable lubricant. A small amount of graphite powder lubricant was also put between the Teflon sheets and the surfaces of the apparatus and the specimen. In this way, the specimen underwent fairly large compressive strain without appreciable barreling so that the deformation was kept uniform.

The dimensions of the rectangular specimen were 20.32×24.13×13.97 mm (0.80×0.95×0.55 inch) in direction 1, 2, and 3, respectively. It was machined from Ta and Ta-2.5W bar stock with 25.40 mm (1.00 inch) in diameter. The final cuts in the machining process were limited to 0.0254 mm (0.001 inch) each in order to avoid any work hardening due to machining. The surfaces of the specimen were also polished using Buehler's Metaserv Grinder-Polisher in order to further reduce friction.

Strain gages (KFE-2-120-C1, Kyowa Inc., Japan) were mounted on the free surface of the specimen in both directions 1 and 2 to give the strain measurements of ϵ_1 and ϵ_2 .

3. Experimental data correction

In the torsion–tension experiments, the axial load and torque were accurately obtained from the MTS machine. However, the displacement and angle outputs from the machine included the deformations of machine elements. It was found to be larger than the actual deformation of the specimen. Two deformation components, axial and shear, must be determined accurately in the torsion–tension experiment. In this study, strain gage rosette was used to measure the deformation. The configuration of the specimen was changed significantly during torsional test when the deformation was large. The strain gage mounted on the surface of the specimen would also change its configuration. The data obtained from the three-element rosette strain gage were corrected in order to get accurate deformation information (Huang and Khan, 1991a).

In the small deformation test, shear strain can be calculated from the readings of the three elements of the rosette by using transformation equations based on the assumption of infinitesimal deformation. However, since the specimen was subjected to a rotation that was finite, the rosette mounted on the surface of the specimen also rotated. The configuration change of the strain gage would be significant so that the angles among the three elements would change and the equations for calculating strain in small deformation could not be used directly to give the large shear and axial deformation. Therefore, a correction must be performed based on the outputs of the rosette.

For the rosette strain gage used in the research, its three elements were arranged in three special directions in the undeformed configuration, $\beta_1 = 45^\circ$, $\beta_2 = 90^\circ$, $\beta_3 = 135^\circ$, as shown in Fig. 3. When deformation is very small, the axial strain is given by ϵ_2 and the shear strain of the specimen can be calculated by the following equation

$$\gamma = \epsilon_1 - \epsilon_3 \quad (1)$$

where ϵ_1 , ϵ_2 , and ϵ_3 are the gage outputs in direction 1, 2, and 3 after the Wheatstone bridge nonlinearity and gage factor corrections (Huang and Khan, 1991a; Khan and Liang, 1999). When deformation is large, the strain gage will also rotate and deform with the specimen, therefore, the angles between each element will deviate from their initial values; Eq. (1) cannot be used directly to calculate large shear strain in the case of large tension and large rotation and ϵ_2 will also have a very large difference with the actual axial deformation when finite torsion is involved.

Based on the previous work of Wu et al. (1992) and Huang et al. (1993), Khan and Chen (1999) derived the following formulae for getting the corrected nominal strains based on the direct strain-gage measurements ϵ_1 , ϵ_2 , and ϵ_3 .

Nominal shear strain is

$$\gamma = \omega R_m \quad (2)$$

Nominal axial strain is

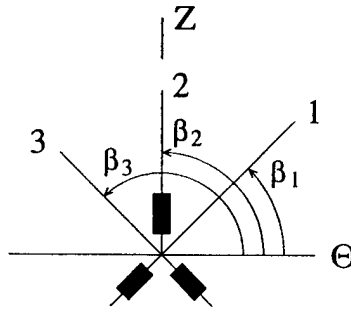


Fig. 3. Three-element rosette strain gage and its mounting position with respect to axis Z of the tubular specimen.

$$e_Z = \lambda - 1 \quad (3)$$

Nominal radial and circumferential (hoop) strains are

$$\epsilon_R = \alpha - 1 \quad (4)$$

$$\epsilon_\Theta = \alpha - 1 \quad (5)$$

where

$$\begin{aligned} \alpha &= \sqrt{1 + 2(\epsilon_1 + \epsilon_3 - \epsilon_2) + \epsilon_1^2 + \epsilon_3^2 - \epsilon_2^2} \\ \omega R_m &= \frac{\epsilon_1 - \epsilon_3}{\alpha^2} \left[1 + \frac{1}{2}(\epsilon_1 + \epsilon_3) \right] \\ \lambda &= \sqrt{(1 + \epsilon_2)^2 - \omega^2 \alpha^2 R_m^2} \end{aligned} \quad (6)$$

and R_m is the mean undeformed radius for the thin-walled tubes.

4. Experimental results and model predictions

The experimental results and model predictions were shown in the following figures. The constitutive model is expressed as (Khan and Liang, 1999)

$$\begin{aligned} \sigma &= \left[A + B \left(1 - \frac{\ln \dot{\epsilon}}{\ln D_0^p} \right)^{n_1} \epsilon^{n_0} \right] \dot{\epsilon}^C (1 - T^{*m}) \\ T^* &= (T - T_r) / (T_m - T_r) \end{aligned} \quad (7)$$

where σ , ϵ , and $\dot{\epsilon}$ are von Mises equivalent stress, strain, and strain rate, respectively; T is the absolute temperature; T_m is the melting temperature of the material; and, T_r

is a reference temperature. Six materials constants, A , B , n_0 , n_1 , C , and m were determined in the previous paper (Khan and Liang, 1999). D_0^p is chosen to be 10^6 s^{-1} in the study.

4.1. Torsion–tension loading

The experimental results of torsion–tension tests are shown in the following figures. The constitutive model predictions are also given. The material constants in the model are those obtained in the previous paper (Khan and Liang, 2000) using the uniaxial experiments without any modifications. Strain, strain rate, and stress were calculated using the von Mises equivalent strain, strain rate, and stress.

Figs. 4, 6, and 8 give the corrected experimental data for Ta, Ta–2.5W, and Aer-Met 100, respectively. The specimen underwent torsion first (free end), followed by tension (holding torque constant), and then torsion again (holding force constant). There was a dramatic strain-rate reduction when changing from torsion to tension since the rotation increased more quickly in order to keep the torque constant during tension. After experimental data correction for gage rotation, axial strain changes are shown in the figures.

Figs. 5, 7, and 9 show the corresponding experimental stress–strain relations for the three materials using von Mises equivalent strain and stress. The predictions

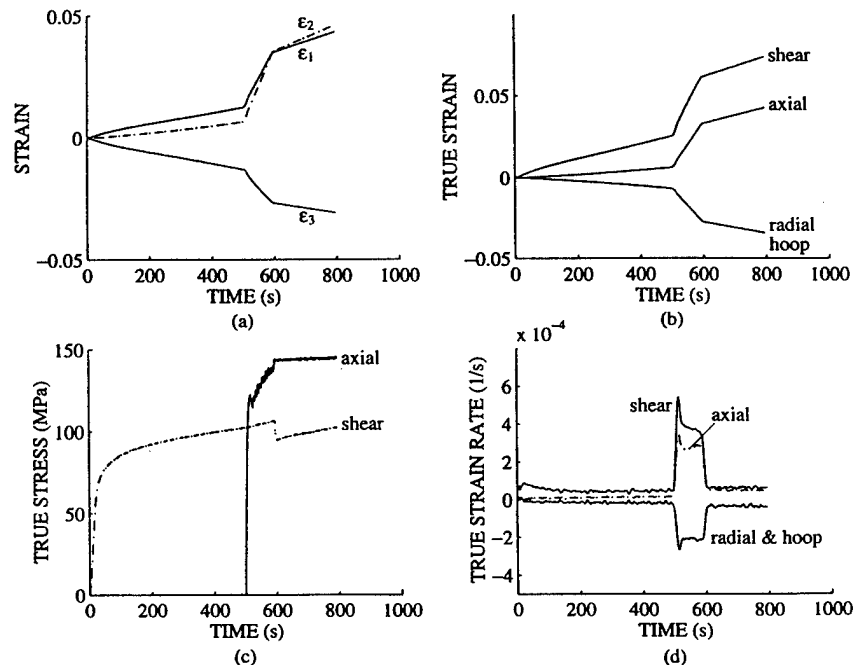


Fig. 4. Experimental strain, stress, and strain-rate data for Ta in torsion (free end) → tension (hold torque) → torsion (hold force) test: (a) strains from three-element rosette strain gage after nonlinearity and gage factor correction; (b) true strains; (c) true axial and shear stresses; (d) true strain rates.

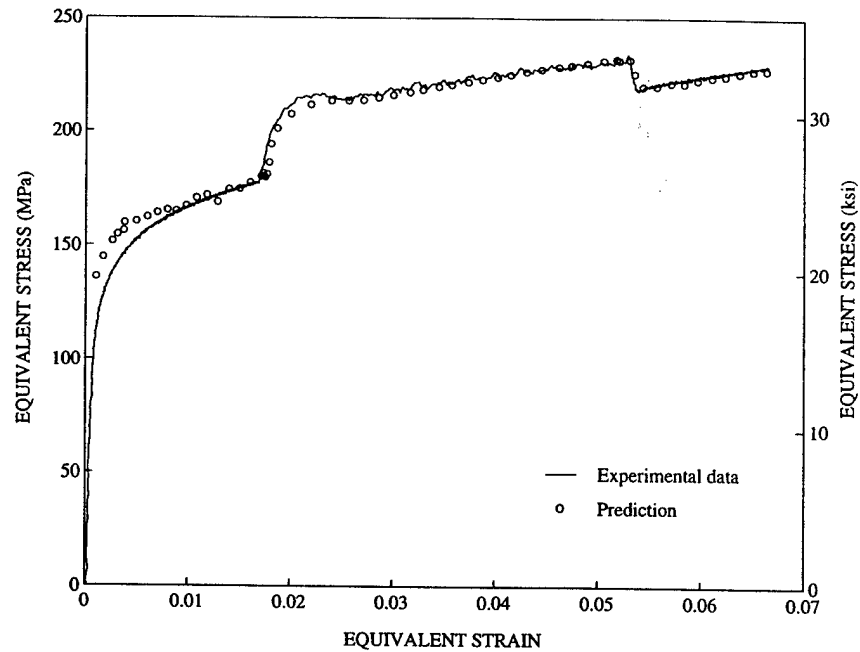


Fig. 5. Comparison of the experimental and predicted stress–strain relations for Ta in torsion (free end) → tension (hold torque) → torsion (hold force) test.

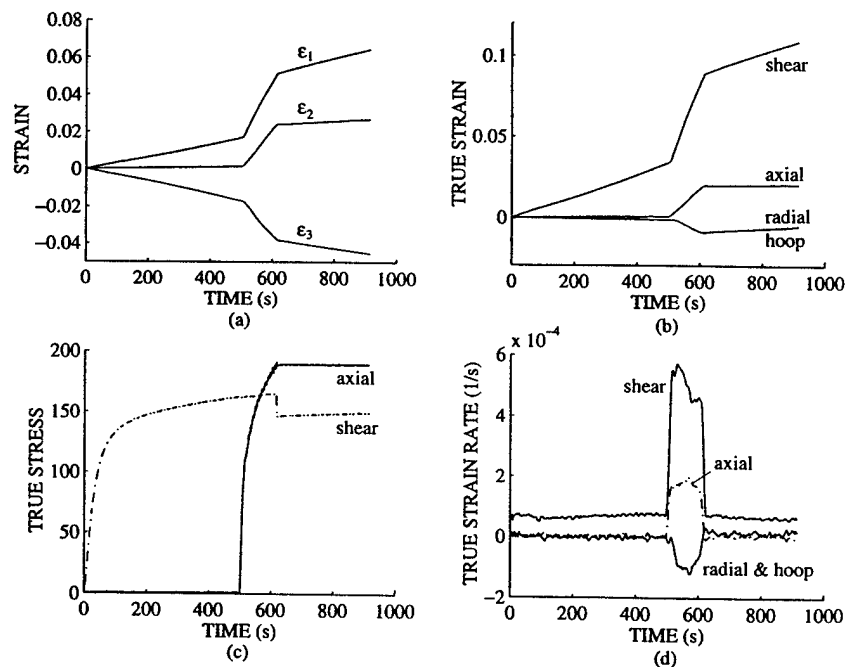


Fig. 6. Experimental strain, stress, and strain-rate data for Ta-2.5W in torsion (free end) → tension (hold torque) → torsion (hold force) test: (a) strains from three-element rosette strain gage after nonlinearity and gage factor correction; (b) true strains; (c) true axial and shear stresses; (d) true strain rates.

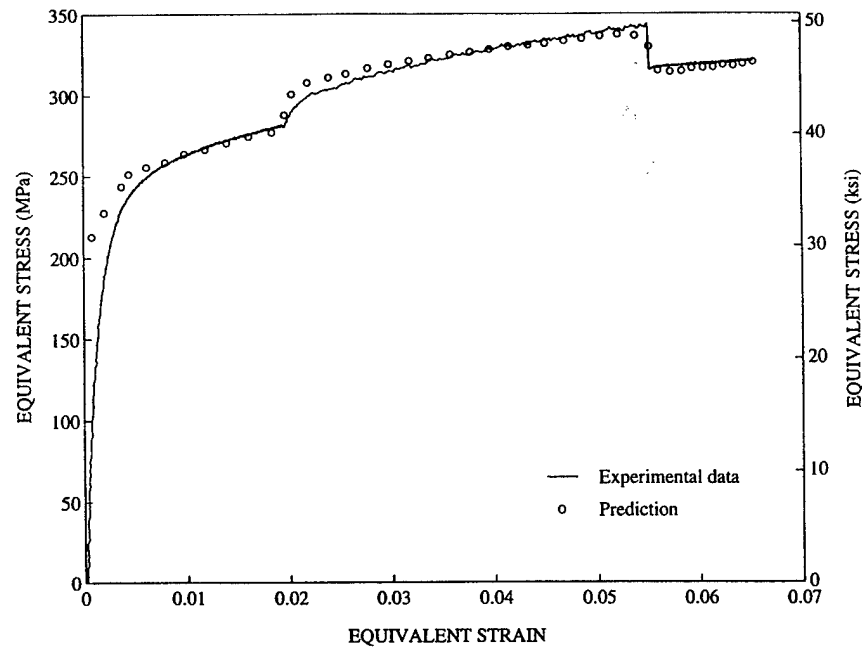


Fig. 7. Comparison of the experimental and predicted stress-strain relations for Ta-2.5W in torsion (free end)→tension (hold torque)→tension (hold force) test.

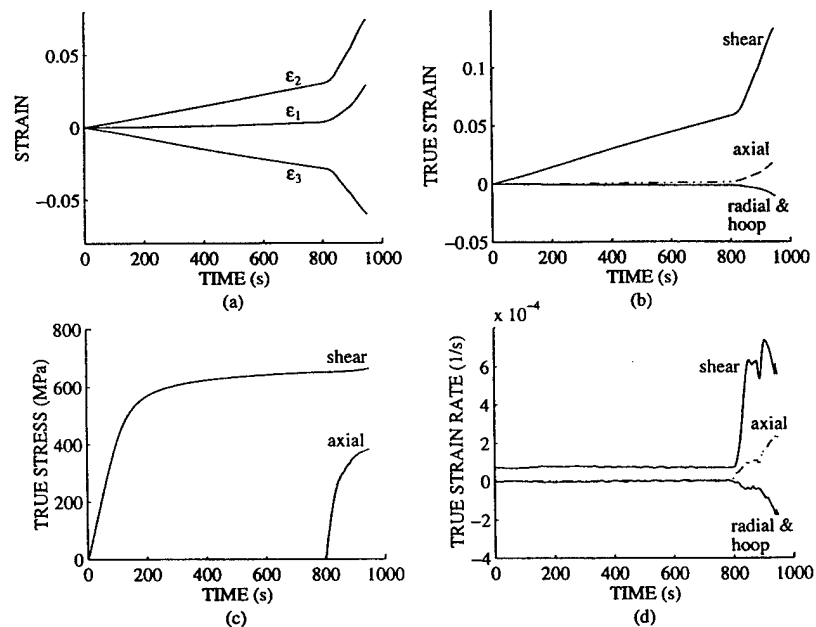


Fig. 8. Experimental strain, stress, and strain-rate data for AerMet 100 in torsion (free end)→tension (hold torque) test: (a) strains from three-element rosette strain gage after nonlinearity and gage factor correction; (b) true strains; (c) true axial and shear stresses; (d) true strain rates.

from the constitutive model are also presented in the figures to compare with the experimental data. The model stress predictions are calculated based on measured strains and strain-rates. The material constants are those obtained from the constant strain-rate experiments (Khan and Liang, 1999) and shown in Table 1. The prediction is quite close to the observed response except in the initial change of direction, where the agreement is still quite reasonable.

4.2. Biaxial compressive loading

In the non-proportional biaxial compressive experiments, a rectangular block specimen first underwent uniaxial compression and then, after finite deformation, it was subjected to large deformations under biaxial compression. Figs. 10, 11, 13, and 14 show the strain and stress measurements during the tests for Ta and Ta-2.5W.

Table 1
Material constants for the constitutive model

	A (MPa)	B (MPa)	n_0	n_1	C	m
Ta	318.47	153.20	0.6088	3.1547	0.0759	0.400
Ta-2.5W	400.76	410.37	0.5989	1.0589	0.0522	0.415
AerMet 100	872.57	536.86	0.1036	1.9284	0.0524	1.150

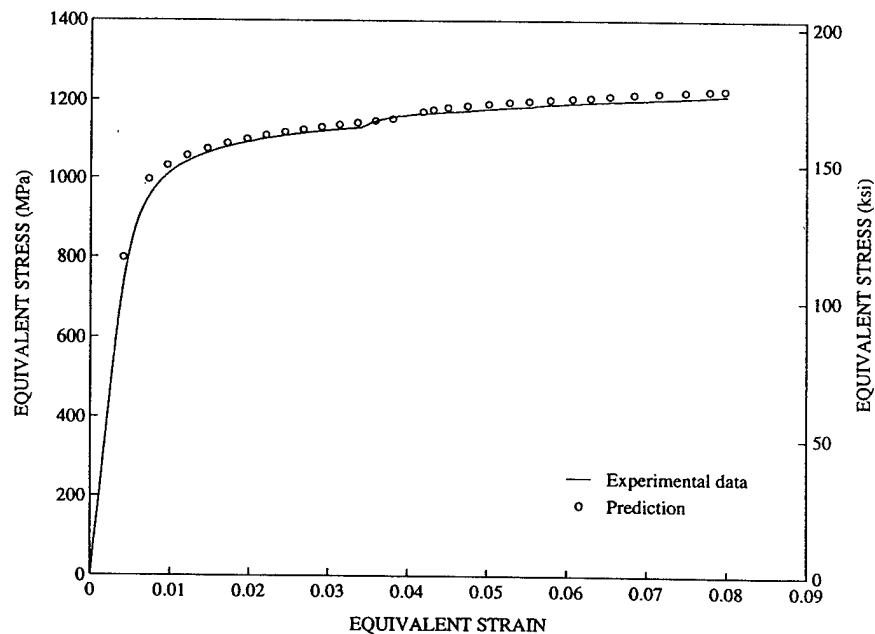


Fig. 9. Comparison of the experimental and predicted stress-strain relations for AerMet 100 in torsion (free end) → tension (hold torque) test.

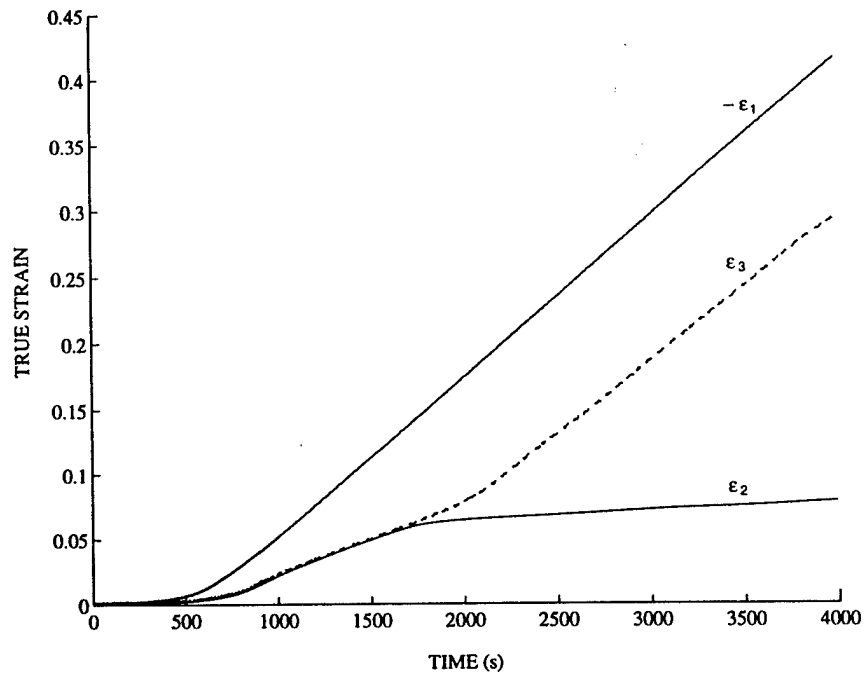


Fig. 10. Strains in three directions for Ta in biaxial compressive experiment.

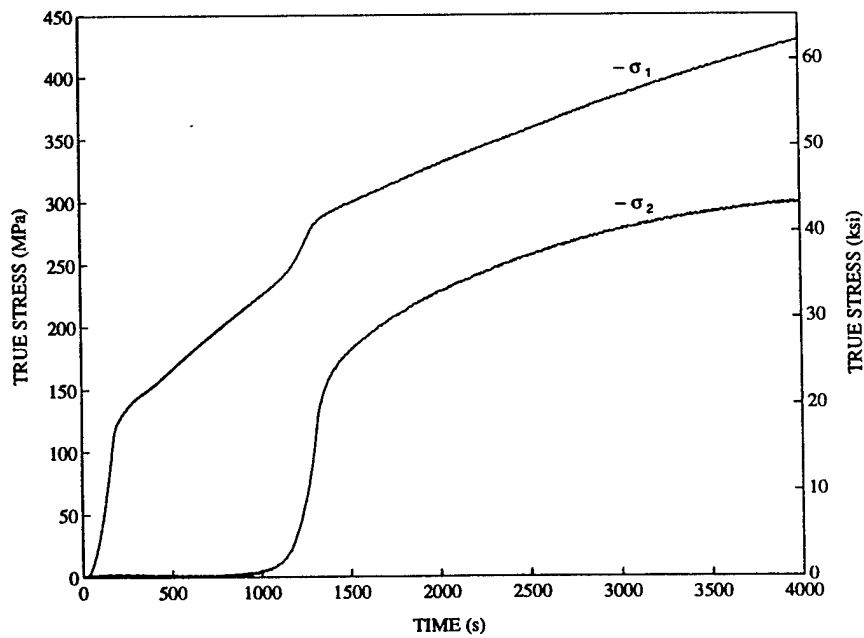


Fig. 11. Stresses in directions 1 and 2 for Ta in biaxial compressive experiment.

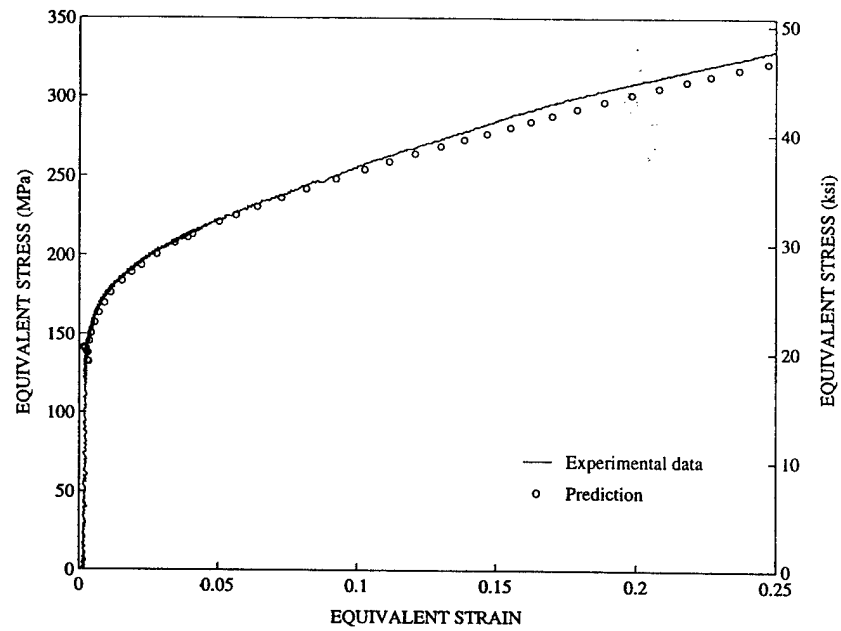


Fig. 12. Comparison of the experimental and predicted stress-strain relations for Ta in biaxial compressive test.

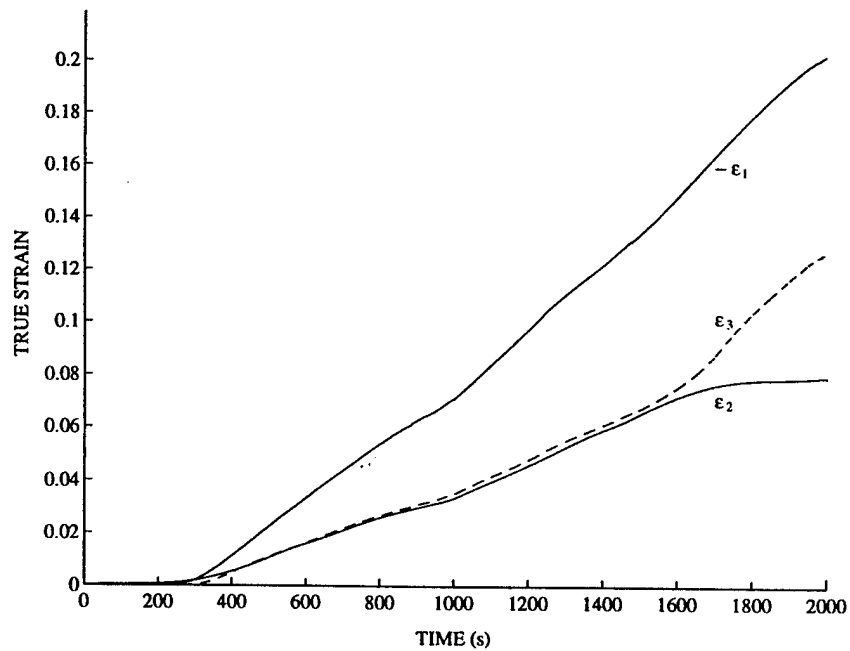


Fig. 13. Strains in three directions for Ta-2.5W in biaxial compressive experiment.

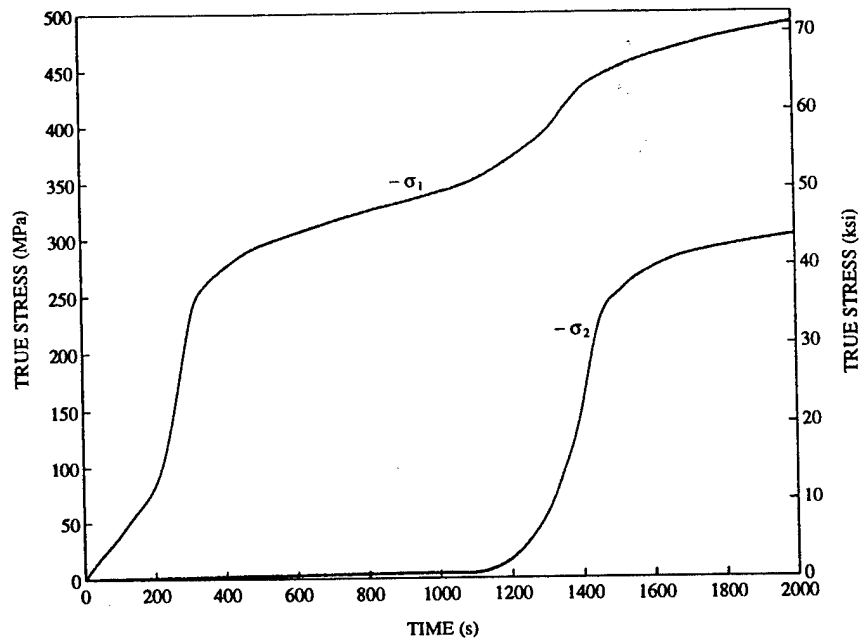


Fig. 14. Stresses in directions 1 and 2 for Ta-2.5W in biaxial compressive experiment.

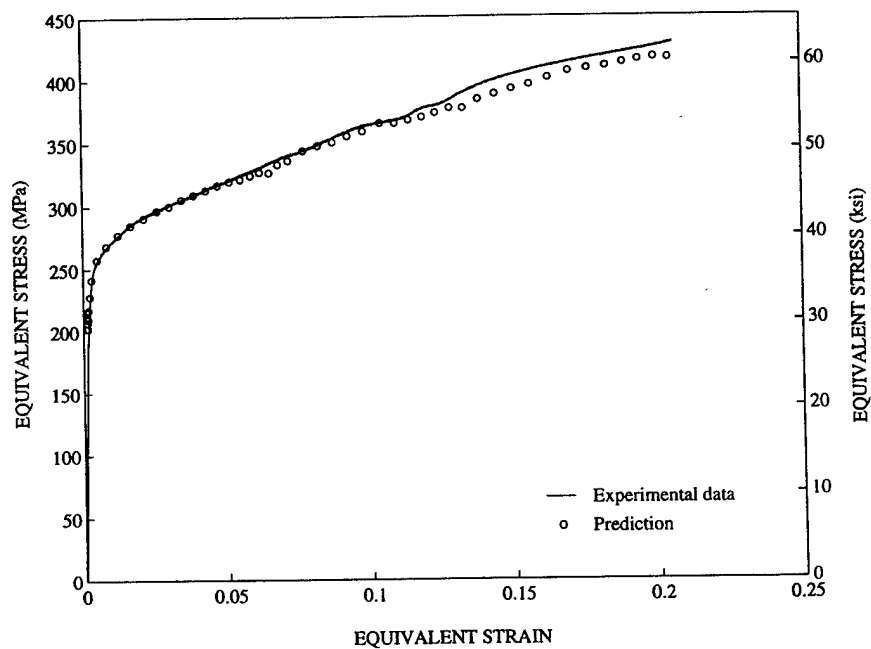


Fig. 15. Comparison of the experimental and predicted stress-strain relations for Ta-2.5W in biaxial compressive test.

Strains ϵ_1 and ϵ_2 were measured from strain gages mounted on the free surfaces of the specimen. The direct outputs were modified for the Wheatstone bridge non-linearity correction and gage factor correction as described in Huang and Khan (1991a) and Khan and Liang (1999). Strain ϵ_3 was obtained from the output of the clip gage. Stress σ_1 was calculated from the recorded load of the MTS machine and stress σ_2 was converted from the outputs of the strain gages mounted on the side walls of the die.

Figs. 12 and 15 present the calculated stress–strain relation for von Mises equivalent stress and strain. The predicted stress–strain relations from the constitutive model are also shown in these figures. The strain-rate data needed in the constitutive model to calculate the stress–strain relation are von Mises equivalent strain rate, which are computed from the three strain histories.

5. Conclusions

Non-proportional torsion–tension and biaxial-compressive experimental results were presented on tantalum, tantalum alloy with 2.5% tungsten, and AerMet 100 steel. These test results formed a comprehensive set of data to show the material behaviors at complex strain and strain-rate deformation. They were necessary for evaluating the constitutive model for describing strain and strain-rate dependent response of finite strain.

Using the parameter set determined from uniaxial constant strain-rate compressive and tensile tests from the previous paper (Khan and Liang, 1999), the capability of the constitutive model to accurately predict complex loading paths of current experimental response were demonstrated. Using von Mises equivalent strain, stress, and strain rate, the constitutive model gave excellent predictions of these non-proportional experimental results. Therefore, the constitutive model can be used to describe complex loading path finite deformation of the material. It should be mentioned here that Khan and Wang (1990) and Huang and Khan (1991b) demonstrated earlier, using the result of channel die experiments on fully annealed 1100 Aluminum, that classical Prandtl-Reuss equation (see Khan and Huang, 1995) failed to predict observed material response. Similar conclusion was made by Khan and Parikh (1986) in case of tension–torsion non-proportional loading of copper tubes.

Acknowledgement

The authors are grateful for the funding of this project by the Army Research Office under cooperative agreement DAAHO4-95-2-0004.

References

- Bell, J.F., 1988. Plane stress, plane strain, and pure shear at large finite strain. *International Journal of Plasticity* 4, 127.

- Bridgman, P.W., 1946. Studies of plastic flow of steel, especially in two-dimensional compression. *Journal of Applied Physics* 17, 225.
- Florenz, M., 1969. Two-Dimensional Plastic Compression of Polycrystalline Aluminum. Master Thesis, The Johns Hopkins University, Baltimore, MD.
- Huang, S., Khan, A.S., 1991a. On the use of electrical-resistance metallic foil strain gages for measuring large dynamic plastic deformation. *Experimental Mechanics*, June, 122–125.
- Huang, S., Khan, A.S., 1991b. An analysis of finite elastic-plastic deformation under biaxial compression. *International Journal of Plasticity* 7, 219–234.
- Huang, S., Khan, A.S., Yan, H., 1993. Shear measurement using strain gages under large deformation and rotation. *Experimental Mechanics* 33, 55.
- Khan, A.S., Chen, X., 1999. Private communication.
- Khan, A.S., Huang, S., 1995. *Continuum Theory of Plasticity*. John Wiley & Sons, Inc.
- Khan, A.S., Liang, R., 1999. Behaviors of three BCC metal over a wide range of strain rates and temperatures: experiments and modeling. *International Journal of Plasticity* 15, 1089–1109.
- Khan, A.S., Parikh, Y., 1986. Large deformation in polycrystalline copper under combined tension-torsion loading and reloading or reverse loading; a study of two incremental theories of plasticity. *International Journal of Plasticity* 2, 379.
- Khan, A.S., Wang, X., 1990. An experimental study of large finite plastic deformation in annealed aluminum during proportional and non-proportional biaxial compression. *International Journal of Plasticity* 6, 484–504.
- Liang, R., Khan, A.S., 1999. A critical review of experimental results and constitutive models for BCC and FCC metals over a wide range of strain rates and temperatures. *International Journal of Plasticity* 15, 963–980.
- Lindholm, V.S., Nagy, A., Johnson, G.R., Hoelfeldt, J.M., 1980. Large strain, high strain rate testing of copper. *Journal of Engineering Material Technology* 102, 376.
- Shrivisatava, S.C., Jonas, J.J., Canova, G., 1982. Equivalent strain in large deformation torsion testing: theoretical and practical consideration. *Journal of the Mechanics and Physics of Solids* 30, 75.
- Swift, W., 1947. Length changes in metals under torsional overstrain. *Engineering* 63, 253.
- Wang, X., 1989. An Experimental Study of Infinitesimal and Finite Plastic Deformation in FCC Polycrystalline Metals. PhD dissertation, The University of Oklahoma, 1989.
- Wu, H.C., Xu, Z.Y., Wang, P.T., 1992. The shear-strain curve determination from torsion test in the large strain range. *Journal of Testing and Evaluation* 20, 396.



PERGAMON

International Journal of Plasticity 15 (1999) 1265–1275

INTERNATIONAL JOURNAL OF
Plasticity

On the evolution of isotropic and kinematic hardening with finite plastic deformation Part I: compression/tension loading of OFHC copper cylinders

Akhtar S. Khan*, Kamili M. Jackson¹

*Department of Mechanical Engineering, University of Maryland Baltimore County, ECS Buildings,
1000 Hilltop Circle, Baltimore, MD 21250, USA*

Received in final revised form 15 June 1999

Abstract

Compression tests followed by tension tests after re-machining were performed on annealed oxygen-free-high-conductivity copper cylinders. These tests were conducted at nine levels of maximum strain ranging from 5 to 50%. From this data, isotropic and kinematic hardening were calculated using 50, 1000 and 2000 microstrain offset definitions. Both isotropic and kinematic hardening were found to depend on the yield definition. Isotropic hardening, which increased with plastic strain with no signs of saturation, also increased with larger offset definition of yield. Kinematic hardening, which increased to 40% strain and appeared to saturate thereafter, decreased with higher offset definitions of yield. © 1999 Published by Elsevier Science Ltd. All rights reserved.

Keywords: Isotropic hardening; Kinematic hardening; Finite plastic deformation

1. Introduction

Most constitutive equations for plastic deformation of solids use either isotropic hardening, kinematic hardening, or a combination of both. Isotropic hardening assumes that the yield surface expands with work hardening while neglecting the distortion and movement of the center of the yield surface. Isotropic hardening can give a good approximation as long as the path of forward loading remains radial or

* Corresponding author. Tel.: +1-410-455-3300; fax: +1-410-455-1052.

E-mail address: khan@engr.umbc.edu (A.S. Khan).

¹ Now at Johns Hopkins University.

proportional. In situations of non-proportional loading or reversals in the path of loading the assumption of isotropic hardening deviates significantly from true behavior. Isotropic hardening is incorporated into plasticity theories with a parameter that usually depends on plastic strain. Most modelers agree that it must be experimentally determined. Specific formulations vary widely among researchers and most only give a general dependence.

Recent models continue to include isotropic hardening in their formulation. A very specific definition used by Lee and Zavenl, and Chaboche is

$$\kappa(\epsilon^p = \kappa_s(1 - e^{-b\epsilon_e^p})) \quad (1)$$

where κ_s represents the stabilized value of κ and b is a material constant (Chaboche, 1977; Lee and Zavenl, 1978).

To further describe the evolution of the yield surface, a kinematic hardening parameter is usually included in plasticity constitutive equations. Kinematic hardening assumes the yield surface translates and neglects the expansion and distortion seen in experimental subsequent yield surfaces. Kinematic hardening was formulated to describe the Bauschinger effect. Like isotropic hardening, a variety of kinematic hardening parameters have been suggested by various researchers. Prager, proposed that the behavior of the yield surface could be described as

$$f(\sigma_{ij} - \alpha_{ij}) = 0 \quad (2)$$

where $f(\sigma_{ij})$ is considered to be the initial yield surface and α_{ij} are the nine coordinates of the new center of the yield surface (Prager, 1955). Most model developers have used a differential form of kinematic hardening. An example of a kinematic hardening relation is

$$\alpha_{ij} = c\epsilon_{ij}^p \quad (3)$$

given by Prager where c is a material constant and the relationship is linear. Dafalias and Popov specified

$$d\alpha = \frac{K_\alpha (n : d\sigma)}{K^p \quad n : \nu} \nu \quad (4)$$

where ν is the unit vector in the direction of translation of kinematic hardening, K_α is the hardening modulus for kinematic hardening, and K^p is the generalized plastic modulus (Dafalias and Popov, 1976). Based on Armstrong and Frederick's non-linear kinematic hardening model, Chaboche suggested

$$d\alpha = \frac{2}{3} c d\epsilon_e^p - \gamma \alpha d\epsilon_e^p \quad (5)$$

where c and γ are material constants and $d\epsilon_e^p$ is the increment of the effective plastic strain (Armstrong and Frederick, 1966; Chaboche, 1977).

Like isotropic hardening, it is clear that there have been many suggestions for the kinematic hardening parameter. However, there is no consensus on its form. Most researchers agree that it should be in an incremental form and a function of plastic strain.

Despite so much attention devoted to the formulation of theories describing isotropic and kinematic hardening, there have been only few experiments to determine the hardenings directly. Many of the experiments that have been performed concentrated on the Bauschinger effect but did not separate isotropic hardening from kinematic hardening. This kind of data would be of particular use to modelers as theories are evaluated.

Helling et al. calculated parameters to describe translation, expansion and distortion directly from yield surfaces found experimentally for 1100-0 aluminum, 70:30 brass, and an overaged aluminum alloy to a prestrain of 30% (Helling et al., 1986). Saturation was seen in the translation parameter, which is comparable to kinematic hardening, for aluminum while a steady increase was seen for brass. The expansion parameter, which is comparable to isotropic hardening, showed a steady increase for 1100-0 aluminum as well as brass and a steady decrease for 2024 aluminum. The distortion parameter, which is based on the change in shape of the yield surface, showed no distinct trend.

Trampczynski did an extensive experimental study of isotropic and kinematic hardening in 18G2A and 21CrMoV57 steels using nine different types of loading (Trampczynski, 1988). In monotonic testing, kinematic hardening was found to increase, while isotropic hardening was found to saturate at about 10% plastic strain. In cyclic studies with a maximum cyclic amplitude of 3%, both cyclic tests with increasing amplitude as well as cyclic tests with decreasing amplitudes showed higher and faster increases in kinematic hardening as opposed to isotropic hardening. Monotonic loading after cyclic loading history in shear, two different sequences of alternating cyclic loading in torsion, cyclic loading in tension-compression, and out of phase loading showed increases in both isotropic and kinematic hardening.

Jackson et al. explored kinematic and isotropic hardening in OFHC copper and 6061 aluminum with monotonic compression followed by tension, shear and reverse shear as well as cyclic tension and compression loading (Jackson et al., 1997). Results showed lower isotropic hardening in shear and cyclic loading as opposed to monotonic compression followed by tension. The cyclic results were based on accumulated strain. In addition, the study showed different results for different definitions of yield for both kinematic and isotropic hardening. Isotropic hardening increased with larger offset yield definition while kinematic hardening decreased. A steady non-linear increase in isotropic hardening was seen in all types of loading. An increase in kinematic hardening followed by saturation was seen in cyclic loading while all others continued to increase without signs of saturation.

Ohno et al. observed the characteristics of isotropic hardening during ratchetting in 316FR steel (Ohno et al., 1998). In this study, Ohno et al. observed a steady increase in isotropic hardening up to 2% plastic strain with no sign of saturation. Ohno et al. also observed that in isotropic hardening associated with ratchetting depended on maximum plastic strain rather than accumulated plastic strain. Miller et al. conducted

experiments to determine isotropic and kinematic hardening parameters directly (Miller et al., 1999). OFHC copper was loaded in tension to five different prestrain levels. They were then tested for their reverse yield point in compression. These data were used to find the isotropic and kinematic hardening at five prestrain levels up to 30% strain using a 50 microstrain definition of yield. The isotropic hardening steadily increased almost linearly, while the kinematic hardening increased nonlinearly and then saturated at about 14% strain and 17.4 ksi (120 MPa).

Kinematic and isotropic hardening is an integral part of most models but every model describes the evolution of kinematic and isotropic hardening differently. However, even though there are many equations describing the evolution of isotropic and kinematic hardening there are few studies experimentally determining the evolution of these hardenings directly especially in the finite plastic deformation regime. This study presents data determining the isotropic and kinematic hardening in oxygen-free-high-conductivity copper at strains ranging from 5 to 50%. This study used a deformation level much higher than all previous published results. It should be mentioned here that the Jackson et al. (1997) study was based on the partial completion of the present investigation.

2. Experimental procedure

Compression specimens were machined of oxygen-free-high-conductivity copper with a 0.85" (21.59 mm) diameter and 2" (50.80 mm) height. All compression specimens were annealed in an oxygen-free atmosphere at 1100°F (593°C) for 1 h and then furnace-cooled to room temperature to relieve effects of machining and thermo-mechanical history before performing each test. This is the annealing used previously by Bell and Khan (1980), Khan and Wang (1993), and Khan and Parikh (1986). Single element strain gages (KFE, Kyowa Ltd., Japan) were mounted with adhesive (AE-15, Micro Measurements Inc). This type of gage and adhesive insured measurements of strains up to 20%. The gages were placed on diametrically opposite sides of the cylinder and connected to strain gage indicators which were then connected to the computer that operated the servo hydraulic testing machine (Materials Testing System, MTS). Force measurements were obtained from the MTS load cell. Teflon tape was used on each end of the specimen to provide lubrication and prevent barreling.

The set of nine annealed cylindrical specimens were compressed to strains of approximately 5–50% and unloaded with the same strain rate of 10^{-4} /s. Specimens requiring more than 20% strain were unloaded at 15% strain and new strain gages were mounted. The specimen was then re-loaded to the required strain level. If no plastic strains were observed upon unloading, small dog bone-shaped tension specimens were machined from the compression specimens with a controlled process. The last several cuts during machining were 0.001 in (0.025 mm) to ensure that the machining did not induce any work hardening in the material. The specimens can be seen in Fig. 1. The gage length of the tension specimens varied because of the different final heights of the specimen. However, each tension specimen had test section

diameter of 0.25 in (6.35 mm). Single element strain gages (KFG-5, Kyowa Ltd., Japan) were mounted on the tension specimens with adhesive (M Bond 200, Micro Measurements). Tension tests were conducted on the MTS with grips designed particularly for the miniature sized specimens. Each specimen was loaded to approximately 3% strain to obtain their yield point under reverse loading. The isotropic hardening and kinematic hardening, respectively, were found from the following equations

$$\sigma_{1H} = (\sigma_A - \sigma_B)/2 \quad (6)$$

$$\sigma_{KH} = (\sigma_A + \sigma_B)/2 \quad (7)$$

where σ_A is the subsequent yield stress during forward loading and σ_B is the yield stress during reverse loading. Fig. 2(a) shows the typical stress-strain curve from one

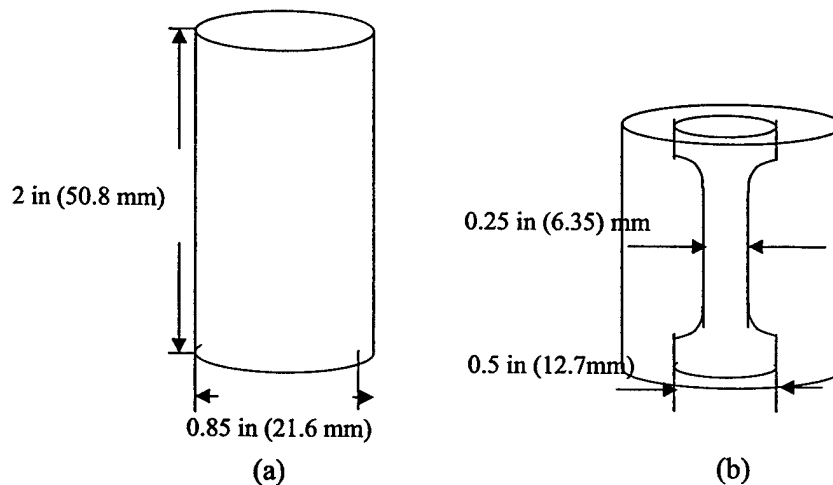


Fig. 1. Specimens (a) compression specimen (b) tension specimen machined from the compressed specimen.

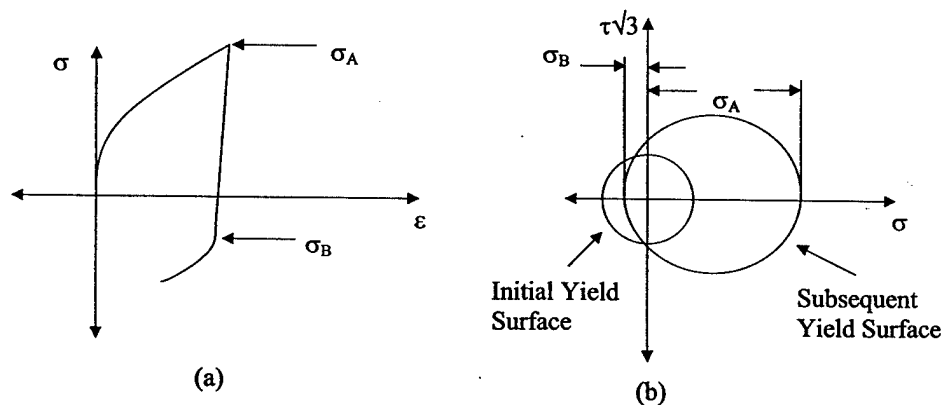


Fig. 2. (a) Method of determining σ_A and σ_B ; (b) representation of σ_A and σ_B on yield surfaces.

specimen and indicates where σ_A and σ_B are measured. Fig. 2(b) shows assumed initial and subsequent von Mises yield surfaces. From Fig. 2, the derivation of Eqs. (6) and (7) becomes a simple matter considering the definitions of isotropic and kinematic hardenings. Isotropic hardening is the expansion of the yield surface quantified by the radius of the subsequent yield surface. Kinematic hardening is the translation of the surface quantified by half the distance from the center of the initial yield surface to the center of the subsequent yield surface. These values were found using 50, 1000 and 2000 microstrain offset yield definitions.

3. Results and discussion

3.1. Stress strain curves

A strain-rate of 10^{-4} /s was used which resulted in an average initial yield stress of 2 ksi (13.86 MPa). Fig. 3 shows the stress-strain curves used to determine the isotropic and kinematic hardening at strains up to approximately 50%. The unloading slopes are consistent with the smaller strain loading tests.

3.2. Isotropic hardening

Fig. 4 shows the results of calculations of isotropic hardening in OFHC copper. Isotropic hardening increases with strain to approximately 50% strain. Isotropic

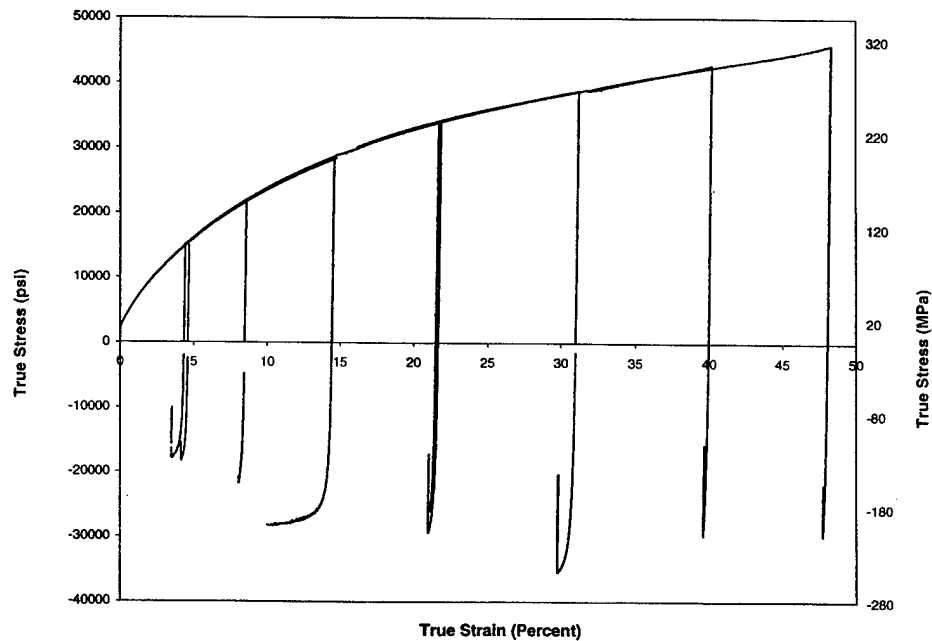


Fig. 3. True stress vs strain curves used to determine isotropic and kinematic hardenings.

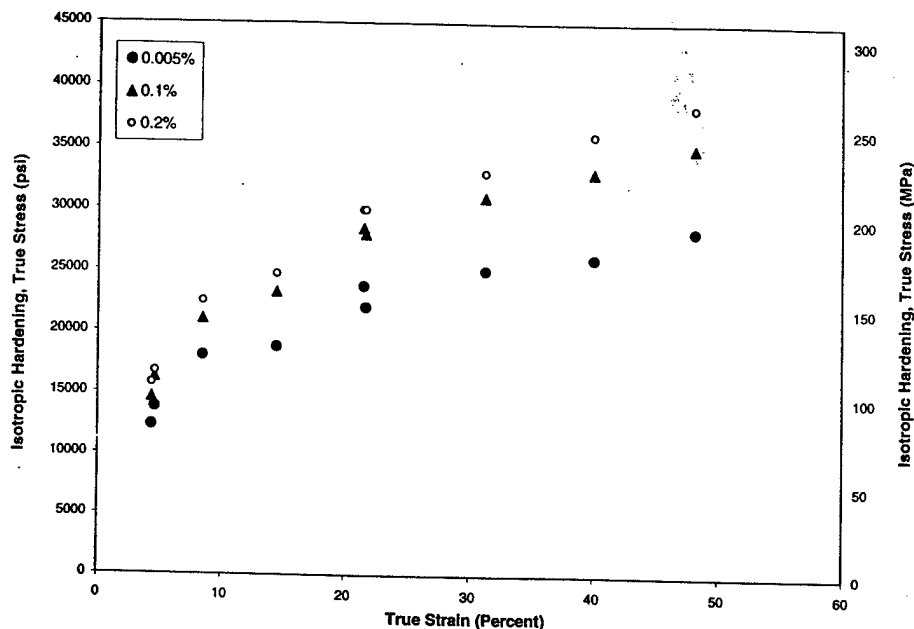


Fig. 4. Isotropic hardening in oxygen-free-high-conductivity copper for various yield definitions.

hardening depends on the definition of yield since the larger offset definitions give higher results. The dependence on definitions of yield was expected since in yield surfaces determined by researchers who use more than one definition of yield, such as Khan and Wang using OFHC copper and Williams and Svensson using 1100 aluminum, have consistently seen larger yield surfaces with larger definitions of yield (Williams and Svensson, 1970, 1971; Khan and Wang, 1993). The steady increase in isotropic hardening was also expected since experiments show continued expansion in yield surfaces with increasing plastic strain. It was not known how much it would continue to increase with plastic strain since previous experiments stopped at 30% strain. Isotropic hardening is essentially a measure of strain hardening. The deformation mechanisms by which strain hardening occurs are well known in FCC polycrystalline materials such as copper. Dislocations pile up in the slip planes at barriers in the crystal. Barriers are formed as dislocations interact with other dislocations moving in different directions or on different planes. Barriers can also occur as interactions at grain and subgrain boundaries. These barriers produce a back stress that opposes the applied stress in the slip plane. As plastic strain increases the interactions of dislocation and boundaries also increase. Therefore, an increase in isotropic hardening with increased plastic strain is observed. The increase in isotropic hardening with the definition of yield can be explained in a similar manner. A larger definition of yield includes a larger region of plastic strain in the analysis. The larger region of plastic strain includes more of the interactions of the microstructure causing the isotropic hardening to increase with larger definitions of yield.

Fig. 5 shows the isotropic hardening data at 50 microstrain as compared to previous cyclic data at the same definition of yield. It can be seen that isotropic hardening in

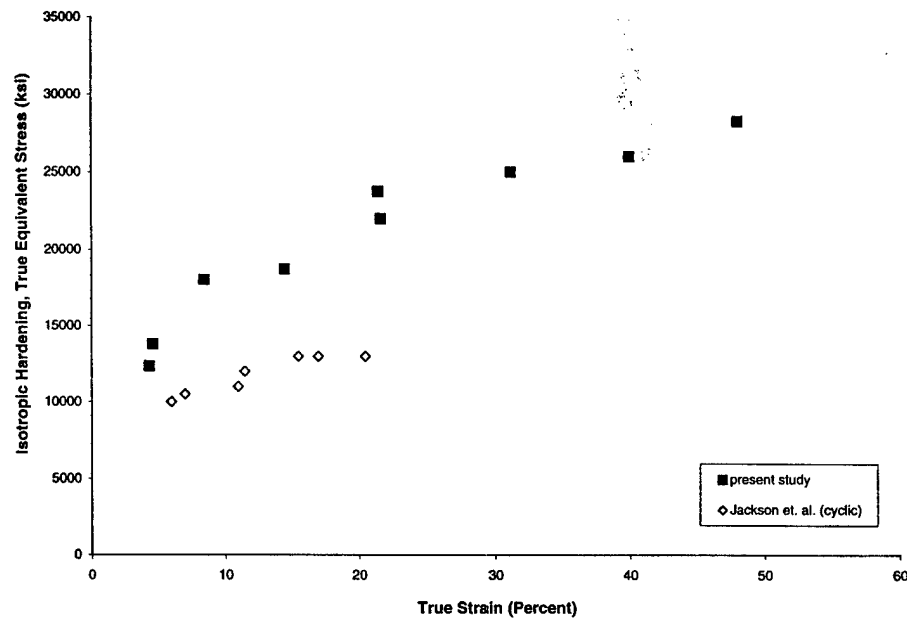


Fig. 5. Isotropic hardening: comparison of data at small offset definitions of yield.

the cyclic data is lower than the monotonically loaded data. The cyclic data is based on accumulated plastic strain. This means the strain indicated is the total sum of the magnitudes of both the positive and negative strain on the specimen as opposed to the actual strain level.

3.3. Kinematic hardening

Fig. 6 shows the results of kinematic hardening in OFHC copper. Kinematic hardening also increased with accumulated strain, but unlike isotropic hardening it appears to saturate at higher strains. In this study kinematic hardening saturated at 18.25 ksi (125.8 MPa), 10.00 ksi (68.95 MPa), and 7.25 ksi (49.99 MPa) at 50, 100 and 2000 microstrain offset yield definitions, respectively. This saturation occurred between 30 and 40% strain. Kinematic hardening also depended on the definition of the yield point and decreased as the definition of yield increased. The decrease was expected since studies such as Khan and Wang using copper and Williams and Svensson using aluminum show that the distortion features in experimental yield surfaces are less evident with increasing definition of yield offset (Williams and Svensson, 1970, 1971; Khan and Wang, 1993). This lessening of the distortion features moves the center of the surface closer to the initial center. In this way, translation in yield surfaces is less pronounced at higher definitions of yield.

Kinematic hardening represents the Bauschinger effect which is present in all metals to some extent. As discussed earlier, strain hardening is a result of the barriers formed by dislocation pile ups. When a metal is stressed in the direction opposite original loading there are fewer obstacles and slip occurs more freely. The lack of obstacles to dislocations result in the lowered reverse yield stress. Behavior

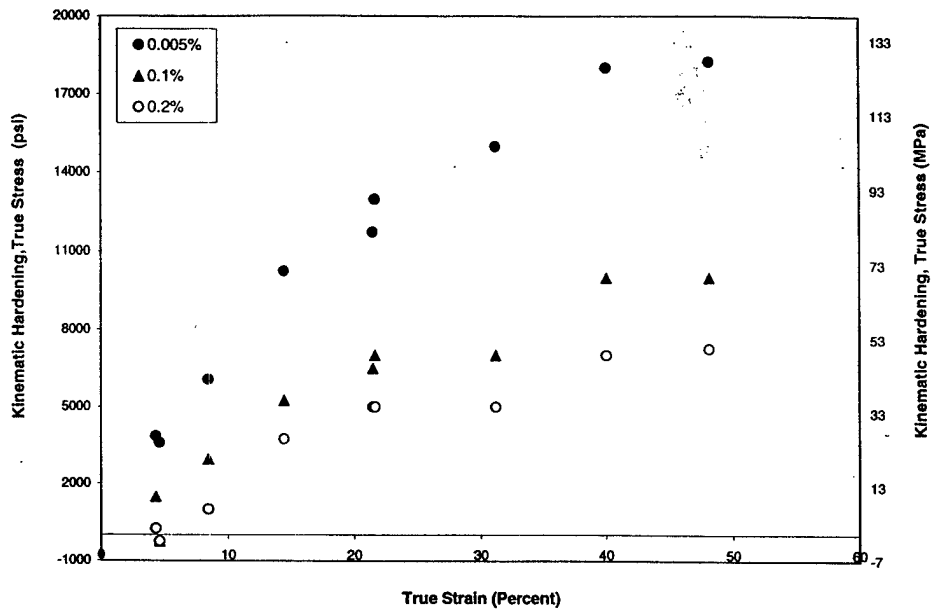


Fig. 6. Kinematic hardening in oxygen-free-high-conductivity copper at various offset yield definitions.

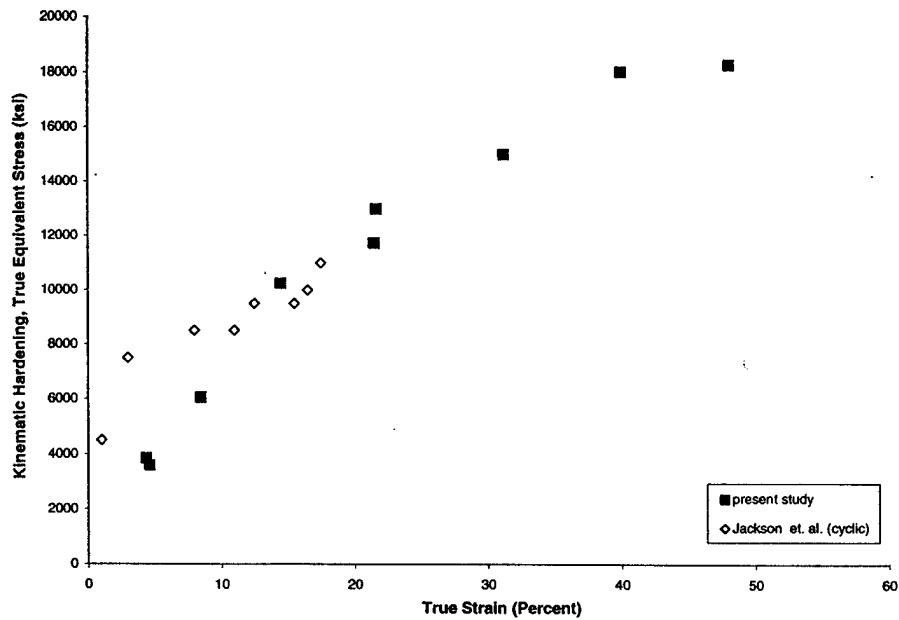


Fig. 7. Kinematic hardening: comparison of data at small offset definitions of yield.

seen immediately following the stress reversal is sometimes called the transient behavior. After transient behavior, strain hardening begins in the reverse direction with the same mechanisms as mentioned previously. The original rate of strain hardening behavior resumes but there is some permanent softening that cannot be

recovered. At small definitions of yield, kinematic hardening is measuring the result of the immediate freedom of movement that the dislocations exhibit upon reverse loading. It is seen from Fig. 6 that the smallest definition shows the highest values of kinematic hardening. After plastic strain in the reverse direction, the dislocations once again have barriers and the Bauschinger effect is less pronounced. A larger definition of yield takes more of the reverse plastic behavior in to account and results in lower values of kinematic hardening as seen in Fig. 6. Fig. 7 gives a comparison using the same data as that of Fig. 6. It can be seen that the cyclic data is higher than monotonic data till about 12% strain.

4. Conclusion

For the first time quasi-static, room temperature experiments in finite strain at a strain rate of 10^{-4} /s were performed using OFHC copper for the determination of isotropic and kinematic hardening with increasing deformation. Isotropic and kinematic hardening was calculated with data at nine levels of strain ranging from 5 to 50%. Isotropic hardening showed a steady increase to 50% strain with increased hardening at larger offset definitions of yield. This study also found isotropic hardening to increase nonlinearly which is true of several other researchers for smaller plastic deformations.

Kinematic hardening showed an increase to 40% strain followed by saturation at 18.1 ksi (125 MPa) for 50 microstrain offset definition of yield. Studies by other researchers show the same trend with steady increase to values of strain up to 30% strain. Kinematic hardening also depended on the definition of offset with larger values of offset giving smaller values of kinematic hardening. This trend is also apparent in other studies for infinitesimal plastic deformation.

Acknowledgements

The authors gratefully acknowledge funding of this research by the Army Research Office through contract no. DAAH0495-2-0004

References

- Armstrong, P.L., Frederick, C.O., 1966. A mathematical representation of the Multiaxial Bauschinger effect. G.E.G.B. Report RD/B/N 731.
- Bell, J.F., Khan, A.S., 1980. Finite plastic strain in annealed copper during non-proportional loading. *International Journal of Solids and Structures* 16, 683.
- Chaboche, J.L., 1977. Viscoplastic constitutive equations for the description of cyclic and anisotropic behavior of metals. *Bulletin de l'Academie Polonaise des Sciences. Serie des Sciences Techniques* 25 (1), 33.
- Dafalias, Y.F., Popov, E.P., 1976. Plastic internal variables formalism of cyclic plasticity. *Journal of Applied Mechanics* 98, 645.

- Helling, D.E., Miller, A.K., Stout, M.G., 1986. An experimental investigation of the yield loci of 1100-0 aluminum, 70:30 brass, and an overaged 2024 aluminum alloy after various prestrains. *Journal of Materials Engineering and Technology* 108, 313.
- Jackson, K., Watts, M., Chen, X., Centala, P., Wang, X., Khan, A., 1997. Evolution of isotropic and kinematic hardenings during finite deformation for OFHC copper and 6061-T0 aluminum. *Physics and Mechanics of Finite Plastic and Viscoplastic Deformation — Proceedings of PLASTICITY '97 NEAT Press, Fulton, MD*, p. 39.
- Khan, A.S., Parikh, Y., 1986. Large deformation in polycrystalline copper under combined tension-torsion loading, unloading and reloading or reverse loading: a study of two incremental theories of plasticity. *International Journal of Plasticity* 2, 379.
- Khan, A.S., Wang, X., 1993. An experimental study of subsequent yield surfaces after finite shear prestraining. *International Journal of Plasticity* 9, 889.
- Lee, D., Zavenl Jr., F., 1978. A generalized strain rate dependent constitutive equation for anisotropic metals. *Acta Metallurgica* 29, 1771.
- Miller, M.P., Harley, E.J., Bammann, D.J., 1999. Reverse yield experiments and internal variable evolution in polycrystalline metals. *International Journal of Plasticity* 15, 93.
- Ohno, N., Abdel-Karim, M., Kobayashi, M., Igari, T., 1998. Ratchetting characteristics of 316FR steel at high temperature, part 1: strain controlled ratchetting experiments and simulations. *International Journal of Plasticity* 14, 355.
- Prager, W., 1955. The theory of plasticity: a survey of recent achievements. *Proceedings, Institution of Mechanical Engineerings* 169, 41.
- Tramczynski, W., 1988. The experimental verification of the evolution of kinematic and isotropic hardening in cyclic plasticity. *Journal of Mechanics and Physics of Solids* 36, 417.
- Williams, J.F., Svensson, N.L., 1970. Effect of tensile prestrain on the yield locus of 1100-F aluminum. *Journal of Strain Analysis* 2 (2), 128.
- Williams, J.F., Svensson, N.L., 1971. Effect of torsional prestrain on the yield locus of 1100-F aluminum. *Journal of Strain Analysis* 6 (4), 26.

Nanocrystalline Material by Mechanical Alloying and Investigation of Suitability for Armor Applications

A comprehensive study on the response of nanocrystalline iron and copper to quasi-static and dynamic loading was performed. Bulk solid nanocrystalline iron and copper specimens used in static and dynamic loading experiments were made by compaction and hot sintering of the nanocrystalline powders. The powders, with grain size 16-96 nm, were obtained by using high energy ball milling. The stress/strain response of dense nanocrystalline iron is found to be grain size and strain rate dependent. The KHL model is modified by incorporating Hall-Petch relation (i.e. yield stress dependence on grain size) and is used to represent the behavior of fully compacted nanocrystalline material. A good correlation with the experimental results is demonstrated. The details of this phase is given in the enclosed copy of a paper, "Mechanical response and modeling of fully compacted nanocrystalline iron and copper".

A detailed investigation on the response of a nanocrystalline iron and copper mixture (80% Fe and 20% Cu) to quasi-static and dynamic loading is performed. The constitutive model developed earlier by Khan, Huang, & Liang (KHL) is extended to include the responses of nanocrystalline metallic materials. The strain rate and grain size dependent behaviors of porous nanocrystalline iron-copper mixture were determined experimentally for both static and dynamic loading. A viscoplastic model is formulated by associating the modified KHL model (representing the fully dense matrix behavior), and Gurson's plastic potential, which provides the yield criteria for porous material. Simulations of uniaxial compressive deformations of iron-copper mixture with different initial porosity, grain size, and at a wide range of strain-rate ($10^{-4} - 10^3 \text{ s}^{-1}$) are made. The numerical results correlate well with the experimental observations. An enclosed copy of a paper, "Mechanically alloyed nanocrystalline iron and copper mixture : behavior and constitutive modeling over a wide range of strain rates" contains the results of this investigation.

Scientific Personnel:

In addition to the P.I. and senior investigator, Dr. Akhtar S. Khan & Dr. Laszlo Takacs, a doctoral student, Ms. Hayoue Zhang, was supported on the project. Ms. Zhang received a Ph.D. degree under the support of this investigation in May 2000.

List of Manuscripts Published or Submitted:

- (i) Akhtar S. Khan, Haoyue Zhang, and Laszlo Takacs, "Mechanical response and modeling of fully compacted nanocrystalline iron & copper," The International Journal of Plasticity, vol. 16, pp. 1459-1476, 2000.
- (ii) Akhtar S. Khan & Haoyue Zhang, "Mechanically alloyed nanocrystalline iron and copper mixture: behavior and constitutive modeling over a wide range of strain rates," The International Journal of Plasticity, vol. 16, pp. 1477-1492, 2000.

Inventions:

None



PERGAMON

International Journal of Plasticity 16 (2000) 1459–1476

INTERNATIONAL JOURNAL OF
Plasticity

www.elsevier.com/locate/ijplas

Mechanical response and modeling of fully compacted nanocrystalline iron and copper

Akhtar S. Khan^{a,*}, Haoyue Zhang^{a,1}, Laszlo Takacs^b

^a*Department of Mechanical Engineering, University of Maryland Baltimore County, Baltimore, MD, 21250, USA*

^b*Department of Physics, University of Maryland Baltimore County, Baltimore, MD, 21250, USA*

Received in final revised form 22 February 2000

Abstract

A comprehensive study on the response of nanocrystalline iron and copper to quasi-static and dynamic loading is reported. Bulk solid nanocrystalline iron and copper specimens used in static and dynamic loading experiments were made by compaction and hot sintering of the nanocrystalline powders. The powders, with grain size 16–96 nm, were obtained by using high energy ball milling. The stress/strain response of dense nanocrystalline iron is found to be grain size and strain rate dependent. The KHL model is modified by incorporating Hall–Petch relation (i.e. yield stress dependence on grain size) and is used to represent the behavior of fully compacted nanocrystalline material. A good correlation with the experimental results is demonstrated. © 2000 Elsevier Science Ltd. All rights reserved.

Keywords: Nanocrystalline material response; Split–Hopkinson–Bar technique; Finite visco-plastic deformation

1. Introduction

Nanocrystalline materials are single- or multi-phase polycrystals with grain sizes in the nanometer region. The desirable grain sizes are generally below 100 nm in at least one dimension, since it is in this size range that physical, mechanical, and chemical properties begin to change significantly because of confinement effects. The mechanical properties of nanocrystalline materials substantially differ from those of coarse-grained counter-parts. For example, some nanocrystalline materials may

* Corresponding author.

¹ Now at Halliburton Engineering Services, Dallas, Texas.

E-mail address: khan@engr.umbc.edu (A.S. Khan), haoyue.zhang@halliburton.com (H. Zang), takacs@umbc.edu (L. Takacs).

exhibit increased strength/hardness, reduced elastic modulus and decreased ductility (Gleiter, 1992; Siegel and Fougere, 1995). And it is still not clear whether the description of the mechanical behavior requires new models or may be derived by expanding the rules valid in conventional grain-size regions to the nanometer regions.

In order to study the mechanical behavior of nanocrystalline materials, one has to obtain metal powders with grain size in nm, and make these powders into bulk solid specimens with the requirement that the grain size of the specimens is still in nm.

There are several ways to obtain the powder with grain size in nm, such as inert gas condensation (Gertsman et al., 1993; Edelstein and Cammarata, 1996), mechanical alloying (Chang et al., 1992; Pardavi-Horvath and Takacs, 1995; Edelstein and Cammarata, 1996), and crystallization techniques (Lu, 1996a,b). The method of inert gas condensation is impractical because yield rate hardly provides enough powder to prepare samples for extensive mechanical testing. Hence, mechanical alloying has been proven as the best route to produce sufficient quantities of materials with nanometer-size grains (Jain and Christman, 1994; Takacs, 1996). Also, the mechanical alloying technique is simple and of low cost. All these advantages make mechanical alloying one of the priority choices in producing nanocrystalline metal powders. Cold compaction followed by hot sintering is a commonly used technique to produce bulk, ultrafine-grained solids (Andrievski, 1994). The sintering temperature and time are crucial to the grain size and density of the nanocrystalline bulk solids. It is often very difficult to get a desired grain size at the same time as getting a fully dense solid. When producing nanocrystalline solids by the sintering of powders, the material obtained were often fully dense, but with micron-sized grains or grains of several nm, but only partially dense (Hahn et al., 1990).

The mechanical behavior of nanocrystalline materials are found to depend on grain-size (Nieman et al., 1991). It was found that the mechanical properties such as strength and hardness were improved with the decrease of grain size within certain ranges (Siegel and Fougere, 1994; Sanders et al., 1996). The influence of grain-size reduction on the mechanical behavior of materials has been discussed in terms of various models (Siegel and Fougere, 1995; Wang et al., 1995). For example, for conventional polycrystals with grain sizes ranging from several to hundreds of micrometers, the grain size dependence of hardness or yield strength usually expressed in the terms of the Hall–Petch equation:

$$\sigma_y = a_0 + \frac{k_0}{\sqrt{d}} \quad (1)$$

where d is the average grain size, and a_0 and k_0 are material constants. However, the mechanical behavior of materials with nanometer-sized grains is still a matter of controversy (Nieman et al., 1991; Gertsman et al., 1994; Siegel and Fougere, 1994; Wang et al., 1995). Discussion has been concentrated on whether such a model still works when the grain size is well below the micrometer range.

Relatively little research has been done measuring the bulk mechanical properties of nanocrystalline metals. The main difficulty is consistently producing samples large enough for mechanical testing. Little is understood about the high-rate deformations of nanocrystalline metals. There is not enough experimental data on both fully

dense and porous nanocrystalline metals under static and dynamic deformation to develop a firm basis for constitutive models. The objective of this research is to develop a reproducible sample preparation method with the grain size in nm, characterize the mechanical behavior of near fully dense and porous nanocrystalline iron and copper over a wide range of strain rates (10^{-4} to 10^3 /s) at room temperature with the consideration of grain-size effect, porosity effect and strain-rate sensitivity. Only compressive deformations are examined so that void collapse rather than void growth is the microstructural evolution of interest. Nanocrystalline iron and copper powders were prepared by ball milling and consolidated into bulk specimens through room-temperature compaction and hot sintering. The average grain size of both the metal powders and solid specimens were examined and confirmed through the analysis of X-ray diffraction results. Static and dynamic compression tests with strain rates in the range of 10^{-4} to 10^3 /s were performed on solid cylindrical specimens.

Experimental study indicated that nanocrystalline iron was a porous strain-rate-dependent material with some ductility. The mechanical behaviors were strongly dependent on the grain size. Constitutive models that recognize effects of porosity, strain rate-dependence and grain-size effects, are therefore required to adequately describe the mechanical behavior of nanocrystalline materials.

Conventional plasticity theory assumes volumetric incompressibility during plastic deformation. In contrast, the constitutive equations for a porous material must reflect volumetric plastic deformation and a hydrostatic pressure dependence. With the presence of the voids in ductile materials, the hydrostatic component of stress can cause macroscopic volume change and affect plastic yield. The incompressibility assumption is no longer valid for porous materials, and the yielding is no longer independent of hydrostatic stress component. Conventional plasticity theories and their associated flow rules are not applicable to fit the response of plastic deformation of porous materials.

In previous studies of modeling porous materials (Carroll and Holt, 1972; Gurson, 1977; Spitzig et al., 1988; Marin and McDowell, 1996), it has been assumed that the porous material consists of a continuum matrix of homogeneous isotropic solid and pores represented by a scalar internal variable-void volume fraction. The matrix material is conventional incompressible solid which can be modeled by classical plasticity theory. The mechanical response of the porous material will depend on the response properties of the matrix material and on the pore geometry, e.g. the size, shape and distribution of the pores.

Careful study of the mechanical behavior of the matrix is a prerequisite for the constitutive modeling of porous materials. The appropriate mathematical expression of matrix material should describe the mechanical properties, such as yielding, work hardening and strain-rate sensitivity, without the porosity effect. Then such an information can be related to the hydrostatic pressure-sensitive flow rule and yield criteria to model the material response which includes the volumetric plastic deformation.

Gurson (1977) first developed approximate yield criteria and flow rules for ductile porous materials. In this model, the matrix material is idealized as a rigid-perfectly plastic solid. Gurson's model has been modified by Pan et al. (1983) and Tvergaard and Needleman (1986) to solve rate dependent problems by modeling the matrix

material as elastic-viscoplastic. In most models of porous materials (Kim and Carroll, 1987; Spitzig et al., 1988; Hom and McMeeking, 1989), a power law has been used to describe the work hardening of the matrix material surrounding the voids. In Bonnenfant et al. (1998), a time-dependent viscoplastic relation was used for the matrix material.

The approach used here involved modeling the mechanical behavior of the near full density iron with grain size in nm over a wide range of strain rates. It is assumed that the response of the near full density iron with grain size in nm, represents the response of the matrix in this material. No porosity effect is considered initially. Once the model development of matrix material has been completed, additional study of the porosity effect for nanocrystalline material will be discussed in Khan and Zhang (2000).

The Khan–Huang–Liang (KHL) model (Khan and Huang, 1992; Khan and Liang, 1999, 2000) will be modified as the constitutive relation for the almost fully dense iron with grain size in nm. In Khan and Liang's (1999) study of mechanical behavior of tantalum and aermet 100 steel, a coupling effect between strain and strain rate on the work-hardening behavior was found. The work-hardening behavior of material was determined to be dependent on strain, strain rate, and temperature. It was found that current constitutive models for BCC materials undergoing finite plastic deformation, e.g. Johnson–Cook and Zerilli–Armstrong models, failed to give accurate predictions about strain-rate dependency of work-hardening behavior (Liang and Khan, 1999). A coupled strain and strain-rate effects are included on the description of work-hardening behavior of the material in the KHL model. The modeling of the fully compacted material is based on the experimental observation that the almost fully dense iron with grain size in nm is a rate-sensitive and work-hardening material, with grain-size effect given by Hall–Petch relation in a certain range of grain size. Material constants for such an elastic–viscoplastic model are determined through experimental data. The correlation between the modified finite deformation elastic–viscoplastic model and experimental results for almost fully dense iron with grain size in nm is examined in a wide range of strain rates and grain sizes in this paper.

2. Ball milling procedure and consolidation of nanocrystalline iron and copper

Copper and iron powder with the grain size in nm were obtained through high energy ball milling–mechanical alloying for this investigation. The principle of ball milling is to transmit mechanical energy through collisions between balls or a ball and the wall of the milling container. The metal powder particles are subjected to large deformation during the milling and the size of the powder particles are refined progressively. The variation of final particle size of the metal powder is determined by the properties of the material and by the milling energy, which is related to the type of mill, the milling frequency, size and number of balls, amount of powder, etc. (Takacs, 1993). A reduction of the average grain size is observed typically from 50 to 100 μm to sizes ranging from 2 to 20 nm (Edelstein and Cammarata, 1996). However it was

found that the grain size of the metal powder obtained from mechanical alloying usually ceased to decrease after a certain milling time. The saturated grain size of 5 to 10 nm was observed by Hellstern et al. (1989), 9 nm for BCC and 13 nm for HCP elements (Fecht et al., 1990). It is difficult to reduce FCC materials to a very fine size (Ranganathan et al., 1996). The ball-milled productions of iron and copper powder with nanometer size grains were examined by X-ray diffraction. Grain sizes of the powders were determined through the analysis of X-ray peak broadening.

Compaction and sintering technique were used to make the bulk solid specimen from nanocrystalline copper and iron powder. The powder was first compacted into a raw shape during which the metal particles are forced to extrude into nearby pores and fill most of the available empty space (Hirschhorn, 1969). The powder compact was then subjected to high temperature for densification. The sample densifies as vacancies leave the pores and the pores shrink during the high temperature sintering. The grain sizes of bulk solid specimens obtained through compaction were examined and verified through X-ray diffraction.

2.1. High energy ball milling

High energy ball milling–mechanical alloying was performed in a laboratory Fritsch P- 5 Planetary Mill in this study. During the milling process, shown in Fig. 1, the powder was subjected to high energy compressive impaction when it came in between the balls or the ball and the wall of the milling vial; the vial was rotated at high speed by electrical motor. Iron powder with the initial particle size of –325 mesh and the purity of 98.5%, and copper powder of –325 mesh and 99% purity were used for present experiments. The powders and hardened steel milling balls of half an inch diameter were loaded and sealed in the milling vial in an argon glove box. A constant ball-to-powder ratio of 16 to 1 was maintained during the whole operation. The milling speed was kept at 120 rpm. The automatic controlling routine of milling was 15 min milling and 15 min rest in order to avoid the increase of the temperature inside the vial which held the milling ball and metal powder during the milling process. At the same time, the vial temperature was kept near room temperature during the milling by fan cooling. It has been reported that metals as copper and iron tend to coalesce and stick to the milling tools during milling in argon. This welding tendency can be overcome using a small quantity of process control agents. Therefore, a small amount of stearic acid was added as a lubricant after each 20 h of milling. The milling time schedule and the amount of stearic acid during each milling period for iron and copper powder are shown in Table 1.

Powders with different grain size in nm were obtained from a single milling process by interrupting it after certain milling times. For example, after 5 h milling, certain amount of powder was taken out of the milling vial in order for the consolidation of bulk specimens for mechanical tests and X-ray diffraction grain-size analysis. A certain number of milling balls were also removed at the same time to keep a constant ball-to-powder weight ratio. All the processing was handled in argon atmosphere to minimize the contamination with oxygen, nitrogen, and humidity. The vial and milling balls were cleaned by wet milling silicon dioxide after each batch of milling operation.

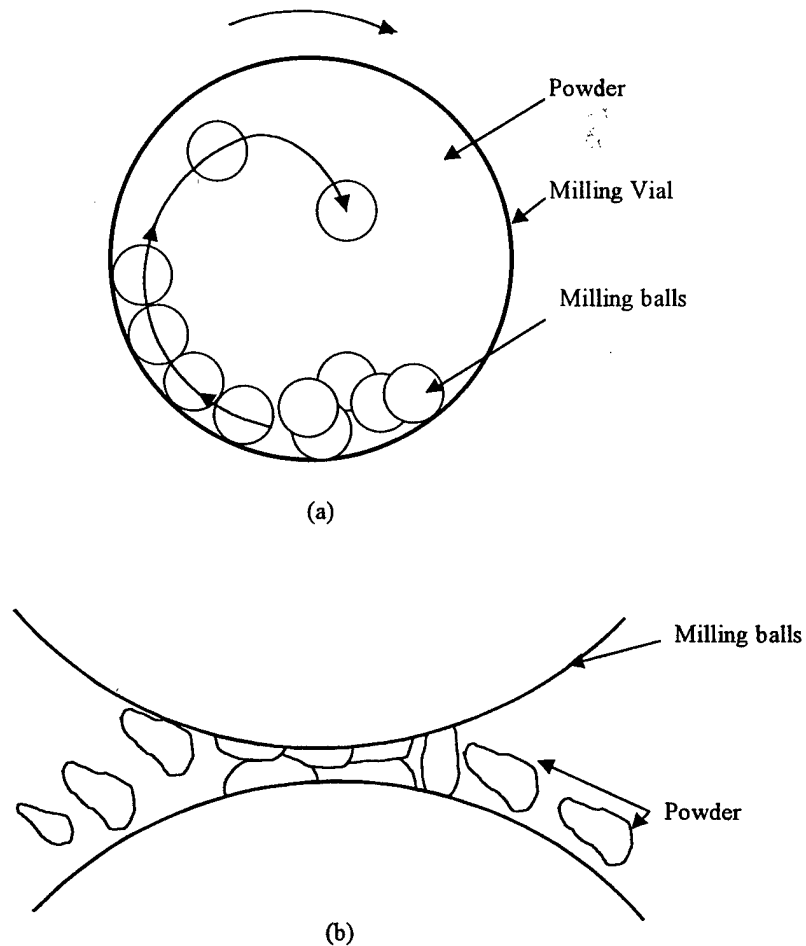


Fig. 1. Schematic sketch of the process of ball milling of metal powder.

Table 1
Milling schedule of pure iron and copper powders

Milling time (h)	0	5	10	15	20	40	60	80
Stearic acid (%)	0.4	0.4	0.4	0.4	0.63	0.98	1.68	1.68

The X-ray diffraction patterns were collected by using Cu- K_{α} wave ($\lambda = 0.1542$ nm) radiation. The mean grain size was determined from the half maximum breadth of the X-ray peaks, after instrumental broadening.

2.2. Compaction and sintering

The iron or copper powder of a certain grain size obtained from ball milling was placed in a die in an Argon glove box for subsequent compaction and sintering. The die used for the compaction and sintering was made of Vasco Max C-350 and heat

treated to its maximum strength. The inner and outer diameters of the die were 0.875 and 2.1 inches, respectively. A cylindrical split inner die made of the same material allowed the specimen to be removed from the die after compaction and sintering. A thin layer of graphite (about 0.3 g) was put into the bottom and top of the die (before and after filling with the iron or copper powder) in order to prevent the involvement of oxygen and nitrogen during the later processing.

The first stage of the consolidation of nanocrystalline iron or copper is to produce a compacted powder. A compaction pressure of 280 ksi was exerted on the powder in the die via punches located at the bottom and upper end of the column of metal powder. The pressure held for 2 min at room temperature. The application of pressure during the powder compaction step displaced most of the argon out of the specimen and forced metal particles to move into nearby pores and fill most of the empty space. A lower density raw shape specimen was obtained after cold compaction. After the room temperature compaction, the powder was reloaded at 600°C under the pressure of 140 ksi for 1 h. A low heating rate of 0.25°C/s was used for sintering to avoid unequal heating of the specimen, based on earlier indications that the specimen experienced thermal gradients during the heat-up (Edelstein and Cammarata, 1996). If the outside of the specimen was hotter than the inside, it densified at a faster rate and quickly turned into a hard shell. The hard shell prevented the inside of the specimen from shrinking and large pores were formed as a result. Another 11 h of non-pressure sintering was carried out under the same temperature in order to spheroid the pores and achieve maximum mechanical strength of the iron or copper. Finally the specimen was annealed at 600°C for 1 h. The compaction and sintering schedule minimized grain growth and maximized densification during the consolidation. The compaction and sintering pressure and temperature for iron and copper are shown in Table 2.

Axial-symmetrical cylindrical specimens of 0.37 inch (9.4 mm) in diameter and 0.12 to 0.60 inch as (3.1 to 15.24 mm) in length, which were suitable for dynamic and quasi-static experiments, respectively, were machined from raw bulk samples obtained through compaction and sintering.

3. Mechanical characterization experiments

Published data on the mechanical behavior of nanostructured materials has been based mostly on microhardness measurements (Koch et al., 1995; Lu, 1996b). There

Table 2
Compact and hot sintering schedule for iron and copper

Material	Iron or copper			
Loading pressure (ksi)	280	140	0 (with die)	0 (out of die)
Temperature (°C)	24	600	600	600
Time (h)	0.03	1	11	1

has been some controversy about nanocrystalline materials because of the limited experimental data obtained by conventional mechanical testing of bulk solid specimen by standard tension or compression tests. For example, some studies have revealed material softening with decreasing grain size, while other studies observed material hardening with decreasing grain size (Siegel and Fougere, 1995).

Precision density measurements, based on the Archimedes principle (Garofalo and Wriedt, 1962), were made on iron samples by weighing them in water and air. All measurements were made using Mettler Toledo 261 Deltarange Semimicro balance with a nominal sensitivity of 10 μg .

Each sample and the hanging copper wire of 0.005 inch diameter were first weighed individually in air. They were then prepared for weighing in liquid by prior submersion in LiquiNox (Alconox Inc.) which minimizes surface tension effects and less air would be trapped between the sample and the liquid when weighing in the water in the next step. The sample was then hung by the copper wire and submersed into water contained in a beaker (50 ml), which would be put onto the balance and weighed.

The porosity defined by the void volume fraction of the specimen is given by

$$f = 1 - \frac{V_M}{V} = 1 - \frac{\rho}{\rho_M} \quad (2)$$

where ρ and V are the density and total volume of the voided solid nanocrystalline sample, respectively. The notations ρ_M , V_M refer to the matrix density, which is the theoretical standard density, and matrix volume, respectively.

Vickers microhardness measurements were performed on bulk specimens obtained through the compaction and sintering of the powder with different milling time and grain size. These measurements were carried out to determine the hardness of the nanocrystalline iron samples under room temperature. The microhardness measurements were made using a Buehler Micromet I microhardness tester. Hardness was defined as load divided by projected area of indent. The two ends of the sample were polished before the measurements in order to improve the accuracy of the reading. A right pyramidal diamond indenter with a square base having the angle between the opposite faces of 136° was loaded with 500 g force to the sample surface for 5 s. At least eight separate tests were performed on both ends of each sample and the arithmetic average was obtained. The results of the Vickers hardness tests were plotted as an inverse function of the square root of grain size ($d^{-1/2}$) to determine whether the hardness dependence of grain size for nanocrystalline iron would followed the Hall–Petch relation.

The grain size was analyzed through X-ray diffraction. The quasi-static loading experiments, with the strain rates from 10^{-4} to $10^0/\text{s}$ were preformed on MTS 809 Axial/Torsion Material Test System. The dynamic tests with the strain rates up to $10^3/\text{s}$ were completed using Split Hopkinson Pressure Bar (SHPB) technique and Direct Disc Impact (DDI) technique. The details of these experimental techniques are given in Khan and Huang (1991, 1992) and Liang and Khan (1999).

4. Experimental results and discussions

The grain size of pure iron powder after certain time of ball milling was obtained through the analysis of X-ray diffraction results. The relation between milling time and grain size of iron is shown in Fig. 2. After 5 h milling, the average grain size is already in the nanometer range (96 nm). The grain size decreased dramatically with the increase of milling time. But after a certain time of milling, (60 h for iron powder), when the grain size reached 16 nm, the grain size ceased to decrease. This is consistent with the observation that the decrease of grain size in the course of ball milling will saturate at a certain value (Ranganathan et al., 1996).

The X-ray diffraction analysis of three solid iron samples made from powder after 20 h milling indicated that the average grain sizes were about 28, 48, and 50 nm, respectively, while the grain sizes of three solid samples from powder after 40 h milling were 39, 41, and 45 nm, respectively. After the high temperature sintering, the growth in the grain size was about 10 to 20 nm.

The Vickers hardness of the iron samples was plotted against the inverse of the square root of grain size to examine whether the relationship between hardness and grain size still can be described by the Hall–Petch relation [Eqn. (1)] when the material grain is nano-size. It was found that the Vicker's hardness increased with decreasing grain size, with the exception of one data point after 60 h milling, which corresponded to the grain size of 16 nm, as shown in Fig. 3. For nanocrystalline iron, the

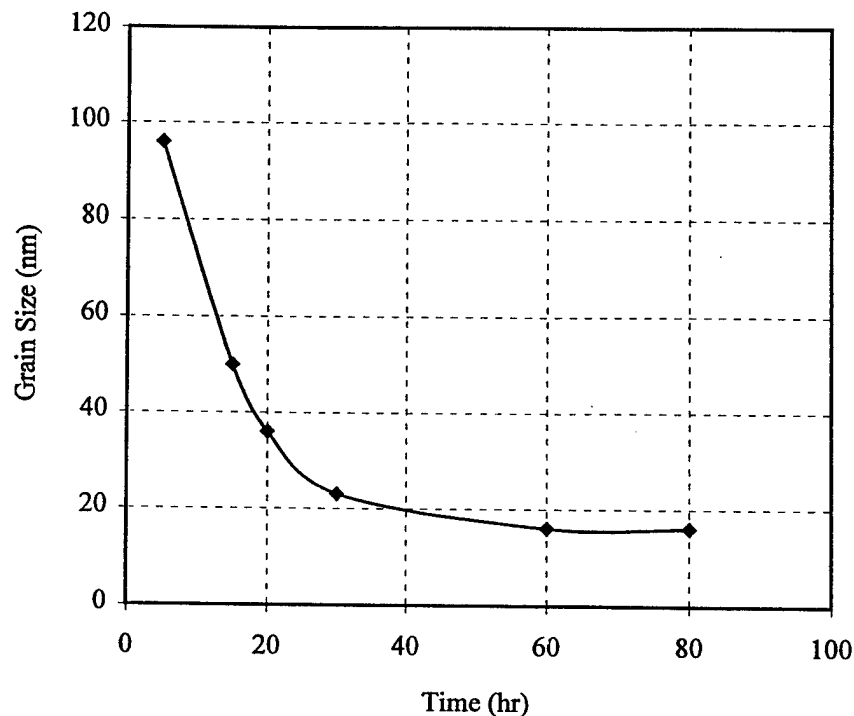


Fig. 2. Grain size of iron powder versus milling time.

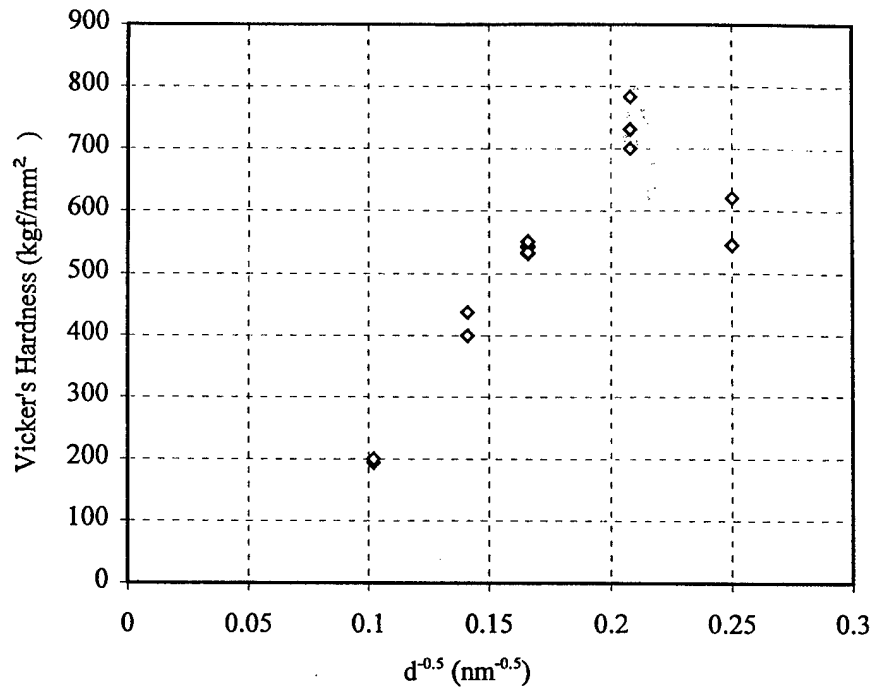


Fig. 3. Vicker's hardness versus grain size $d^{-0.5}$ for iron powder.

Hall–Petch plots yield positive values of K , i.e. they exhibited Hall–Petch behavior for a grain size larger than 16 nm. When grain size was lower than this critical size, an abnormal Hall–Petch relation with a negative K was observed.

The porosity of the iron samples made using the previously described compaction and sintering schedule were all around 3–7%, which is the best result after numerous trial on different sintering time, pressure, and temperature.

A series of compression tests was performed at room temperature at the strain rate of 10^{-4} /s. The stress/strain curves of iron samples made from the powder with different milling time and grain size are shown in Fig. 4. The strength and the fracture stress increased significantly with the increase of milling time, or decrease of grain size. However, at the same time, the sample lost its ductility gradually, an almost totally brittle behavior was found from the sample from powder of 16 nm grain size that was obtained from 60 h milling. The elongation was around 1% when the powder grain size was smaller than 50 nm. For those specimens made from powder subjected to less than or equal to 10 h milling, the elongation was larger than 3%, where the experiments were stopped, and there was no visible flaw and damage on the surface of the specimen.

Similar stress strain responses at strain rate of 0.0001/s were also observed on copper samples made from powder with different milling time, as shown in Fig. 5. No failure happened to any of the copper specimens before unloading.

The stress/strain curves of pure iron under different strain rate are shown in Fig. 6. All the experiments were performed on the samples made from the pure iron powder

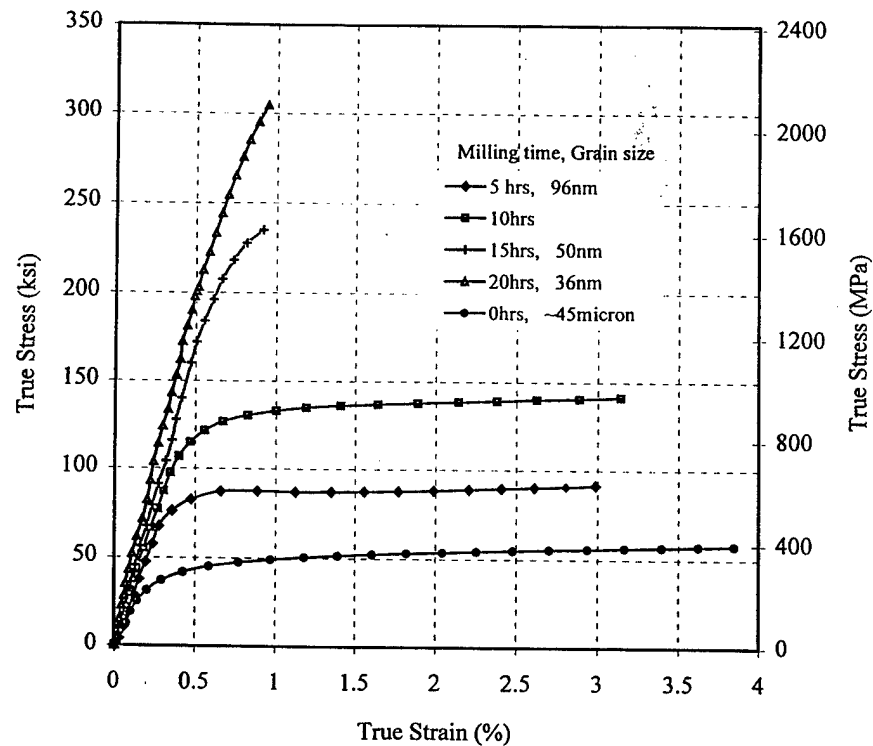


Fig. 4. Stress/strain response of nano-iron from powders with different milling time and grain size. The strain rate is 0.0001/s.

of 10 h milling. It can be seen that nanocrystalline iron was strain rate sensitive, the material response at different strain rates changes significantly.

5. An elastic-viscoplastic model for fully compacted nanocrystalline material

Khan and Huang (1992) proposed a constitutive model (KH model) to predict the work hardening behavior in a large strain rate range for 1100 aluminum on the approximation of isotropic hardening during large deformation. The general form of the KH model is based on the decomposition of the total deformation rate into elastic and plastic components, where the elastic deformation rate is related to the Cauchy stress rate by the generalized Hooke's law, and the plastic deformation rate is assumed to be proportional to the deviator of the Cauchy stress.

In order to describe the coupled work-hardening dependence on strain, strain rate and temperature, a new relation between J_2 and D_2^p was proposed in the KHL model (Khan and Liang, 1999)

$$J_2 = f_1(\epsilon_2, D_2^p) f_2(T) \quad (3)$$

where, J_2 , D_2^p and ϵ_2 are the second invariant of deviatoric stress, the second invariant of the plastic deformation rate, and the equivalent strain, respectively. $f_1(\epsilon_2, D_2^p)$

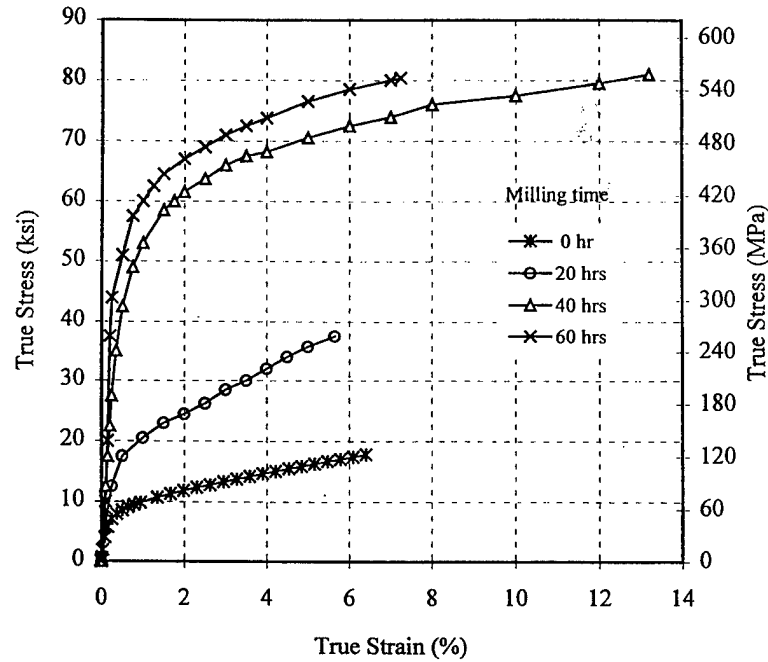


Fig. 5. Stress/strain response of copper from powders with different milling time. The strain rate is 0.0001/s.

is a function describing the coupled strain and strain rate effects on the work hardening behavior. The one dimensional functional form chosen was

$$\sigma = \left[A + B \left(1 - \frac{\ln \dot{\epsilon}}{\ln D_0^p} \right)^{n_1} \epsilon^{n_0} \right] \dot{\epsilon}^C (1 - T^{*m}) \quad (4)$$

$$T^* = (T - T_r) / (T_m - T_r) \quad (5)$$

where σ , ϵ and $\dot{\epsilon}$ are von Mises equivalent stress, strain, and strain rate, respectively. T is the absolute temperature, T_m is the melting temperature of the material, and T_r is a reference temperature. T_m is 1808 K for iron and T_r is taken as room temperature 273 K in the current study. A , B , n_0 , n_1 , C , and m are material constants. This model was shown to give good correlation with uniaxial loading experiments (Khan and Liang, 1999) and good predictions during multiaxial experiments (Khan and Liang, 2000).

Even though the experimental results on iron with grain size in nm were all obtained at room temperature, the temperature rise during the high strain rate deformation has to be considered in the formulation. High strain rate deformation can be approximated as adiabatic and part of the deformation work is transformed into heat, which causes the temperature increase in the specimen. The temperature rise leads to the thermal softening behavior in high strain rate dynamic tests. For

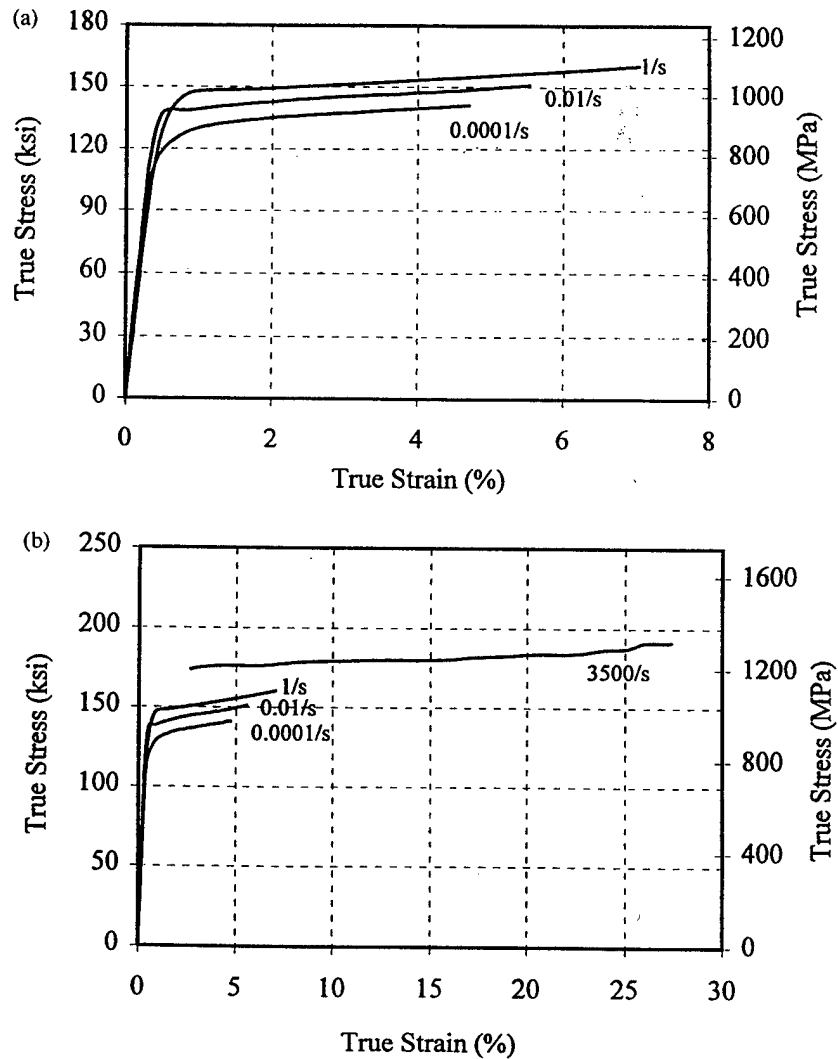


Fig. 6. Stress/strain response of nano-iron under different strain rate. The samples are from the powder of 10 h milling: (a) quasi-static tests, (b) quasi-static and dynamic tests.

metals, 90% of the work of deformation is considered to be changed to heat (Meyers et al., 1995). The temperature rise is expressed as

$$\Delta T = \frac{0.9}{\rho C_p} \int_0^\epsilon \sigma(\epsilon) d\epsilon \quad (6)$$

where ρ is the density and C_p is the heat capacity of the material. For pure iron, ρ is 7.87 g/cm³ and C_p is 0.108 cal/gK.

In Eq. (4), the material constant A is actually the yield stress of material at the reference strain rate. Based on the experimental observation that the yield stress and Vicker's hardness increase with decreasing the grain size; A is dependent on grain

size. The Hall–Petch relation, [Eq. (1)], is adopted to give the yield stress dependence on the grain size.

The material behavior of iron with grain size in nm is described by generalized Hookes law before yielding, while the KHL model, modified by grain size effect, is used to reflect the stress/strain behavior after yielding.

$$\sigma = \left[\left(a_0 + \frac{k_0}{\sqrt{d}} \right) + B \left(1 - \frac{\ln \dot{\epsilon}}{\ln \dot{\epsilon}_0} \ln D_0^p \right)^{n_1} \dot{\epsilon}^{n_0} \right] \dot{\epsilon}^C (1 - T^{*m}) \quad (7)$$

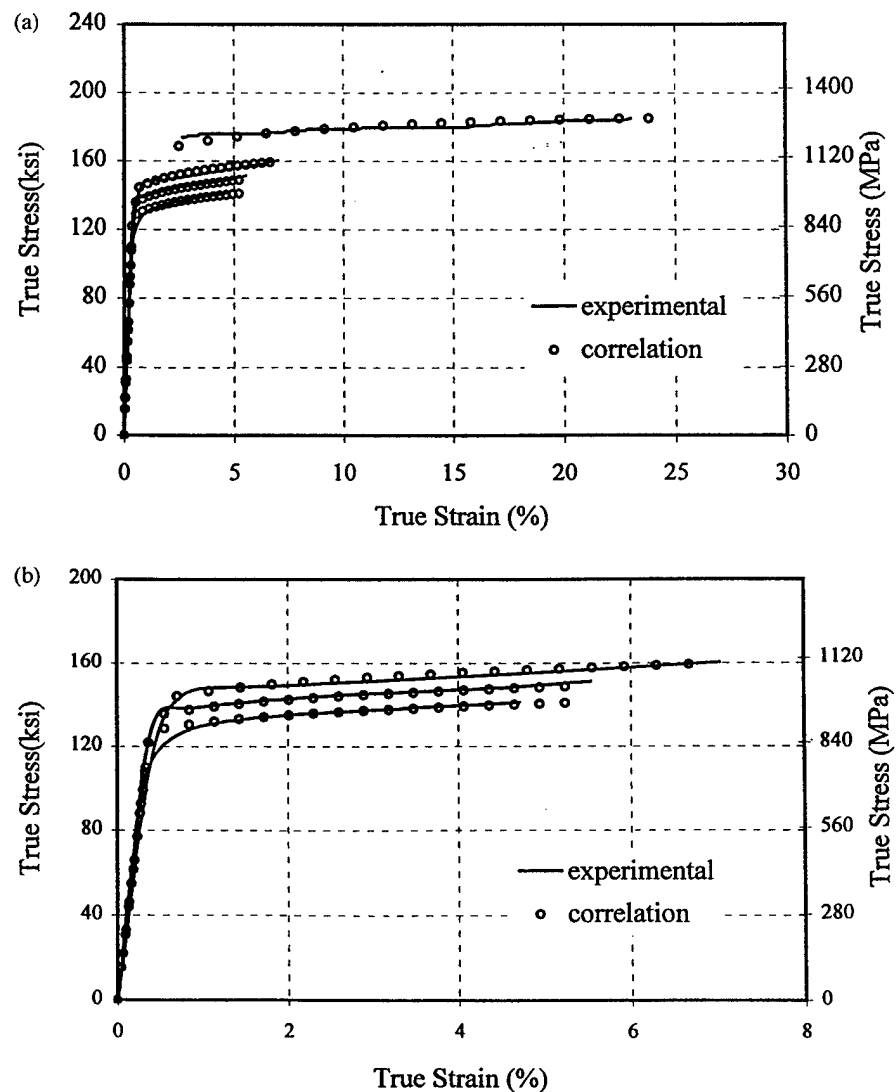


Fig. 7. Comparison between experimental data from the samples made after 10 h milling and predicted stress/strain response: (a) quasi-static and dynamic results; (b) enlargement of the quasi-static results.

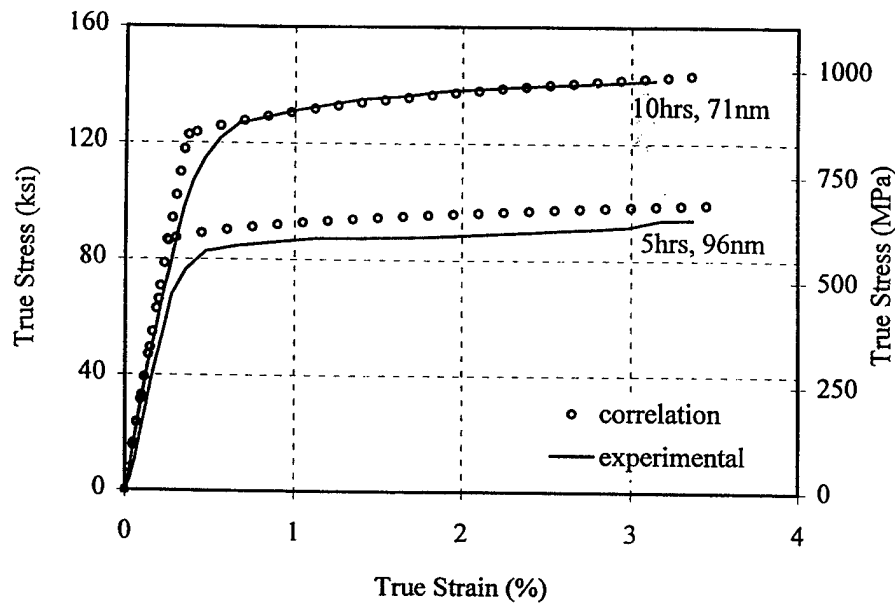


Fig. 8. Comparison between experimental data, at a strain rate of 0.001/s, and predicted stress/strain response with different grain size (71 and 96 nm).

The temperature rise due to adiabatic heating during high strain rate deformation is calculated by using Eq. (6). Therefore, the adiabatic experimental response at high strain rates is converted to isothermal behavior.

Seven materials constants are a_0 , k_0 , B , n_0 , n_1 , C , and m . D_0^p is chosen to be 10^6 . The parameters a_0 and k_0 are determined from the experimental yield stress and grain size relation shown in Fig. 7. Only data points yielding positive values of k_0 which means they exhibited a normal Hall–Petch behavior under these grain sizes, are used in the calculation. The initial values of other constants are obtained by using uniaxial test results at different strain rates using the detail procedure as described by Khan and Liang (1999).

The material constants obtained for almost fully dense iron with grain size in nm were $B = 65.103$, $n_0 = 0.1691$, $n_1 = 0.2087$, $C = 0.0172$, and $m = 1.3354$, respectively. This developed constitutive model gives excellent correlations with the experimental response of iron with grain size in nm, as shown in Figs. 7 and 8. The grain size of 10 h milling iron powder was obtained through interpolation within the grain size-milling time experimental data shown in Fig. 2.

6. Conclusions

For the first time, a comprehensive study was made on nanocrystalline materials over a wide range of strain rates (10^{-4} to 10^3 /s). A high energy ball milling–mechanical alloying schedule was used to produce metal powders with grain size in nm. Near fully dense bulk solid specimens which were suitable for static and

dynamic loading experiments were made from the nano-microstructured powder through a well designed room temperature compaction and hot sintering schedule. The nano-ranged grain size of the powder and some of the specimen was examined and verified by using an X-ray diffraction technique.

Compressive tests with different strain rates were performed on near fully dense iron samples with grain size in nm with the quasi-static tests on MTS machine and dynamic tests on SHPB equipment. Compressive tests were also performed on samples with different grain size under the same strain rate. The Hall–Petch relation was found to be valid over a broad grain size range for nanocrystalline iron, but was not applicable once a critical grain size of about 16 nm was reached. The increases in hardness and yield stress, and the decrease of ductility, were significant with the decrease of grain size for nanocrystalline iron. Iron with grain size in nm found to be rate sensitive material having an increased strength and yield stress when the strain rate increased.

The KHL viscoplastic constitutive model was modified to include grain size dependence, work hardening, rate sensitivity and temperature effect to present the behavior of fully compacted nanocrystalline iron. The yield-stress dependence on grain size was introduced through the Hall–Petch relation. The KHL model was based on a coupled effect of strain and strain rate on the work-hardening behavior of the material. The influence of temperature rise in the adiabatic dynamic experiment was considered when predicting the stress/strain response.

A total of seven material constants were required in this model and were determined through experimental results on different strain rates and grain sizes. The model gave a good correlation with both isothermal and adiabatic experimental results.

Acknowledgements

The authors are grateful for the funding of this project by the Army Research Office under cooperative agreement DAAH04-95-2-0004.

References

- Andrievski, R.A., 1994. Compaction and sintering of ultrafine powders. *The International Journal of Powder Metallurgy* 30 (1), 59–66.
- Bonnenfant, D., Mazerolle, F., Suquet, P., 1998. Compaction of powders containing hard inclusions: experiments and micromechanical modeling. *Mechanics of Materials* 29, 93–109.
- Carroll, M.M., Holt, A.C., 1972. Static and dynamic pore-collapse relations for ductile porous materials. *Journal of Applied Physics* 43 (4), 1626–1635.
- Chang, H., Altstetter, C.J., Averbach, R.S., 1992. Characteristics of nanophase tial produced by inert gas condensation. *Journal of Materials Research* 7 (11), 2962–2969.
- Edelstein, A.S., Cammarata, R.C., 1996. In *Nanomaterials: Synthesis, Properties and Applications*. Institute of Physics Publishing, Bristol and Philadelphia, pp. 23–54.
- Fecht, H.J., Hellstern, E., Fu, Z., Johnson, W.L., 1990. Nanocrystalline metals prepared by high-energy ball milling. *Metallurgical Transaction* 21a, 2333.

- Garofalo, F., Wriedt, H.A., 1962. Density change in an austenitic stainless steel deformed in tension or compression. *Acta Metallurgica* 10, 1007.
- Gertsman, V.Y., Hoffmann, M., Gleiter, H., Birringer, R., 1994. The study of grain size dependence of yield stress of Cu for a wide grain size range. *Acta Metallurgica Materials* 42 (10), 3539–3544.
- Gurson, A.L., 1977. Continuum theory of ductile rupture by void nucleation and growth: part I. Yield criteria and flow rules for porous ductile media. *Journal of Engineering Materials and Technology* 99, 2–15.
- Gleiter, H., 1992. Materials with ultrafine microstructures: retrospectives and perspectives. *Nanostructured materials* 1, 1–19.
- Hahn, H., Logas, J., Averback, R.S., 1990. Sintering characteristic of nanocrystalline TiO_2 . *Journal of Materials Research* 5 (3), 609–614.
- Hellstern, E., Fecht, H.J., Fu, Z., Johnson, W.L., 1989. Structural and thermodynamic properties of heavily mechanically deformed Ru and AlRu. *Journal of Applied Physics* 65f, 305–310.
- Hirschhorn, J.S., 1969. *Introduction to Powder Metallurgy*, American Powder Metallurgy Institute, New York.
- Hom, C.L., McMeeking, R.M., 1989. Void growth in elastic-plastic materials. *Journal of Applied Mechanics* 56, 309–317.
- Huang, S., Khan, A.S., 1991. On the use of electrical-resistance metallic foil strain gages for measuring large dynamic plastic deformation. *Experimental Mechanics*, pp. 122–125.
- Jain, M., Christman, T., 1994. Synthesis, processing, and deformation of bulk nanophase Fe-28-2cr intermetallic. *Acta Metallurgica Materials* 42 (6), 1901–1911.
- Khan, A.S., Huang, S., 1992. Experimental and theoretical study of mechanical behavior of aluminum in the strain rate range 10^{-5} – 10^4 . *International Journal of Plasticity* 8, 397–424.
- Khan, A.S., Liang, R., 1999. Behaviors of three BCC metal over a wide range of strain rates and temperatures: experiments and modeling. *International Journal of Plasticity* 15, 1089–1109.
- Khan, A.S., Liang, R., 2000. Behaviors of three BCC metals during non-proportional multi-axial loadings: experiments and modeling. *International Journal of Plasticity* 16, 1443–1458.
- Khan, A.S., Zhang, H., 2000. Mechanically alloyed nanocrystalline iron and copper mixture: behavior and constitutive modeling over a wide range of strain rates. *International Journal of Plasticity*, 16, 1477–1492.
- Kim, K.T., Carroll, M., 1987. Compaction equations for strain hardening porous materials. *International Journal of Plasticity* 3, 67–73.
- Koch, C.C., Shen, T.D., Malow, T., Spaldon, O., 1995. Mechanical hardness as a probe of nanocrystalline materials. *Material Research Society Symposium Proceeding* 362, 253–265.
- Liang, R., Khan, A.S., 1999. A critical review of experimental results and constitutive models for BCC and FCC metals over a wide range of strain rates and temperatures. *International Journal of Plasticity* 15, 963–980.
- Lu, K., 1996a. Thermodynamics and kinetics of the amorphous-to-nanocrystalline transformation In: *Processing and Properties of Nanocrystalline Materials*, p. 23.
- Lu, K., 1996. Nanocrystalline metals crystallized from amorphous solids: nanocrystallization, structure, and properties. *Materials Science and Engineering* 16 (4), 161–221.
- Marin, E.B., McDowell, D.L., 1996. Associative versus non-associative porous viscoplasticity based on internal state variable concepts. *International Journal of Plasticity* 12 (5), 629–669.
- Meyers, M.A., Chen, Y.J., Marquis, F.D.S., Kim, D.S., 1995. High-strain, high-strain-rate behavior of tantalum. *Metallurgical and Materials Transactions A* 26a, 2493–2501.
- Nieman, G.W., Weertman, J.R., Siegel, R.W., 1991. Mechanical behavior of nanocrystalline Cu and Pd. *Journal of Material Research* 6 (5), 1012–1027.
- Pan, J., Saje, M., Needleman, A., 1983. Localization of deformation in rate-sensitive porous plastic solids. *International Journal of Fracture* 21, 261–278.
- Pardavi-Horvath, M., Takacs, L., 1995. Magnetic nanocomposites by reaction milling. *Scripta Metallurgica et Materialia* 33 (10/11), 1731–1740.
- Ranganathan, S., Murty, B.S., Nagarajan, T., Chattopadhyay, K., 1996. In: Suryanarayana, C., Singh, J., Froes, F. H. (Eds.), *Processing and Properties of Nanocrystalline Materials*. The Minerals, Metals and Materials Society, pp. 37–47.

- Sanders, P.G., Eastman, J.A., Weertman, J.R., 1996. Tensile behavior of nanocrystalline Cu. In: Suryanarayana, C., Singh, J., Froes, F.H. (Eds.), *Processing and Properties of Nanocrystalline Materials*, the Minerals, Metals and Materials Society, pp. 379–386.
- Siegel, R.W., Fougere, G.E., 1994. Mechanical properties of nanophase materials. In: Hadjipanayis, G.C., Siegel, R.W. (Eds.), *Nanophase Materials* Kluwer Academic Publishers, pp. 233–261.
- Siegel, R.W., Fougere, G.E., 1995. Grain size dependent mechanical properties in nanophase materials. In: Ottoni, M.A., Armstrong, R.W., Grant, N.J. and Ishizaki, K., (Eds.), *Materials Research Society Symposium Proceedings*, Materials Research Society, pp. 219–229.
- Spitzig, W.A., Smelser, R.E., Richmond, O., 1988. The evolution of damage and fracture in iron compacts with various initial porosities. *Acta Metall.* 36 (5), 1201–1211.
- Tvergaard, V., Needleman, A., 1986. Effect of material rate sensitivity on failure modes in the charpy V-notch test. *Journal of Mechanics and Physics of Solids* 34, 213–241.
- Takacs, L., 1993. Nanocomposite formation and combustion induced by reaction milling. *Material Research Society Symposium Proceeding* 286, 413–418.
- Takacs, L., 1996. Nanocrystalline materials by mechanical alloying and their magnetic properties. In: Suryanarayana, C., Singh, J. Froes, F.H. (Eds.), *Processing and Properties of Nanocrystalline Materials*, the Minerals, Metals, and Materials Society, pp. 453–464.
- Wang, N., Wang, Z., Aust, K.T., Erb, U., 1995. Effect of grain size on mechanical properties on nanocrystalline materials. *Acta Metallurgical Materials* 43, 519–528.



PERGAMON

International Journal of Plasticity 16 (2000) 1477–1492

INTERNATIONAL JOURNAL OF
Plasticity

www.elsevier.com/locate/ijplas

Mechanically alloyed nanocrystalline iron and copper mixture: behavior and constitutive modeling over a wide range of strain rates

Akhtar S. Khan*, Haoyue Zhang¹

*Department of Mechanical Engineering, University of Maryland, ECS Building, 100 Hilltop Circle,
Baltimore County, MD 21250, USA*

Received in final revised form 22 February 2000

Abstract

A comprehensive study on the response of a nanocrystalline iron and copper mixture (80% Fe and 20% Cu) to quasi-static and dynamic loading is performed. The constitutive model developed earlier by Khan, Huang & Liang (KHL) is extended to include the responses of nanocrystalline metallic materials. The strain rate and grain size dependent behaviors of porous nanocrystalline iron-copper mixture were determined experimentally for both static and dynamic loading. A viscoplastic model is formulated by associating the modified KHL model (representing the fully dense matrix behavior), and Gurson's plastic potential which provides the yield criteria for porous material. Simulations of uniaxial compressive deformations of iron-copper mixture with different initial porosity, grain size and at a wide range of strain rate (10^{-4} to 10^3 s⁻¹) are made. The numerical results correlate well with the experimental observations. © 2000 Elsevier Science Ltd. All rights reserved.

Keywords: Nanocrystalline material response; Split-Hopkinson-Bar technique; Viscoplastic response

1. Introduction

Micromechanical models that reflect a porosity and pressure dependent yield criterion are normally used to describe the approximate macroscopic response of the porous material under the applied loading. Theories describing materials with void (Gurson, 1977; Gologanu et al., 1994; Marin and McDowell, 1996) suggest that the yield criterion is not only a function of the second invariant of the deviatoric stress

* Corresponding author. Tel.: +1-410-455-3300; fax: +1-410-455-1052.

¹ Now at Halliburton Engineering Services, Dallas, Texas.

E-mail address: khan@engr.umbc.edu (A. Khan).

tensor, but also a function of the first invariant of the stress tensor, which is the hydrostatic stress, and thus allow plastic volume change through the normality rule. The classical plasticity theory, in which the incompressibility is assumed during plastic deformation, is not suitable for the constitutive modeling of porous materials. A yield criterion and a flow rule for porous ductile materials have to be adopted to show the role of hydrostatic stress in plastic yield and void growth.

The implicit assumption in the continuum treatment of porous material is that the voids with spherical, cylindrical, or ellipsoidal shape are distributed in a homogeneous incompressible matrix of certain properties, such as elastoplasticity, viscoplasticity, etc.. Usually the voids are represented by a scalar internal variable, void volume fraction. Some of the models involving pore medium are evolution equations describing growth of voids in a viscous matrix material (Lee and Mear, 1994), ideally plastic materials (Carroll and Holt, 1972), or time dependent viscoplastic material (Bonnenfant et al., 1998), and not a macroscopic constitutive model for porous ductile material. Hom and McMeeking (1989) studied the growth of initially spherical voids and interaction between neighboring voids through three-dimensional finite element computations. Spitzig et al. (1988) modified Gurson's model to predict the compressive and tensile behavior of iron compacts of various initial porosity and the evolution of porosity, pore size and pore shape. Kim and Carroll (1987) developed a theoretical compaction equation through a hollow sphere model for strain hardening porous materials. Marin and McDowell (1996) studied the role of specific void growth models in both associative and non-associative viscoplastic flow rules and established a general constitutive framework for porous viscoplasticity.

The plastic response of a material containing microscopic voids has been modeled by Gurson (1977). In the Gurson's model, an approximate yield criterion in the form of Eq. (1), for hydrostatic pressure sensitive ductile porous materials, was introduced and the matrix material was idealized as rigid-perfectly plastic and obeying the von Mises yield criterion.

$$\Phi(\sigma_e, \sigma_M, f) = 0 \quad (1)$$

Here σ_e is the average macroscopic Cauchy stress tensor, σ_M is an equivalent tensile flow stress representing the actual microscopic stress state in the matrix material, and f is the current void volume fraction. It has been modified in later years to account for voids interactions and rate-sensitivity (Tvergaard, 1981; Tvergaard and Needleman, 1986).

Generally, in most of the modified versions of Gurson model, the yield function has been extended to the form

$$\phi = \frac{\sigma_e^2}{\sigma_M^2} + 2q_1 f^* \cos h\left(\frac{\sigma_{kk}}{2\sigma_M}\right) - (1 + (q_3 f^*)^2) = 0 \quad (2)$$

where σ_M is microscopic effective stress of the matrix material without pores, through which different matrix behavior is associated into Gurson's plastic potential. σ_e is the macroscopic effective stress, σ_{kk} is the macroscopic hydrostatic stress, and f^*

is a function of the void volume fraction f , as suggested by Tvergaard and Needleman (1984) to provide a better representation of the drastic loss of stress-carrying capacity associated with void coalescence when f^* is greater than a critical value f_c . The parameters q_1 , q_2 and q_3 are introduced to bring predictions of the model into closer agreement with numerical analyses (Tvergaard, 1981, 1987), representing the effect of the nonhomogeneous stress field around the voids and the interaction of the neighboring voids. The values $q_1 = q_2 = q_3 = 1$ and $f^* = f$ correspond to the original Gurson model. As compared to other models, the Gurson model has a simpler form and a fewer number of material constants.

Even though the Gurson model and its modified versions have been used quite frequently to model the behavior in porous ductile material, there have not been any comparisons of the predictions based on these models with experiments on porous ductile materials. Also the constitutive modeling of nanocrystalline material is lacking due to the absence of extensive experimental studies on these materials, especially at high strain rates. The experiments and modeling in this investigation fill this void.

In this paper, experiments on nanocrystalline iron-copper mixture Fe80Cu20 (80% iron and 20% copper in weight) at a wide range of strain rates are performed. The response of nano-Fe80Cu20 under different initial porosity at high strain rates are also included. A rate-dependent extension of the Gurson model, which includes porosity and strain rate effects, is proposed. The mechanical behavior of the fully dense matrix is assumed to represent the constitutive behavior of the matrix for the porous materials, as discussed in Khan et al. (2000). The void volume fraction is assumed to be sufficient in describing the porosity effect. Only compressive deformations are considered, so that void shrinkage, rather than void growth, is the microstructural evolution of interest. The correlation between the proposed model and experimental results for nano-Fe80Cu20 is examined for deformation at a wide range of strain rates and grain size in the nano-range.

2. Experimental procedures

Iron (98.5% purity) powder and copper (99% purity) powder were used to produce the nanocrystalline mixtures with the weight ratios of 80% iron and 20% copper. The initial powder property, milling condition, milling schedule, equipment and processing procedures are the same as those used in the milling of pure iron and pure copper powder, as reported in Khan et al. (2000).

The Fe80Cu20 mixture powder with the grain size in the nano-range were made into bulk solid specimen through cold compaction and hot sintering. The pressing schedule, equipment and processing procedure were the same as those used in the compaction and sintering of pure iron and pure copper specimen, as discussed in Khan et al. (2000). In order to study the porosity effect on the mechanical behavior on nanocrystalline material, specimens with larger porosity were obtained by reducing the pressing load during both cold and hot compaction.

The grain size was analyzed through X-ray diffraction. The Vickers microhardness was measured using Buehler Micromet I microhardness tester. The quasi-static

loading experiments, with the strain rates from 10^{-4} to $10^0/s$ were preformed on MTS 809 Axial/Torsion Material Test System. The dynamic response with the strain rates up to $10^3/s$ were determined using Split Hopkinson Pressure Bar (SHPB) technique and Direct Disc Impact (DDI) technique. The details of these experimental techniques are given in Khan and Huang (1992) and Liang and Khan (1999).

The initial relative density of the specimen was measured by using the water-immersion method. In order to determine the porosity evolution under uniaxial compressive plastic deformation, the relative density of different specimen with different final strains were measured. The density measurement was also used to determine the plastic compressibility. Several specimens were compressed to varying true plastic strains at a particular strain rate, and then the relative density of the deformed specimen was measured using the well known water-immersion method based on Archimedes' principle

3. Experimental results and discussions

The X-Ray diffraction analysis on Fe80Cu20 powder indicated that the grain size of iron was around 35 nm after 10 hours of milling, and about 23 nm after 15 hours milling. The particle size of copper could not be determined since copper was dissolved into iron during the mechanical alloying. The analysis of Fe80Cu20 solid mixture samples gave a grain size of only iron particles between 60 and 100 nm. However, the broadening of the peak was not large enough for accurate size determination for individual iron and copper particles, even though the copper was separated from iron after the hot sintering and annealing. Thus the particle size increased during sintering and annealing, but it was still in nano-range.

Fig. 1(a) shows the increase of relative density during compressive deformation of Fe80Cu20 samples with different initial porosity. Only two data points are shown since only initial and final densities were measured. The decrease in porosity due to compressive plastic deformation for each specimen is given in Fig. 1(b). These samples were made from powder after 10 h or 15 h milling, and were subjected to plastic deformation at an average strain rate of $10^{-2}/s$. The porosity decrease with strain during compressive deformation, is represented by a linear approximation, $f = f_0 - 0.131\epsilon_a^p$, where f_0 is the initial porosity of the sample, ϵ_a^p is the axial plastic deformation of the cylindrical specimen subjected to uniaxial compressive loading. Combined with other experimental results, this experimental evaluation of porosity evolution was used to convert the macroscopic response of porous material into pore free "matrix" response for determining the material constants in the proposed constitutive equation.

The variation of Young's modulus E of specimen with different initial porosity is shown in Fig. 2. For porous nanocrystalline Fe80Cu20, it is observed that Young's modulus decreases with increased porosity. The experimental data are approximated by a linear dependence of the Young's modulus on the porosity. The linear relationship is indicated in Fig. (2), $E/E_0 = 1 - 3f$, where E_0 is the Young's modulus for fully dense Fe80Cu20 and f is the porosity. A linear approximation is typical in existing literature (Spitzig et al., 1988, Zhang, 1988).

The stress–strain curves of Fe80Cu20 with different initial porosity, and at the strain rates of 0.0001, 0.01, 1 and 2700 /s, are shown in Fig. 3. The samples were made from powder after 10 h milling. A work hardening and strain rate dependent behavior is obvious for this porous nanocrystalline Fe80Cu20. It should be mentioned here that the experimental data at lower strain values using SHPB technique (2700 /s) are not valid. The porosity influence on the response under dynamic loading is shown in Fig. 4, the decrease in material strength due to the increase of porosity is obvious. Note again that the experimental data at small levels of strain are not accurate in the Split Hopkinson Pressure Bar technique since the stress balance in the specimen is not achieved before elastic–plastic waves are reflected several times from the disc specimen boundaries. Hence the Young's modulus and yield stress dependence on porosity can not be inferred from the dynamic experimental results. The strain rate dependent behavior of Fe80Cu20 is

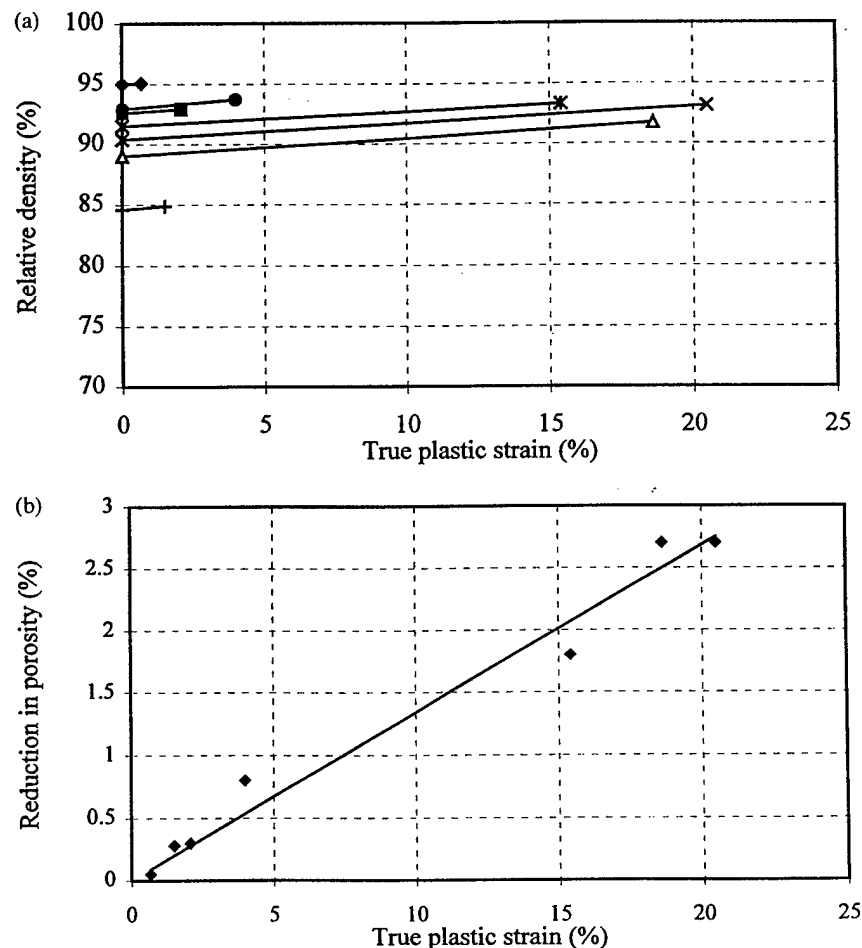


Fig. 1. (a) Relative density of individual Fe80Cu20 samples before and after certain amount of plastic deformation. (b) Porosity changes vs. true plastic strain.

illustrated in Figs. 3 and 5. These curves (Fig. 5) are using specimens from powder after 15 h milling. Fig. 6 has been obtained by comparing the experimental data in Figs. 4 and 5 showing the effect of grain size on the dynamic response of this material.

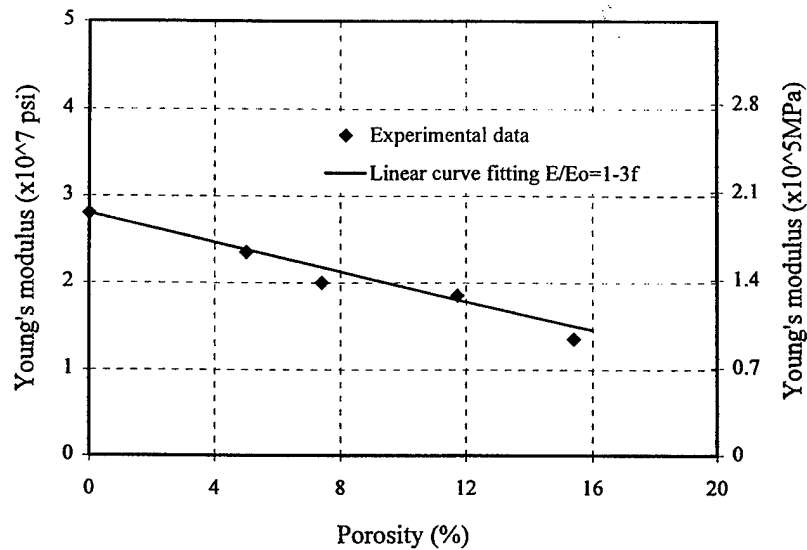


Fig. 2. Young's modulus of Fe80Cu20 samples with various initial porosity from powders after 15 h milling.

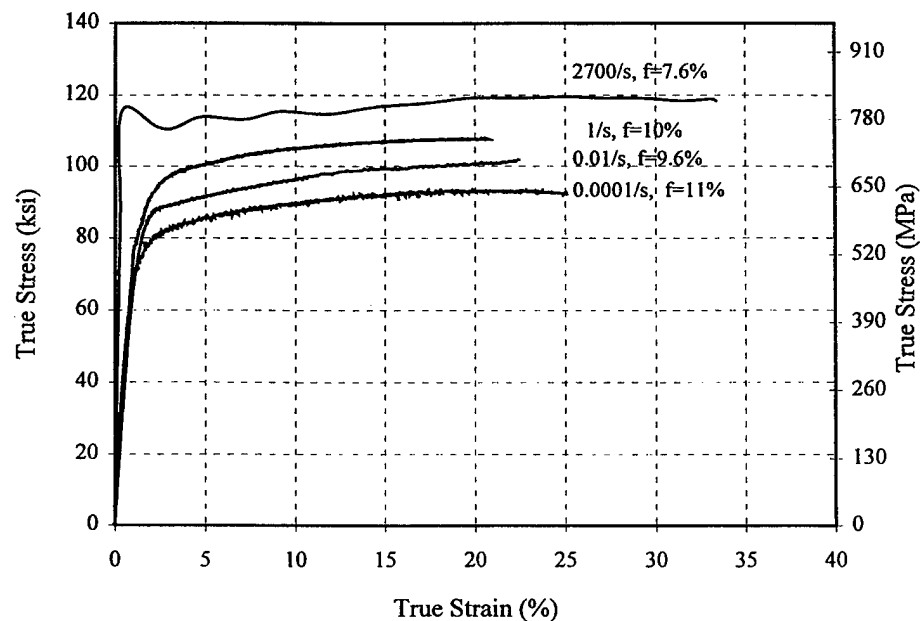


Fig. 3. Stress-strain response of Fe80Cu20 with different initial porosity at strain rates of 0.0001, 0.01 and 2700/s. The samples were made from powder after 10 h milling.

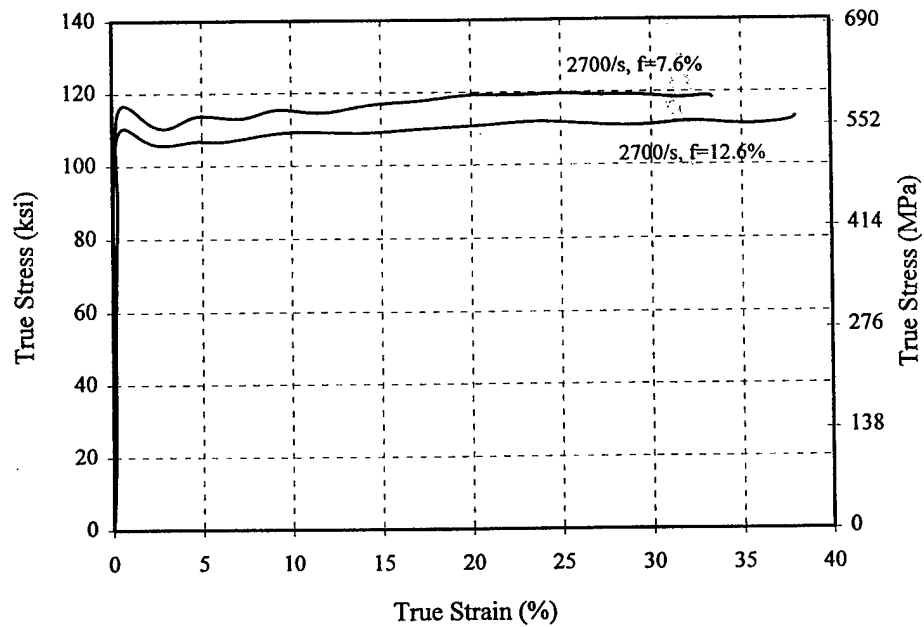


Fig. 4. Stress-strain response of Fe80Cu20 with initial porosities of 7.6% and 12.6%, at a strain rate of 2700/s. The samples were made from powders after 10 h milling.

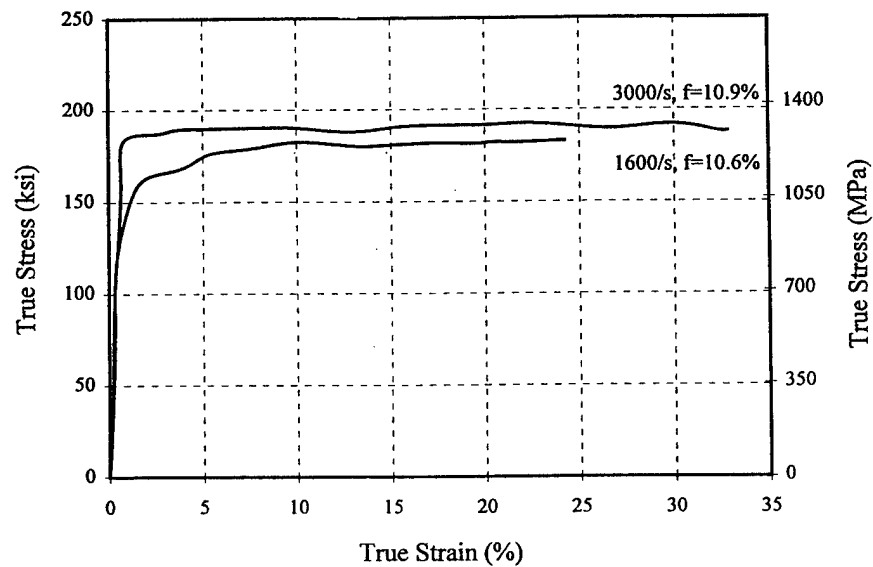


Fig. 5. Stress-strain response of Fe80Cu20 at strain rates of 1600 and 3000/s. The samples were made from powder after 15 h milling.

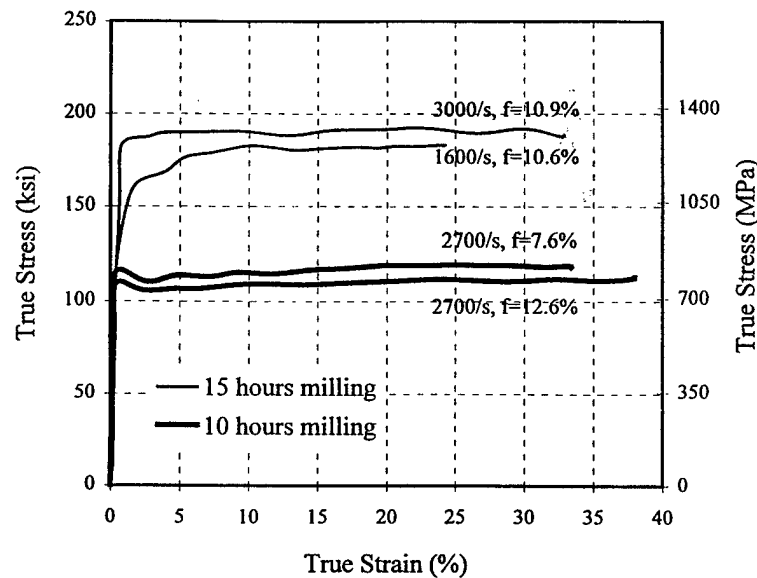


Fig. 6. The effect of grain size on the dynamic response of nanocrystalline Fe80Cu20.

4. Constitutive modeling and correlation with experimental results

The mechanical behavior of nanocrystalline Fe80Cu20 is studied at a wide range of strain rates (10^{-4} to $10^3/s$) and with varying porosity. Only compressive deformation is considered here. The porous nanocrystalline material is represented by a macroscopic volume containing a random distribution of spherical voids. The solid surrounding the void, which is designated as the matrix material, is idealized as initially isotropic, homogeneous, incompressible and viscoplastic. The compressibility at the macroscopic level, is completely due to void growth or shrinkage. The adjective “macroscopic” refers to average values of physical quantities (stress, strain, etc.) which represent the actual mechanical behavior, while the adjective “microscopic” refers to the physical quantities in the matrix material. The macroscopic stress, strain and rate of deformation are denoted by σ_{ij} , ϵ_{ij} and D_{ij} , respectively. The corresponding microscopic stress, strain and rate of deformation are σ_M , ϵ_M and $\dot{\epsilon}_M$ in the matrix material, respectively.

The general method used here to model the void-matrix aggregate is as follows. The model developed earlier by Khan, Huang and Liang (KHL) is used to characterize the microscopic yield and flow behavior of the matrix. This viscoplastic model is then combined with Gurson’s approximate yield function and criteria for porous materials to present the macroscopic stress strain relation. The void will grow while yielding with a positive hydrostatic component of macroscopic stress. The porosity of the nanocrystalline solid is characterized by a scalar void volume fraction f , which is related to the relative density by Eq. (3). It is assumed that the void volume fraction is a sufficient measure of the influence of porosity, the shape and size evolution of the pore is not included in this investigation. The evolution of

the void volume fraction f during inelastic compressive deformations is primarily due to shrinkage or even the collapse of existing voids. We assume that there is no contribution to the porosity change from nucleation or coalescence of voids because of the compressive state.

The model is intended to accommodate porosity, inelastic strain, strain rates and grain size dependence of the mechanical behavior of this interesting class of materials. The yield stress dependence on grain size, the strain rate sensitivity, the coupled strain and strain-rate effect in work hardening description, and the effect of temperature increase in the material during dynamic adiabatic deformation, are all predicted through the response modeling of matrix material using the KHL model. The fully dense nanocrystalline material response described in a previous paper (Khan et al., 2000) is used to give the response of the matrix, i.e. the microscopic behavior of the solid regions of the porous material.

4.1. Constitutive modeling

The porous plastic constitutive relation suggested by Gurson (1977) is based on a yield condition of the form as given in Eq. (1). The original formulation for the Gurson plastic potential, which also serves as a yield function, is given below.

$$\Phi = \frac{\sigma_e^2}{\sigma_M^2} + 2f \cosh\left(\frac{\sigma_{kk}}{2\sigma_M}\right) - (1 + f^2) = 0 \quad (3)$$

where $\sigma_{kk} = \delta_{ij}\sigma_{ij}$ is the macroscopic hydrostatic (mean) stress, δ_{ij} is Kroneker delta. If in terms of the stress deviator $\sigma'_{ij} = \sigma_{ij} - \frac{1}{3}\sigma_{kk}$, the macroscopic effective stress σ_e is $\sigma_e = (\frac{3}{2}\sigma'_{ij}\sigma'_{ij})^{1/2}$. f is the void volume fraction, σ_M is the microscopic effective stress of the matrix through which the material hardening, rate sensitivity, and other properties are described.

The macroscopic rate of deformation tensor, D_{ij} , is written as the sum of an elastic part and a viscoplastic part:

$$D_{ij} = D_{ij}^e + D_{ij}^{vp} \quad (4)$$

Assuming the elastic part of the rate of deformation still follows the generalized Hookes law

$$D_{ij}^e = \frac{1+\nu}{E} \dot{\sigma}_{ij} - \frac{\nu}{E} \delta_{ij} \dot{\sigma}_{kk} \quad (5)$$

and the viscoplastic part of rate of deformation follows the normality rule

$$D_{ij}^{vp} = \Lambda \frac{\partial \Phi}{\partial \sigma_{ij}} \quad (6)$$

Where Gurson's yield function serves as the plastic potential function whose partial differentials in stress space give the plastic strain rate direction. Λ is a proportionality

factor. Assuming the equivalence of macroscopic and microscopic plastic work rate, the microscopic stress and strain rate are related to microscopic stress and strain rate

$$(1-f)\sigma_M \dot{\epsilon}_M^p = \sigma_{ij} D_{ij}^{vp} \quad (7)$$

The elastic–viscoplastic response of the matrix of this porous nanocrystalline material is now modeled by using the modified KHL equation (Khan and Liang, 1999, 2000)

$$\sigma_M = [\sigma_0 + B(1 - \frac{\ln \dot{\epsilon}_M}{\ln D_0^p})^{n_1} \epsilon_M^{n_0}] (\dot{\epsilon}_M)^C (1 - T^{*m}) \quad (8a)$$

$$T^* = (T - T_r) / (T_m - T_r) \quad (8b)$$

when σ_M , ϵ_M and $\dot{\epsilon}_M$ are microscopic von Mises equivalent stress, strain, and strain rate, respectively, in the matrix material. T is the absolute temperature, T_m is the melting temperature of the material and T_r is a reference temperature. σ_0 , B , n_0 , n_1 , C , and m are material constants.

The temperature increase in the material during high strain rate deformation is calculated by using the assumption that 90% of the work of deformation is converted to heat during the adiabatic process

$$\Delta T = \frac{0.9}{\rho C_p} \int_0^\epsilon \sigma(\epsilon) d\epsilon \quad (9)$$

where ρ is density and C_p is the heat capacity of the material.

In the original Gurson model, the rate of increase of void volume fraction is the sum of the growth rate of original voids and the nucleation rate of the new voids,

$$\dot{f} = \dot{f}_{\text{growth}} + \dot{f}_{\text{nucleation}}$$

In the present study on the nanocrystalline material, it is assumed that there is no contribution to the f change from nucleation or coalescence of voids because of the compressive stress state. The change in porosity is from the shrinkage/growth of existing voids only. The evolution of the void volume fraction during inelastic compressive deformation is primarily due to the shrinkage or collapse of existing voids.

Assuming the matrix material to be incompressible during plastic deformation, the rate of increase of void volume fraction is obtained by

$$\dot{f} = \dot{f}_{\text{growth}} = (1-f) D_{kk}^p \quad (10)$$

For porous materials, the Young's modulus E is dependent on porosity. A linear relation between E and f was assumed for Fe80Cu20 in this study (See Fig. 2)

$$\frac{E}{E_0} = 1 - 3f \quad (11)$$

where E_0 is the Young's modulus for fully dense Fe80Cu20. Eq. (11) is used to describe the material behavior in the elastic region associated with Eq. (5).

4.2. Correlation with uniaxial compressive behavior

Consider the specific problem of uniaxial compressive loading of a porous cylindrical specimen. The macroscopic stress, strain and rate of deformation in the axial direction are denoted by σ_a , ϵ_a , $\dot{\epsilon}_a$, respectively. The corresponding macroscopic stress, strain and rate of deformation in the radial direction are σ_r , ϵ_r , $\dot{\epsilon}_r$. The microscopic stress, strain and rate of deformation, which represent the matrix behavior, are still denoted as σ_M , ϵ_M , $\dot{\epsilon}_M$. Note that the strain controlled uniaxial loading is in the axial direction, while there is no constraint to the deformation in the radius direction.

When a porous cylindrical specimen is subjected to uniaxial loading, the macroscopic variables in Eqs. (3)–(7) are specified as

$$\sigma_{11} = \sigma_a, \sigma_{22} = \sigma_{33} = \sigma_r = 0, \sigma_{kk} = \sigma_a \quad (12)$$

$$D_{11} = \dot{\epsilon}_a, D_{22} = D_{33} = \dot{\epsilon}_r \quad (13)$$

$$D_{kk}^p = \dot{\epsilon}_a^p + 2\dot{\epsilon}_r^p \quad (14)$$

The macroscopic rate of deformation is now written in a component form

$$\dot{\epsilon}_a = \frac{\dot{\sigma}_a}{E} + \dot{\epsilon}_a^p, \dot{\epsilon}_r = -\frac{\nu}{E} \dot{\sigma}_a + \dot{\epsilon}_r^p \quad (15)$$

$$\begin{aligned} \dot{\epsilon}_a^p &= \frac{\Lambda}{\sigma_M} \left(\frac{2\sigma_a}{\sigma_M} + f \sin h \left(\frac{\sigma_a}{2\sigma_M} \right) \right) \\ \dot{\epsilon}_r^p &= \frac{\Lambda}{\sigma_M} \left(-\frac{\sigma_a}{\sigma_M} + f \sin h \left(\frac{\sigma_a}{2\sigma_M} \right) \right) \end{aligned} \quad (16)$$

the proportional factor of flow rule Λ in above equations is given by

$$\Lambda = \frac{1}{2H} (1 - f) \sigma_M \dot{\epsilon}_M^p \quad (17)$$

$$H = (1 + f^2) - 2f \cos h \left(\frac{\sigma_a}{2\sigma_M} \right) + \frac{1}{2} f \left(\frac{\sigma_a}{\sigma_M} \right) \sin h \left(\frac{\sigma_a}{2\sigma_M} \right)$$

The evolution equation of the void volume fraction with respect of macroscopic axial plastic strain is derived from Eqs. (10), (14) and (16)

$$\frac{df}{d\epsilon_a^p} = 3(1 - f) / \left(1 + \frac{2 \frac{\sigma_a}{\sigma_M}}{f \sin h \left(\frac{\sigma_a}{2\sigma_M} \right)} \right) \quad (18)$$

The microscopic plastic strain in the matrix is

$$\dot{\epsilon}_M^p = \frac{\dot{\epsilon}_a^p \sigma_a}{(1-f)\sigma_M} \quad (19)$$

The viscoplastic behavior of the matrix is the same as in Eq. (8).

Eqs. (8)–(19) are used to determine material constants, correlate and predict the uniaxial compressive behavior of nanocrystalline Fe80Cu20 in current research.

4.3. Determination of material constants

The parameters in the constitutive functions are obtained as follows. In Eq. (8), T_m is taken to be 1356 K, which is the lower melting point between iron (1808 K) and copper (1356 K). Room temperature, 298 K, is used as reference temperature, T_r .

The mixture rule is used in the determination of some physical constants of Fe80Cu20 according to the weight ratio. For example, the density ρ for full dense Fe80Cu20 as 8.084 g/cm³ with the 80% contribution from iron (7.87 g/cm³), and 20% from copper (8.94 g/cm³). Following the same rule, it is found that C_p is 0.105 cal/kg in Eq. (9), and Young's modulus is 2.8E7 psi.

There are six parameters in the set of elastic–viscoplastic constitutive equations for porous Fe80Cu20; σ_0 , B , n_0 , n_1 , C , and m , all of them are associated with the viscoplastic matrix description in Eq. (8). These parameters are determined from the experimental response on Fe80Cu20 with different initial porosity under strain rates of 10^{-4} , 10^{-2} , 10^0 and 2700/s. In order to determine the material constants for matrix material, the experimental stress–strain curves on porous specimens have to be converted to the response of matrix with zero porosity. First, obtain the instantaneous porosity during the compressive plastic deformation according to the linear experimental porosity evolution relation as shown in Fig. 1(b). Second, the macroscopic experimental stress and strain response is converted to microscopic matrix stress and strain by using Eqs. (3) and (19). Then using Eq. (8b), the temperature rising in the specimen during the adiabatic dynamic compression process is calculated. Finally, the material constants are determined by the method developed by Khan and Liang (1999) by using the converted experimental stress, strain and temperature data (see also Khan et al., 2000). Since there are only two sets of grain size and yield stress data (10 and 15 h of milling), it is not necessary to establish a reliable relation between yield stress and grain size. In the prediction for Fe80Cu20, the Hall–Petch relation was not incorporated into the constitutive equation. For specimens from powder after 10 h milling (with grain size around 35 nm), the material constants were found to be $\sigma_0 = 70.0$, $B = 51.11$, $n_0 = 0.048$, $n_1 = 1.2968$, $C = 0.0494$, and $m = 0.8975$. For specimens from powder after 15 h milling (with an approximate grain size of 23 nm), only σ_0 changed to $\sigma_0 = 126.0$, other parameters were the same as those determined for samples from powder after 10 h milling.

4.4. Prediction from constitutive model and correlation with experimental results

The experimental stress–strain behavior is compared with predictions from the proposed viscoplastic constitutive model for porous nanocrystalline material in

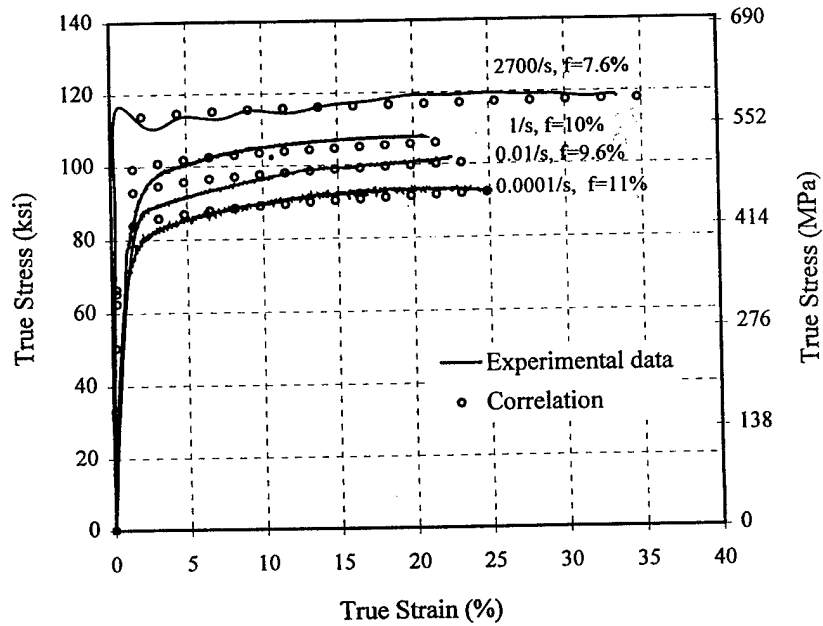


Fig. 7. Stress-strain response for Fe80Cu20 at different strain rates and correlations of the constitutive model.

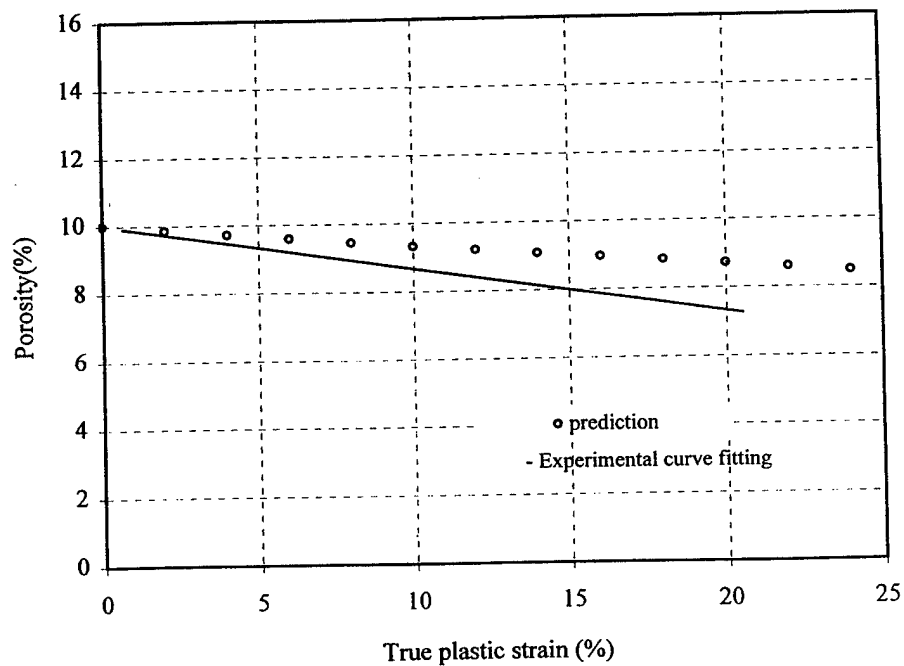


Fig. 8. Comparison between predicted porosity evolution and experimental curve fitting.

which the work hardening, rate sensitivity, porosity effect and grain size effect are reflected.

The comparison between experimental stress–strain response and the prediction for Fe80Cu20 with different initial porosity at strain rates of 0.0001, 0.01, 1 and 2700/s is shown in Fig. 7. Note that the material constants used in this and the following predictions are mainly determined from this set of experimental data. The proposed constitutive model gives reasonably good correlations with the experimental response. However, the work hardening behavior observed in experiment is not well simulated by the model at low strains. This is because the predicted void volume fraction evolution rate is not as accurate as that measured in the experiment, shown in Fig. 8. The similar simulation result from Gurson's plastic potential equation is found in tensile deformation for pure iron compacts (Spitzig et al., 1988), where the predicted void volume fraction also evolves slower than that observed in the experiment. The reason is believed to be that only the initial void volume fraction and the matrix behavior are used in the simulation; the pore geometry is not incorporated into the analysis, which may influence the strength of porous materials.

The predictions of the model on Fe80Cu20 samples with different initial porosity at strain rate of 2700/s are compared to the experimental data in Fig. 9. The samples were made from powder after 10 h milling. The predicted porosity effect on the material strength is in good agreement with the experimental results.

Fig. 10 shows the prediction of the proposed model on Fe80Cu20 samples made from powder after 15 h milling. The strain rate hardening behavior and the grain size effect are well predicted.

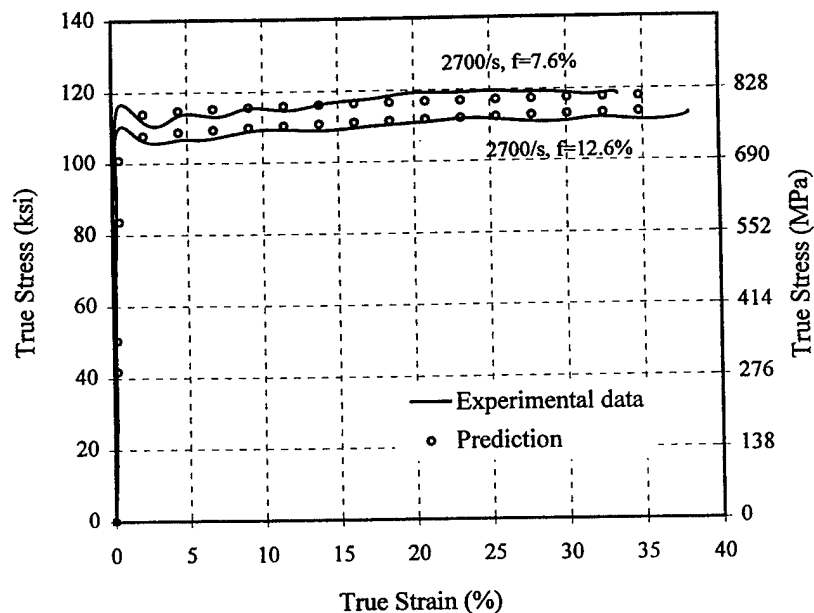


Fig. 9. Comparison of the experimental and predicted stress–strain relation with different initial porosity at strain rate of 2700/s.

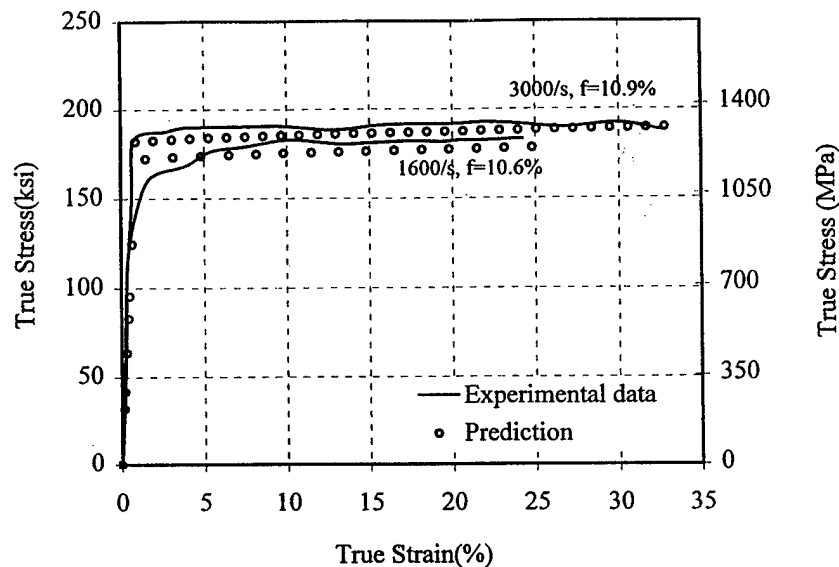


Fig. 10. Comparison of the experimental and predicted stress–strain relation at strain rate of 1600 and 3000/s.

5. Conclusions

A comprehensive study of porous nanocrystalline mechanical mixture was performed for the first time. The rate dependent compressive mechanical property of porous nanocrystalline Fe80Cu20 mixture was measured, and a viscoplastic model was developed by modifying KHL model and combining it to the Gurson's plastic potential to describe the finite deformation of porous nanocrystalline material.

The nanocrystalline Fe80Cu20 response was found to be dependent on strain rate. The yield stress and material strength increased with the decrease of the grain size and increase of strain rate. Porosity had a significant effect on material behavior. Young's modulus and yield stress were found to decrease drastically with the increase of porosity.

The KHL model, valid for finite deformation, was modified to describe the microscopic viscoplastic behavior of the matrix of nanocrystalline Fe80Cu20 at both quasi-static and dynamic strain rates. Gurson's plastic potential was used to establish the yield criteria for porous material. Simulations of uniaxial compressive deformations of Fe80Cu20 with different initial porosity, grain size, and at a wide range of strain rate (10^{-4} – 10^3) were made, the correlations show that the proposed constitutive model provided a reasonable description for porous nanocrystalline Fe80Cu20.

Acknowledgements

The authors are grateful for the funding of this project by the Army Research Office under cooperative agreement DAAH04-95-2-0004.

References

- Bonnenfant, D., Mazerolle, F., Suquet, P., 1998. Compaction of powders containing hard inclusions: experiments and micromechanical modeling. *Mechanics of Materials* 29, 93–109.
- Carroll, M.M., Holt, A.C., 1972. Static and dynamic pore-collapse relations for ductile porous materials. *Journal of Applied Physics* 43 (4), 1626–1635.
- Gologanu, M., Leblond, J.-B., Devaux, D., 1994. Approximate models for ductile metals containing nonspherical voids — case of axisymmetric oblate ellipsoidal cavities. *Journal of Engineering Materials and Technology* 116, 290–297.
- Gurson, A.L., 1977. Continuum theory of ductile rupture by void nucleation and growth: part I. Yield criteria and flow rules for porous ductile media. *Journal of Engineering Materials and Technology* 99, 2–15.
- Hom, C.L., McMeeking, R.M., 1989. Void growth in elastic-plastic materials. *Journal of Applied Mechanics* 56, 309–317.
- Khan, A.S., Huang, S., 1992. Experimental and theoretical study of mechanical behavior of 1100 aluminum in the strain rate range 10^{-5} – 10^4 . *International Journal of Plasticity* 8, 397–424.
- Khan, A.S., Liang, R., 1999. Behaviors of three BCC metal over a wide range of strain rates and temperatures: experiments and modeling. *International Journal of Plasticity* 15, 1089–1109.
- Khan, A.S., Liang, R., 2000. Behaviors of three bcc metals during non-proportional multi-axial loadings: experiments and modeling. *International Journal of Plasticity* 16, 1443–1458.
- Khan, A.S., Zhang, H., Takacs L., 2000. Mechanical response and modeling of fully compacted nanocrystalline iron and copper. *International Journal of Plasticity* 16, 1459–1476.
- Kim, K.T., Carroll, M., 1987. Compaction equations for strain hardening porous materials. *International Journal of Plasticity* 3, 67–73.
- Lee, B.J., Mear, M.E., 1994. Studies of the growth and collapse of voids in viscous solids. *Journal of Engineering Materials and Technology* 116, 348–358.
- Liang, R., Khan, A.S., 1999. A critical review of experimental results and constitutive models for BCC and FCC metals over a wide range of strain rates and temperatures. *International Journal of Plasticity* 15, 963–980.
- Marin, E.B., McDowell, D.L., 1996. Associative versus non-associative porous viscoplasticity based on internal state variable concepts. *International Journal of Plasticity* 12 (5), 629–669.
- Spitzig, W.A., Smelser, R.E., Richmond, O., 1988. The evolution of damage and fracture in iron compacts with various initial porosities. *Acta Metall.* 36 (5), 1201–1211.
- Tvergaard, V., 1981. Influence of voids on shearband instabilities under plane strain conditions. *International Journal of Fracture* 17, 389–407.
- Tvergaard, V., 1987. Effect of yield surface curvature and void nucleation on plastic flow localization. *Journal of the Mechanics and Physics* 35 (1), 43–60.
- Tvergaard, V., Needleman, A., 1986. Effect of material rate sensitivity on failure modes in the charpy V-notch test. *Journal of Mechanics and Physics of Solids* 34, 213–241.
- Zhang, K., 1988. Mesoscopic study of crack tip fracture: stress deformation and void evolution under finite deformation. Study and Application of Mesoscopic Ductile Fracture Mechanics, NPU Press, 75–83 (in Chinese).

High Strain Rate Behavior and Damage Measurements in Glass Reinforced Plastics

Mechanical test and analyses have been systematically conducted in order to characterize the compressive response, failure modes and damage mechanisms of woven S2 – glass reinforced composite, which is plain weave S2 – glass fiber yarns with polyester resin (CYCOM 4102) as binder material. In the first phase of this investigation, the three dimensional macroscopic response of the material was measured under quasi-static uniaxial compressive loading. Fig. 1 gives the orientation of the specimens relative to the geometry of the plate from which the specimens were obtained. The measured variation of the elastic modulus as a function of the angle of the axis in the 1-2 plane and 1-3 plane are shown in Figs. 2 & 3, respectively.

An analytical model was then developed to describe the elastic response of the composite system as function of the constituent material's properties and volume fractions. The model is based on a unit cell representation of the textile composite geometry and thus takes into account the fiber undulation as a characteristic of the weaves and the associated transverse isotropy of the fiber yarns. Quasi – static (i.e. at low to medium strain rates) experiments were performed using the MTS material test system. The uniformity of the material's response was verified by comparing the responses exhibited by different sized and shaped specimens under quasi-static loading. It was found that the overall response was tetragonal, with two of the three orthotropic principal moduli being equal in magnitude. Figs. 4-6 show a comparison of the predicted elastic moduli as a function of fiber yarn volume fraction, with the experimental results for one fiber yarn volume fraction.

In the second phase of this study, the failure modes and dynamic compressive responses of the material were characterized from experimental observations. Compression strength tests were performed, and scanning electron microscopy studies of the fractured specimen surfaces were conducted. The failure modes are complex involving a combination of failure mechanisms. The failure stresses and strains along the ply lay-up direction were higher than those along the plane of the lamina. In Figs. 7 and 8, the failure stress is shown as a function of the orientation of the test sample in 1-2 and 1-3 planes. The dynamic response of the material was determined using both the split Hopkinson pressure bar and the direct disk impact techniques. In the latter method, the disc is impacted directly with the projectile and there is no incidence bar. The material was found to be significantly strain rate sensitive (see Fig. 9).

The damage due to repeated compressive loading of multi-loading woven composite material was examined in the final phase of this investigation. This damage was assessed via macroscopic stress – strain response, the acoustic emission analysis, and scanning electron microscopy. The latter two techniques were employed to identify the damage mechanisms operative at the micro-scale, which enable correlation with the observed macroscopic stress-strain behavior. Acoustic emission, a transient elastic wave generated by the rapid characterizing damage initiation and

propagation. Fig. 10 shows the experimental setup for using the acoustic emission technique for measuring the damage. A normalized acoustic emission count as the function of normalized stress is given in Fig. 11. Based on an extensive set of experimental observations, the damage phenomenon within the material was determined. A dimensionless damage parameter is defined and its evolution is modeled based on the results of these experiments. A damage model was developed. Fig. 12 contains the reduction of elastic moduli as the function of the damage parameter D ; the experimental results are compared with the predictions from the model.

Finally, in an attempt to understand the material's response under triaxial compressive stress state, compression tests under various confined pressures were performed in the laboratory. The experimental arrangement is given in Fig. 13. The material can withstand high hydrostatic pressure and has a low compressibility factor. The material's compressive response was appreciably affected under high confining pressures (see Fig. 14). The compressive strength of the material was significantly higher for increasing confining pressures in the direction perpendicular to the fabric planes; in the other two perpendicular directions, the increase was insignificant.

Scientific Personnel:

In addition to the P.I., Dr. Akhtar S. Khan, a doctoral student, Mr. Prabhakaran K. Centala was supported on the project. Dr. Centala received his Ph.D. degree in 1998 under the sponsorship of this project.

List of Manuscripts published or submitted:

- (i) "Mechanical response and failure modes of woven glass reinforced plastic thick laminate", in Proceed. Of 3rd International Conference on Composite Engineering, New Orleans, USA, July 21-26, 1996.
- (ii) "Dynamic behavior and damage of glass reinforced plastic structural armor", in Proceed. Of 2nd International Symposium on Impact Engineering, Beijing, China, Sept. 2-6, 1996.
- (iii) "Experimental & analytical investigation on the compression response of S2-Glass reinforced polyester thick laminate" in the Proceed. Of 3rd International Conference on Experimental Mechanics, Singapore, Dec. 4-6, 1996.
- (iv) "Dynamic response and damage modeling of woven S2-Glass reinforced polyester" in Physics and Mechanics of Finite Plastic and Viscoplastic Deformation, Edited by A.S. Khan, NEAT Press, Md., 1997.

Inventions:

None.

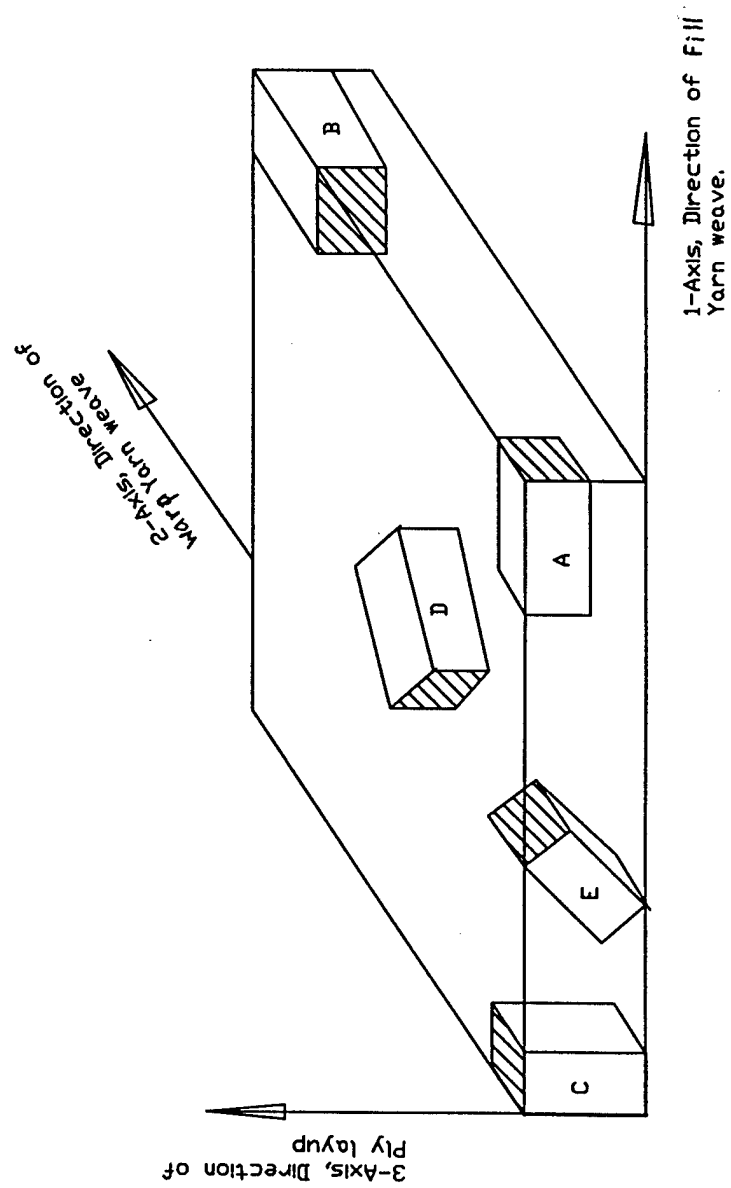


Figure 1 : Coordinate system with specimen orientation

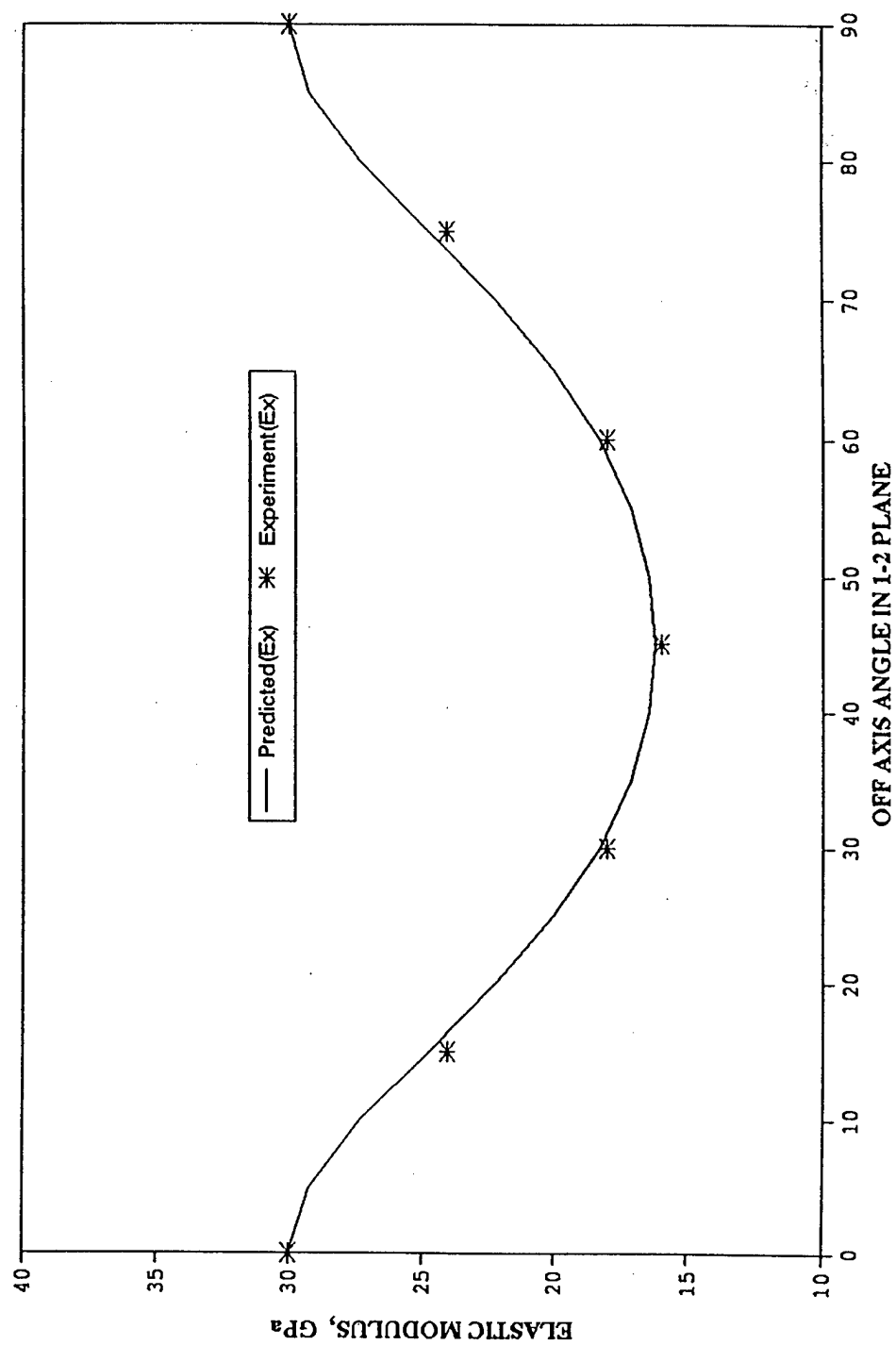


Figure 2 : Variation of elastic moduli with off-axis orientation in 1-2 plane

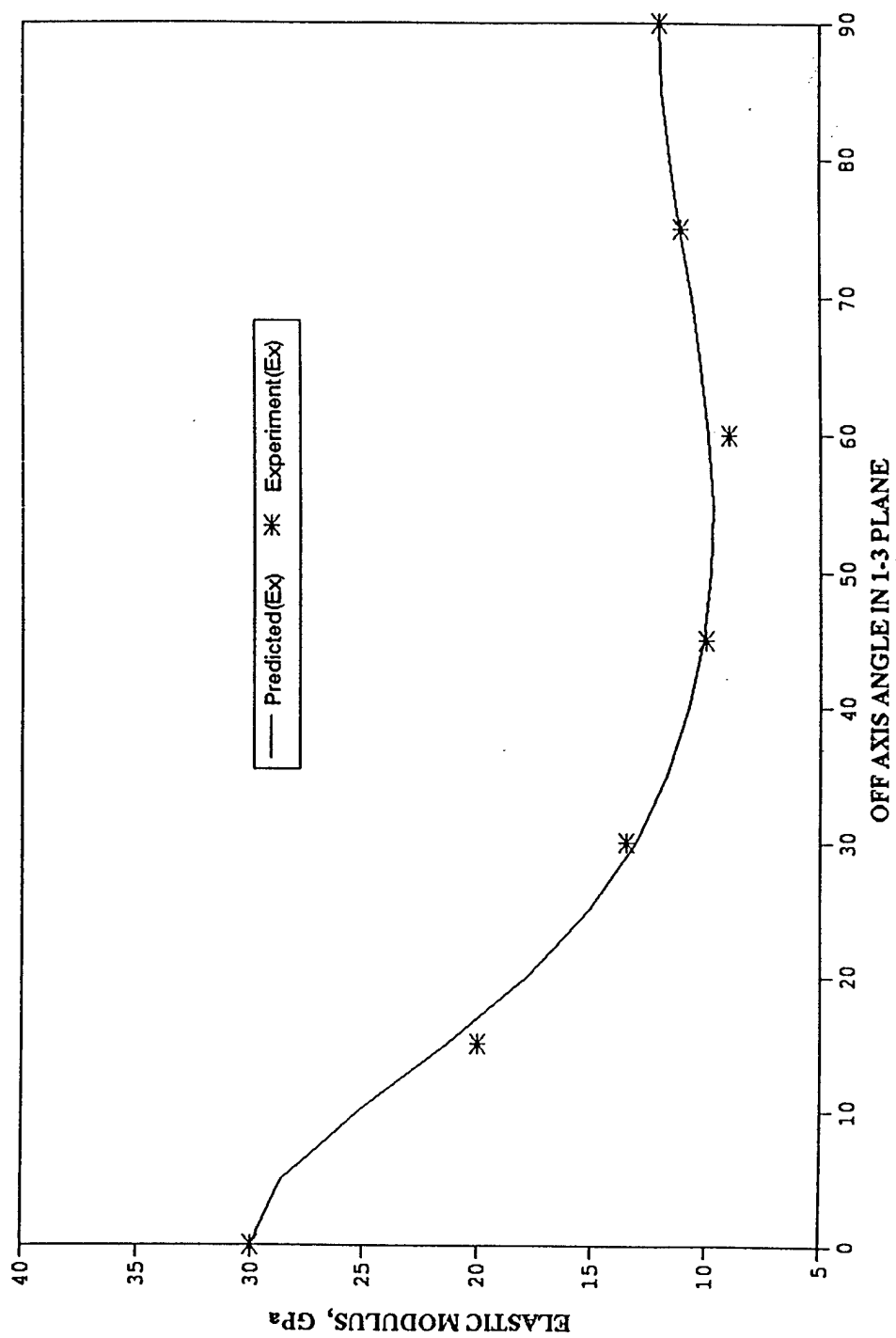


Figure 3 : Variation of elastic modulus with off-axis orientation in 1-3 plane

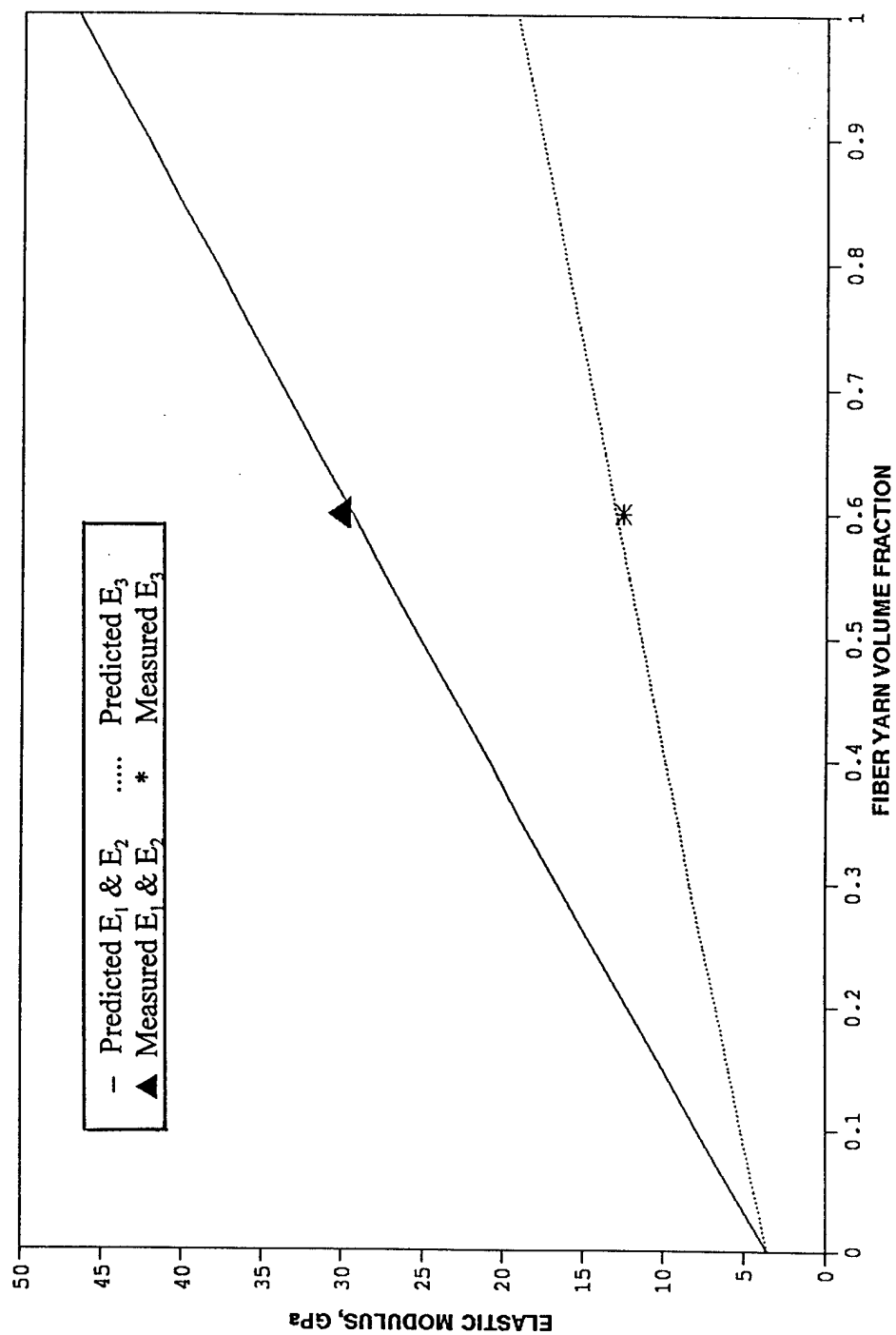


Figure 4 : Elastic moduli variation as a function of fiber yarn volume fraction

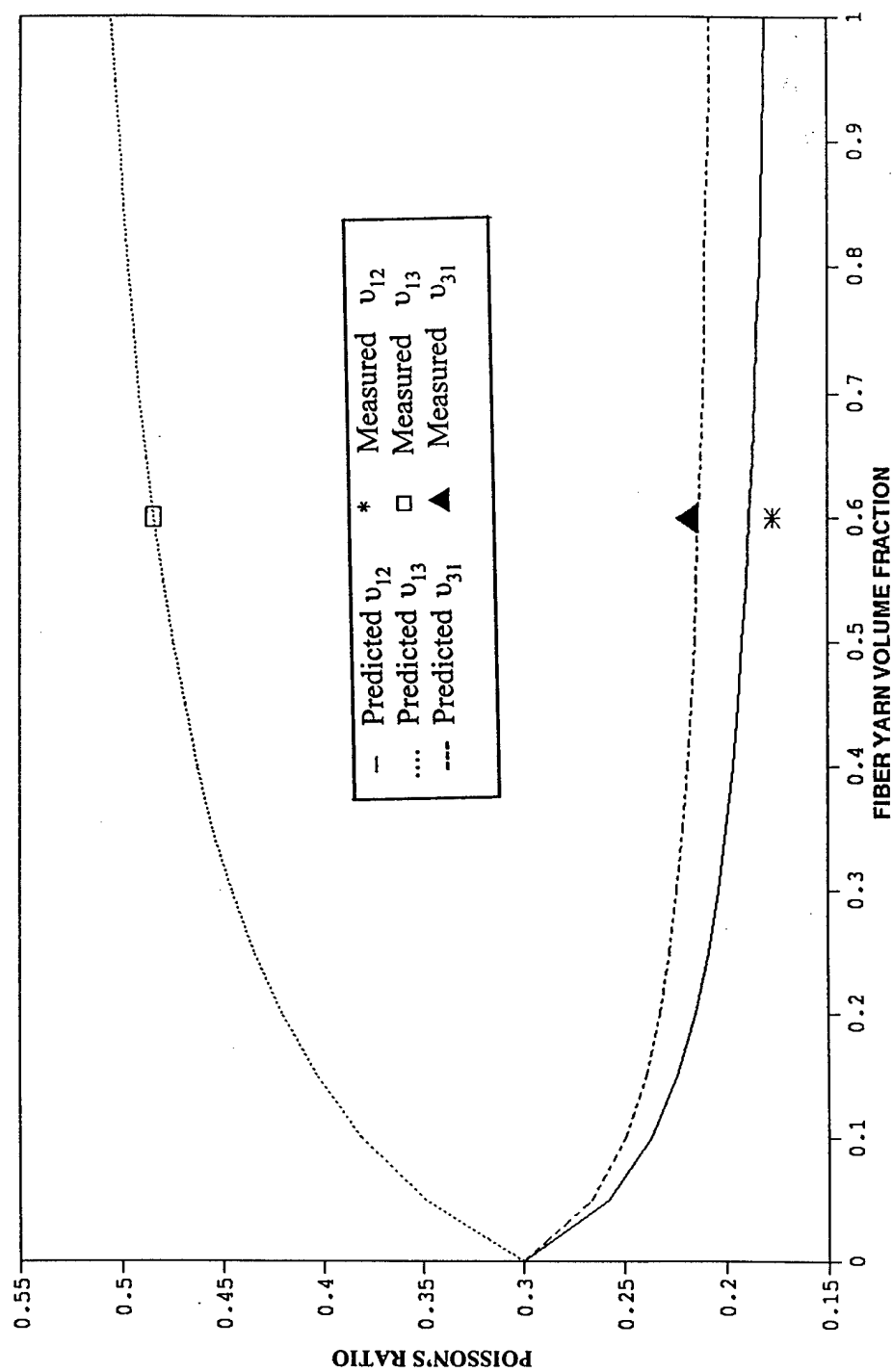


Figure 5 : Elastic moduli variation of a function of fiber yarn volume fraction

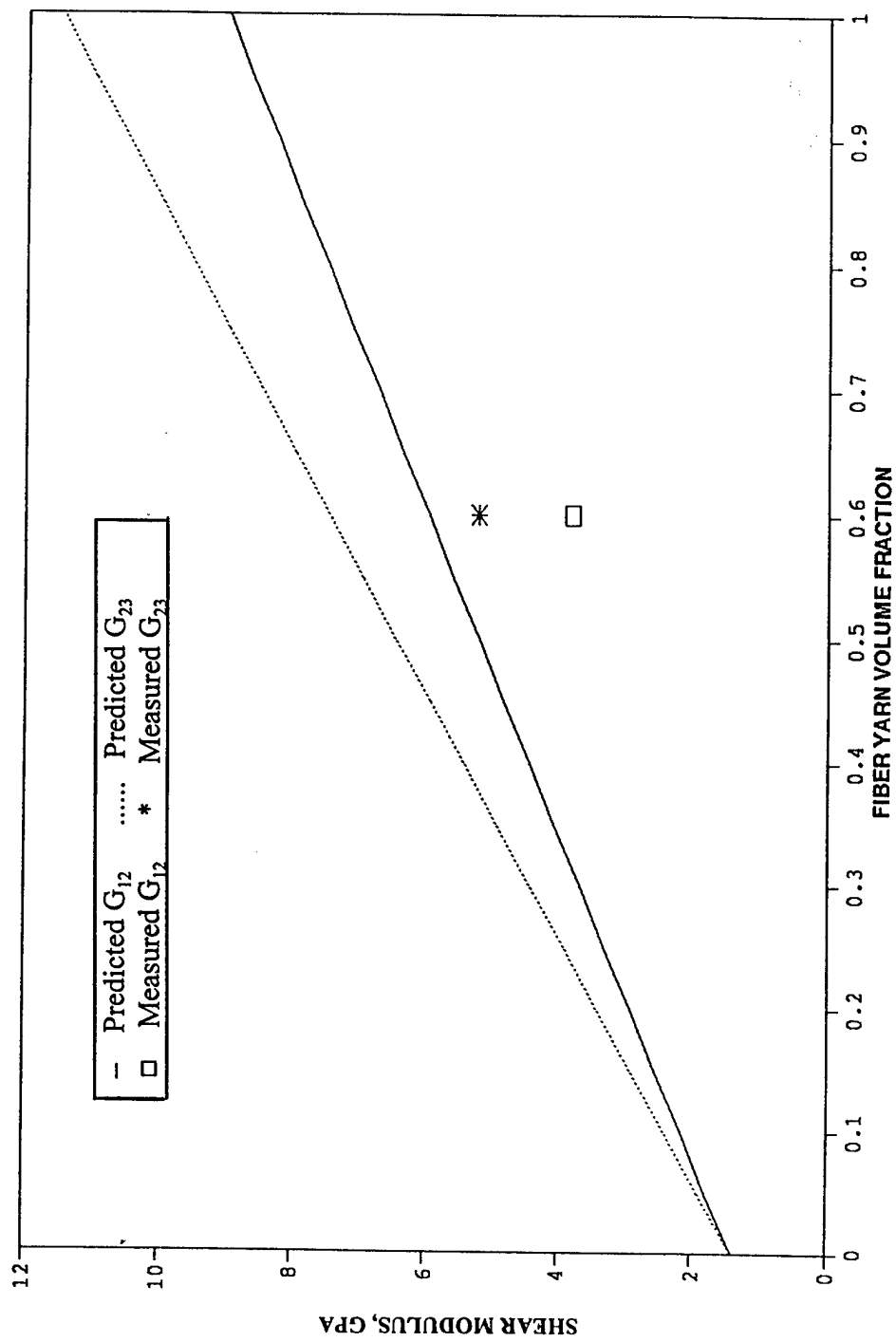


Figure 6 : Shear moduli variation as a function of fiber yarn volume fraction

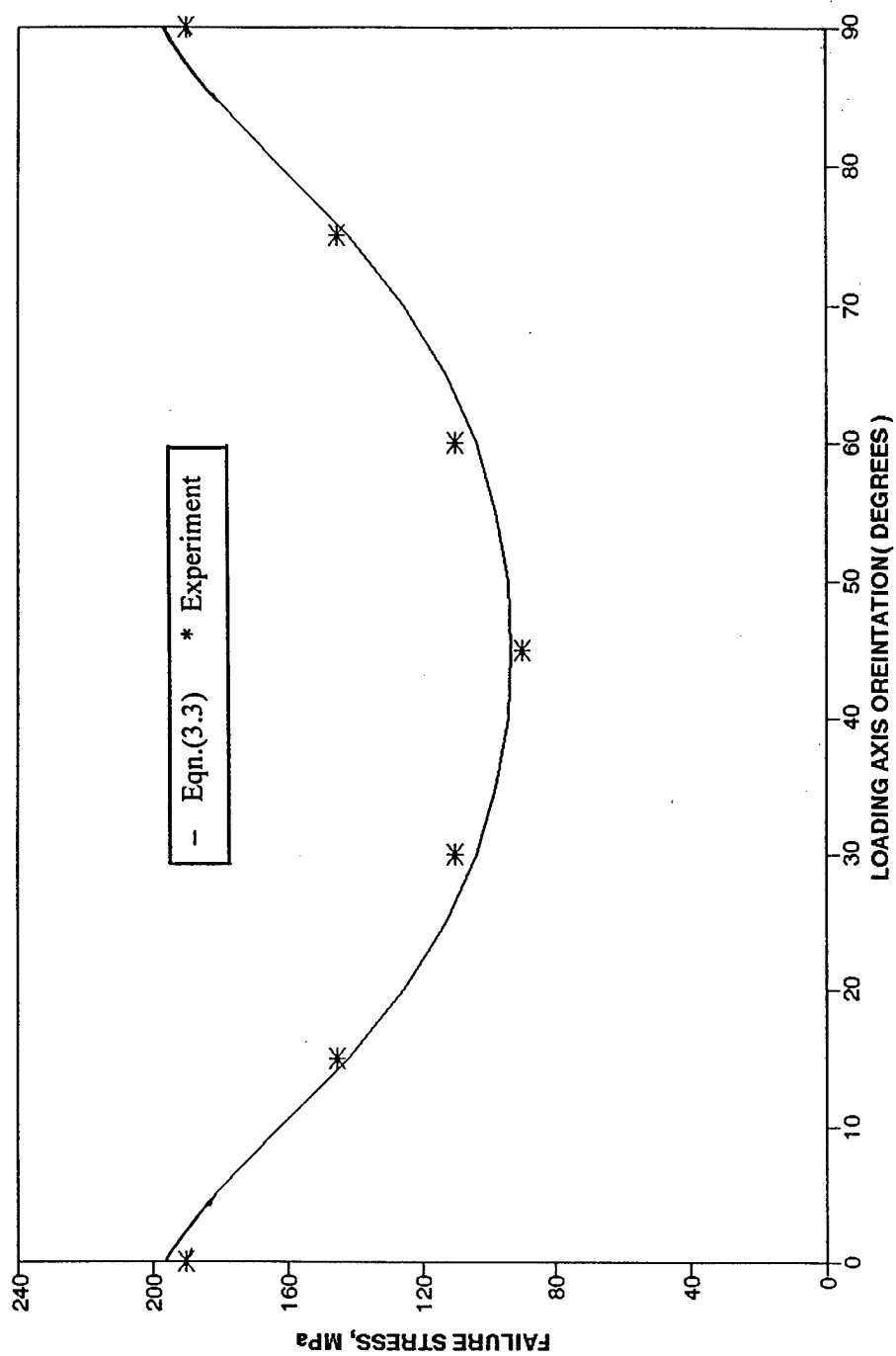


Figure 7 : Off-axis strength of the material in the 1-2 plane and fitting of Eqn.(3.3)

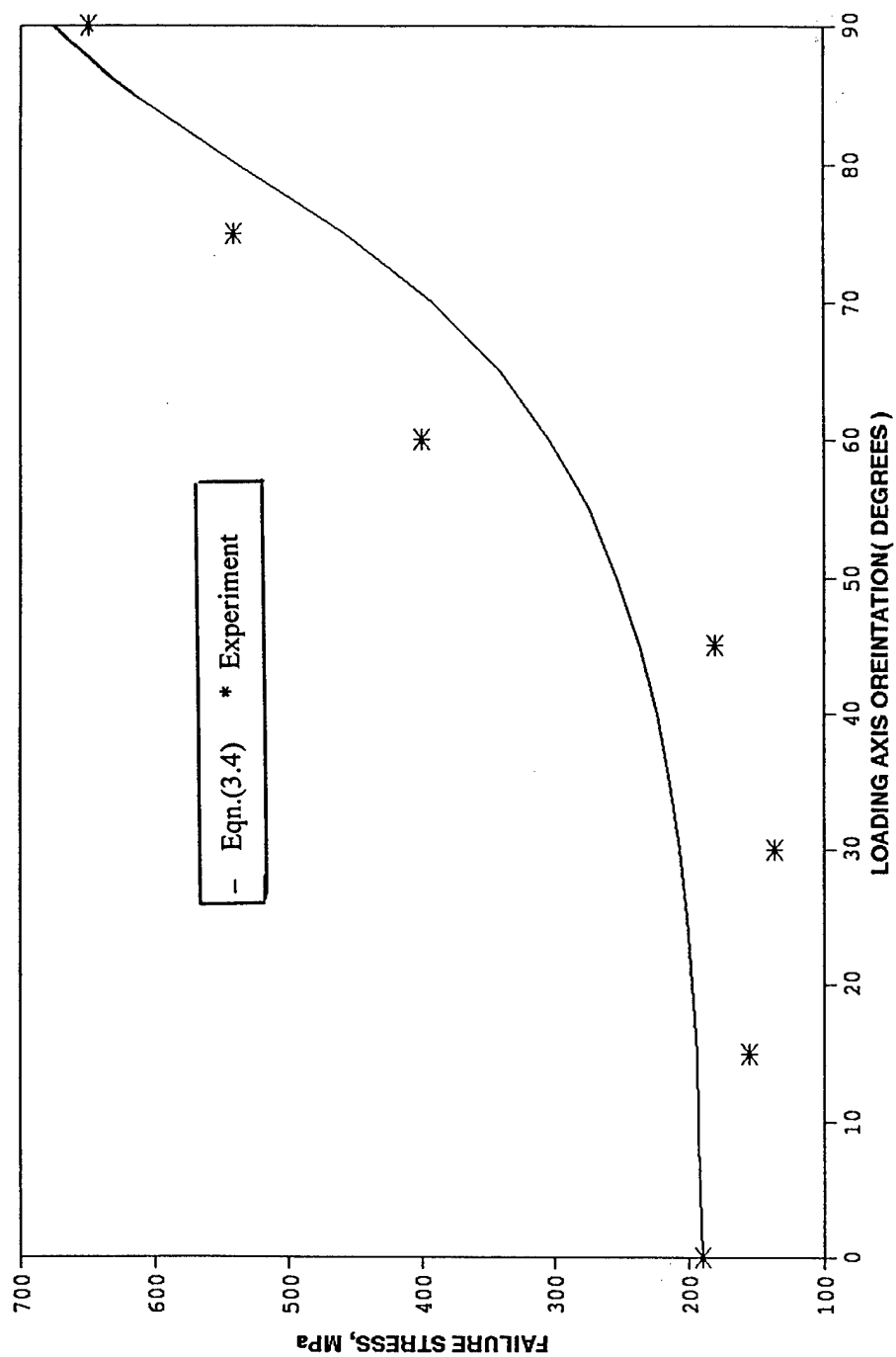


Figure 8 : Off-axis strength of the material in the 1-3 plane and fitting of Eqn.(3.4)

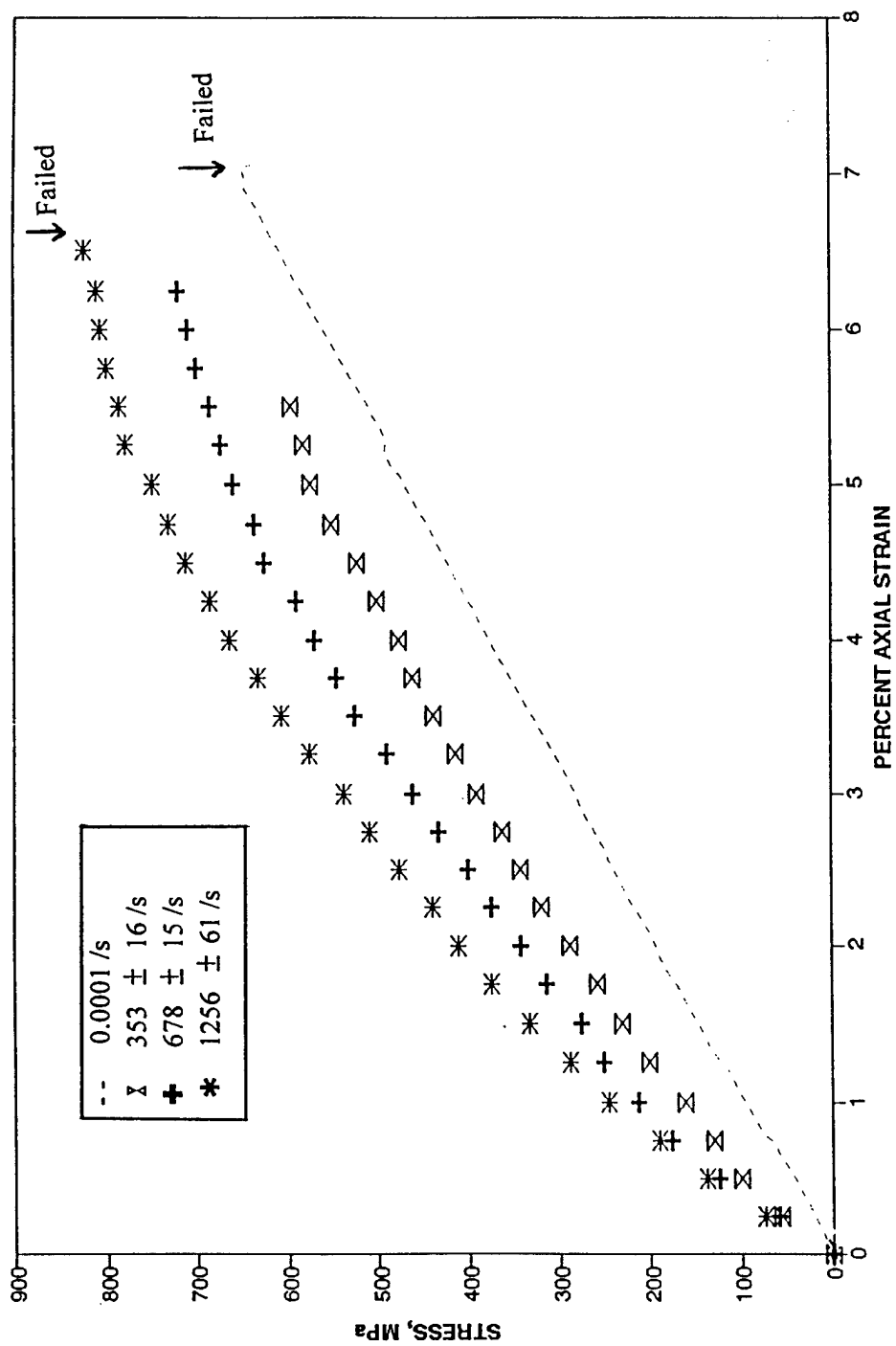


Figure 9 : Dynamic loading response of $\{013 = 90^\circ\}$ orientation specimen from SHPB technique

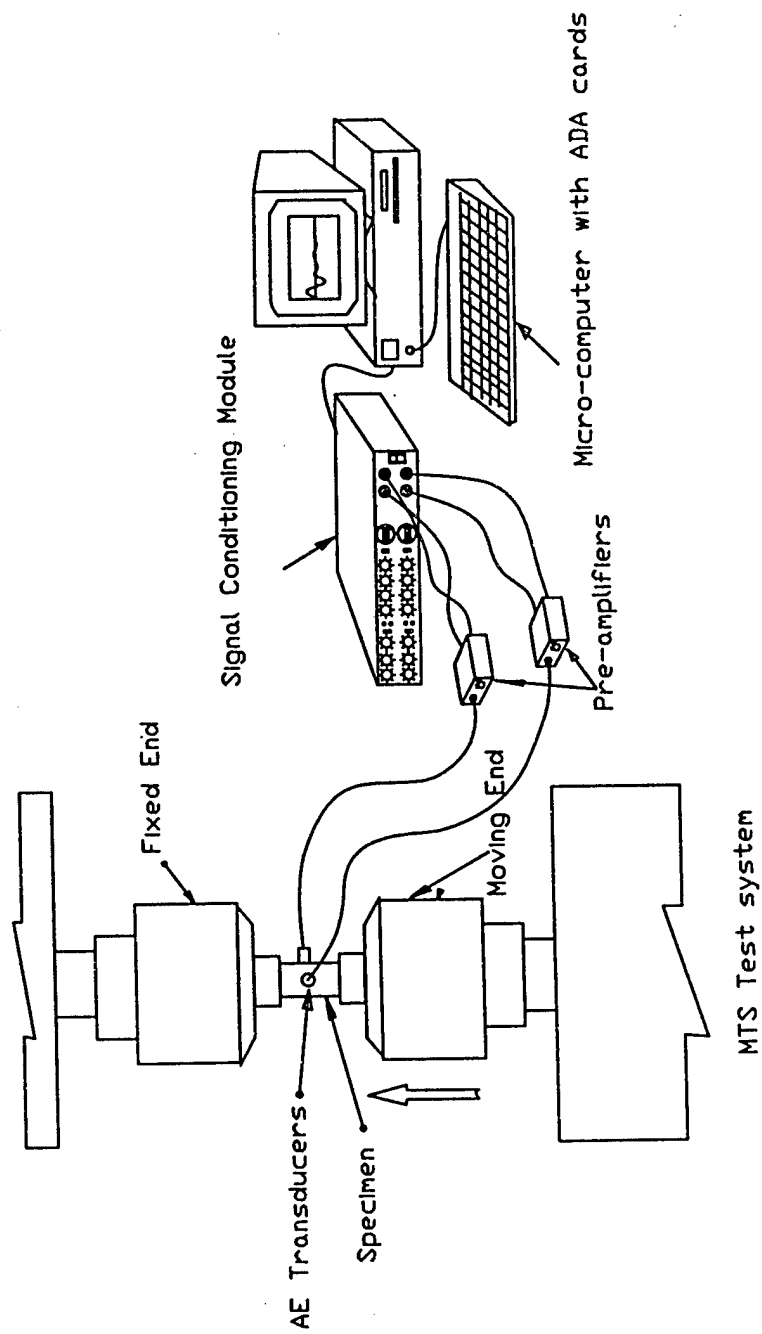


Figure 10: Acoustic emission experimental setup for damage measurements

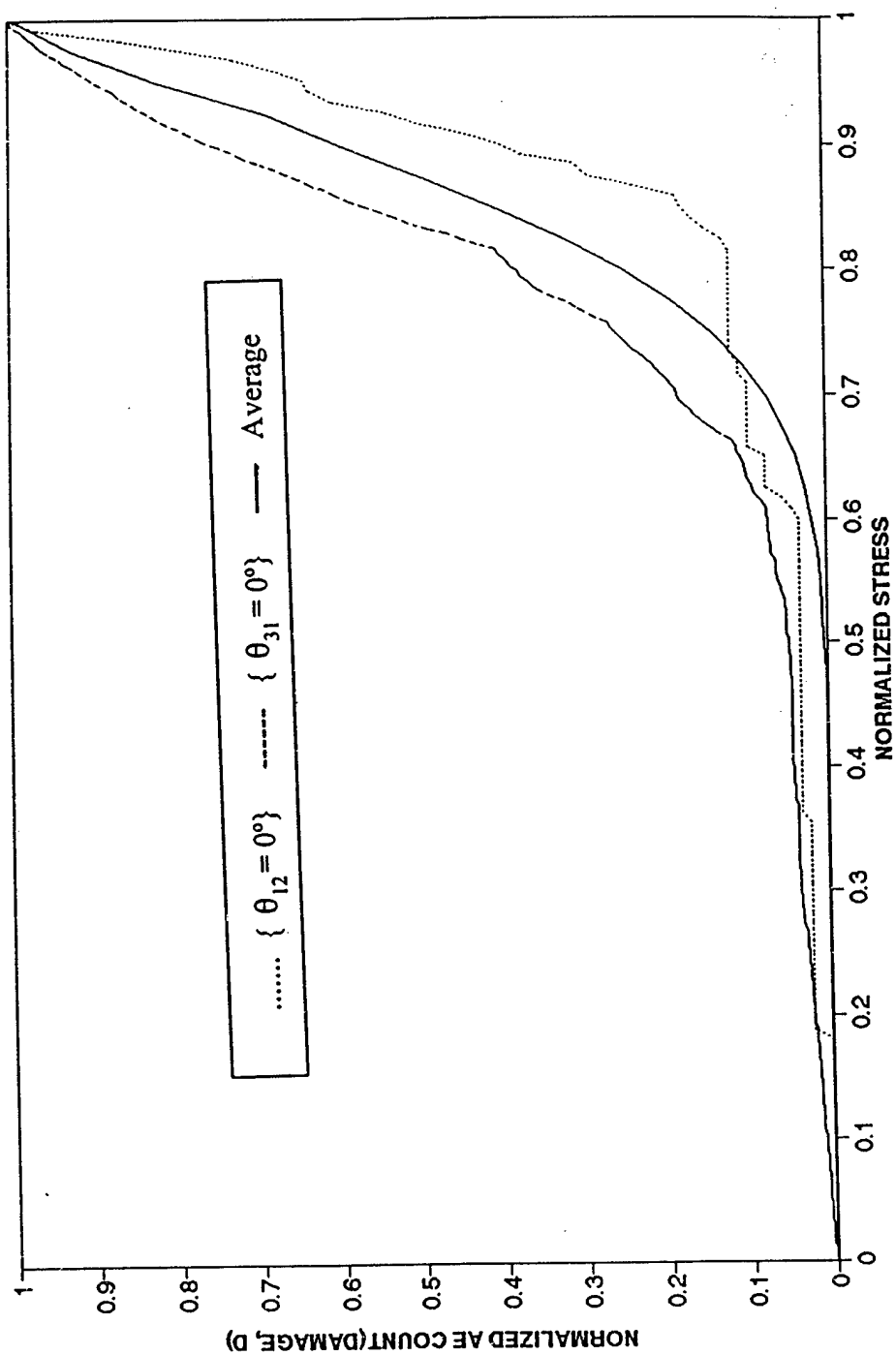


Figure 11: Evolution of damage as function of normalized stress

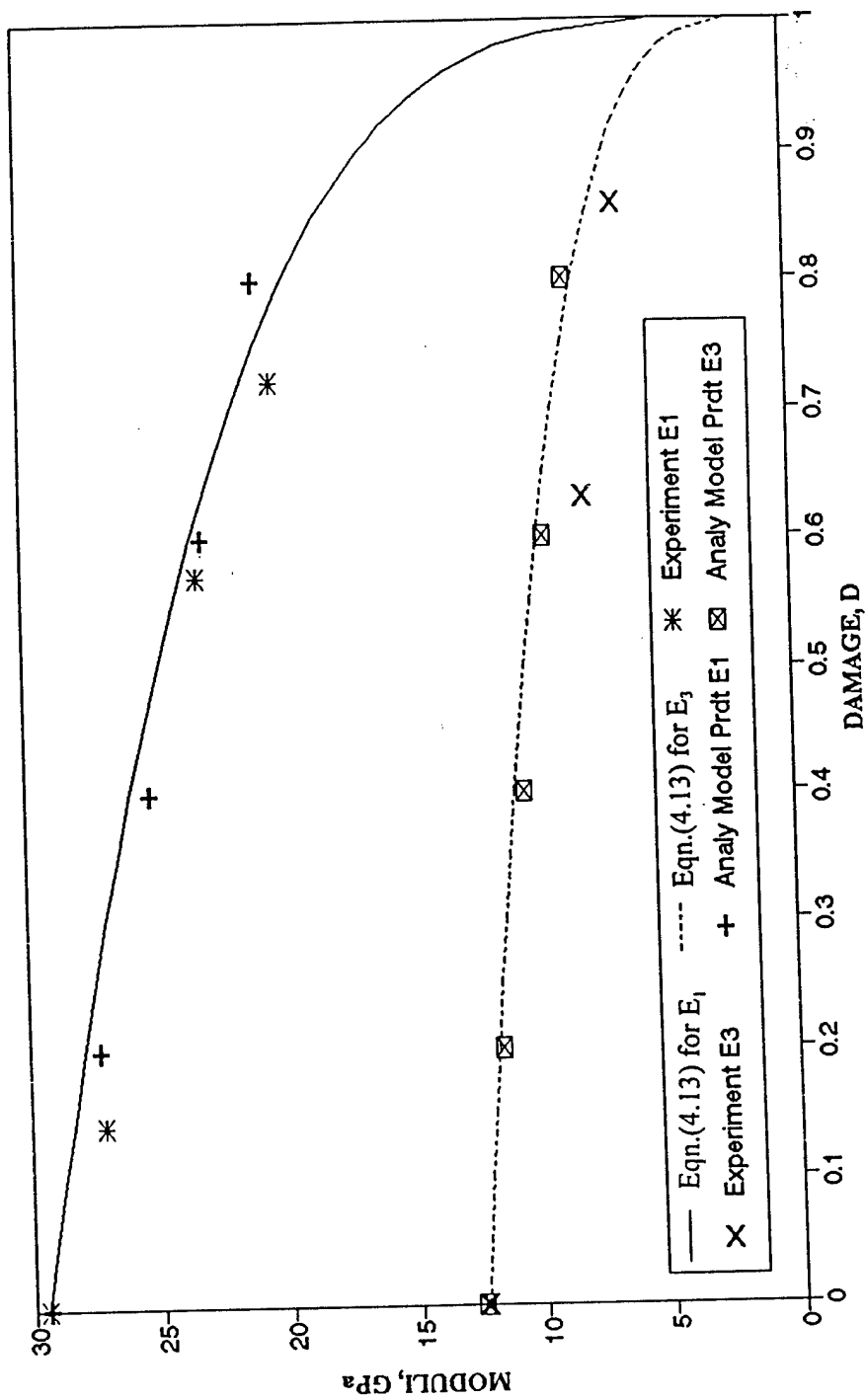


Figure 12 : Analytical model predictions and experimental results as function of damage

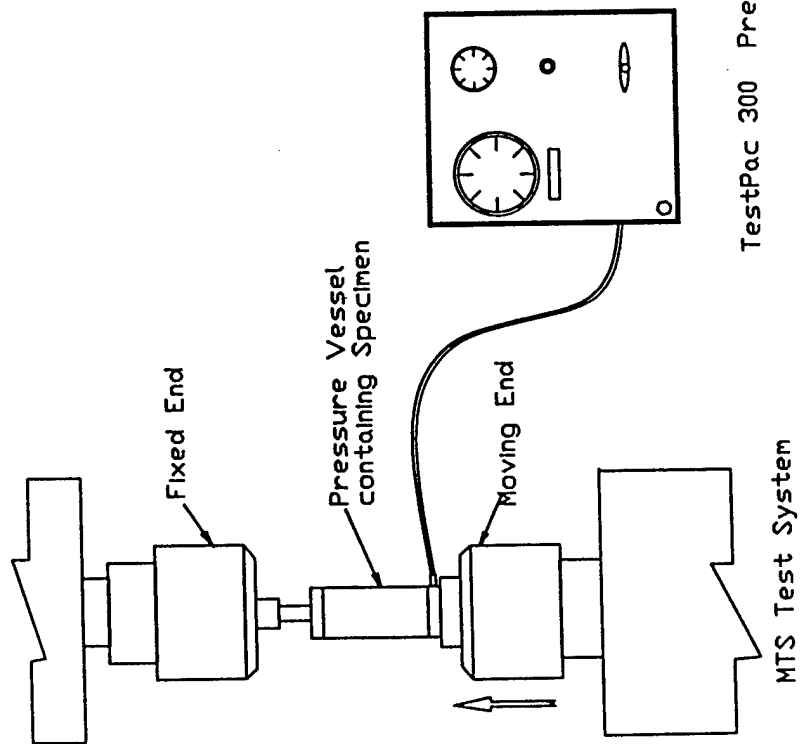


Figure 13 : Confined Pressure Experimental Arrangement

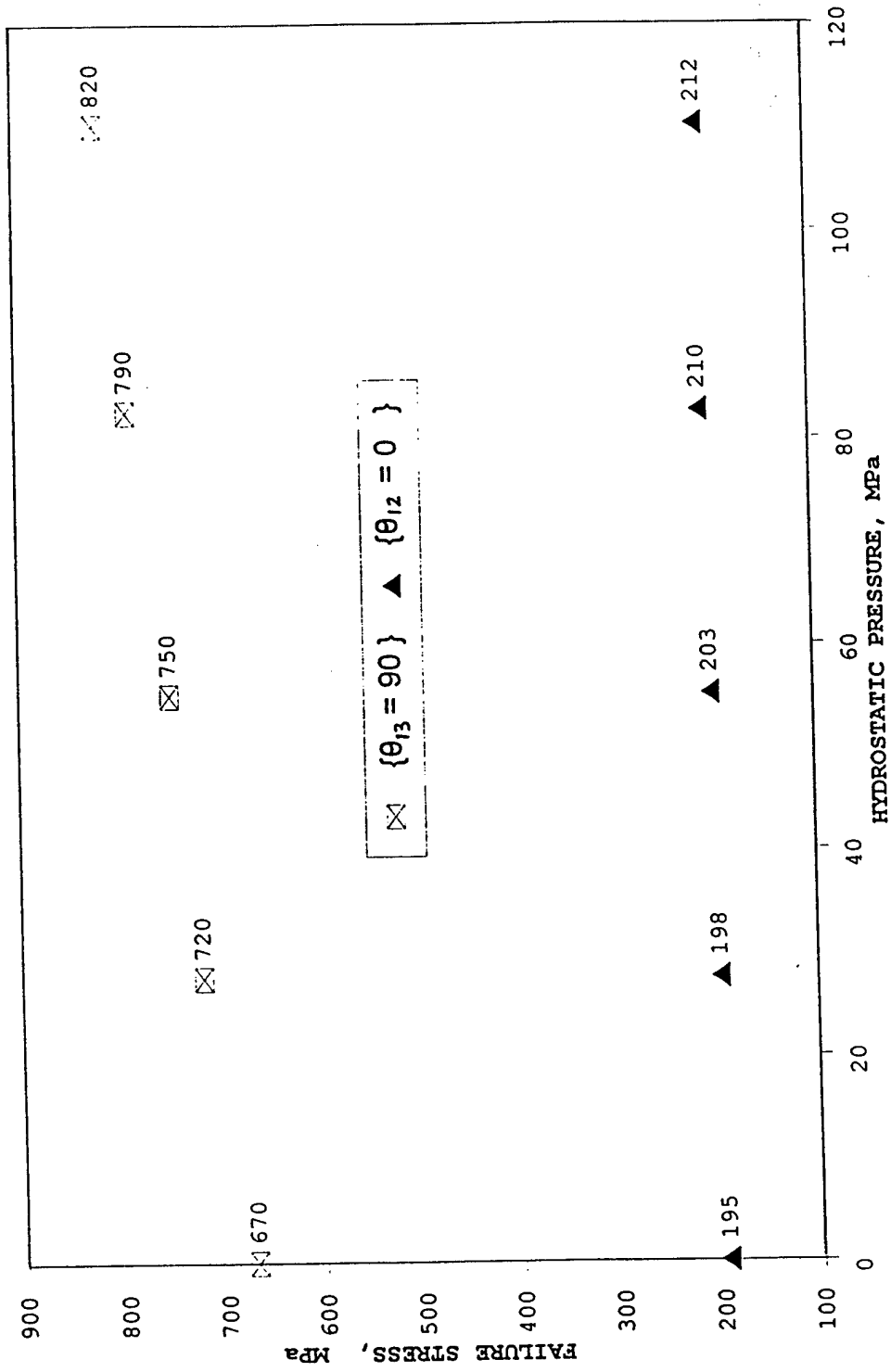


Figure 14: Compressive strength of the material variation with confining pressure

REPORT OF INVENTIONS AND SUBCONTRACTS

(Pursuant to "Patent Rights" Contract Clause) (See Instructions on back)

OMB No. 2000-0098
Expires Aug 31, 2001

The public reporting burden for this collection of information is estimated to average 1 hour per response, including the time for reviewing instructions, searching existing data sources, gathering and maintaining the data needed, reviewing and completing the collection of information, and sending the collection of information. Send comments regarding this burden estimate or any other aspect of this collection of information, including suggestions for reducing the burden, to Department of Defense, Washington Headquarters Services, Directorate for Information Operations and Reports (2000-0098), 1215 Jefferson Davis Highway, Suite 1204, Arlington, VA 22202-4302. Respondents should be aware that notwithstanding any other provision of law, no person shall be subject to any penalty for failing to comply with a collection of information if it does not display a currently valid OMB control number.

PLEASE DO NOT RETURN YOUR COMPLETED FORM TO THIS ADDRESS. RETURN COMPLETED FORM TO THE CONTRACTING OFFICER.

1. NAME OF CONTRACTOR/SUBCONTRACTOR University of Maryland Baltimore County		2. NAME OF GOVERNMENT PRIME CONTRACTOR		3. TYPE OF REPORT (X one) a. INTERNAL <input checked="" type="checkbox"/> b. FINAL	
a. CONTRACT NUMBER DAAH04-95-2-0004		c. CONTRACT NUMBER		4. REPORTING PERIOD (YYYYMMDD) a. FROM 1995/06/15 b. TO 1998/07/31	
b. ADDRESS (Include ZIP Code) 1000 Hilltop Circle Baltimore, MD 21250		d. AWARD DATE (YYYYMMDD)		5. AWARD DATE (YYYYMMDD)	

SECTION I - SUBJECT INVENTIONS

5. "SUBJECT INVENTIONS" REQUIRED TO BE REPORTED BY CONTRACTOR/SUBCONTRACTOR (If "None," so state)

NAMES OF INVENTOR(S) (Last, First, Middle Initial)	TITLE OF INVENTION(S)	DISCLOSURE NUMBER, PATENT APPLICATION SERIAL NUMBER OR PATENT NUMBER a.	ELECTION TO FILE PATENT APPLICATIONS (X)				CONFIRMATORY INSTRUMENT OR ASSIGNMENT FORWARDED TO CONTRACTING OFFICER (X)
			(1) UNITED STATES		(2) FOREIGN		
a.	b.	a.	(a) YES	(b) NO	(a) YES	(b) NO	e.
	None						

6. EMPLOYER OF INVENTOR(S) NOT EMPLOYED BY CONTRACTOR/SUBCONTRACTOR		9. ELECTED FOREIGN COUNTRIES IN WHICH A PATENT APPLICATION WILL BE FILED	
(1) (a) NAME OF INVENTOR (Last, First, Middle Initial)	(2) (a) NAME OF INVENTOR (Last, First, Middle Initial)	(2) FOREIGN COUNTRIES OF PATENT APPLICATION	
(b) NAME OF EMPLOYER	(b) NAME OF EMPLOYER		
(c) ADDRESS OF EMPLOYER (Include ZIP Code)	(c) ADDRESS OF EMPLOYER (Include ZIP Code)		

SECTION II - SUBCONTRACTS (Containing a "Patent Rights" clause)

6. SUBCONTRACTS AWARDED BY CONTRACTOR/SUBCONTRACTOR (If "None," so state)				SUBCONTRACT DATES (YYYYMMDD)	
NAME OF SUBCONTRACTOR(S) a.	ADDRESS (Include ZIP Code) b.	SUBCONTRACT NUMBER(S) c.	DESCRIPTION OF WORK TO BE PERFORMED UNDER SUBCONTRACT(S) d.	(2) ESTIMATED COMPLETION	
				(1) AWARD	(2) ESTIMATED COMPLETION

SECTION III - CERTIFICATION

7. CERTIFICATION OF REPORT BY CONTRACTOR/SUBCONTRACTOR (Not required if: (X) as appropriate)		NONPROFIT ORGANIZATION	
I certify that the reporting party has procedures for prompt identification and timely disclosure of "Subject Inventions," that such procedures have been followed and that all "Subject Inventions" have been reported.			
a. NAME OF AUTHORIZED CONTRACTOR/SUBCONTRACTOR OFFICIAL (Last, First, Middle Initial) KHAN, A. S.	b. TITLE Professor & P.I.	c. SIGNATURE Richard S. Khan	d. DATE SIGNED Oct. 28, 98

PREVIOUS EDITION MAY BE USED.

DD FORM 882, JAN 1999 (EG)

WHSDIOR, Jan 98